Modelling and simulation of phase transformation-mechanics coupling using a phase field method

Kais Ammar

ParisTech
INSTITUT DES SCIENCES ET TECHNOLOGIES
PARIS INSTITUTE OF TECHNOLOGY

MINES ParisTech

École doctorale n°432 :
Sciences des Métiers de l'Ingénieur

Doctorat ParisTech

T H È S E

pour obtenir le grade de docteur délivré par

l'École nationale supérieure des mines de Paris

Spécialité « Sciences et Génie des Matériaux »

présentée et soutenue publiquement par

Kais AMMAR

le 20 Janvier 2010

Modelling and Simulation of Phase Transformation-Mechanics coupling Using a Phase Field Method

~ ~ ~

Modélisation et simulation du couplage changement de phases-mécanique par la méthode des champs de phases

Directeurs de thèse : **Georges CAILLETAUD & Samuel FOREST**
Co-encadrement de la thèse : **Benoît APPOLAIRE**

Jury

Thomas ANTRETTER, Professeur, Institut für Mechanik, Montanuniversität Leoben	Rapporteur
Alphonse FINEL, Directeur de Recherche, ONERA Chatillon	Rapporteur
Jean-Baptiste LEBLOND, Professeur, Institut Jean Le Rond d'Alembert, Université Paris VI	Examinateur
Mathis PLAPP, Maitre de Recherche, Lab. Phys. Mat. Cond., Ecole Polytechnique, Palaiseau	Examinateur
Benoit APPOLAIRE, Maitre de Recherche, ONERA Chatillon	Examinateur
Samuel FOREST , Directeur de Recherche, Centre des Matériaux, MINES ParisTech	Examinateur
Georges CAILLETAUD , Professeur, Centre des Matériaux, MINES ParisTech	Examinateur

T H È S E

MINES ParisTech
Centre des Matériaux, UMR CNRS 7633
BP 87, 91003 Evry Cedex, France

Remerciements

Le présent travail a été effectué au Centre des Matériaux de l'Ecole Nationale Supérieure des Mines de Paris. J'adresse mes remerciements à Monsieur Esteban Busso, directeur du Centre des Matériaux, pour m'avoir offert l'opportunité de mener à bien cette thèse dans un environnement de travail efficace et agréable.

Durant ces 3 ans, j'ai eu la grande chance de pouvoir travailler sous la direction d'une Troïka formée de Georges CAILLETAUD, Samuel FOREST et Benoit APPOLAIRE. Je leur suis très reconnaissant pour leur soutien, leurs encouragements, leur enthousiasme et pour tout le temps qu'ils m'ont consacré pour me faire partager leur savoir et leur créativité, et ce malgré un emploi du temps très chargé. Les agréables moments passés ensemble au cours de ces trois années m'ont énormément apporté autant sur le plan humain que sur le plan scientifique. Cette expérience enrichissante sera très utile pour la suite de ma carrière. J'espère que ce travail est le début d'une longue collaboration entre nous.

Je souhaite remercier tous les membres de mon jury de thèse, Alphonse FINEL et Thomas ANTRETTER pour avoir accepté d'en être les rapporteurs, Jean-Baptiste LEBLOND, président de ce jury, ainsi que Mathis PLAPP pour avoir participé au jury. Je les remercie surtout pour leur esprit critique et leurs conseils enrichissants, qui m'ont permis d'éclaircir mes idées afin de bien poursuivre les développements de mes travaux.

Tendres pensées pour tout le personnel du Centre des Matériaux, aux équipes: administrative, accueil, bibliothèque, VAL et COCAS... et tous ceux qui ont contribué de près ou de loin à ce travail.

Clin d'oeil à tous mes amis, avec qui j'ai passé le plus de temps et qui m'ont supporté lors de ces trois années, mes amis de bureau b108 : Filip, Benoît, Yoann et Lingtao, mes amis de foot, ainsi que tous les thésards du Centre des Matériaux. Ce fut un plaisir de travailler à leurs côtés dans la bonne humeur.

Je ne trouverai jamais les mots assez justes pour vous remercier: mes parents, mon frère Sofien et mes deux sœurs Khawla et Meriem, pour votre amour, vos encouragements et la patience que vous avez eue à m'écouter baragouiner des heures sur mes recherches. J'espère arriver un jour à vous donner un peu de tout ce que j'ai pu recevoir de votre part.

Résumé

Nous proposons un cadre générique, permettant l'incorporation des différentes lois de comportement de mécanique linéaires ou non-linéaires (i.e. élastoviscoplastique) dans les approches des champs de phases utilisées pour la modélisation et la simulation de la mobilité d'interfaces diffuses. Dans ce cadre, une formulation par éléments finis des modèles couplés champ de phases-élastoplasticité pour les alliages binaires est développée dans le formalisme général de la thermodynamique des milieux continus. Cette formulation est basée sur la théorie d'équilibre des microforces, proposée par Gurtin, où une équation supplémentaire, fonction du paramètre d'ordre et de son gradient, est introduite. La formulation est employée pour simuler les évolutions morphologiques complexes des microstructures hétérogènes et décrire l'interface diffuse entre deux phases en présence des contraintes induites par transformation de phase.

En utilisant les principes de la thermodynamique des processus irréversibles, les lois de comportement et les équations d'évolution sont clairement exposées et séparées dans la formulation de sorte que des modèles non-linéaires et fortement couplés puissent être implantés plus facilement dans un code par éléments finis. Cette formulation peut être appliquée aux corps finis périodiques et non périodiques, aux microstructures hétérogènes. Les conditions initiales et les conditions aux limites en paramètre d'ordre et en concentration ainsi que leurs quantités duales sont clairement énoncées. Des techniques d'homogénéisation ont été utilisées pour décrire le comportement dans les interfaces diffuses. Les conséquences de ces choix de modélisation ont été déterminées en ce qui concerne les effets des contraintes mécaniques sur les équilibres de phases et la cinétique de transformation. L'ensemble des équations d'évolution couplées, à savoir l'équation d'équilibre statique local, l'équation de champ de phases et l'équation de conservation de la masse, est résolu en utilisant la méthode des éléments finis pour la discrétisation spatiale et un schéma implicite des différences finies pour la discrétisation temporelle.

Afin d'illustrer l'intérêt de l'approche proposée, des calculs par éléments finis ont été effectués sur des situations élémentaires telles que le calcul des concentrations d'équilibre des phases en présence de contraintes et la croissance de précipités dans une matrice élastique ou élasto-plastique, situations pour lesquelles des solutions analytiques pour des interfaces parfaites sont disponibles.

Abstract

A general constitutive framework is proposed to incorporate linear and nonlinear mechanical behaviour laws (i.g. elastoviscoplasticity) into a standard phase field model. A finite element formulation of a coupled phase field/diffusion/mechanical problem for alloys is proposed within the general framework of continuum thermodynamics. This formulation is based on the concept of generalized stresses as proposed by Gurtin, where an additional balance equation for generalized stresses, called microforces, associated with the order parameter and its first gradient, is postulated. The formulation is used to simulate the complex morphological evolutions of the heterogeneous microstructures and to describe the diffuse interface between two phases in the presence of the stresses induced by phase transformation.

Using the principles of the thermodynamics of irreversible processes, the balance and constitutive equations are clearly separated in the formulation. Also, boundary and initial conditions for the displacement, concentration and order parameter and their dual quantities are clearly stated within the formulation. The theory is shown to be well-suited for a finite element formulation of the initial boundary value problems on finite size specimens with arbitrary geometries and for very general non-periodic or periodic boundary conditions. In the diffuse interface region where both phases coexist, mixture rules taken from homogenization theory are introduced into the formulation. The consequences of the choice of a specific interface behaviour is investigated, with regard to the mechanical effect on phase equilibria (equilibrium compositions and volume fractions of the coexisting phases), as well as on the transformation kinetics. The set of coupled evolution equations, which are the local static equilibrium, the balance of generalized stresses and the balance of mass, is solved using a finite element method for the space discretization and a finite difference method for the temporal discretization.

To validate the numerical finite element implementation and to illustrate the ability of the proposed model to handle precipitation together with mechanical contribution effect, some elementary initial boundary value problem in coupled diffusion-elasto-plasticity on finite size specimens has been solved and validated against corresponding sharp interface analytical solutions.

Table des matières

I Introduction **1**
I.1 Context of the thesis . . . 2
I.2 Phase transformation-mechanics coupling . . . 2
I.3 Aims . . . 5
I.4 Outline of the thesis . . . 5
I.5 Notation . . . 6

II Finite element formulation of a phase field model **11**
II.1 Introduction . . . 12
II.2 Balance of generalized stresses . . . 13
II.2.1 Principle of virtual power . . . 13
II.2.2 State laws and dissipation potential . . . 14
II.3 Finite element implementation . . . 16
II.3.1 Variational formulation . . . 16
II.3.2 Discretization . . . 17
II.4 Formulations of the homogeneous free energy . . . 19
II.4.1 Introduction . . . 19
II.4.2 Polynomial formulation . . . 19
II.4.3 Interpolating free energy densities . . . 20
II.4.4 Identification of parameters . . . 23
II.4.5 Phase equilibrium compositions . . . 24
II.5 Numerical simulations . . . 24
II.5.1 Plane interface evolution . . . 24
II.5.1.1 Mass conservation condition . . . 27
II.5.1.2 Effect of the free energy height b_i . . . 27
II.5.2 Growth of a single precipitate . . . 28
II.5.2.1 Gibbs-Thomson equation . . . 28
II.5.2.2 Mesh sensitivity . . . 32
II.5.3 Phase field simulation for Ostwald ripening . . . 35
II.6 Application: oxidation of zirconium . . . 35
II.7 Conclusion . . . 38

III Elasto-plastic phase field model **43**
III.1 Introduction . . . 44
III.2 Phase-field/diffusion/mechanical model . . . 46
III.2.1 Principle of virtual power and balance equations . . . 46
III.2.2 Thermodynamical formulation . . . 47
III.3 Free energy and dissipation potential . . . 49
III.3.1 Partition of free energy and dissipation potential . . . 49
III.3.2 Chemical contribution . . . 49

III.3.3 Mechanical contribution . . . 50
III.4 Phase field approach and homogenization methods . . . 50
III.4.1 Multiphase approach . . . 50
III.4.2 Voigt/Taylor model . . . 53
III.4.3 Reuss/Sachs model . . . 54
III.4.4 Comparison with existing interpolation schemes . . . 54
III.4.5 Expression of the phase field-elastic coupling terms . . . 55
III.5 Two-phase elastoplastic alloy with hardening . . . 57
III.6 Implementation in a finite element code . . . 59
III.6.1 Discretization . . . 60
III.6.2 Programming of finite element constitutive equations . . . 62
III.6.2.1 Runge-Kutta method . . . 63
III.6.2.2 Θ-method . . . 67
III.7 Conclusions . . . 67

IV Coupled diffusion-elastoplasticity problems 71
IV.1 Introduction . . . 72
IV.2 Two-dimensional problems . . . 72
IV.2.1 Plane strain . . . 72
IV.2.2 Axisymmetric case . . . 73
IV.2.3 Generalized plane strain element (2.5D) . . . 74
IV.3 Coherent phase diagram in microelasticity . . . 74
IV.3.1 Cahn-Larché coherent phase diagram . . . 74
IV.3.1.1 Cahn-Larché analytical solutions . . . 74
IV.3.1.2 Phase field calculations . . . 77
IV.3.2 Effect of composition-dependent elastic strain . . . 81
IV.3.2.1 Analytical solutions . . . 81
IV.3.2.2 Numerical calculations . . . 82
IV.4 Growth kinetics of an oxide layer . . . 84
IV.4.1 Mechanical behavior of the misfitting planar oxide layer problem . . . 84
IV.4.2 Interfacial equilibrium concentration . . . 85
IV.4.3 Growth kinetics . . . 86
IV.4.4 Numerical results . . . 87
IV.5 Growth of an isotropic misfitting cylindrical precipitate . . . 91
IV.5.1 Elastic analysis . . . 91
IV.5.2 Numerical calculations against the analytical solutions . . . 93
IV.6 Growth of an isotropic spherical matrix . . . 97
IV.6.1 Analytical analysis . . . 97
IV.6.2 Equilibrium concentration at the interface . . . 99
IV.6.3 Phase field calculations . . . 99
IV.7 Conclusion . . . 103

Conclusions and future work 105

References 110

A Algorithm to calculate equilibrium concentrations of both phases 123

B Derivation of the elastic strain and the effective elasticity tensor 129

C Expression of the total strain rate tensors for both phases 131

D Calculation of the stiffness matrices 133

E Calculation of the residual vector R and jacobian matrix J for the elastoplastic phase field model 135

F Expressions of the equilibrium compositions and the molar fraction for the two-phase coherent phase equilibria 139

G Mechanical equilibrium of a misfitting planar oxide layer 141

H Mechanical equilibrium of an isotropic misfitting cylindrical precipitate in an isotropic matrix 145

I Mechanical solution for a misfitting spherical precipitate in an isotropic matrix 151

Chapitre -I-

Introduction

Contents

I.1 Context of the thesis 2
I.2 Phase transformation-mechanics coupling 2
I.3 Aims 5
I.4 Outline of the thesis 5
I.5 Notation 6

I.1 Context of the thesis

This project is supported by the SYSTEM@TIC PARIS-REGION ("World class" French Cluster). It is the competitive Cluster of Ile-de-France, which has been created in 2005 and devoted to complex systems and software. It brings together more than 200 players involved in 37 cooperative R&D projects, such as AIRBUS, CEA, DASSAULT SYSTEMES, EADS INNOVATION WORKS, ONERA, SNECMA... This thesis is a part of a larger research project, developed within System@TIC. The project is organized as a "sub-projects cluster", which are IOLS (Infrastructures and Software Tools for Simulation) and its follow-up EHPOC (High Performance Environment for Optimization and Design). Each sub-project is driven by precise goals. The main targets of IOLS/EHPOC projects were:

- The design and the development of generic software and platforms for products and process global design and optimisation (coupling, large-scale meshes, visualisation...).
- The development of industrial platforms, multiscale and multiphysics software dedicated to global design in order to produce robust numerical design tools, especially in the materials field, enabling robust multidisciplinary optimization of complex products and systems. These platforms and software suite are a corner stone for industrial innovation and competitiveness, design and development cycles reduction, productivity improvement.

I.2 Phase transformation-mechanics coupling

Many of the important properties of a material can be engineered by controlling its solid state phase transformations and the accompanying microstructure evolution. Modeling phase transformations is thus a primordial task for finding new materials with new properties, for improving the performance of existing materials, or designing new processes. Mechanical properties of all important materials of modern technology are strongly dependent on their microstructure, i.e. on the shape and spatial arrangement of the different phases in the materials. It is thus important, from both fundamental and industrial viewpoints to understand and to combine the properties of different coexisting phases, and even to achieve better properties thanks to particular spatial distributions and morphologies, which introduce internal scales besides the scale of the interfaces. These distributions and morphologies are most of the time complex because they result from complex evolutions controlled by the interaction between different phenomena: e.g. chemical diffusion, interfacial energies, mechanics (elasticity, plasticity ...), electro-magnetism.

In crystalline solids, diffusional phase transformations are usually accompanied by deformation induced by change in crystalline structures between coexisting phases, i.e. difference of crystal spatial rearrangement of orientation and lattice mismatch between two coherent phases (Khachaturyan, 1983). The stresses arising from coherency strain can have a strong influence on phase equilibrium (e.g., equilibrium compositions of coexisting phases and their equilibrium volume fractions), driving forces for nucleation, growth and coarsening, thermodynamic factors in diffusivity, and precipitate shape and spatial distribution. Incorporation of the elastic interactions in models of phase transformations not only allows for developing a fundamental understanding of the formation of these microstructures, but also provides the opportunity to engineer new microstructures of salient features for novel applications. Therefore, it is desirable to have a model that is able to overcome the nonlinear free boundary problem as well as to predict the formation and time-evolution of coherent microstructural patterns. The main difficulty of such a task lies in the tight coupling between the complex interfaces evolutions and the fields, common to many free boundary problems, with multi-physics coupling. One observes in current literature a strong endeavour to develop microstructure evolution simulation schemes coupled

with complex mechanical material behaviour ranging from heterogeneous elasticity to general elastoviscoplasticity. Generally, there are generally two types of approaches for treating the free boundary problems (interfaces): the sharp interface description (Fratzl et al., 1999) and the diffuse-interface models (Cahn, 1961; Emmerich, 2003).

In a sharp-interface description, different phases are modelled as distinct regions in space separated by interfaces with zero thickness. There are two versions of the sharp-interface model, which we shall call the static and dynamic versions. For a diffusion-controlled process, microstructure evolution is modelled by solving the non-steady state diffusion equation with appropriate boundary conditions specified at the interfaces (Langer and Sekerka, 1975). However these sharp interface approaches, so-known also as front tracking techniques, lead to significant difficulties due to the requirement of tracking interface position with complex shapes every time step, during microstructure evolutions in handling topological changes in interface pattern such as merging or splitting of objects (precipitates, bubbles...), especially in three dimensions. Hence, some attempts to achieve this goal have circumvented the difficulty by undertaking standard finite element calculations with prescribed interface kinetics, i.e. without the feedback of mechanics on phase transformation, e.g. (Ganghoffer et al., 1994; Barbe et al., 2008).

The second model which has been proposed for describing microstructure evolution induced by diffusive phase is the phase field model. The idea was to replace the sharp interface by diffuse regions with a certain thickness using a physically motivated or artificial, continuous, non-conserved phase field. Across the diffuse interfaces between different phases or domains, the field variables vary continuously from one uniform value corresponding to one type of phase or domain to another uniform value corresponding to another phase or domain. Instead of defining a moving boundary condition, the interface movement, and thus the microstructure evolution, is described by the temporal evolution of the phase field according to a set of well established kinetic equations (Cahn, 1961; Allen and Cahn, 1979). The phase-field approach offers a number of advantages:

1. The phase field approach is suitable for modeling free boundary problems without having to explicitly track the usually complicated interfaces, for different shapes, during a microstructure evolution, with the help of order parameters that vary smoothly in space. This presents great advantages for modelling the evolution of complex three-dimensional microstructures and arbitrary morphologies for which conventional front-tracking approaches would have been impossible.

2. It can be applied to a wide range of microstructural evolution problems related to vastly different materials processes by appropriately choosing either physical or artificial field variables. It have been successfully applied to many different materials processes such as alloy solidification (Wang et al., 1993a; Bi and Sekerka, 1998; Charach and Fife, 1999; Ode et al., 2000; Dejmek et al., 2004; Takaki et al., 2005), solid-state precipitation (Wang et al., 1998; Guo et al., 2008; Ma et al., 2002), spinodal decomposition (Seol et al., 2003), microstructural evolution in polycrystalline materials (Warren et al., 2003; Gránásy et al., 2006), crystal nucleation (Landheer et al., 2009), recrystallization process (Takaki et al., 2006; Abrivard, 2009), dendritic growth (Suzuki et al., 2002; Bragard et al., 2002; George and Warren, 2002; Kaoui et al., 2005), coarsening and grain growth (Dreyer and Müller, 2000; Dreyer and Müller, 2001; Ratke and Voorhees, 2002; Simmons et al., 2004), thin film patterning (Liu et al., 2003; Eggleston, 2001) and many others.

3. It is possible to link phase-field models with existing or future thermodynamic, kinetic and crystallographic databases for obtaining the materials parameters for applications to more complicated systems such as multicornponent alloys. It is also possible to directly construct the free energy function of a phase-field model from existing databases using the CALPHAD method for instance (Grafe et al., 2000a; Grafe et al., 2000b; Zhu et al.,

2002). The compositional dependence of atomic mobilities from databases can also easily be incorporated.

4. Finally, phase-field method has been extended and utilized across many fields of materials science, which can incorporate, systematically, the effect of the coherency induced by lattice mismatch and the applied stress and dislocation dynamics (Wang et al., 2001; Koslowski et al., 2002; Rodney et al., 2003; Zhou et al., 2007) as well as the ferroelectric materials (Schrade et al., 2006; Schrade et al., 2007; Su and Landis, 2007), magnetic fields (Koyama, 2008) and fracture (Karma et al., 2001; Karma and Lobkovsky, 2004; Marconi and Jagla, 2005).

Indeed, the phase field method has emerged as the most powerful method for tackling microstructure evolutions during phase transformations, especially when elastic coherency stresses are generated in solids. The introduction of the elastic coherency strains in the phase field models for solid-solid phase transformations, initiated by Khachaturyan (Khachaturyan, 1983) and have succeeded in predicting some complex microstructure evolutions driven by the interplay of diffusion and elasticity, (Onuki, 1989; Wang et al., 1993b; Wang and Khachaturyan, 1995a; Le Bouar et al., 1998; Wang et al., 1998). It is only very recently that some phase field models have been enriched with nonlinear mechanical behaviour, extending the range of applications and materials which can be handled by the phase field approach (Guo et al., 2005; Uehara et al., 2007; Ubachs et al., 2005; Guo et al., 2008; Yamanaka et al., 2008; Zhou et al., 2008).

For a general point of view, the description of elasto-viscoplastic behavior of solid heterogeneous media with multiphase materials during solid-solid phase transformations is a very difficult task. In order to achieve this goal and circumvent this difficulty, two ways are mainly used. In the first method, the material behaviour is described by a unified set of constitutive equations including material parameters that depend on the nature of the phase. The prediction of mechanical properties of heterogeneous materials can be obtained through statistical averaging of their limit values known for each phase (Gaubert et al., 2008; Gaubert et al., 2009). Numerical modelling of the non-linear behavior in solids during diffusive phase transformation have been also established by (Leblond et al., 1986a; Leblond et al., 1986b; Fischer et al., 2000). This method is recently used to incorporate viscoplasticity laws into the standard phase field approach in (Ubachs et al., 2004; Ubachs et al., 2005) for tin–lead solders. In the second method, one distinct set of constitutive equations is attributed to each individual phase α at any material point. The local behaviour law relating the macroscopic variables, at this material point, is obtained by averaging the corresponding non-uniform local stress and strain in each phase using the well–known homogenization schemes inside the smooth interface zone. Each phase at a material point then possesses its own stress/strain tensor $\underset{\sim}{\sigma}_k, \underset{\sim}{\varepsilon}_k$. The overall strain and stress quantities at this material point must then be averaged or interpolated from the values attributed to each phases. Thus, No correspondence of material parameters is then needed between the phase behaviour laws. Several homogenization methods in the mechanics of heterogeneous materials are available to perform this averaging or interpolation, in the region where both phases coexist.. They are based on the definition of a representative volume element (RVE) at each material point in which mean strain and stress can be defined for each phase (Suquet, 1997; Jeulin and Ostoja-Starzewski, 2001).

Many numerical methods have been proposed to solve the coupled phase field/diffusion/mechanics field equations. They are those commonly used to solve partial differential equations. Hence, the finite volume scheme is adopted in (Appolaire and Gautier, 2003; Furtado et al., 2006; Appolaire et al., 2009) whereas a mixed finite difference-finite element scheme is used in (Nakajima et al., 2006). In (Gaubert et al., 2008; Chen and Hu, 2004), the Fourier method is used for heterogeneous microstructures. Previous attempts to apply the finite element method to phase transformations problems have been presented in (Chan and Rey, 1995; Ubachs et al.,

2005) for solving Cahn–Hilliard equation, in (Danilov and Nestler, 2005) for the simulation of solidification processes and in (Schrade et al., 2007) for ferroelectric materials. The finite element method is generally well–suited for handling such initial boundary value problems on finite size specimens, in contrast to the Fourier methods classically used for heterogeneous microstructures with periodic unit cell simulations.

I.3 Aims

The aims of this present work are:

- To develop a general framework that combines standard phase field approaches with a different complex mechanical behaviour for each phase. The formulation is built step by step by incorporating complex material behaviour, ranging from pure diffusion problem to general diffusion-nonlinear mechanics models, into the phase field approach following a consistent continuum thermodynamic framework in conjunction with the concept of generalized stresses as proposed by Gurtin (Gurtin, 1996). Mixture rules taken from homogenization theory are introduced into the formulation.

- To describe the finite element implementation and programming of the proposed non-linear elastoplastic phase field model with different homogenization schemes in the finite element code Zebulon.

- To solve some elementary initial boundary value problems in coupled diffusion-elasto-plasticity on finite size specimens and to validate the numerical finite element implementation against corresponding sharp interface analytical solutions. The simulations presented in this work are performed with the finite element model recently proposed in (Ammar et al., 2009a; Ammar et al., 2009c).

I.4 Outline of the thesis

This whole work has been broadly structured into three chapters, where each one is motivated by the conclusions of previous ones, and motivates the following developments. It is organized as follows:

In chapter II, a finite element formulation of a phase field model for alloys is proposed within the general framework of continuum thermodynamics in conjunction with the concept of generalized stresses as proposed by Gurtin (Gurtin, 1996). A generalized principle of virtual power is postulated involving generalized stresses and used to derive the balance equations for generalized stresses. The principles of the thermodynamics of irreversible processes, which are the energy and entropy principles, are explicited in the isothermal case. Consequently, balance and constitutive equations are clearly separated in the formulation. Also, boundary conditions for the concentration and order parameter and their dual quantities are clearly stated. The clear analogy between the proposed variational formulation and that of conventional computational mechanics leads us to the derivation of an implicit finite element scheme to solve the considered initial boundary value problem, based on time and space discretizations. For an illustrative purpose, the model is used to investigate the formation and the evolution of a plane and curved diffuse interface between two phases. In order to study the sensitivity of numerical results, several validation calculations were carried out concerning the choice of the free energy density and its parameters, the mesh size and the types of elements. Finally, finite element calculations were performed to investigate the growth of an oxide layer at the surface of a pure zirconium slab and to study in particular the effect of initial free surface roughness on subsequent oxidation. The effect of initial free surface

roughness on morphological stability of the oxide layer has been studied in order to show the ability of the finite element method to handle arbitrary conditions on complex boundaries.

The balance and boundary conditions of a fully coupled phase field/diffusion/mechanical problem is presented in chapter III. The constitutive equations for chemical and mechanical processes are formulated by means of the expressions of the free energy potential and the dissipation potential for chemical and mechanical dissipative processes where a specific decomposition of these two potentials into chemical and mechanical contributions is presented. Two mixture rules for strain and stress within the diffuse interface, which are based on the Voigt/Taylor and Reuss/Sachs well–known homogenization schemes, are introduced and compared to the commonly used mixture rules in phase field models. Finally, the implementation of the proposed non-linear elastoplastic phase field model with different homogenization schemes in the finite element code Zebulon is detailed. For the sake of simplicity, the theory is expressed within the small perturbation framework (small strain), under isothermal conditions.

Chapter IV provides a background on the application of the proposed non-linear elastoplastic phase field model to solve some elementary initial boundary values problems in coupled diffusion-elastoplasticity, where the numerical results have been validated against corresponding sharp interface analytical solutions. In order to illustrate the implication of the choice of specific mixture rules for these behaviour laws in the diffuse interface region on the coherent two-phase equilibria, large series of calculations have been undertaken to predict coherent phase diagram in microelasticity when internal stresses are generated by transformation eigenstrains (Cahn and Larché, 1984). Then, the attention is focused on the mechanical effect through the phase field on the transformation kinetics of a planar layer growing at the surface of a pure zirconium slab. The growth mechanism of the oxide layer has been studied considering the effects of the misfit generated stress, the oxide elasticity moduli and the plastic relaxation of the of the transformation strain energy. Finally, the growth of an isotropic misfitting precipitate in an isotropic matrix is investigated. Two particle shapes are considered, which cylindrical and spherical particles. The stored elastic energy effect on the diffusion-controlled growth of an isolated precipitate in a supersaturated matrix has been studied to investigate the effect of plastic accommodation processes on the transformation kinetics, compared with the corresponding pure elastic state and pure chemical transformation.

I.5 Notation

The notations used throughout this work are the following: zeroth, first, second and fourth-rank tensors are respectively denoted by $a, \underline{\boldsymbol{a}}, \underset{\sim}{\boldsymbol{a}}, \underset{\approx}{\boldsymbol{a}}$. The simple and double contractions read . and :. The tensor product is denoted by $\otimes$. The nabla operator is denoted by $\boldsymbol{\nabla}$. It is used extensively to compute the gradient or divergence of scalars, vectors and tensors. For example, $\boldsymbol{\nabla}.\underset{\sim}{\boldsymbol{a}}$ is the divergence of the second order tensor $\underset{\sim}{\boldsymbol{a}}$. The gradient of the scalar a is denoted by $\boldsymbol{\nabla} a$. The time derivative of a is $\dot{a}$. The phases are denoted by indexes α and β.

Notation	Formula
$x = \underline{\boldsymbol{a}} \,.\underline{\boldsymbol{b}}$	$x = a_i b_i$ (scalar product)
$\underline{\boldsymbol{x}} = \underset{\sim}{\boldsymbol{a}}.\underline{\boldsymbol{b}}$	$x_i = a_{ij} b_j$
$\underset{\sim}{\boldsymbol{x}} = \underset{\sim}{\boldsymbol{a}}.\underset{\sim}{\boldsymbol{b}}$	$x_{ij} = a_{ik} b_{kj}$
$x = \underset{\sim}{\boldsymbol{a}} : \underset{\sim}{\boldsymbol{b}}$	$x = a_{ij} b_{ij}$
$\underset{\sim}{\boldsymbol{x}} = \underset{\approx}{\boldsymbol{A}} : \underset{\sim}{\boldsymbol{b}}$	$x_{ij} = A_{ijkl} b_{kl}$
$\underline{\boldsymbol{x}} = \underline{\boldsymbol{a}} \times \underline{\boldsymbol{b}}$	$x_i = \varepsilon_{ijk} a_j b_k$
$\underset{\sim}{\boldsymbol{x}} = \underline{\boldsymbol{a}} \otimes \underline{\boldsymbol{b}}$	$x_{ij} = a_i b_j$
$\underset{\approx}{\boldsymbol{x}} = \underset{\sim}{\boldsymbol{a}} \otimes \underset{\sim}{\boldsymbol{b}}$	$x_{ijkl} = a_{ij} b_{kl}$
Δx	$x_\alpha - x_\beta$

The following symbols are used in this paper:

Symbol	Meaning
a_α, a_β	Equilibrium concentrations at incoherent state
A_k	Thermodynamical force associated with internal variable V_k
b, b_α, b_β	Height of the free energy barrier
c, c_α, c_β	Coherent equilibrium concentrations
c_0	Initial concentration
$c^\star$	Virtual concentration
$\underset{\approx}{\boldsymbol{C}}, \underset{\approx}{\boldsymbol{C}}_\alpha, \underset{\approx}{\boldsymbol{C}}_\beta, \underset{\approx}{\boldsymbol{C}}_{\text{eff}}$	Fourth-order tensor of elasticity moduli
D	Residual dissipation rate
D_ϕ	Phase field dissipation rate
D_c	Chemical dissipation rate
D_u	Mechanical dissipation rate
D_α, D_β	Chemical diffusivities
$\mathcal{D}$	Subdomain of body
E, E_α, E_β	Young's moduli
e	Internal energy density
$\mathcal{E}$	Internal energy of the body
F	Total free energy
f, f_α, f_β	Free energy densities
f_{ch}	Chemical free energy density
$f_e, f_{e\alpha}, f_{e\beta}$	Elastic free energy densities
$f_p, f_{p\alpha}, f_{p\beta}$	Plastic free energy densities
f_u	Mechanical free energy density
$\underline{\boldsymbol{f}}$	Volume force density
g	Double well potential
g_α, g_β	Yield function
$\underline{\boldsymbol{J}}$	Diffusion flux
j	Outgoing diffusion flux

k, k_α, k_β	Curvature of the free energy density
$\mathcal{K}$	Kinetic energy
L	Onsager coefficient
$\underline{\boldsymbol{n}}$	Normal unit vector
$p^{(i)}$	Virtual power density of internal forces
$p^{(e)}$	Virtual power density of long range volume forces
$p^{(c)}$	Virtual power density of generalized contact forces
r_α, r_β	Isotropic hardening variables
R_α, R_β	Scalar variables of isotropic hardening
s	Entropy density
$\underset{\approx}{\boldsymbol{S}}, \underset{\approx}{\boldsymbol{S}}_\alpha, \underset{\approx}{\boldsymbol{S}}_\beta, \underset{\approx}{\boldsymbol{S}}_{\mathrm{eff}}$	Fourth-order compliance tensors
$\mathcal{S}$	Area
t	Time
$\underline{\boldsymbol{t}}$	Traction vector
$\underline{\boldsymbol{u}}$	Displacement field
V	Volume
$\mathcal{V}$	Material representative volume element
V_k	Internal variable
W	Height of double-well barrier
$\underset{\sim}{\boldsymbol{X}}_\alpha, \underset{\sim}{\boldsymbol{X}}_\beta$	Tensor variables of kinematic hardening
$\underline{\boldsymbol{\xi}}$	Vector microstress
z	Volume fraction
α	Composition gradient energy coefficient
$\underset{\sim}{\boldsymbol{\alpha}}_\alpha, \underset{\sim}{\boldsymbol{\alpha}}_\beta$	Kinematic hardening variables
β	Material parameter related to the interface mobility
δ	Interfacial thickness
$\underset{\sim}{\boldsymbol{\varepsilon}}, \underset{\sim}{\boldsymbol{\varepsilon}}_\alpha, \underset{\sim}{\boldsymbol{\varepsilon}}_\beta$	Total strains
$\underset{\sim}{\boldsymbol{\varepsilon}}^e, \underset{\sim}{\boldsymbol{\varepsilon}}^e_\alpha, \underset{\sim}{\boldsymbol{\varepsilon}}^e_\beta$	Elastic strains
$\underset{\sim}{\boldsymbol{\varepsilon}}^\star, \underset{\sim}{\boldsymbol{\varepsilon}}^\star_\alpha, \underset{\sim}{\boldsymbol{\varepsilon}}^\star_\beta$	Eigenstrains
$\underset{\sim}{\boldsymbol{\varepsilon}}^p, \underset{\sim}{\boldsymbol{\varepsilon}}^p_\alpha, \underset{\sim}{\boldsymbol{\varepsilon}}^p_\beta$	Plastic strains
$\gamma, \underline{\boldsymbol{\gamma}}$	Scalar and vector external microforces
$\mu, \mu_\alpha, \mu_\beta$	Chemical potentials
ν_α, ν_β	Poisson's ratios
$\omega_\alpha, \omega_\beta$	Grand potentials
Ω	Dissipation potential
Ω_c	Chemical dissipation potential
Ω_ϕ	Phase field dissipation potential
$\Omega_u, \Omega_{u\alpha}, \Omega_{u\beta}$	Mechanical dissipation potentials
ϕ	Order parameter
$\underline{\boldsymbol{\Phi}}$	Entropy flux
π	Scalar microstress
π_{dis}	Chemical force associated with the dissipative processes

$\underset{\sim}{\boldsymbol{\sigma}}, \underset{\sim}{\boldsymbol{\sigma}}_\alpha, \underset{\sim}{\boldsymbol{\sigma}}_\beta$	Cauchy stress tensor
γ	Interfacial energy
$\sigma_\alpha^{\mathrm{eq}}, \sigma_\beta^{\mathrm{eq}}$	Von Mises equivalent stress
$\sigma_\alpha^0, \sigma_\beta^0$	Initial yield stress
ζ	Surface density of microtraction

Chapitre -II-

Finite element formulation of a phase field model based on the concept of generalized stresses

Contents

II.1 Introduction . . . 12
II.2 Balance of generalized stresses . . . 13
II.2.1 Principle of virtual power . . . 13
II.2.2 State laws and dissipation potential . . . 14
II.3 Finite element implementation . . . 16
II.3.1 Variational formulation . . . 16
II.3.2 Discretization . . . 17
II.4 Formulations of the homogeneous free energy . . . 19
II.4.1 Introduction . . . 19
II.4.2 Polynomial formulation . . . 19
II.4.3 Interpolating free energy densities . . . 20
II.4.4 Identification of parameters . . . 23
II.4.5 Phase equilibrium compositions . . . 24
II.5 Numerical simulations . . . 24
II.5.1 Plane interface evolution . . . 24
II.5.1.1 Mass conservation condition . . . 27
II.5.1.2 Effect of the free energy height b_i . . . 27
II.5.2 Growth of a single precipitate . . . 28
II.5.2.1 Gibbs-Thomson equation . . . 28
II.5.2.2 Mesh sensitivity . . . 32
II.5.3 Phase field simulation for Ostwald ripening . . . 35
II.6 Application: oxidation of zirconium . . . 35
II.7 Conclusion . . . 38

II.1 Introduction

A continuum thermodynamics framework was proposed in (Fried and Gurtin, 1993; Fried and Gurtin, 1994; Gurtin, 1996) to formulate phase field models accounting for the diffusion of chemical species and phase changes. According to this theory, an additional balance equation for generalized stresses, called microforces in the original theory and associated with the order parameter and its first gradient, is postulated. A clear separation is enforced between basic balance laws, which are general and hold for large classes of materials behaviour, and constitutive equations which are material specific. Consequently, the derivation of the appropriate material constitutive relationships can be further generalized in the presence of dissipative processes such as heat transfer and plastic deformation. This formulation can be applied to finite size non periodic samples and heterogeneous materials where the initial conditions and the boundary/interface conditions for the concentration and order parameter must be clearly stated.

The finite element method is generally well–suited for handling such initial boundary value problems on finite size specimens, in contrast to the Fourier methods classically used for heterogeneous microstructures with periodicity conditions (Chen and Hu, 2004). Previous attempts to apply the finite element method to phase transformations problems have been presented in (Chan and Rey, 1995) for solving Cahn–Hilliard equation, in (Danilov and Nestler, 2005) for the simulation of solidification processes and in (Schrade et al., 2007) for ferroelectric materials.

The objective of the present chapter is to derive a finite element formulation for the phase field diffusion problem from the thermodynamic formulation based on generalized stresses. It will be shown that this enables the use of large classes of constitutive equations and that it fits into the general computational thermomechanical framework used in engineering mechanics as presented in (Besson et al., 2001).

The present model belongs to the class of diffuse interface models, where the local state of an inhomogeneous microstructure is described by a conservative concentration field c and a non-conservative field ϕ associated with the crystalline nature of the phases, the so-called order parameter. It is based on the time-dependent Ginzburg-Landau equation:

$$\beta\dot{\phi} = \alpha\Delta\phi - \frac{\partial f_0}{\partial \phi} \tag{II.1}$$

In the phase field approach, the free energy density for an inhomogeneous system can be approximated by the Ginzburg-Landau coarse-grained free energy functional, which contains a local free energy density $f_0(c,\phi)$ and a gradient energy term:

$$f(c,\phi) = f_0(c,\phi) + \frac{\alpha}{2}\nabla\phi.\nabla\phi \tag{II.2}$$

where the usual specific quadratic contribution with respect to $\nabla\phi$ is adopted here but can be generalized if needed.

This chapter is organized as follows. First, a generalized principle of virtual power is postulated involving generalized stresses. It is used to derive the balance equations for generalized stresses. The introduced power of internal forces then appears in the energy balance equation. The energy and entropy principles of continuum thermodynamics are explicited in the isothermal case. Second, the clear analogy between the proposed variational formulation and that of conventional computational mechanics leads us to the derivation of an implicit finite element scheme to solve the considered initial boundary value problem, based on time and space discretizations. Numerical simulations were performed to investigate the formation and the evolution of a plane and curved diffuse interface between two phases. In order to study the sensitivity of numerical results, several validation calculations were carried out concerning the choice of the free energy density and

its parameters, the mesh size and the types of elements. Finally the method is applied to the prediction of the kinetics of the growth of an oxide layer on zirconium. The finite element method is suitable to study in particular the effect of initial free surface roughness on subsequent oxidation and to investigate morphological stability of the oxide layer.

II.2 Balance of generalized stresses and fundamental statements of thermodynamics

II.2.1 Principle of virtual power

The method of virtual power provides a systematic and straightforward way of deriving balance equations and boundary conditions in various physical situations (Germain, 1973a; Germain, 1973b). The application of this principle to an isolated region requires the determination of the virtual powers of the system of generalized forces applied to the body, in which the generalized stresses are not introduced directly but by the value of the virtual power they produce for a given virtual order parameter $\phi^\star$. Note that macroscopic mechanical effects are not introduced in this chapter. The wording "generalized forces and stresses" is associated with primarily chemical events contributing to the energy equation and correspond to the notion of microforce in (Fried and Gurtin, 1994; Gurtin, 1996).

Guided by Gurtin's theory (Gurtin, 1996), we suppose the existence of a system of generalized forces, defined by a scalar internal microstress π and a vector microstress $\underline{\boldsymbol{\xi}}$ that perform work in conjunction with changes in the configurations of atoms, characterized by the order parameter ϕ and its first gradient. The virtual power of internal generalized forces is defined by the integral over the volume V of a power density, which is assumed a priori to be a linear form represented by the generalized stress measures π and $\underline{\boldsymbol{\xi}}$:

$$\mathcal{P}^{(i)}(\phi^\star, V) = \int_V (\pi\phi^\star - \underline{\boldsymbol{\xi}}.\boldsymbol{\nabla}\phi^\star)\, dv \tag{II.3}$$

$$= \int_V (\pi + \boldsymbol{\nabla}.\underline{\boldsymbol{\xi}})\phi^\star\, dv - \int_{\partial V} (\underline{\boldsymbol{\xi}}.\underline{\boldsymbol{n}})\phi^\star ds \tag{II.4}$$

The next step is to introduce the virtual power of external forces applied to the considered body. It can be split into a virtual power density of long range volume forces, which can include, in general, a volume density of scalar external microforce γ and a vector of external microforce $\underline{\boldsymbol{\gamma}}$:

$$\mathcal{P}^{(e)}(\phi^\star, V) = \int_V (\gamma\phi^\star + \underline{\boldsymbol{\gamma}}.\boldsymbol{\nabla}\phi^\star)\, dv \tag{II.5}$$

$$= \int_V (\gamma - \boldsymbol{\nabla}.\underline{\boldsymbol{\gamma}})\phi^\star\, dv + \int_{\partial V} (\underline{\boldsymbol{\gamma}}.\underline{\boldsymbol{n}})\phi^\star\, ds \tag{II.6}$$

and a virtual power density of generalized contact forces, schematically represented by a surface density ζ of microtraction:

$$\mathcal{P}^{(c)}(\phi^\star, V) = \int_{\partial V} \zeta\phi^\star\, ds \tag{II.7}$$

We do not envisage here a possible power of inertial microforces ($\mathcal{P}^{(a)}(\phi^\star, V) = 0$). According to the principle of virtual power, the total virtual power of all forces vanishes on any subdomain $\mathcal{D} \subset V$ and for any virtual order parameter field $\phi^\star$:

$\forall\phi^\star, \forall\mathcal{D} \subset V$

$$\mathcal{P}^{(i)}(\phi^\star, \mathcal{D}) + \mathcal{P}^{(c)}(\phi^\star, \mathcal{D}) + \mathcal{P}^{(e)}(\phi^\star, \mathcal{D}) + \mathcal{P}^{(a)}(\phi^\star, \mathcal{D}) = 0 \tag{II.8}$$

$$\int_{\mathcal{D}} (\pi + \boldsymbol{\nabla}.\underline{\boldsymbol{\xi}} + \gamma - \boldsymbol{\nabla}.\underline{\boldsymbol{\gamma}})\phi^\star \, dv + \int_{\partial\mathcal{D}} (\zeta - \underline{\boldsymbol{\xi}}.\underline{\boldsymbol{n}} + \underline{\boldsymbol{\gamma}}.\underline{\boldsymbol{n}})\phi^\star \, ds = 0 \tag{II.9}$$

This identity can be satisfied for any field $\phi^\star$ and $\forall\mathcal{D}$ if and only if:

$$\boldsymbol{\nabla}.(\underline{\boldsymbol{\xi}} - \underline{\boldsymbol{\gamma}}) + \pi + \gamma = 0 \quad \text{in} \quad V \tag{II.10}$$

$$\zeta = (\underline{\boldsymbol{\xi}} - \underline{\boldsymbol{\gamma}}).\underline{\boldsymbol{n}} \quad \text{on} \quad \partial V \tag{II.11}$$

Equation (II.10) expresses the general form of balance of generalized stresses. It is identical with Gurtin's balance of microforces, except the external microforce contribution $\underline{\boldsymbol{\gamma}}$ that may exist in general. In the remainder of this work, however, it is assumed that $\gamma = 0$ and $\underline{\boldsymbol{\gamma}} = 0$ for the sake of brevity. The equation (II.11) represents the boundary condition for the generalized traction vector.

II.2.2 State laws and dissipation potential

According to the first principle of thermodynamics, which is called principle of conservation of energy, the time variation of kinetic $\mathcal{K}$ and internal energy, in a material subdomain $\mathcal{D}$ and for an isothermal transformation, is due to the power of external forces $\mathcal{P}^{(e)}(\underline{\boldsymbol{v}})$:

$$\dot{\mathcal{K}} + \dot{\mathcal{E}} = \mathcal{P}^{(ext)} \tag{II.12}$$

The thermodynamics framework is formulated here in the isothermal case for simplicity. In absence of inertial forces, the total energy is reduced to the internal energy with density e. Taking the principle of virtual power, the energy balance is stated as:

$$\begin{aligned} \dot{\mathcal{E}} &= \int_{\mathcal{V}} \dot{e} \, dv = \mathcal{P}^{ext} = -\mathcal{P}^{int} \\ &= \int_{\partial V} (\underline{\boldsymbol{\xi}}.\underline{\boldsymbol{n}})\dot{\phi} \, ds = \int_V \boldsymbol{\nabla}.(\underline{\boldsymbol{\xi}}\,\dot{\phi}) \, dv \end{aligned} \tag{II.13}$$

This identity is valid for any subdomain $\mathcal{D} \subset V$. The local form of the energy balance is obtained:

$$\dot{e} = \boldsymbol{\nabla}.(\dot{\phi}\,\underline{\boldsymbol{\xi}}) \tag{II.14}$$

The second principle, called the entropy principle, is formulated as follows:

$$\int_V \dot{s} \, dv \geq -\int_{\partial V} \underline{\boldsymbol{\Phi}}.\underline{\boldsymbol{n}} \, ds \quad \text{and} \quad \underline{\boldsymbol{\Phi}} = -\mu\frac{\underline{\boldsymbol{J}}}{T} \tag{II.15}$$

where s is the entropy density, $\underline{\boldsymbol{\Phi}}$ the entropy flux, $\underline{\boldsymbol{J}}$ the chemical flux and μ the diffusion potential.
Using the equation of local conservation of mass:

$$\dot{c} = -\boldsymbol{\nabla}.\underline{\boldsymbol{J}} \tag{II.16}$$

we obtain the following local form of the entropy inequality:

$$T\dot{s} - \boldsymbol{\nabla}.(\mu\underline{\boldsymbol{J}}) \geq 0 \tag{II.17}$$

Combining the equation of the free energy density $\dot{f} = \dot{e} - T\dot{s}$ in the isothermal case with Eqs. (II.14)–(II.17), leads to the Clausius-Duhem inequality:

$$-\dot{f} - \pi\dot{\phi} + \underline{\boldsymbol{\xi}}.\boldsymbol{\nabla}\dot{\phi} - \underline{\boldsymbol{J}}.\boldsymbol{\nabla}\mu - \mu\boldsymbol{\nabla}.\underline{\boldsymbol{J}} \geq 0 \tag{II.18}$$

The free energy density is assumed to be a function of concentration c, order parameter ϕ, as well as its gradient $\boldsymbol{\nabla}\phi$. The Clausius-Duhem inequality can then be written as follows:

$$\left(\mu - \frac{\partial f}{\partial c}\right)\dot{c} - \left(\pi + \frac{\partial f}{\partial \phi}\right)\dot{\phi} + \left(\underline{\boldsymbol{\xi}} - \frac{\partial f}{\partial \boldsymbol{\nabla}\phi}\right).\boldsymbol{\nabla}\dot{\phi} - \underline{\boldsymbol{J}}.\boldsymbol{\nabla}\mu \geq 0 \tag{II.19}$$

For every admissible process and for any given (c, ϕ,$\boldsymbol{\nabla}\phi$), the inequality (II.19) must hold for arbitrary values of $\dot{c}$, $\dot{\phi}$ and $\boldsymbol{\nabla}\dot{\phi}$. The microstress $\underline{\boldsymbol{\xi}}\,(c, \phi, \boldsymbol{\nabla}\phi)$ and the chemical potential $\mu(c, \phi, \boldsymbol{\nabla}\phi)$ are assumed independent of $\boldsymbol{\nabla}\dot{\phi}$ and $\dot{c}$, in which these latter appear linearly in the inequality above (see e.g. (Coleman and Noll, 1963; Coleman and Gurtin, 1967)). The following state laws are deduced:

$$\mu = \frac{\partial f}{\partial c} = \frac{\partial f_0}{\partial c} \tag{II.20}$$

$$\underline{\boldsymbol{\xi}} = \frac{\partial f}{\partial \boldsymbol{\nabla}\phi} = \alpha \boldsymbol{\nabla}\phi \tag{II.21}$$

when the specific form (II.2) is adopted. The Clausius-Duhem inequality then reduces to the residual dissipation:

$$D = -\underline{\boldsymbol{J}}.\boldsymbol{\nabla}\mu - \pi_{dis}\dot{\phi} \geq 0 \quad \text{with} \quad \pi_{dis} = \pi + \frac{\partial f}{\partial \phi} \tag{II.22}$$

where π_{dis} is the chemical force associated with the dissipative processes, as introduced in (Gurtin, 1996).

In order to define the complementary laws related to the dissipative processes, we postulate the existence of a dissipation potential function $\Omega(\boldsymbol{\nabla}\mu, \pi_{dis})$. The retained specific isotropic form is the following:

$$\Omega(\boldsymbol{\nabla}\mu, \pi_{dis}) = \frac{1}{2}L(\phi)\boldsymbol{\nabla}\mu.\boldsymbol{\nabla}\mu + \frac{1}{2}(1/\beta)\pi_{dis}^2 \tag{II.23}$$

where $L(\phi)$ and β are material parameters or functions.

The complementary evolution laws derive from the dissipation potential:

$$\dot{\phi} = -\frac{\partial \Omega}{\partial \pi_{dis}} = -(1/\beta)\pi_{dis} \tag{II.24}$$

$$\underline{\boldsymbol{J}} = -\frac{\partial \Omega}{\partial \boldsymbol{\nabla}\mu} = -L(\phi)\boldsymbol{\nabla}\mu \tag{II.25}$$

The convexity of the dissipation potential ensures the positivity of dissipation.

Combining Eq. (II.22) and Eq. (II.24), we get:

$$\pi = -\beta\,\dot{\phi} - \frac{\partial f}{\partial \phi} \tag{II.26}$$

The substitution of the two state laws and the complementary laws, into the balance equations for mass concentration and generalized stresses respectively, leads to the evolution equations for concentration and order parameter:

$$\dot{c} = -\boldsymbol{\nabla}.(-L(\phi)\boldsymbol{\nabla}\mu) = -\boldsymbol{\nabla}.\left(-L(\phi)\boldsymbol{\nabla}\frac{\partial f}{\partial c}\right) \tag{II.27}$$

$$\boldsymbol{\nabla}.\underline{\boldsymbol{\xi}} + \pi = -\beta\dot{\phi} + \alpha\Delta\phi - \frac{\partial f}{\partial \phi} = 0 \tag{II.28}$$

The usual diffusion and Ginzburg-Landau equations are thus retrieved.

Accordingly, the phase field problem can be formulated as follows:
Find $\{c(\underline{\boldsymbol{x}}\,,t), \phi(\underline{\boldsymbol{x}}\,,t)\}$ satisfying

$$\left|\begin{array}{l} \text{at} \quad t=0 \\ \quad c(\underline{\boldsymbol{x}}\,,0) = c_0(\underline{\boldsymbol{x}}\,) \\ \quad \phi(\underline{\boldsymbol{x}}\,,0) = \phi_0(\underline{\boldsymbol{x}}\,) \\ \\ \text{at each instant t} > 0 \\ \dot{c} = -\boldsymbol{\nabla}.\underline{\boldsymbol{J}} \quad \text{in} \quad \mathcal{V} \\ \boldsymbol{\nabla}.\underline{\boldsymbol{\xi}} + \pi = -\beta\dot{\phi} + \alpha\Delta\phi - \dfrac{\partial f}{\partial \phi} = 0 \quad \text{in} \quad \mathcal{V} \\ \\ j = \underline{\boldsymbol{J}}\,.\underline{\boldsymbol{n}} \quad \text{in} \quad \partial\mathcal{V} \\ \zeta = \underline{\boldsymbol{\xi}}\,.\underline{\boldsymbol{n}} \quad \text{in} \quad \partial\mathcal{V} \end{array}\right. \tag{II.29}$$

where j is outgoing diffusion flux.

II.3 Finite element implementation

II.3.1 Variational formulation

The variational formulation of the phase field partial differential equation directly follows from the formulated principle of virtual power (II.8):

$$\Im(\phi^\star) = \int_V (\pi\phi^\star - \underline{\boldsymbol{\xi}}\,.\boldsymbol{\nabla}\phi^\star)\,dv + \int_{\partial V} \zeta\phi^\star\,ds = 0 \tag{II.30}$$

The weak form of the diffusion equation is completely equivalent to the strong representation, where the boundary conditions are already included within the formulation. Multiplying the diffusion equation by an arbitrary field of virtual concentration $c^\star$ and integrating by parts over an arbitrary element, the following integral representation is obtained:

$$\int_V (\dot{c} + \boldsymbol{\nabla}.\underline{\boldsymbol{J}})c^\star\,dv = 0 \quad \text{in} \quad V, \quad \forall c^\star(\underline{\boldsymbol{x}}\,) \tag{II.31}$$

Integrating by parts and using the divergence theorem, we deduce:

$$\begin{aligned} \int_V c^\star\boldsymbol{\nabla}.\underline{\boldsymbol{J}}\,dv &= \int_V (\boldsymbol{\nabla}.[c^\star\underline{\boldsymbol{J}}] - \boldsymbol{\nabla}c^\star.\underline{\boldsymbol{J}}\,)\,dv \\ &= \int_{\partial V} c^\star\underline{\boldsymbol{J}}\,.\underline{\boldsymbol{n}}\,ds - \int_V \boldsymbol{\nabla}c^\star.\underline{\boldsymbol{J}}\,dv \end{aligned} \tag{II.32}$$

Taking the boundary condition for concentration into account, the usual weak form of the diffusion equation is obtained:

$$\Im(c^\star) = \int_V (\dot{c}c^\star - \underline{\boldsymbol{J}}\,.\boldsymbol{\nabla}c^\star)\,dv + \int_{\partial V} jc^\star\,ds = 0 \tag{II.33}$$

Consequently, the above phase field problem (II.29) can be written as follows:

Find $\{c(\underline{\boldsymbol{x}}\,,t), \phi(\underline{\boldsymbol{x}}\,,t)\}$ satisfying

$$\left|\begin{array}{l} \text{at} \quad t=0 \\ \quad c(\underline{\boldsymbol{x}}\,,0) = c_0(\underline{\boldsymbol{x}}\,) \\ \quad \phi(\underline{\boldsymbol{x}}\,,0) = \phi_0(\underline{\boldsymbol{x}}\,) \\ \\ \text{at each instant t} > 0,\ \forall \phi^\star(\underline{\boldsymbol{x}}\,),\ \forall c^\star(\underline{\boldsymbol{x}}\,) \\ \quad \Im(c^\star) = \displaystyle\int_V (\dot{c}c^\star - \underline{\boldsymbol{J}}\,.\boldsymbol{\nabla} c^\star)\, dv + \int_{\partial V} j c^\star\, ds = 0 \\ \quad \Im(\phi^\star) = \displaystyle\int_V (\pi\phi^\star - \underline{\boldsymbol{\xi}}\,.\boldsymbol{\nabla}\phi^\star)\, dv + \int_{\partial V} \zeta\phi^\star\, ds = 0 \end{array}\right. \tag{II.34}$$

II.3.2 Discretization

In order to obtain a finite element solution, the spatial domain is subdivided into N elements. The nodal degrees of freedom are the values at nodes of phase and concentration. The fields c and ϕ are approximated within each element and at every time t, in terms of nodal values by means of interpolation functions, within each element:

$$\begin{aligned} c(\underline{\boldsymbol{x}}\,,t) &= \sum_{i=1}^{n} N_i^e(\underline{\boldsymbol{x}}\,)c_i(t), \qquad \phi(\underline{\boldsymbol{x}}\,,t) = \sum_{i=1}^{n} N_i^e(\underline{\boldsymbol{x}}\,)\phi_i(t) \\ c^\star(\underline{\boldsymbol{x}}\,,t) &= \sum_{i=1}^{n} N_i^e(\underline{\boldsymbol{x}}\,)c_i^\star(t), \quad \phi^\star(\underline{\boldsymbol{x}}\,,t) = \sum_{i=1}^{n} N_i^e(\underline{\boldsymbol{x}}\,)\phi_i^\star(t) \\ \boldsymbol{\nabla} c(\underline{\boldsymbol{x}}\,,t) &= \sum_{i=1}^{n} B_i^e(\underline{\boldsymbol{x}}\,)c_i(t), \quad \boldsymbol{\nabla}\phi(\underline{\boldsymbol{x}}\,,t) = \sum_{i=1}^{n} B_i^e(\underline{\boldsymbol{x}}\,)\phi_i(t) \end{aligned} \tag{II.35}$$

where n is the number of nodes in the element e containing $\underline{\boldsymbol{x}}$ and the shape functions are denoted by N_i. The matrix $[B^e(\underline{\boldsymbol{x}}\,)]$ is defined by the first derivatives of the shape functions, which read in the 2D case:

$$[B^e(\underline{\boldsymbol{x}}\,)] = \begin{bmatrix} \dfrac{\partial N_1^e}{\partial x} & \dfrac{\partial N_2^e}{\partial x} & \cdots & \dfrac{\partial N_n^e}{\partial x} \\ \\ \dfrac{\partial N_1^e}{\partial y} & \dfrac{\partial N_2^e}{\partial y} & \cdots & \dfrac{\partial N_n^e}{\partial y} \end{bmatrix} \tag{II.36}$$

Regarding time discretization, the Euler implicit method is applied. Using the notation $c(t)$ and $\phi(t)$ for the known values of the current time step t, $\phi(t+\Delta t)$ and $c(t+\Delta t)$ at time $t+\Delta t$ are estimated by solving the following equations:

$$\dot{c}(t+\Delta t) = \frac{c(t+\Delta t) - c(t)}{\Delta t} \tag{II.37}$$

$$\dot{\phi}(t+\Delta t) = \frac{\phi(t+\Delta t) - \phi(t)}{\Delta t} \tag{II.38}$$

$$c(0) = c_0, \quad \phi(0) = \phi_0 \tag{II.39}$$

Δt indicates the time increment, and c_0, ϕ_0 are the initial conditions for the concentration and order parameter.

After substituting the nodal approximation and the time discretization into Eq. (II.34), we deduce the element residual, which can be written in the following form:

$$\{\mathcal{R}^e(c,\phi)\} \quad = \quad \left\{ \begin{array}{c} \mathcal{R}^e_c(c,\phi) \\ \mathcal{R}^e_\phi(\phi) \end{array} \right\} \tag{II.40}$$

where $\mathcal{R}^e_\phi(\phi)$ and $\mathcal{R}^e_c(c,\phi)$ are respectively the element residuals for the variational formulation of phase field (II.30) and classical diffusion (II.33), defined as follow:

$$(\mathcal{R}^e_c)_i = \int_{V^e} \left(N^e_i N^e_j \, \dot{c}^e_j - [B^e]_{ij} \, J_j \right) dv + \int_{\partial V^e} N^e_i \, j \, ds \tag{II.41}$$

$$(\mathcal{R}^e_\phi)_i = \int_{V^e} \left(N^e_i \pi(\phi) \, - [B^e]_{ij} \, \xi_j \right) dv + \int_{\partial V^e} N^e_i \, \zeta \, ds \tag{II.42}$$

The global residual vector can be obtained by assembling the element residuals for all finite elements using the matrix assembly $[A^e]$:

$$\{\mathcal{R}(\phi)\} = \sum_{e=1}^{N} [A^e] \, . \, \{\mathcal{R}^e(\phi)\} = \{0\} \tag{II.43}$$

following the usual definition in computational mechanics (Besson et al., 2001).

Given a known set of nodal degrees of freedom at time t, and assuming that the residual vanishes at the next time step $t + \Delta t$, a set of non-linear equations results for the nodal degrees of freedom at $t + \Delta t$. It is solved with the Newton-Raphson method in an iterative manner. This requires the computation of the element generalized stiffness matrix which is obtained by derivation of the residual vector with respect to the degrees of freedom (c, ϕ):

$$[K^e_t] = \left[\frac{\partial \mathcal{R}^e}{\partial \delta^e} \right] = \left[\begin{array}{cc} [K^e_{cc}] & \left[K^e_{c\phi}\right] \\ \left[K^e_{\phi c}\right] & \left[K^e_{\phi\phi}\right] \end{array} \right] \tag{II.44}$$

$$\text{with} \quad \{\delta^e\} = \left\{ \begin{array}{c} \{c^e\} \\ \{\phi^e\} \end{array} \right\}$$

The element generalized stiffness matrix is divided into four submatrices. Referring to Eqs. (II.41)–(II.42), the individual components $(K^e_{cc})_{ij}$, $(K^e_{c\phi})_{ij}$, $(K^e_{\phi c})_{ij}$ and $(K^e_{\phi\phi})_{ij}$ are:

$$(K^e_{cc})_{ij} = \frac{\partial (\mathcal{R}^e_c)_i}{\partial c^e_j} = \int_{V^e} \left(\frac{1}{\Delta t} N^e_i N^e_j - [B^e]_{ik} \left[\frac{\partial \underline{\boldsymbol{J}}}{\partial c^e} \right]_{kj} \right) dv \tag{II.45}$$

$$(K^e_{c\phi})_{ij} = \frac{\partial (\mathcal{R}^e_c)_i}{\partial \phi^e_j} = \int_{V^e} - [B^e]_{ik} \left[\frac{\partial \underline{\boldsymbol{J}}}{\partial \phi^e} \right]_{kj} dv \tag{II.46}$$

$$(K^e_{\phi c})_{ij} = \frac{\partial (\mathcal{R}^e_\phi)_i}{\partial c^e_j} = \int_{V^e} N^e_i \left(\frac{\partial \pi}{\partial c^e} \right)_j dv \tag{II.47}$$

$$(K^e_{\phi\phi})_{ij} = \frac{\partial (\mathcal{R}^e_\phi)_i}{\partial \phi^e_j} = \int_{V^e} \left(N^e_i \left(\frac{\partial \pi}{\partial \phi^e} \right)_j - [B^e]_{ik} \left[\frac{\partial \underline{\boldsymbol{\xi}}}{\partial \phi^e} \right]_{kj} \right) dv \tag{II.48}$$

The elements used in this work are linear elements and quadratic elements with reduced integration (4 Gauss points in quadrilateral elements for instance).

II.4 Formulations of the homogeneous free energy in phase field models

II.4.1 Introduction

The formulation, presented here, allows the application of any arbitrary form for the free energy. In current literature, several free energy functional have been presented, such as Khachaturyan model (Wang and Khachaturyan, 1995b), Kim-Kim-Suzuki (KKS) model (Kim et al., 1998; Kim et al., 1999) and Folch-Plapp model (Folch and Plapp, 2005)...

Otherwise, the choice of the homogeneous free energy is a crucial point in the phase field models since it determines not only the kind of system which can be studied (i.e. the phase diagram that can be recovered at equilibrium) but also the efficiency of the calculations, in term of quantitative results and convergence rate of the numerical scheme used to solve the final partial differential equations.

II.4.2 Polynomial formulation, extension of KKS energy density

The essential advantage of this model is that it is thermodynamically acceptable, i.e. the evolution equations are expressed according to the variational derivative of the free energy of the system. Moreover, simpler phase field equation is obtained, which is characterized by a linear form of the chemical potential according to the concentration and the order parameter.

Following Kim et al. (Kim et al., 1998), the free energies of the two phases are interpolated for intermediate values of ϕ with a polynomial $h(\phi)$ varying in a monotonic way between both phases. A double well potential to this free energy landscape, $g(\phi)$, is added. This is a function of the order parameter, accounting for the free energy penalty of the interface (Fig. II.1):

$$f_0(c,\phi) = \psi(c,\phi) + Wg(\phi) \tag{II.49}$$

where

$$\psi(c,\phi) = h(\phi)f_\alpha(c) + [1-h(\phi)]f_\beta(c) \tag{II.50}$$

where W is the height of the double-well barrier. A possible functional form for $g(\phi)$ is

$$g(\phi) = \phi^2(1-\phi)^2 \tag{II.51}$$

which has a local maximum at $\phi = 1/2$ and two minima at $\phi = 0$ and $\phi = 1$ (Chen, 2004).

The choice of the function, $h(\phi)$ in Eq. (II.50), can be any odd polynomial in ϕ, which is required to have the following properties:

$$h(0) = 0, \quad h(1) = 1, \quad \left.\frac{\partial h}{\partial \phi}\right|_{\phi=0} = \left.\frac{\partial h}{\partial \phi}\right|_{\phi=1} = 0 \tag{II.52}$$

These properties ensure that the equilibrium values, 0 and 1, for the order parameter in the double-well potential are not affected by the chemical free energies f_α and f_β and the equilibrium concentrations on the axes $\phi = 0$ and $\phi = 1$ are local minima. An example, which satisfies the conditions given in Eq. (II.52) is the following three-order polynomial (Wang et al., 1993a):

$$h(\phi) = \phi^2(3-2\phi) \tag{II.53}$$

For simplicity, the free energy densities of both phases f_α and f_β have been described by simple quadratic functions of the concentration c (Echebarria et al., 2004):

$$f_i(c) = \frac{1}{2}k_i(c-a_i)^2 + b_i \tag{II.54}$$

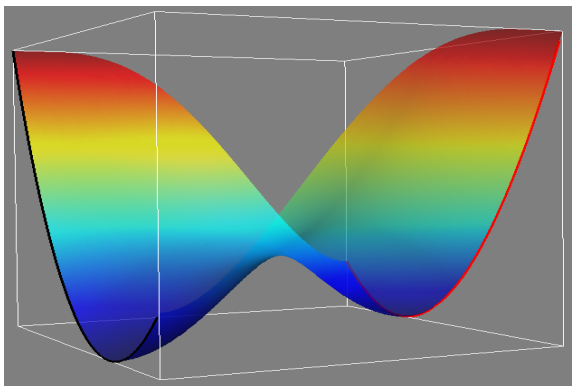

Figure II.1 : Double well potential, approximated as quadratic degree polynomial and visualized as a surface which relate the local free energy density of both phases f_α and f_β.

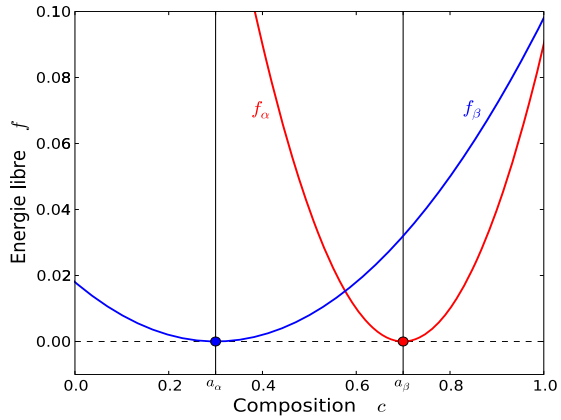

Figure II.2 : Free energies of two phases in equilibrium described by simple quadratic functions Eq.(II.54) with $(a_\alpha = 0.7, a_\beta = 0.3)$, $(b_\alpha = b_\beta = 0)$ and $(k_\alpha = k_\beta)$

where $i = \{\alpha, \beta\}$ denotes phase α or β.
The constants k_α, k_β are the curvatures of the free energies with respect to concentration (positive to avoid any spinodal decomposition); b_α, b_β are the heights of the free energies and a_α, a_β are the equilibrium concentrations of both phases delimiting the two-phases region in the phase diagram, and corresponding to the minima of f_α and f_β for the particular quadratic functions chosen.

Figure (II.2) displays the projection of the total free energy, defined by two curves. The first curve, which is plotted by a blue line, represents the homogeneous free energy of the disordered phase β $(\phi = 0)$ and the red curve corresponds to the free energy of the ordered phase α $(\phi = 1)$. Since we have taken $b_\alpha = b_\beta$, the tangent line common to f_α and f_β is simply the x axis, which determines the equilibrium compositions $c_\alpha = 0.7$ and $c_\beta = 0.3$ respectively.

II.4.3 Interpolating free energy densities, extension of Plapp-Folch energy density

The critical point of the previous construction is the calibration of the interfacial energy through the relationship between the parameter α in front of $(\boldsymbol{\nabla}\phi)^2$, and the interfacial thickness δ. In a system homogeneous in temperature, the conditions of equilibrium can be expressed as:

$$\frac{\partial f_\alpha}{\partial c} = \frac{\partial f_\beta}{\partial c} = \mu_{\text{eq}} \tag{II.55}$$

$$\omega_\alpha = \omega_\beta \tag{II.56}$$

with μ_{eq} is the chemical potential at equilibrium and ω_k the grand potential of phase k defined as:

$$\omega_k = f_k - \mu_{\text{eq}}\, c_k \tag{II.57}$$

These conditions are strictly equivalent to the equality of the chemical potentials in all the phases in equilibrium, for all chemical species, and to its geometrical interpretation of a tangent line common to the free energies of all phases. For the particular case, the tangent line common to f_α and f_β is simply the x axis (Fig. (II.2)). At equilibrium, the phase field equation (III.33), for a planar front, reads:

$$\alpha \frac{\partial^2 \phi}{\partial x^2} = \frac{\partial f}{\partial \phi} = \frac{\partial \psi}{\partial \phi} + W \frac{\partial g}{\partial \phi} \tag{II.58}$$

Furthermore, the partial derivative of the grand potential with respect to concentration and order parameter is:

$$\begin{aligned} d\omega &= \frac{\partial \omega}{\partial c} dc + \frac{\partial \omega}{\partial \phi} d\phi \\ &= (\frac{\partial \psi}{\partial c} - f_c) dc + \frac{\partial \omega}{\partial \phi} d\phi \end{aligned} \tag{II.59}$$

At equilibrium $\partial_c \psi = \mu_{\text{eq}}$, the above equation is then reduced to:

$$d\omega = \frac{\partial \omega}{\partial \phi} d\phi \tag{II.60}$$

Substituting Eq.(III.72) into Eq.(II.58), we get:

$$\alpha \frac{\partial^2 \phi}{\partial x^2} = \frac{\partial \omega}{\partial \phi} + W \frac{\partial g}{\partial \phi} \tag{II.61}$$

Integrating this equation from $x = -\infty$ (phase α) to x after multiplying $d\phi/dx$ on both sides results in:

$$\frac{\partial \phi}{\partial x} = \sqrt{\frac{2}{\alpha}} (\omega(x) - \omega^- + W g(\phi))^{1/2} \tag{II.62}$$

where ω^- is the value of the grand potential at $x = -\infty$.

The interfacial energy is defined as:

$$\gamma = \alpha \int_{-\infty}^{+\infty} \left(\frac{d\phi}{dx} \right)^2 dx \tag{II.63}$$

Substituting Eq.(II.62) in the above equation of interfacial energy leads to:

$$\gamma = \sqrt{2\alpha} \int_0^1 (\omega - \omega^- + W g(\phi))^{1/2} d\phi \tag{II.64}$$

This equation makes clear that there are two contributions to the interfacial energy: the first one is related to the double well potential, independent of the concentration and temperature and the second one is related to the variation in composition across the interface. This second contribution can be a source of many problems when choosing the parameters α and δ to recover physical values, such as the interfacial energy. Indeed, the larger the interfacial width α, the larger the difference between the effective interfacial energy and the desired value.

In order to avoid this spurious effect, it is necessary to make the concentration contribution to the energy of interface vanish, i.e. $\partial w/\partial \phi = \partial f_0/\partial \phi = 0$.

According to Plapp-Folch formulation (Folch and Plapp, 2005), a quadratic function of the concentration is adapted to define the free energy density as follows:

$$f_0(\phi, c) = \frac{1}{2} k(\phi)(c - a(\phi))^2 + b(\phi) \tag{II.65}$$

The condition $\partial w^0/\partial \phi = 0$ can be written as follows:

$$\frac{\partial f}{\partial \phi} = -k(\phi)(c - a(\phi)) \frac{\partial a}{\partial \phi} + \frac{\partial b}{\partial \phi} + \frac{1}{2}(c - a(\phi))^2 \frac{\partial k(\phi)}{\partial \phi} = 0 \tag{II.66}$$

is equivalent to:

$$\frac{(\mu_{\text{eq}})^2}{2} \frac{\partial (1/k(\phi))}{\partial \phi} = \frac{\partial b}{\partial \phi} - \mu_{\text{eq}} \frac{\partial a}{\partial \phi} \tag{II.67}$$

For the specific form of the free energy (II.65), the chemical potential at equilibrium is expressed as:

$$\mu_{\text{eq}} = \frac{\partial f_0}{\partial c} = k(\phi)(c - a(\phi)) \tag{II.68}$$

Assuming that $k(\phi)$ is chosen to be function of $a(\phi)$ and $b(\phi)$, two similar interpolation functions for $a(\phi)$ and $b(\phi)$ are proposed:

$$b(\phi) = h(\phi)b_\alpha + (1 - h(\phi))b_\beta \tag{II.69}$$

$$a(\phi) = h(\phi)a_\alpha + (1 - h(\phi))a_\beta \tag{II.70}$$

Indeed, we get:

$$\frac{(\mu_{\text{eq}})^2}{2}\frac{\partial(1/k(\phi))}{\partial\phi} = (\Delta b - \mu_{\text{eq}}\Delta a)\frac{\partial h(\phi)}{\partial\phi} \tag{II.71}$$

which can easily be integrated from $\phi = 0$, i.e. in phase β, to ϕ:

$$\left(\frac{1}{k(\phi)} - \frac{1}{k_\beta}\right)\frac{(\mu_{\text{eq}})^2}{2} = (\Delta b - \mu_{\text{eq}}\Delta a)h(\phi) \tag{II.72}$$

where $\Delta b = b_\alpha - b_\beta$ and $\Delta a = a_\alpha - a_\beta$.

Hence, the curvature of the free energy density is:

$$k(\phi) = \frac{k_\beta}{1 + k_\beta h(\phi)\Delta} \quad \text{where} \quad \Delta = \frac{2(\Delta b - \mu_{\text{eq}}\Delta a)}{(\mu_{\text{eq}})^2} \tag{II.73}$$

While choosing $k(\phi)$ to be a function of $a(\phi)$ and $b(\phi)$, we cannot directly control the value of free energy curvature of phase α; $k_\alpha = k_\beta/(1 + k_\beta\Delta)$. Thus, it is preferable to express $b(\phi)$ function of $k(\phi)$ as follows:

$$b(\phi) - b_\beta = \mu_{\text{eq}}(a(\phi) - a_\beta) + \frac{(\mu_{\text{eq}})^2}{2}\left(\frac{1}{k(\phi)} - \frac{1}{k_\beta}\right) \tag{II.74}$$

Consequently, b_α is defined in terms of $a_\alpha, a_\beta, k_\alpha$ and k_β by:

$$b_\alpha - b_\beta = \mu_{\text{eq}}(a_\alpha - a_\beta) + \frac{(\mu_{\text{eq}})^2}{2}\left(\frac{1}{k_\alpha} - \frac{1}{k_\beta}\right) \tag{II.75}$$

Assuming that $k(\phi) = h(\phi)k_\alpha + (1 - h(\phi))k_\beta$, the function $b(\phi)$ is not necessarily monotonous, which can generate serious problems on the stability and the convergence rate of the numerical scheme. Consequently, it is better that $k(\phi)$ is expressed as follows:

$$k(\phi) = \frac{\bar{k}}{k_\alpha + h(\phi)\Delta k} \qquad \text{where} \qquad \begin{cases} \bar{k} = k_\alpha k_\beta \\ \Delta k = k_\alpha - k_\beta \end{cases} \tag{II.76}$$

Substituting the previous equations into Eq.(II.74), the interpolation form for the free energy height $b(\phi)$, which is shown in Fig. II.3, reads

$$b(\phi) - b_\beta = \mu_{\text{eq}}\left(\Delta a + \frac{(\mu_{\text{eq}})^2\Delta k}{2\bar{k}}\right)h(\phi) \tag{II.77}$$

Thus, the proposed interpolating free energy density is summarised as:

$$f_0(\phi, c) = \frac{1}{2}k(\phi)(c - a(\phi))^2 + b(\phi) \tag{II.78}$$

where

$$a(\phi) = a_\beta + \Delta a h(\phi), \quad k(\phi) = \frac{\bar{k}}{k_\alpha + h(\phi)\Delta k} \quad \text{and} \quad b(\phi) = b_\beta + \mu_{\text{eq}}\left(\Delta a + \frac{(\mu_{\text{eq}})^2\Delta k}{2\bar{k}}\right)h(\phi)$$

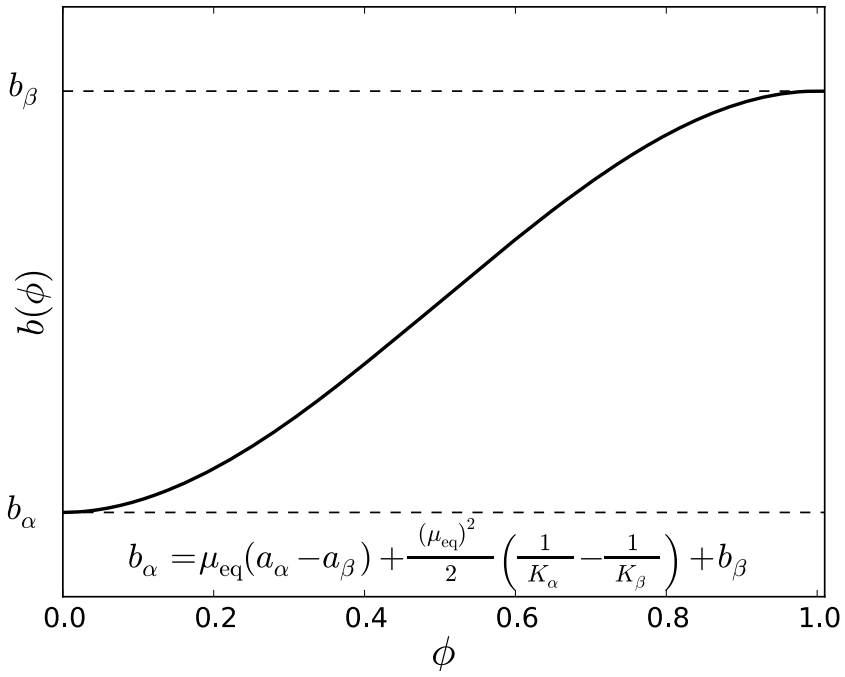

Figure II.3 : Interpolation function for the free energy curvature $b(\phi)$ vs order parameter

II.4.4 Identification of parameters

The phase field parameters α and W have been related to the interface energy γ and the interface thickness δ (Kim et al., 1998; Ammar et al., 2009a; Ammar et al., 2009c). Indeed, at a plane interface at equilibrium, the stationary one-dimensional equation Eq. (II.1) becomes:

$$\alpha \frac{d^2\phi_{eq}}{dx^2} = \frac{\partial f_0}{\partial \phi_{eq}} \tag{II.79}$$

where x is the distance normal to the interface.

This equation can be integrated to get the phase field expression at equilibrium $\phi_{eq}(x)$:

$$\phi_{eq} = \frac{1}{2}\left(1 - \tanh(\frac{x}{\delta})\right) \tag{II.80}$$

where

$$\gamma = \sqrt{\alpha W}/(3\sqrt{2}) \tag{II.81}$$
$$\delta = 2.94\sqrt{2\alpha/W} \tag{II.82}$$

with 2.94 in the last relation comes from the way the interface width δ has been defined, i.e. for values of ϕ in the range $[0.05; 0.95]$.

It must be noted that taking values for k_α and k_β of the same order of magnitude as W would disqualify Eq.(II.82) for relating the interfacial energy and the double well height W. This could have some large effects on the results, especially on the phenomena involving interface curvatures, such as morphological stabilization/destabilization as studied in the following subsection.

The Onsager coefficient $L(\phi)$ is defined with respect to the chemical diffusivities D_α and D_β in both phases by means of the interpolation function $h(\phi)$:

$$L(\phi) = h(\phi)D_\alpha/k_\alpha + (1 - h(\phi))D_\beta/k_\beta \tag{II.83}$$

where the k_i ensure that Fick's law is recovered in the bulk phases. Finally, the phase field mobility $1/\beta$ has been set by successive trials with decreasing β such as to obtain a diffusion controlled mode of growth.

II.4.5 Phase equilibrium compositions

We shall consider a two-phase isothermal system consisting of a precipitate phase α, lying within the matrix phase β. Once the free energy to be extremized at equilibrium has been identified, we recall the equilibrium thermodynamic conditions given by equations (II.55) and (II.56) in order to define the equilibrium concentrations in both phases. The first one is the equality of the diffusion potentials:

$$\frac{\partial f_\alpha}{\partial c} = \frac{\partial f_\beta}{\partial c} = \mu_{\text{eq}} \quad \Rightarrow \quad k_\alpha(c_\alpha - a_\alpha) = k_\beta(c_\beta - a_\beta) \tag{II.84}$$

The second one relates the grand potentials in both phases:

$$\begin{aligned} \omega_\alpha &= \omega_\beta \\ \frac{1}{2}k_\alpha(c_\alpha - a_\alpha)^2 + b_\alpha - k_\alpha(c_\alpha - a_\alpha)c_\alpha &= \frac{1}{2}k_\beta(c_\beta - a_\beta)^2 + b_\beta - k_\beta(c_\beta - a_\beta)c_\beta \end{aligned} \tag{II.85}$$

Substituting Eq. (II.84) into Eq. (II.85) leads to the following relationship::

$$\Delta\tilde{k}\mu_{\text{eq}}^2 - \Delta c\,\mu_{\text{eq}} + \Delta b = 0 \tag{II.86}$$

where

$$\Delta c = c_\alpha - c_\beta \ , \ \Delta b = b_\alpha - b_\beta \ \text{ and } \ \Delta\tilde{k} = \frac{1}{2\,k_\alpha} - \frac{1}{2\,k_\beta} \tag{II.87}$$

Assuming equal curvatures $k_\alpha = k_\beta = k$ for simplicity, the equilibrium concentrations c_α, c_β in both phases are expressed as:

$$a_\alpha = c_\alpha - \frac{1}{k}\frac{\Delta b}{\Delta c} \qquad \text{and} \qquad a_\beta = c_\beta - \frac{1}{k}\frac{\Delta b}{\Delta c} \tag{II.88}$$

The equilibrium concentration expressions, in the general case with non-equal curvatures, are provided in Appendix A.

II.5 Numerical simulations

II.5.1 Plane interface evolution

The proposed model has been implemented in the finite element code ZeBuLoN and used to investigate diffuse interface evolution between two phases. One-dimensional calculations have been performed assuming a two-phase binary alloy, where α and β phases are separated by a plane diffuse interface.

The material parameters used for computation works are summarised in Table II.5.1 for each phase. All parameters are dimensionless and scaled with the mesoscopic length L (typically the system size), and the characteristic time $\tau = \beta/k$ related to the interface motion and all the energy related parameters are measured in terms of the chemical free energies curvature k. One chooses $\delta/L = 0.01$ and $\gamma/(kL) = 0.1$.

phase	$\beta(\phi = 0)$	$\alpha(\phi = 1)$
a_i	0.3	0.7
b_i	0	0
$D_i\,\tau/L^2$	0.1	0.1

Tableau II.1 : Values of the material parameters in each phase

The finite element mesh is composed of linear 4-node quadrangular elements, assuming zero order parameter flux and no exchange of mass at the boundary of the domain:

$$j = \underline{\boldsymbol{J}} . \underline{\boldsymbol{n}} = 0 \qquad \text{and} \qquad \zeta = \underline{\boldsymbol{\xi}} . \underline{\boldsymbol{n}} = 0 \tag{II.89}$$

In order to define the steady-state concentrations of both phases at the interface, an initial unstable state is well-described by a homogeneous initial condition $c_0 = 0.5$ and a one-dimensional order parameter profile as $\tanh$ function along one direction, which corresponds to coexisting α and β phases separated by a plane diffuse interface.

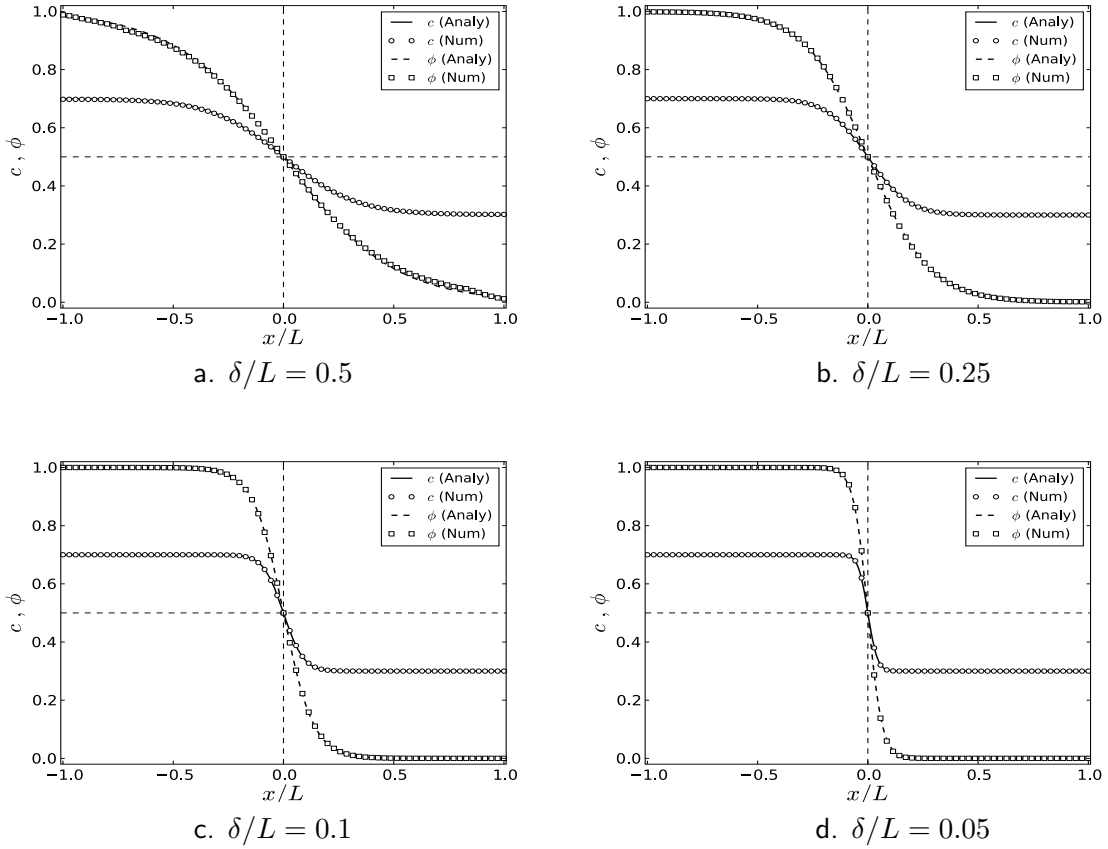

a. $\delta/L = 0.5$ b. $\delta/L = 0.25$

c. $\delta/L = 0.1$ d. $\delta/L = 0.05$

Figure II.4 : Mass fraction and order parameter profiles at equilibrium for a one-dimensional plane interface for different diffuse interface scaled thicknesses $\delta/L = 0.5, 0.25, 0.1$ and 0.05. The analytical profiles of concentration and order parameter, given by equations (II.80) and (II.88), are respectively plotted with continuous and dashed lines.

The equilibrium profiles of the composition and order parameter are given schematically in Fig. II.4 for different values of interface thickness δ/L. The concentration profile, initially uniform, begins to evolve, by a local equilibrium in the interfacial region, which represents the formation and the evolution of the diffuse interface between the mother phase and the new phase in a non-equilibrium state. At the steady-state, the concentrations of the phases take their equilibrium values; $c_\alpha = a_\alpha = 0.7$ and $c_\beta = a_\beta = 0.3$. The numerical profiles for the concentration and order parameter are in very good agreement with the analytical solution. Moreover, equivalent numerical results were obtained using polynomial and interpolating free energy densities as shown in Fig. II.5.

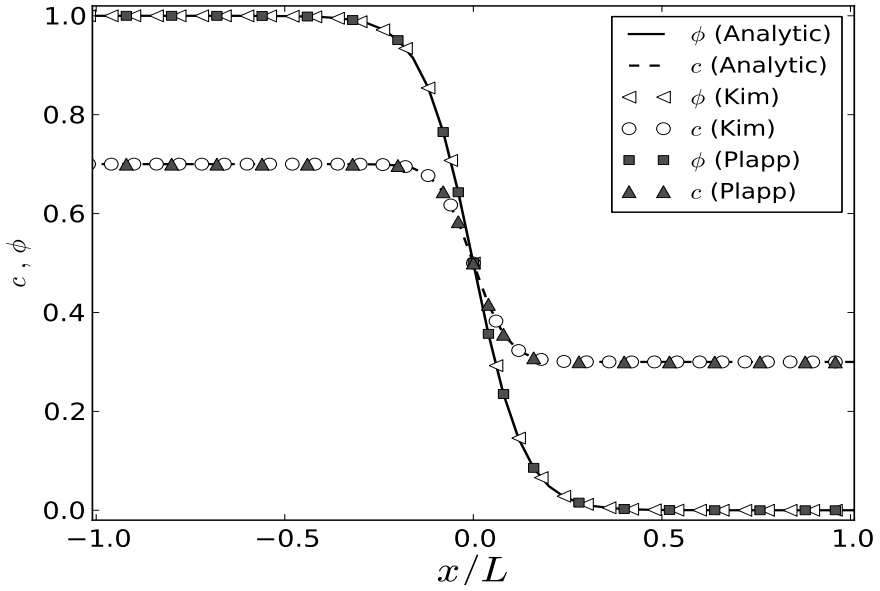

Figure II.5 : Comparison of analytical/numerical results for the equilibrium profiles of composition and order parameter field. The continuous and dashed lines represent respectively the analytical profiles of concentration and order parameter. The numerical results, using polynomial (Kim) and interpolating (Plapp) free energies, are respectively plotted, with open and filled symbols. The numerical results obtained with these two free energy densities are strictly equivalent.

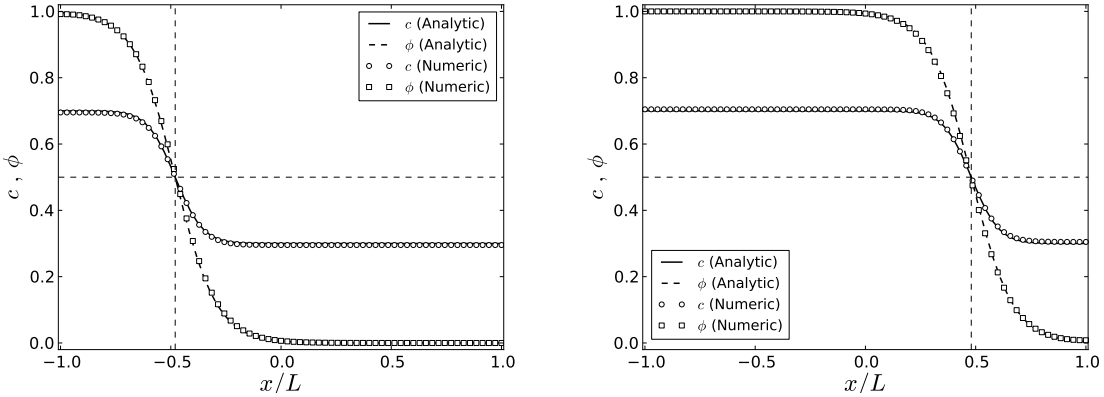

a. $c_0 = 0.4$ b. $c_0 = 0.6$

Figure II.6 : Equilibrium profiles of composition and order parameter fields for diffuse interface thicknesses $\delta/L = 0.1$ and for two overall concentrations $c_0 = 0.4$ and $c_0 = 0.4$. The continuous and dashed lines correspond respectively to the analytical profiles of concentration and order parameter.

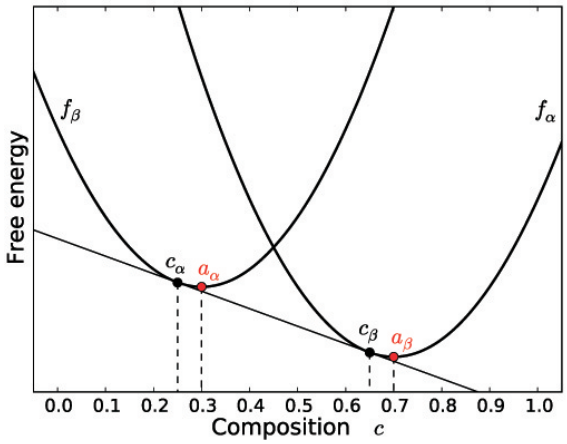

Figure II.7 : Specific free energy vs composition curves for both phases, calculated from the equation (II.88) with $(a_\alpha = 0.7, a_\beta = 0.3)$, $(k = k_\alpha = k_\beta)$ and $(\Delta b/k = 0.02)$

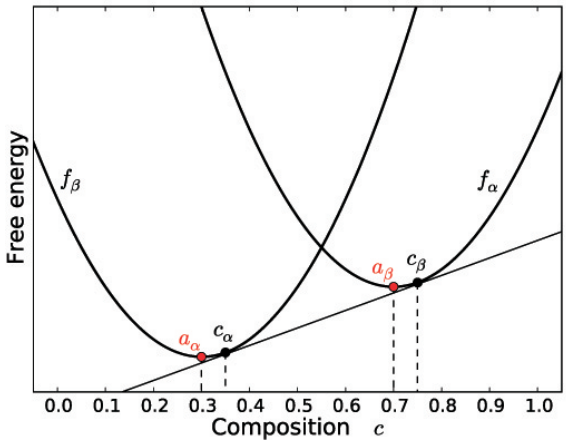

Figure II.8 : Specific free energy vs composition curves for both phases, calculated from the equation (II.88) with $(a_\alpha = 0.7, a_\beta = 0.3)$, $(k = k_\alpha = k_\beta)$ and $(\Delta b/k = -0.02)$

II.5.1.1 Mass conservation condition

Since zero mass exchange through the external surface is imposed, the volume fraction of both phases are determined in function of the equilibrium phase compositions by the mass conservation condition:

$$c_0 = \frac{1}{\mathcal{V}} \int_{\mathcal{V}} c dv = z\, c_\alpha + (1 - z)\, c_\beta \tag{II.90}$$

where z is the volume fraction of α phase.

In order to ensure numerically the conservation of the global mass fraction throughout the entire system (closed domain), the equilibrium profile of the composition and order parameter are shown in Fig. II.6, for two overall concentrations ($c_0 = 0.4$ and $c_0 = 0.6$). The diffuse interface front moves driven by the mass conservation, so as to reach the proper equilibrium value of the composition and order parameter.

II.5.1.2 Effect of the free energy height b_i

In the previous simulations, an equal free energy height has been chosen for α and β phases ($b_\alpha = b_\beta$), so that the tangent line common to f_α and f_β is simply the x axis. For this particular case, the equilibrium concentrations c_α and c_β are simply reduced to the minima of the chemical free energies of both phases a_α and a_β respectively.

In order to illustrate the effect of the free energy height b_i on the equilibrium concentrations, two calculations of the same process have been undertaken with two different values, namely $\Delta b/k = 0.02$ and $\Delta b/k = -0.02$, as respectively shown in Fig. II.7 and Fig. II.8. From these figures, it is clear that the equilibrium concentrations, that can be found by the common tangent construction to the free energy curves, are different from the free energy minima. Their values can be obtained by Eq.(II.88), for equal curvatures. Figures II.9 and Figure II.10 display the equilibrium profiles of the composition and order parameter, corresponding respectively to the specific free energy (II.7) and Fig. II.8. The good agreement between the numerical results and the analytical solutions show the ability of the proposed model to ensure the dependency of the equilibrium phase compositions on the free energy height, using polynomial (Kim) and interpolating (Plapp) free energies.

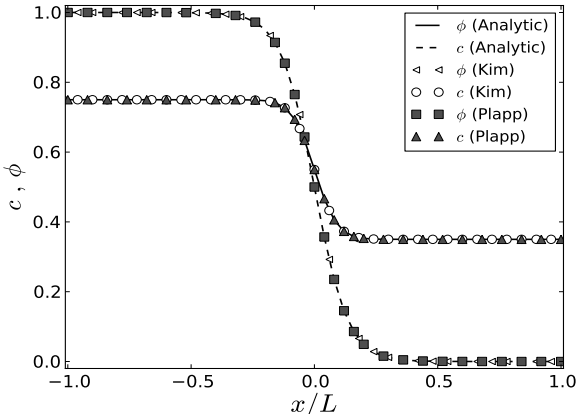

Figure II.9 : Equilibrium profiles of composition and order parameter fields, corresponding to the specific free energy density, plotted in Fig. II.7.

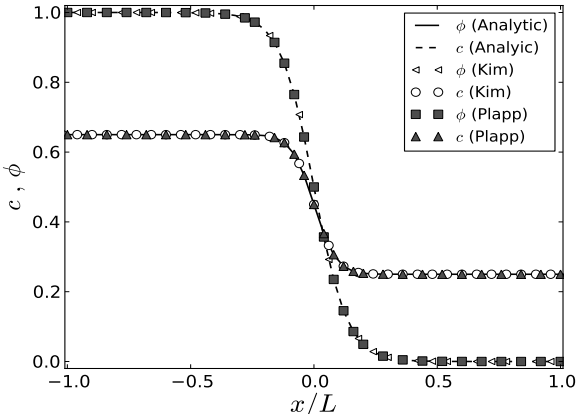

Figure II.10 : Equilibrium profiles of composition and order parameter fields, corresponding to the specific free energy density, plotted in Fig. II.8.

II.5.2 Growth of a single precipitate

II.5.2.1 Gibbs-Thomson equation

When considering a curved interface, the value of the chemical potential is higher than for a planar interface due to the existence of the interfacial energy. The change in chemical potential induces equilibrium concentrations in each phase that are different from what they would be for the planar interface. The dependencies of interfacial concentrations on the interface curvature are determined by the Gibbs-Thomson equation (Ratke and Voorhees, 2002; Hillert, 2008)

$$c_{eq\alpha} = a_\alpha + \frac{1}{k_\alpha \Delta c}(\Delta b + \kappa\gamma), \qquad c_{eq\beta} = a_\beta + \frac{1}{k_\beta \Delta c}(\Delta b + \kappa\gamma) \tag{II.91}$$

where κ is the mean curvature of the interface, assumed to be positive for a single particle of β. The mean curvature is related to the principal radii of the interface curvatures R_α and R_β as:

$$\kappa = 1/R_\alpha + 1/R_\beta \tag{II.92}$$

where $(R_\alpha = R_\beta = R,\ \kappa = 2/R)$ for a spherical particle and $(1/R_\beta = 0,\ \kappa = 1/R_\alpha)$ for a cylindrical precipitate.

In order to understand the formation and displacement of a concave interface and to study the effect of the interface curvature on the change of the equilibrium concentrations, 2D finite element computer simulations have been performed considering the growth of an isotropic precipitate growing in a square region matrix, which has been meshed with linear 4-node quadrangular elements. The finite element mesh is shown in Fig. A.2-c. The boundary conditions and material parameters are the same as in the previous case for the plane interface, except that the dimensionless interfacial energy is taken as $\gamma/(kL) = 5 \cdot 10^{-3}$.

The chosen initial state consists of a small ordered new phase particle α $(\phi = 1)$, which was put at the centre of a supersaturated disordered matrix $\beta\,(\phi = 0)$, with homogeneous initial condition $c_0 = 0.5$. Two initial particle shapes are considered, circular (Fig. II.11) and square (Fig. II.12) shapes, where the equilibrium volume fraction of the ordered phase is about 10%.

The temporal shape evolution of the circular ordered particle during growth is shown in Fig. II.11. Assuming an isotropic phase binary alloy, the existing particle grows by the depletion of matrix saturation, maintaining a circular shape. The composition contour lines around it have

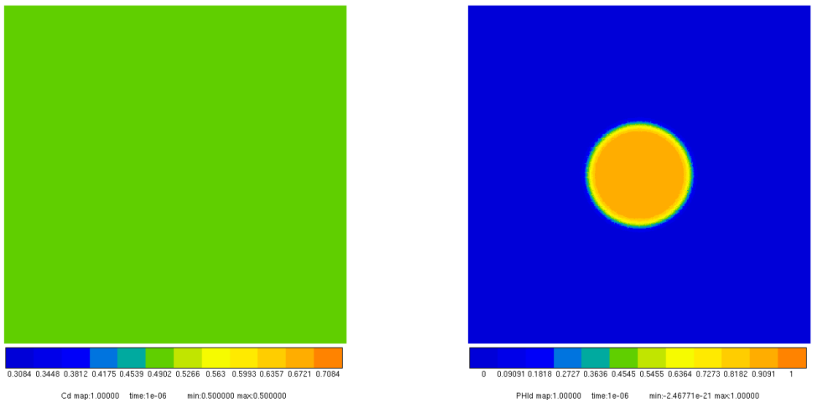

a. $t = 1$

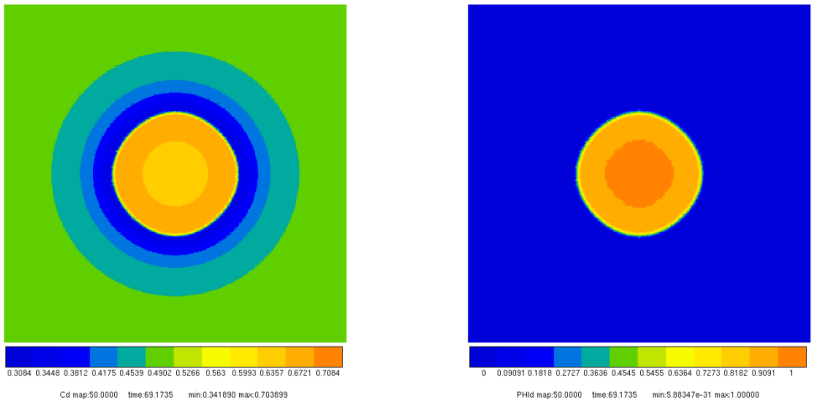

b. $t = 50$

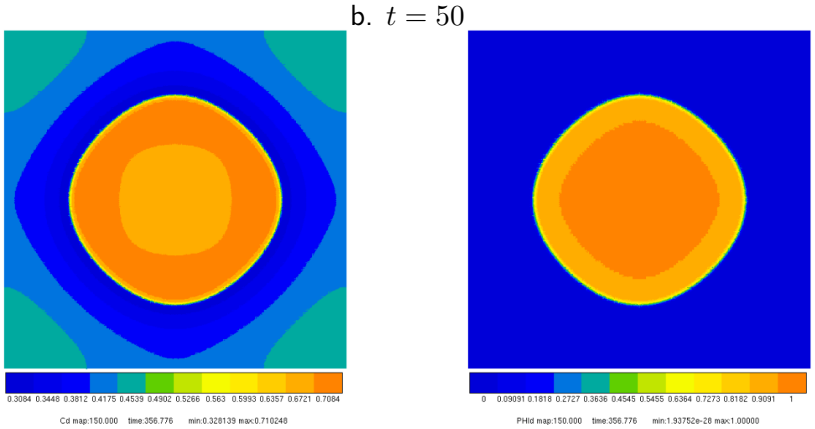

c. $t = 150$

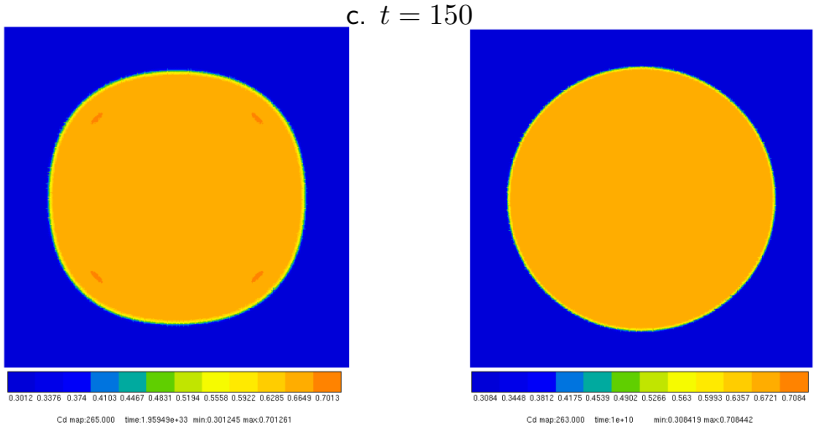

d. $t = 265$

Figure II.11 : Temporal shape evolution of a circular ordered particle during growth. The concentration (left) and the order parameter (right) fields are plotted : (a) t=1, (b) 50,(c) 150,(d) 265 time steps.

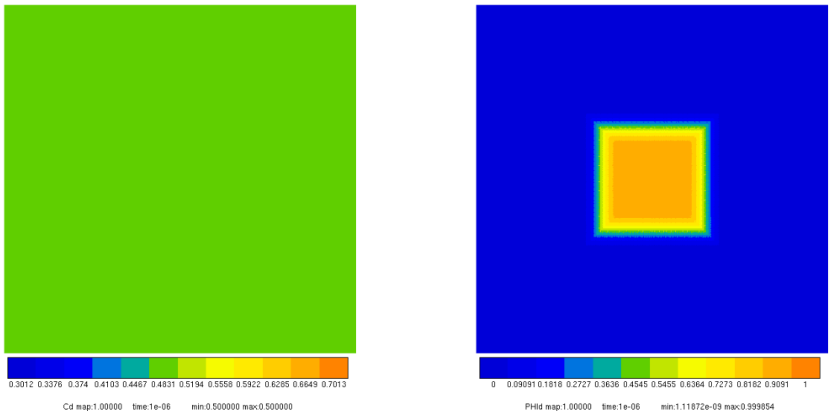

a. $t = 1$

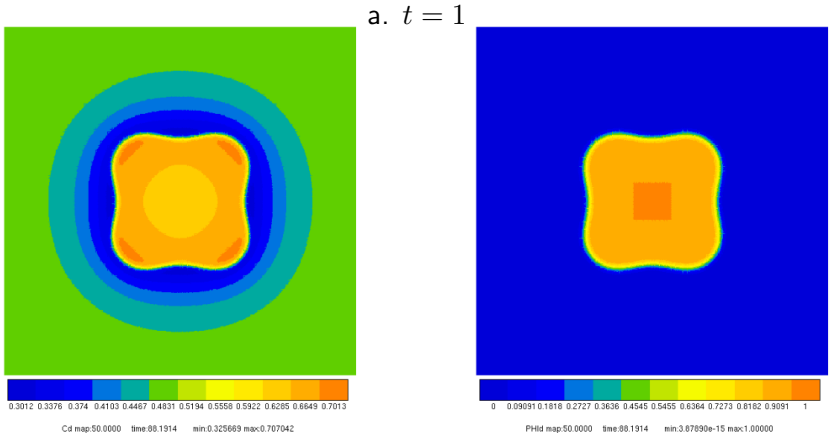

b. $t = 50$

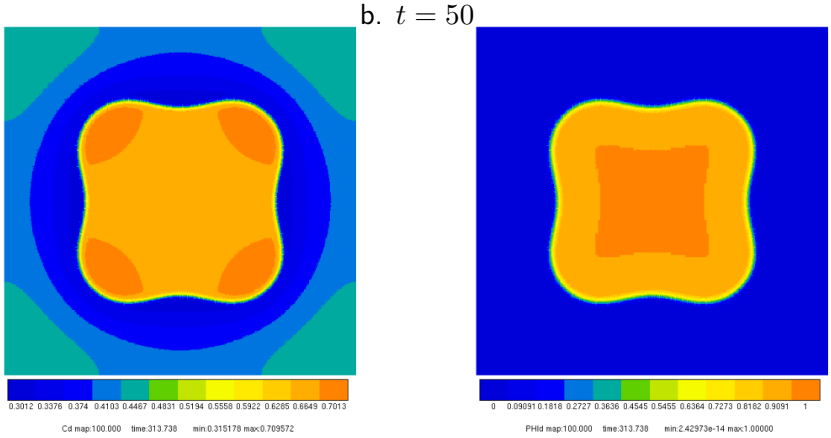

c. $t = 100$

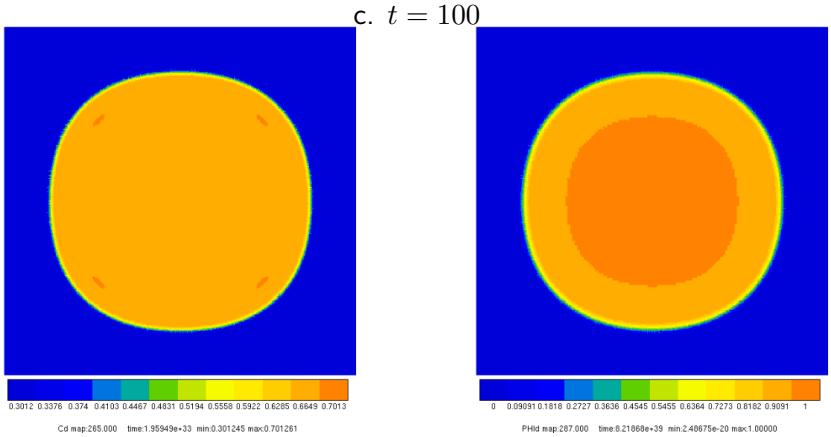

d. $t = 265$

Figure II.12 : Temporal evolution of the concentration (left) and the order parameter (right) fields during the growth of a square particle at: (a) t=1, (b) 50,(c) 100,(d) 265 time steps.

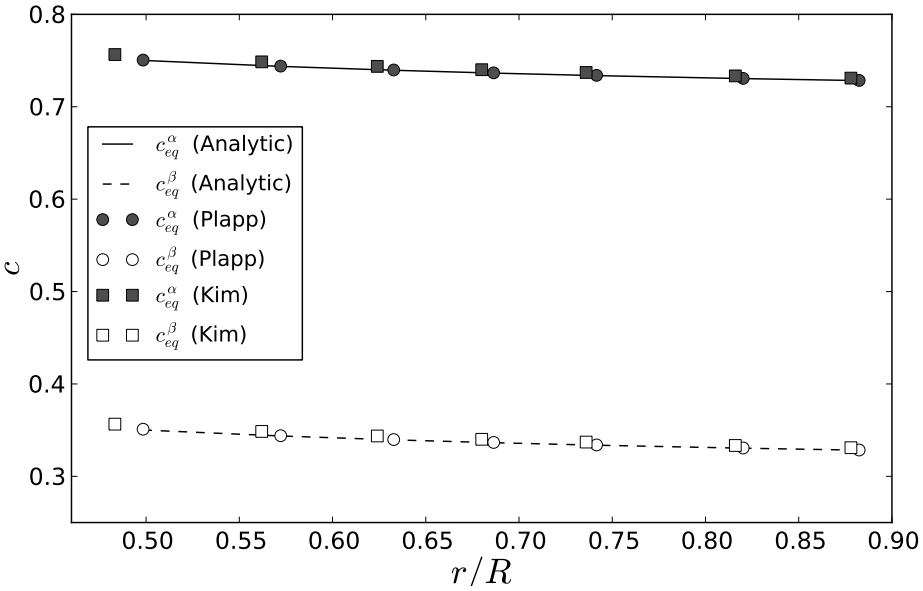

Figure II.13 : Equilibrium concentrations of both phases versus the scaled particle radius r/R. The analytical concentrations c^{α}_{eq} and c^{β}_{eq} , given by Eq. (II.91) , are respectively plotted with continuous and dashed lines, open and black symbols correspond to the numerical results, obtained with Polynomial (Kim) and interpolating (Plapp) free energies.

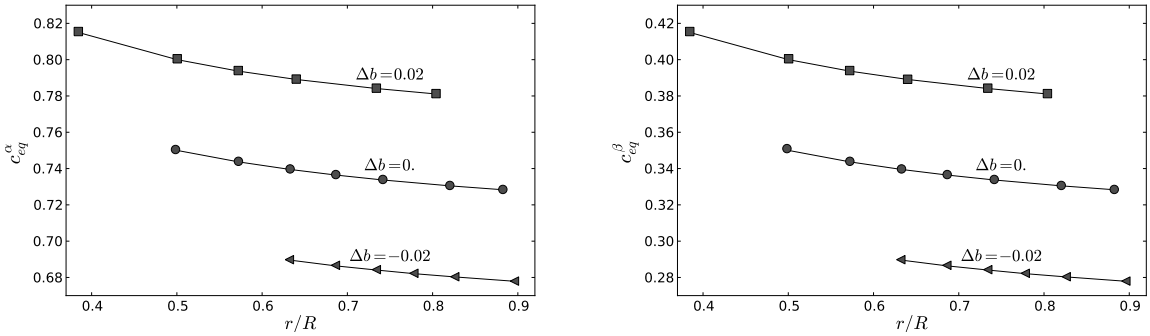

Figure II.14 : Comparison of analytical/numerical results for the equilibrium concentrations c^{α}_{eq} (left) and c^{β}_{eq} (right) as a function of the scaled particle radius r/R for different values of free energy height, i.e $\Delta b = 0, -0.02$ and 0.02.

also circular shapes when the particle is relatively small (see Fig. II.11-b). When the particle reaches a certain size, the super-saturation vanishes and the coexisting phases are assumed to have already reached their equilibrium compositions. For larger particle size, the α precipitate starts interacting with the free surface due to the boundary condition, which results in a deviation of the shape of the contour lines (Fig. II.11-d).

Figure II.12 displays various steps on the evolution growth of a square particle. Since the corners have the maximum exposure area per unit volume to the oncoming diffusional flux of solute atoms, the growth rate at corners is substantially faster, as it can be seen in Fig. II.12-b. The final shape of the solid becomes a circle and the equilibrium composition changes depending on the curvature of the solid.

In order to examine whether the model correctly reproduces the Gibbs-Thomson equation, the equilibrium compositions of both phases have been calculated and plotted in Fig. II.13. The numerical results, obtained using polynomial and interpolating free energy densities, are in very good agreement with the analytical solution, given by Eq. (II.91). As shown in Figure II.14, the dependencies of the numerical equilibrium phase compositions c_α and c_β on the solid radius for different values of free energy height, i.e $\Delta b = 0, -0.02$ and 0.02 are shown to be in a good agreement with the well-known analytical solution given by Eq. (II.91).

II.5.2.2 Mesh sensitivity

A mesh sensitivity analysis is performed considering the effects of finite element type, mesh size and type on the equilibrium profiles of the composition and order parameter. In figure II.15, four different meshes have been used, where the node number in the diffuse interface varies from 5 to 14. The different finite element mesh densities are shown in Fig. A.2. As it can be seen in Fig. II.15, the equilibrium profiles of composition and order parameter field for the different mesh densities and the corresponding analytical profiles are plotted. Indeed, numerical tests suggest that the mesh density should be chosen so that the interfacial region contains approximately 5 to 6 nodes through thickness, in order to ensure an accurate representation of hyperbolic tangent phase-field profile across the diffuse interface thickness. Beyond five nodes in the interfacial region, the numerical results seems to be independent of mesh size.

The quantitative analysis of the mesh sensitivity was carried out here using two different mesh types, which are regular and free meshes. The equilibrium profiles of concentration and order parameter, for the two types of meshes are plotted in figure II.17. As seen in this figure, the choice of mesh type has no significant influence on the numerical equilibrium profiles, which are in excellent agreement with the analytical solution. Moreover, finite element calculations were investigated with two different element types. The first one is performed with linear elements with full integration whereas the second one calls on quadratic elements. Figure II.16 displays the results for the composition and the order parameter equilibrium profiles, which are shown to be about the same for both element types.

The effect of the choice of the interpolating function $h(\phi)$ on the equilibrium profiles of composition and the order parameter fields is plotted in Fig. II.18. Indeed, the advantage of recasting Eq. (II.50) into the free energy density proposed by (Kim et al., 1998) is that the interpolation along ϕ between the free energies $f_i(c)$ is transparent. Indeed, the interpolating function (II.53) can easily be replaced by another odd polynomial, which satisfies the conditions II.52, commonly encountered with a sharper transition between $\phi = 0$ and $\phi = 1$:

$$h(\phi) = \phi^3(6\phi^2 - 15\phi + 10) \tag{II.93}$$

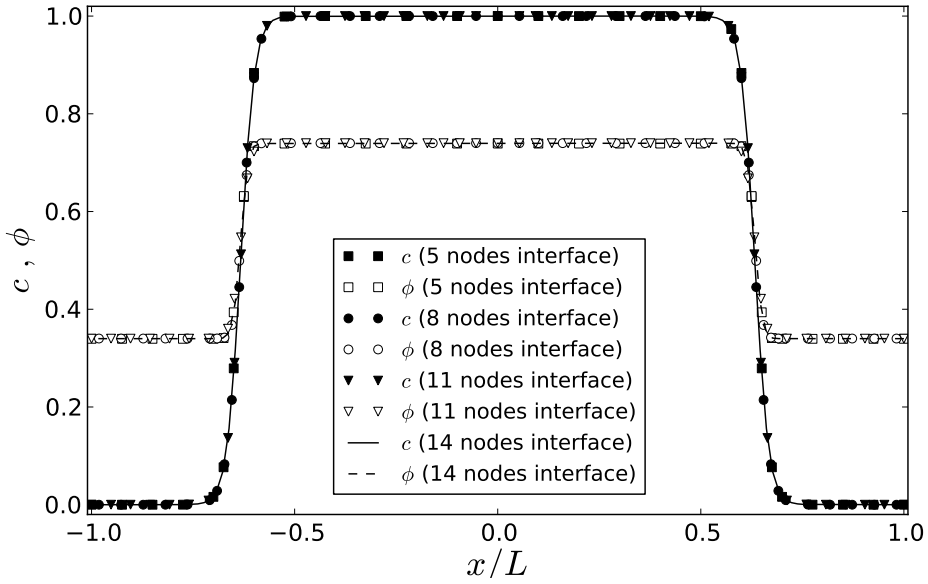

Figure II.15 : Effect of the mesh size on the equilibrium profiles of composition and order parameter fields. Simulations have been performed for four different meshes (5, 8, 11 and 14 nodes in the diffuse interface), for the same boundary value problem and material parameters.

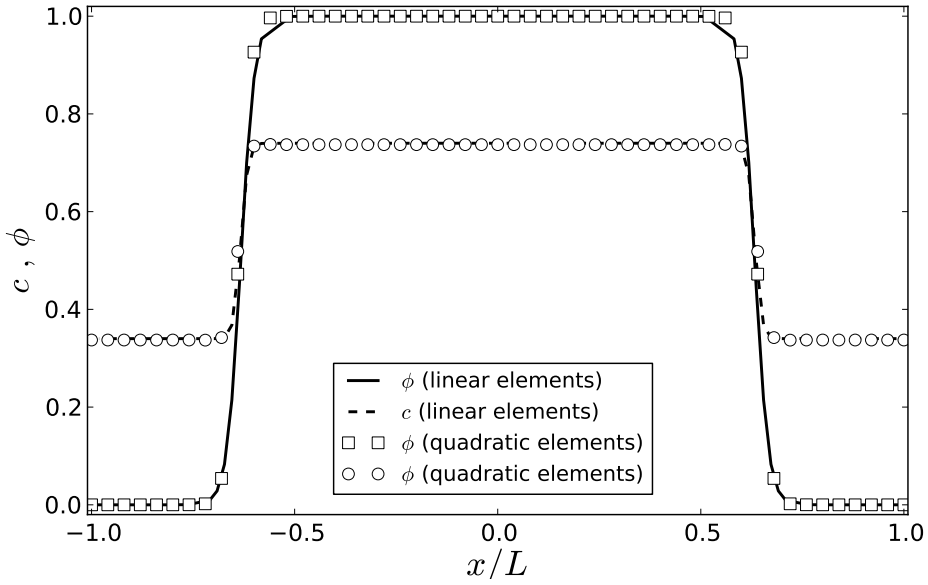

Figure II.16 : Effect of the choice of the finite element type on the equilibrium profiles of composition and order parameter fields. Comparison of results obtained with linear elements (continuous and dashed lines) and quadratic elements (open symbols)

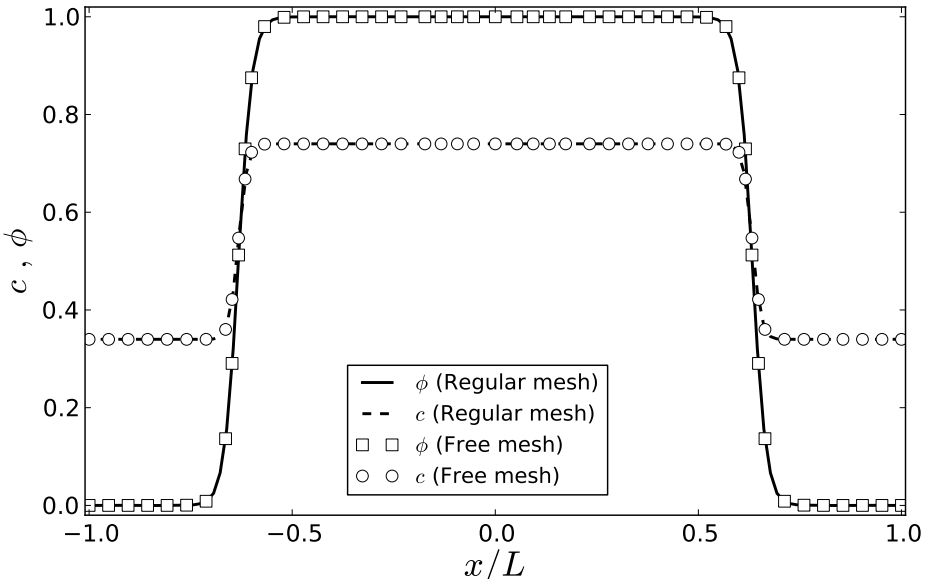

Figure II.17 : Effect of mesh type on the equilibrium profiles of composition and order parameter fields. The continuous and dashed lines depict respectively the numerical profiles of order parameter and composition, obtained with regular mesh. The numerical profiles, using free mesh, are plotted with open symbols.

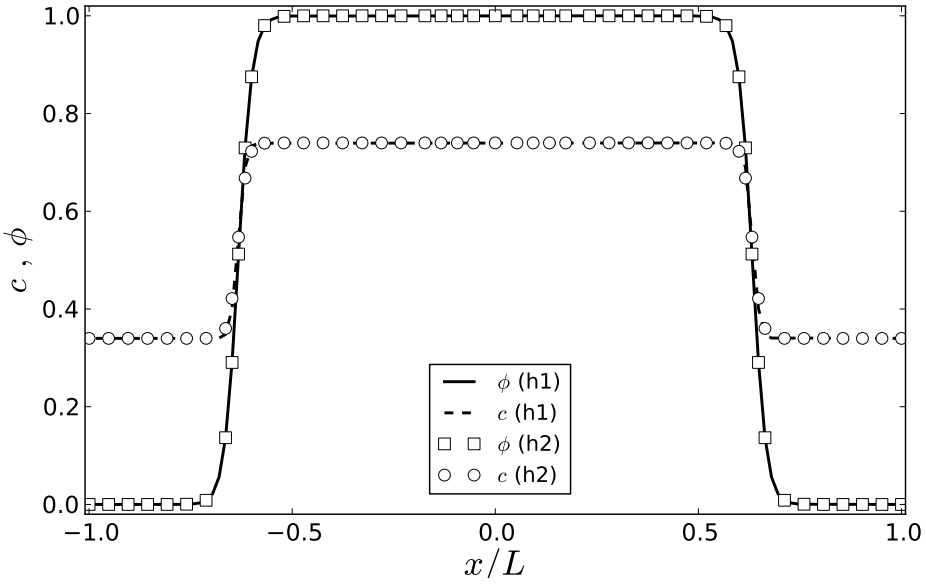

Figure II.18 : Effect of interpolating function $h(\phi)$ on the equilibrium profiles of composition and order parameter fields. The function $h(\phi)$ is used to interpolate the free energies of both phases are interpolated, as presented in Eq.(II.50). Simulations have been performed with two interpolating functions $h_1(\phi) = \phi^2(3-2\phi)$ and $h_2(\phi) = \phi^3(6\phi^2-15\phi+10)$, which are respectively plotted with black lines and open symbols.

Tableau II.2 : Parameters and data used for the zirconium-oxygen system at $350°$C.

β (J s/ m^3)	1.78×10^5	
γ (J/ m^2)	0.1	
δ (m)	2×10^{-8}	
α (J/m)	7.14×10^{-9}	
W (J/m^3)	2.5×10^7	
V_m (m^3/ mole)	10^{-5}	
phase	Zr ($i = \beta$)	ZrO_2 ($i = \alpha$)
A_i (mole fraction)	0.24	0.66
$k_i V_m$ (J/ mole)	1	1
D_i (m^2/ s) from (Parise, 1996)	1.722×10^{-20}	6.368×10^{-18}

II.5.3 Phase field simulation for Ostwald ripening

Ostwald ripening is a process related to the coarsening of one phase dispersed in a matrix phase. It is the last stage of a first-order phase transition for condensation of a metastable phase. The first stage is nucleation when a new phase forms from the mother phase, maintained in a super-saturated state. As the super-saturation decreases due to particle growth, the nucleation barrier and the stable cluster size increase. The system usually forms a microstructure with particles in a matrix. Even after full exhaustion of the driving force, the particles in the matrix are not in thermodynamic equilibrium. The system can further decrease its total free energy by decreasing the overall interface area between the particles and the matrix. The decrease of total interface area progresses by a process where the large particles grow at the expense of the smaller particles. The average size of the particles of the dispersed phase increases during coarsening due to diffusion through the matrix phase, and their total number decreases. This process is known as coarsening, or Ostwald ripening phenomenon.

For modelling Ostwald ripening analysis in two-phase alloy, a square area has been meshed with 250×250 linear quadrangular elements. Several solid particles ($\phi = 1$) of different forms and radius were randomly put in the area ($\phi = 0$). The initial solute compositions of both phases are homogeneous and set to be equal to $c_0 = 0.5$. The simulated result for the Ostwald-ripening process is shown in Fig. II.19.

II.6 Application: oxidation of zirconium

The model has been used to study the growth of oxide layer in α phase at 350℃ in the simple Zr-O binary system. The parameters are reported in Tab. II.2. An interfacial energy of 100 mJ/m^2 corresponds to a coherent/semi-coherent interface between the oxide and zirconium (Penelle et al., 1971). An interface thickness δ about two orders of magnitude larger than a realistic value has been chosen to render the computations tractable.

A regular mesh with 1000 linear elements has been used to discretize a 1 μm long 1D slab. An adaptive time step implemented in ZeBuLoN as a standard option has been used for the calculations: small time steps of the order of 10^{-6} s were necessary to achieve a good convergence at the beginning of the process, whereas large time steps of the order of 10^3 s were reached at the end of the calculations. The following boundary conditions to the system have been applied on the right side: $\underline{\boldsymbol{\xi}}.\underline{\boldsymbol{n}} = 0$ and $\underline{\boldsymbol{J}}.\underline{\boldsymbol{n}} = 0$; and on the left side corresponding to the surface: $\underline{\boldsymbol{\xi}}.\underline{\boldsymbol{n}} = 0$ and $c = 0.68$. The Dirichlet condition imposed at the left side is assumed to mimic the reaction between the oxide surface and the oxidizing atmosphere. A value slightly above

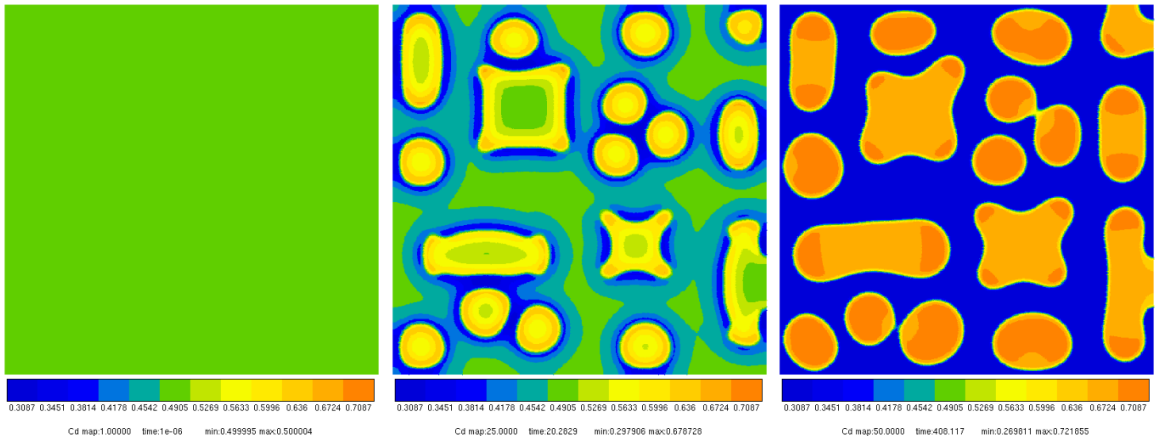

a. $t = 1$ b. $t = 25$ c. $t = 50$

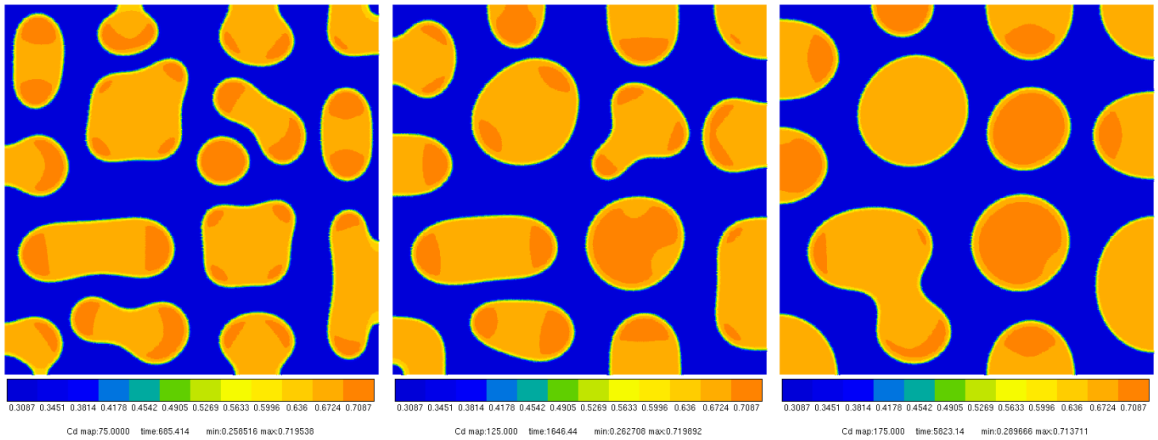

d. $t = 75$ e. $t = 125$ f. $t = 175$

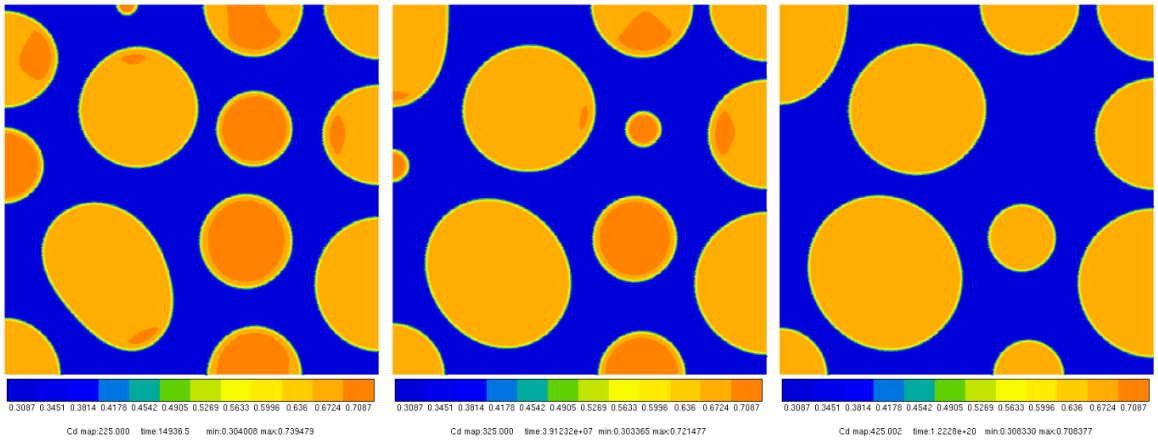

g. $t = 225$ h. $t = 325$ i. $t = 425$

Figure II.19 : Time history of Ostwald ripening process: (a) 1, (b) 25, (c) 50, (d) 75, (e) 125, (f) 175, (g) 225, (h) 325, and (i) 425 time steps.

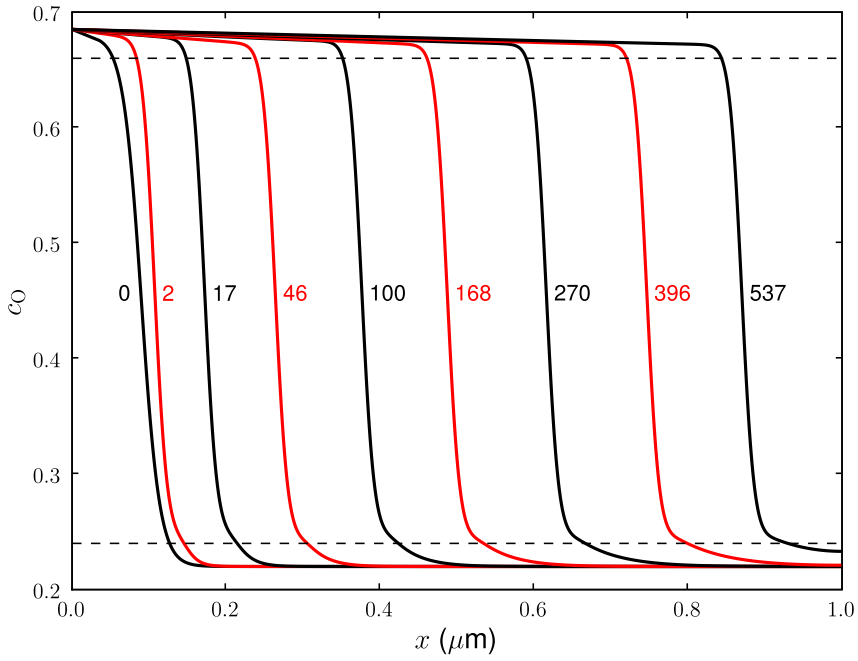

Figure II.20 : Evolution of the concentration profile in oxygen (in mole fraction) near the surface of the slab; numbers labelling the curves are the related holding times in hours. Horizontal dashed lines are the equilibrium concentrations.

the stoichiometric concentration has been chosen to rapidly initiate the growth of the layer and shorten an initial transient regime.

A profile of ϕ in $\tanh$ has been set corresponding to an initial 84 nm thick ZrO_2 layer at the surface of the zirconium slab. A decreasing concentration profile has been prescribed in ZrO_2 between the surface and the interface at equilibrium. A flat profile is imposed at 0.22 a value below equilibrium in α corresponding to α phase undersaturated in oxygen (Fig. II.20).

The concentration profiles are shown at different times in Fig. II.20. The steep gradients locate the interface between the oxide and the metal. At the beginning of the process (e.g. the curve after 2h of isothermal holding), the concentrations at interface are slightly higher than the equilibrium ones (dashed lines), due to the dissipation of free energy associated with interfacial kinetics and with diffusion of oxygen across interface. These dissipation processes are magnified because of the unrealistically large interface width (Tab. II.2), chosen for computational purpose as commonly done in phase field simulations. These spurious effects can be eliminated by performing a careful asymptotic analysis (e.g. (Echebarria et al., 2004)) together with using an adaptive mesh refinement technique as discussed thoroughly in (Provatas et al., 2005). These improvements will be undertaken in a forthcoming study. Very quickly, a gradient in oxygen content develops in α in front of the growing oxide. The inward growth process is thus driven by diffusion of oxygen in both phases.

The time evolution of the oxide thickness Δe shown in Fig. II.21 has been deduced from the profiles by tracking the position of $\phi = 0.5$. Apart from the beginning of the process which is strongly influenced by the initial conditions, the growth law is parabolic, i.e. $\Delta e = K\sqrt{t}$. The growth constant $K = 7.5 \cdot 10^{-10}$ m/s has been determined by linear regression of $(\ln(\Delta e), \ln(t))$, discarding the first points. This value is in good agreement with the value of $7.75 \cdot 10^{-10}$ m/s given by the analytical solution of (Appolaire and Gouné, 2006). The difference can be attributed to the dissipation of the driving force by the interfacial phenomena. Moreover, it must be noticed that a good agreement with the experimental measurements of (Parise, 1996) is achieved, as

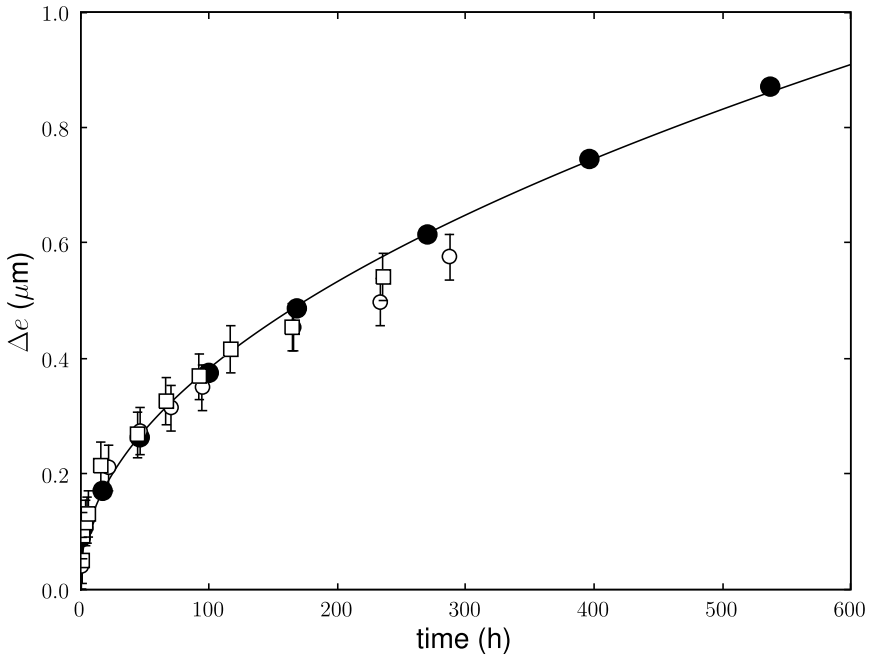

Figure II.21 : The growth kinetics of the oxide layer: black dots are related to the profiles in Fig. II.20; the continuous line corresponds to the best fit with a parabolic law. Experimental data from (Parise, 1996) obtained in Zircaloy-4 have been superimposed with open symbols.

shown in Fig. II.21.

In order to illustrate the advantage of the finite element formulations over the other methods used in phase field modeling, 2D calculations have been performed to investigate a problem where the surface geometry may play a role: the morphological stability of the oxide layer. The finite element mesh is composed of 15000 quadrangular linear elements, and time steps similar to the 1D case have been used for the calculations. As shown in (Appolaire and Gouné, 2006) for the nitriding of pure iron, the configuration of the diffusion fields has a stabilizing effect with respect to fluctuations, at both the layer/matrix interface and the layer surface. Hence, small sine fluctuations have been imposed initially either at the interface (Fig. II.22), or at both surface and interface (Fig. II.23), with different wavelengths. In both cases, it is observed that the corrugations have completely disappeared after thousand seconds, i.e. on a short time scale when compared to the growth process. This result is again in accordance with the analytical analysis of a similar problem (Appolaire and Gouné, 2006), and shows the potentiality of the present formulation and implementation for the phase field modeling.

II.7 Conclusion

A finite element formulation for a phase field model has been presented, based on the introduction of generalized stresses and their balance, and on the framework of the thermodynamics of irreversible processes. Using the finite element method to discretize space and the finite difference method to discretize time, numerical simulations were performed to investigate the oxidation kinetics of pure zirconium. Moreover, numerical calculations were performed to investigate the evolution of a plane and curved diffuse interface between two phases. The formulation presented here allows, on the one hand, the application of any arbitrary form of the free energy, such as Khachaturyan models (Wang and Khachaturyan, 1995b) and Folch-Plapp (Folch and Plapp,

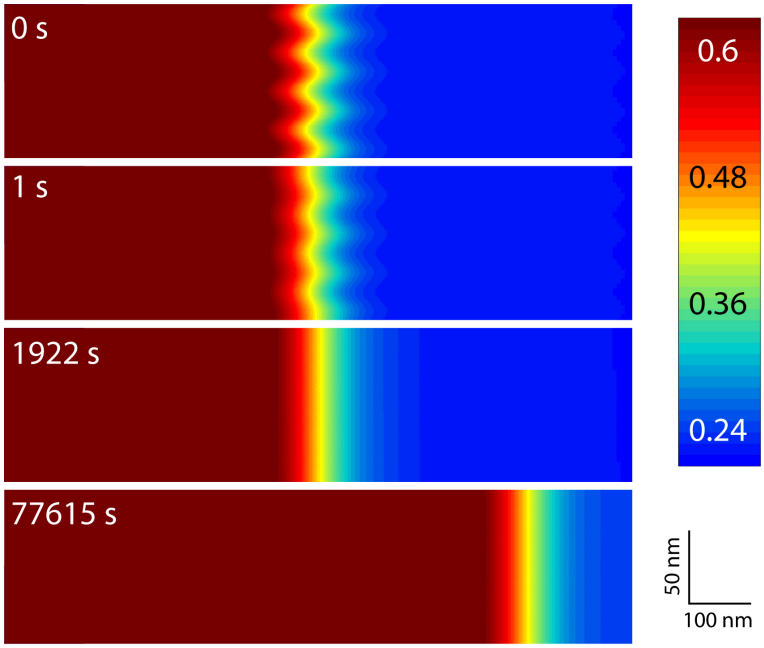

Figure II.22 : Evolution vs. time of the concentration field in oxygen during the growth of an oxide with an interface initially destabilized by a sine.

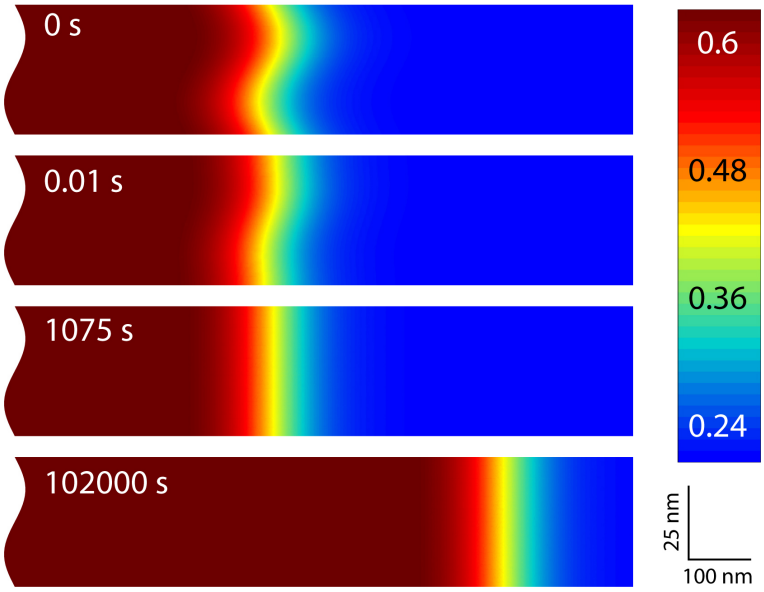

Figure II.23 : Evolution vs. time of the concentration field in oxygen during the growth of a sinusoidal oxide layer.

2005) and, on the other hand, the use of finite size samples with arbitrary geometries and very general non-periodic or periodic boundary conditions. Furthermore, an extension of the present model will be obtained by introducing other general processes that include dissipation, like in the coupling with mechanics, especially plasticity.

Abstract

A finite element formulation of a phase field model for alloys is proposed within the general framework of continuum thermodynamics in conjunction with the concept of generalized stresses as proposed by Gurtin (Gurtin, 1996). Using the principles of the thermodynamics of irreversible processes, balance and constitutive equations are clearly separated in the formulation. Also, boundary conditions for the concentration and order parameter and their dual quantities are clearly stated. The theory is shown to be well-suited for a finite element formulation of the initial boundary value problem. The set of coupled evolution equations, which are the phase field equation and the balance of mass, is solved using an implicit finite element method for space discretization and a finite difference method for time discretization. Numerical simulations were performed to investigate the formation and the evolution of a plane and curved diffuse interface between two phases and to study the sensitivity of numerical results on the choice of the free energy density and its parameters, the mesh size and the types of elements. For an illustrative purpose, the model is used to investigate the growth of an oxide layer at the surface of a pure zirconium slab. Calculations in 1D show a good agreement with an analytical solution for the growth kinetics. Then, 2D calculations of the same process have been undertaken to investigate morphological stability of the oxide layer in order to show the ability of the finite element method to handle arbitrary conditions on complex boundaries.

Chapitre -III-

Combining phase field approach and homogenization methods for modelling phase transformation in elastoplastic media

Contents

III.1 Introduction 44
III.2 Phase-field/diffusion/mechanical model 46
III.2.1 Principle of virtual power and balance equations 46
III.2.2 Thermodynamical formulation 47
III.3 Free energy and dissipation potential 49
III.3.1 Partition of free energy and dissipation potential 49
III.3.2 Chemical contribution 49
III.3.3 Mechanical contribution 50
III.4 Phase field approach and homogenization methods 50
III.4.1 Multiphase approach 50
III.4.2 Voigt/Taylor model 53
III.4.3 Reuss/Sachs model 54
III.4.4 Comparison with existing interpolation schemes 54
III.4.5 Expression of the phase field-elastic coupling terms 55
III.5 Two-phase elastoplastic alloy with hardening 57
III.6 Implementation in a finite element code 59
III.6.1 Discretization 60
III.6.2 Programming of finite element constitutive equations 62
III.6.2.1 Runge-Kutta method 63
III.6.2.2 Θ-method 67
III.7 Conclusions 67

III.1 Introduction

One observes in current literature a strong endeavour to develop microstructure evolution simulation schemes coupled with complex mechanical material behaviour ranging from heterogeneous elasticity to general elastoviscoplasticity. The main difficulty of such a task lies in the tight coupling between the complex interfaces evolutions and the fields, common to many free boundary problems. Hence, some attempts to achieve this goal have circumvented the difficulty by undertaking standard finite element calculations with prescribed interface kinetics, i.e. without the feedback of mechanics on phase transformation, e.g. (Ganghoffer et al., 1994; Barbe et al., 2008). If valuable insights have been obtained into internal stresses generated by evolving microstructures, the missing coupling prevents to use the predictions for materials undergoing phase transformations with complex changes in morphology and phase distribution. In parallel, the phase field approach has emerged as a powerful method for easily tackling the morphological evolutions involved in phase transformations. Phase field models have incorporated elasticity quite early (Onuki, 1989; Wang et al., 1993b) and have succeeded in predicting some complex microstructure evolutions driven by the interplay of diffusion and elasticity, e.g. (Le Bouar et al., 1998; Boussinot et al., 2009). It is only very recently that some phase field models have been enriched with nonlinear mechanical behaviour, extending the range of applications and materials which can be handled by the phase field approach (Guo et al., 2005; Uehara et al., 2007; Guo et al., 2008; Yamanaka et al., 2008; Zhou et al., 2008; Gaubert et al., 2008; Gaubert et al., 2009).

There are essentially two ways of introducing linear and nonlinear mechanical constitutive equations into the standard phase field approach:

1. The material behaviour is described by a unified set of constitutive equations including material parameters that explicitly depend on the concentration or the phase variable. Each parameter is usually interpolated between the limit values known for each phase. This is the formulation adopted in the finite element simulations of Cahn–Hilliard like equations coupled with viscoplasticity in (Ubachs et al., 2004; Ubachs et al., 2005) for tin–lead solders, also derived in (Forest, 2008; Forest, 2009). The same methodology is used in (Gaubert et al., 2008; Gaubert et al., 2009) to simulate the role of viscoplasticity on rafting of γ' precipitates in single crystal nickel base superalloys under load. For instance, when an elastic phase coexists with an elastic–plastic one, the plastic yield limit is interpolated between the real value in the plastic phase and a very high unreachable value in the elastic phase, e.g. (Cha et al., 2009).

2. One distinct set of constitutive equations is attributed to each individual phase k at any material point. Each phase at a material point then possesses its own stress/strain tensor $\underset{\sim}{\boldsymbol{\sigma}}_k, \underset{\sim}{\boldsymbol{\varepsilon}}_k$. The overall strain and stress quantities $\underset{\sim}{\boldsymbol{\sigma}}, \underset{\sim}{\boldsymbol{\varepsilon}}$ at this material point must then be averaged or interpolated from the values attributed to each phases. This is particularly important for points inside the smooth interface zone. At this stage, several mixture rules are available to perform this averaging or interpolation. This approach makes possible to mix different types of constitutive equations for each phase, like hyperelastic nonlinear behaviour for one phase and conventional elastic–plastic model with internal variables for the other one. No correspondence of material parameters is needed between the phase behaviour laws. This is the approach proposed in (Steinbach and Apel, 2006) for incorporating elasticity in a multi–phase field model. For that purpose, the authors resort to a well–known homogeneous stress hypothesis taken from homogenization theory in the mechanics of heterogeneous materials (Nemat-Nasser and Hori, 1999; Qu and Cherkaoui, 2006). This approach has been applied to compute the effect of chemical induced strain on pearlite growth kinetics in (Steinbach and Apel, 2007). In the present work, we propose to generalize this procedure to nonlinear material behaviour and to other mixture rules also taken from homogenization

theory.

It must be emphasized that this procedure is very similar to what has already been proposed for handling diffusion in phase field models by (Kim et al., 1999). Two concentration fields c_α and c_β are indeed introduced, and the real concentration field is obtained by a mixture rule together with an internal constraint on the diffusion potentials, called quasi-equilibrium constraint in (Eiken et al., 2006). Introducing two concentration fields gives an additional degree of freedom for controlling the energy of the interface with respect to its thickness. If this possibility is not obvious when mechanics is introduced, adding a degree of freedom for describing the stresses/strains within a diffuse interface could be valuable to get rid of some spurious effects due to unrealistic interface thickness.

The objective of the present chapter is thus twofold:

1. To set a general framework that combines standard phase field approaches with a different complex mechanical behaviour for each phase. The approach will be shown to be amenable to practical simulations by presenting a simple finite element analysis of the growth of an elastic–plastic phase within an elastic matrix.

2. To compare the implication of the choice of specific mixture rules for these behaviour laws in the diffuse interface region on the predicted coherent phase diagram. Two interpolation rules taken from homogenization methods classically used in the mechanics of heterogeneous materials, will be evaluated and compared to the usual interpolation rule of standard phase field models. The comparison will be drawn for a simple microelasticity/phase field/diffusion problem for which an analytical solution is available.

The homogenization methods in the mechanics of heterogeneous materials have reached a high level of sophistication by providing bounds and estimations for the effective properties of elastic and nonlinear composites (Suquet, 1997; Jeulin and Ostoja-Starzewski, 2001). They are based on the definition of a representative volume element (RVE) at each material point in which mean strain and stress can be defined for each phase. The basic assumption is that the local behaviour of phases inside the RVE can be represented by classical continuum mechanics. This is no longer the case when the RVE is a collection of atoms including different atom species, as it is usually the case in the volume element of phase field models. In particular the average relationships derived in continuum micromechanics are not valid for replacing a discrete set of atoms by a continuum with diffusion/mechanics effective properties. Discrete–continuum homogenization schemes exist in some cases for phase field models (Rodney et al., 2003) but remain limited in terms of physical situations. That is why no specific arrangement of phases will be considered inside the RVE for the theory proposed in this chapter. Instead, each relationship taken from micromechanical approaches will be adopted as a phenomenological ansatz in our model. Since there exists a large variety of such micromechanical mixture rules, it is worth evaluating some of them in the context of phase field/diffusion/mechanics models.

The numerical methods available to solve the coupled phase field/diffusion/mechanics field equations are those commonly used to solve partial differential equations. Hence, the finite volume scheme is adopted in (Appolaire and Gautier, 2003; Appolaire et al., 2009) whereas a mixed finite difference-finite element scheme is used in (Nakajima et al., 2006). In (Gaubert et al., 2008), the Fourier method is used for periodic unit cell simulations. Finally, the simulations in (Ubachs et al., 2005) are carried out by means of a finite element method prevailing in the field of nonlinear mechanics. The simulations presented in this chapter are performed with the finite element model recently proposed in (Ammar et al., 2009a; Ammar et al., 2009d). Its setting is based on a variational formulation of the phase field equations in terms of generalized stresses as initially introduced by (Fried and Gurtin, 1993; Fried and Gurtin, 1994; Gurtin, 1996).

The chapter is organized as follows. The balance and boundary conditions of a fully coupled phase field/diffusion/mechanical problem are given in section III.2. The constitutive equations for chemical and mechanical processes are formulated by means of the expression of the free energy potential. A dissipation potential is then introduced for chemical and mechanical dissipative processes. A specific decomposition of these two potentials into chemical and mechanical contributions is given in section III.3. Two mixture rules for strain and stress within the diffuse interface are analyzed in section III.4, which are based on the Voigt/Taylor and Reuss/Sachs well–known homogenization schemes. They are compared to the commonly used mixture rules in phase field models. This last section III.6 is devoted to the introduction of the proposed non-linear elastoplastic phase field model with different homogenization schemes in the finite element code. For the sake of simplicity, the theory is expressed within the small perturbation framework (small strain), under isothermal conditions.

III.2 Phase-field/diffusion/mechanical model

III.2.1 Principle of virtual power and balance equations

As shown in chapter II, the principle of virtual power has proved to be an efficient tool for deriving governing force balance equations and boundary conditions. Following this principle, the overall powers of internal, external and contact generalized forces, for all virtual order parameter $\phi^\star$ and virtual displacement $\underline{\boldsymbol{u}}^\star$ and for all subdomain $\mathcal{D}$ of body V, are assumed to admit power densities:

$$\mathcal{P}^{(i)}(\phi^\star, \underline{\boldsymbol{u}}^\star, V) = \int_V p^{(i)}(\phi^\star, \underline{\boldsymbol{u}}^\star)\, dv, \quad \mathcal{P}^{(e)}(\phi^\star, \underline{\boldsymbol{u}}^\star, V) = \int_V p^{(e)}(\phi^\star, \underline{\boldsymbol{u}}^\star)\, dv,$$
$$\mathcal{P}^{(c)}(\phi^\star, \underline{\boldsymbol{u}}^\star, V) = \int_{\partial V} p^{(c)}(\phi^\star, \underline{\boldsymbol{u}}^\star)\, ds \tag{III.1}$$

The power density of internal forces is taken as a general linear form, associated with generalized stresses $\{-\pi, \underline{\boldsymbol{\xi}}, \underset{\sim}{\boldsymbol{\sigma}}\}$ power-conjugates to $\{\phi^\star, \boldsymbol{\nabla}\phi^\star, \boldsymbol{\nabla}\underline{\boldsymbol{u}}^\star\}$ as:

$$p^{(i)}(\phi^\star, \underline{\boldsymbol{u}}^\star) = \pi\phi^\star - \underline{\boldsymbol{\xi}}.\boldsymbol{\nabla}\phi^\star - \underset{\sim}{\boldsymbol{\sigma}} : \boldsymbol{\nabla}\underline{\boldsymbol{u}}^\star \tag{III.2}$$

where π and $\underline{\boldsymbol{\xi}}$ respectively are the scalar and vector microstresses, as introduced in (Gurtin, 1996) and $\underset{\sim}{\boldsymbol{\sigma}}$ is the Cauchy stress tensor.

Similarly, the virtual power density of external generalized forces reads :

$$p^{(e)}(\phi^\star, \underline{\boldsymbol{u}}^\star) = \gamma\phi^\star + \underline{\boldsymbol{\gamma}}.\boldsymbol{\nabla}\phi^\star + \underline{\boldsymbol{f}}.\underline{\boldsymbol{u}}^\star \tag{III.3}$$

where $\underline{\boldsymbol{f}}$ is the volumetric density of force and the external microforces are represented by the scalar γ and the vector $\underline{\boldsymbol{\gamma}}$ (Ammar et al., 2009a; Ammar et al., 2009b).

The contact generalized forces applied to the body are given by a surface density of microtraction ζ and a surface density of cohesion forces $\underline{\boldsymbol{t}}$ for the purely mechanical part over the boundary. Then, the virtual power density of contact generalized forces is expressed as:

$$p^{(c)}(\phi^\star, \underline{\boldsymbol{u}}^\star) = \zeta\phi^\star + \underline{\boldsymbol{t}}.\underline{\boldsymbol{u}}^\star \tag{III.4}$$

Assuming that no inertial microforces exist, the principle of virtual power requires that the virtual powers of externally and internally acting forces are balanced on any subdomain $\mathcal{D} \subset V$, for any choice of the virtual order parameter and displacement fields:

$\forall\phi^\star, \forall\underline{\boldsymbol{u}}^\star, \forall\mathcal{D} \subset V$

$$\mathcal{P}^{(i)}(\phi^\star, \underline{\boldsymbol{u}}^\star, \mathcal{D}) + \mathcal{P}^{(c)}(\phi^\star, \underline{\boldsymbol{u}}^\star, \mathcal{D}) + \mathcal{P}^{(e)}(\phi^\star, \underline{\boldsymbol{u}}^\star, \mathcal{D}) = 0 \tag{III.5}$$

$$\int_{\mathcal{D}} (\pi + \boldsymbol{\nabla}.\underline{\boldsymbol{\xi}} + \gamma - \boldsymbol{\nabla}.\underline{\boldsymbol{\gamma}})\phi^\star + (\boldsymbol{\nabla}.\underset{\sim}{\boldsymbol{\sigma}} + \underline{\boldsymbol{f}}).\underline{\boldsymbol{u}}^\star \, dv + \int_{\partial\mathcal{D}} (\zeta - \underline{\boldsymbol{\xi}}.\underline{\boldsymbol{n}} + \underline{\boldsymbol{\gamma}}.\underline{\boldsymbol{n}})\phi^\star + (\underline{\boldsymbol{t}} - \underset{\sim}{\boldsymbol{\sigma}}.\underline{\boldsymbol{n}}).\underline{\boldsymbol{u}}^\star \, ds = 0 \quad \text{(III.6)}$$

The exploitation of the method of virtual power leads, on the one hand, to the balance equation associated with order parameter ϕ and boundary condition for the generalized microtraction vector:

$$\boldsymbol{\nabla}.(\underline{\boldsymbol{\xi}} - \underline{\boldsymbol{\gamma}}) + \pi + \gamma = 0 \quad \text{in} \quad V, \qquad \text{and} \quad \zeta = (\underline{\boldsymbol{\xi}} - \underline{\boldsymbol{\gamma}}).\underline{\boldsymbol{n}} \quad \text{on} \quad \partial V \qquad \text{(III.7)}$$

and, on the other hand, to the classical local static equilibrium and the associated boundary condition:

$$\boldsymbol{\nabla}.\underset{\sim}{\boldsymbol{\sigma}} + \underline{\boldsymbol{f}} = 0 \quad \text{in} \quad V, \qquad \text{and} \quad \underline{\boldsymbol{t}} = \underset{\sim}{\boldsymbol{\sigma}}.\underline{\boldsymbol{n}} \quad \text{on} \quad \partial V \qquad \text{(III.8)}$$

The balance equation (III.7) is similar to Gurtin's microforce balance (Gurtin, 1996), with a slight extension represented by the presence of a possible prescribed volume density of vector external microforce $\underline{\boldsymbol{\gamma}}$, which has been introduced for the sake of generality.

III.2.2 Thermodynamical formulation

The thermodynamical framework presented in chapter II is now complemented by the contribution coming from mechanics. The first principle of thermodynamics is formulated here in the absence of thermal and acceleration effects. The time variation of internal energy $\mathcal{E}$ is due to the power of external generalized forces, which is represented by volume and contact forces:

$$\dot{\mathcal{E}} = \int_V \dot{e} \, dv = \mathcal{P}^{(e)} + \mathcal{P}^{(c)} \qquad \text{(III.9)}$$

where e is the internal energy density.

Taking the principle of virtual power (III.5) into consideration, the local form of the energy principle then reads:

$$\dot{e} = -\pi\dot{\phi} + \underline{\boldsymbol{\xi}}.\boldsymbol{\nabla}\dot{\phi} + \underset{\sim}{\boldsymbol{\sigma}} : \dot{\underset{\sim}{\boldsymbol{\varepsilon}}} \qquad \text{(III.10)}$$

where $\underset{\sim}{\boldsymbol{\varepsilon}}$ is the total strain, which may be partitioned into the elastic strain $\underset{\sim}{\boldsymbol{\varepsilon}}^e$, the eigenstrain $\underset{\sim}{\boldsymbol{\varepsilon}}^\star$ due to phase transformation and the plastic strain $\underset{\sim}{\boldsymbol{\varepsilon}}^p$:

$$\underset{\sim}{\boldsymbol{\varepsilon}} = \underset{\sim}{\boldsymbol{\varepsilon}}^e + \underset{\sim}{\boldsymbol{\varepsilon}}^\star + \underset{\sim}{\boldsymbol{\varepsilon}}^p \qquad \text{(III.11)}$$

According to the thermodynamics of irreversible processes, the second law states that the variation of entropy is always larger than or equal to the rate of entropy flux induced by diffusion:

$$T\dot{s} - \boldsymbol{\nabla}.(\mu\underline{\boldsymbol{J}}) \geqslant 0 \qquad \text{(III.12)}$$

where s is the entropy density, $\underline{\boldsymbol{J}}$ is the diffusion flux and μ is the chemical potential.

Introducing the free energy density $\dot{f} = \dot{e} - T\dot{s}$, and using the equation of mass balance $\dot{c} = -\boldsymbol{\nabla}.\underline{\boldsymbol{J}}$, the fundamental inequality containing first and second principles in the isothermal case is written as the Clausius-Duhem inequality:

$$-\dot{f} - \pi\dot{\phi} + \underline{\boldsymbol{\xi}}.\boldsymbol{\nabla}\dot{\phi} + \mu\dot{c} - \underline{\boldsymbol{J}}.\boldsymbol{\nabla}\mu + \underset{\sim}{\boldsymbol{\sigma}} : \dot{\underset{\sim}{\boldsymbol{\varepsilon}}} \geqslant 0 \qquad \text{(III.13)}$$

Assuming that the free energy density depends on the order parameter ϕ and its gradient, the concentration c, the elastic strain $\underset{\sim}{\boldsymbol{\varepsilon}}^e$ and the set of internal variables V_k associated to material hardening, the time derivation of f with respect to its state variables is given by the chain rule as:

$$\dot{f}(\phi, \boldsymbol{\nabla}\phi, c, \underset{\sim}{\boldsymbol{\varepsilon}}^e, V_k) = \frac{\partial f}{\partial \phi}\dot{\phi} + \frac{\partial f}{\partial \boldsymbol{\nabla}\phi}.\boldsymbol{\nabla}\dot{\phi} + \frac{\partial f}{\partial c}\dot{c} + \frac{\partial f}{\partial \underset{\sim}{\boldsymbol{\varepsilon}}^e} : \dot{\underset{\sim}{\boldsymbol{\varepsilon}}}^e + \frac{\partial f}{\partial V_k}\dot{V}_k \qquad \text{(III.14)}$$

Consequently, the Clausius-Duhem inequality becomes:

$$-\left(\pi+\frac{\partial f}{\partial \phi}\right)\dot{\phi}+\left(\underline{\boldsymbol{\xi}}-\frac{\partial f}{\partial \boldsymbol{\nabla}\phi}\right).\boldsymbol{\nabla}\dot{\phi}+\left(\mu-\frac{\partial f}{\partial c}\right)\dot{c} + \left(\underset{\sim}{\boldsymbol{\sigma}}-\frac{\partial f}{\partial \underset{\sim}{\boldsymbol{\varepsilon}}^e}\right):\dot{\underset{\sim}{\boldsymbol{\varepsilon}}}^e-\underline{\boldsymbol{J}}.\boldsymbol{\nabla}\mu+\underset{\sim}{\boldsymbol{\sigma}}:\dot{\underset{\sim}{\boldsymbol{\varepsilon}}}^p-\frac{\partial f}{\partial V_k}\dot{V}_k\geqslant 0 \quad \text{(III.15)}$$

This inequality is linear in $\boldsymbol{\nabla}\dot{\phi}$, $\dot{c}$ and $\dot{\underset{\sim}{\boldsymbol{\varepsilon}}}^e$. To ensure that the second law is satisfied in all conceivable processes and for any given thermodynamic variables $(\phi, \boldsymbol{\nabla}\phi, c, \underset{\sim}{\boldsymbol{\varepsilon}}^e, V_k)$, an analysis of the dissipation inequality leads to the following state laws (Coleman and Noll, 1963; Coleman and Gurtin, 1967):

$$\underline{\boldsymbol{\xi}}=\frac{\partial f}{\partial \boldsymbol{\nabla}\phi} \quad , \quad \mu=\frac{\partial f}{\partial c} \quad \text{and} \quad \underset{\sim}{\boldsymbol{\sigma}}=\frac{\partial f}{\partial \underset{\sim}{\boldsymbol{\varepsilon}}} \qquad \text{(III.16)}$$

Similarly, we define the set of thermodynamic forces A_k for each phase by derivation of the free energy density with respect to their associated internal variables:

$$A_k=\frac{\partial f}{\partial V_k} \qquad \text{(III.17)}$$

Taking the above state laws into account, the Clausius-Duhem inequality (III.15) reduces to the residual dissipation:

$$D=-\left(\pi+\frac{\partial f}{\partial \phi}\right)\dot{\phi}-\underline{\boldsymbol{J}}.\boldsymbol{\nabla}\mu+\underset{\sim}{\boldsymbol{\sigma}}:\dot{\underset{\sim}{\boldsymbol{\varepsilon}}}^p-A_k\dot{V}_k\geqslant 0 \qquad \text{(III.18)}$$

Three contributions appear in the above residual dissipation rate. The first is the phase field dissipation, associated with configuration changes of atoms and related to the evolution of the order parameter:

$$D_\phi=-\pi_{\text{dis}}\dot{\phi} \quad \text{with} \quad \pi_{\text{dis}}=\pi+\frac{\partial f}{\partial \phi} \qquad \text{(III.19)}$$

where π_{dis} is the chemical force associated with the dissipative processes (Gurtin, 1996).

The second contribution is the chemical dissipation due to diffusion, associated with mass transport:

$$D_c=-\underline{\boldsymbol{J}}.\boldsymbol{\nabla}\mu \qquad \text{(III.20)}$$

and the last contribution is called mechanical dissipation due to the evolution of the internal variables, which is represented by the products of the thermodynamic force variables with their respective rates of internal variable:

$$D_u=\underset{\sim}{\boldsymbol{\sigma}}:\dot{\underset{\sim}{\boldsymbol{\varepsilon}}}^p-A_k\dot{V}_k \qquad \text{(III.21)}$$

An efficient way of defining the complementary laws related to the dissipative processes and ensuring the positivity of the dissipation for any thermodynamic process is to assume the existence of a dissipation potential $\Omega(\pi_{\text{dis}}, \boldsymbol{\nabla}\mu, \underset{\sim}{\boldsymbol{\sigma}}, A_k)$, which is a convex function of its arguments:

$$\dot{\phi}=-\frac{\partial \Omega}{\partial \pi_{\text{dis}}} \qquad \text{(III.22)}$$

$$\underline{\boldsymbol{J}}=-\frac{\partial \Omega}{\partial \boldsymbol{\nabla}\mu} \qquad \text{(III.23)}$$

$$\dot{V}_k=-\frac{\partial \Omega}{\partial A_k} \quad , \quad \dot{\underset{\sim}{\boldsymbol{\varepsilon}}}^p=\frac{\partial \Omega}{\partial \underset{\sim}{\boldsymbol{\sigma}}} \qquad \text{(III.24)}$$

These equations represent the evolution law for the order parameter Eq. (III.22), the diffusion flux Eq. (III.23) as well as the evolution laws for the internal variables Eq. (III.24).

III.3 Free energy and dissipation potential

III.3.1 Partition of free energy and dissipation potential

The proposed model is formulated within the framework of generalized standard materials (Germain et al., 1983), where the complete elastoplastic behaviour can be described by the knowledge of two potentials. These potentials are namely the thermodynamic potential, which is the total free energy, for the reversible aspects and the dissipative potential related to the dissipative processes.

The total free energy is postulated to have the form of a Ginzburg-Landau free energy functional accounting for interfaces through the square of the order parameter gradient. The total free energy F of the body is then defined by the integral over the volume V of a free energy density f, which can be split into a chemical free energy density $f_{\rm ch}$, a coherent mechanical energy density f_u, and the square of the order parameter gradient:

$$\begin{aligned} F(\phi, \boldsymbol{\nabla}\phi, c, \underset{\sim}{\varepsilon}^e, V_k) &= \int_V f(\phi, \boldsymbol{\nabla}\phi, c, \underset{\sim}{\varepsilon}^e, V_k)\, dv \\ &= \int_V \left[f_{\rm ch}(\phi, c) + f_u(\phi, c, \underset{\sim}{\varepsilon}, V_k) + \frac{\alpha}{2}|\nabla\phi|^2 \right] dv \end{aligned} \tag{III.25}$$

The irreversible behaviour is described by the introduction of a dissipation potential, which can be split into three parts related to the three contributions in the residual dissipation in Eq.(III.18): the phase field part $\Omega_\phi(\phi, c, \pi_{\rm dis})$, the chemical part $\Omega_c(\phi, c, \boldsymbol{\nabla}\mu)$ and the mechanical dissipation potential $\Omega_u(\phi, c, \underset{\sim}{\boldsymbol{\sigma}}, A_k)$:

$$\Omega(\pi_{\rm dis}, \boldsymbol{\nabla}\mu, \phi, c, \underset{\sim}{\boldsymbol{\sigma}}, A_k) = \Omega_\phi(\pi_{\rm dis}) + \Omega_c(\boldsymbol{\nabla}\mu) + \Omega_u(\phi, c, \underset{\sim}{\boldsymbol{\sigma}}, A_k) \tag{III.26}$$

III.3.2 Chemical contribution

The chemical free energy density $f_{\rm ch}$ of the binary alloy is a function of the order parameter ϕ and of the concentration field c. In order to guarantee the coexistence of both phases α and β discriminated by ϕ, $f_{\rm ch}$ must be non-convex with respect to ϕ. Following (Kim et al., 1998), $f_{\rm ch}$ is built with the free energy densities of the two phases f_α and f_β as follows:

$$f_{\rm ch}(\phi, c) = h(\phi) f_\alpha(c) + [1 - h(\phi)] f_\beta(c) + W g(\phi) \tag{III.27}$$

Here, $h(\phi)$ is chosen as $h(\phi) = \phi^2(3 - 2\phi)$, and $g(\phi) = \phi^2(1 - \phi)^2$ is the double well potential accounting for the free energy penalty of the interface. The height W of the potential barrier is related to the interfacial energy σ and the interfacial thickness δ as $W = 6\Lambda\sigma/\delta$. Assuming that the interface region ranges from θ to $1 - \theta$, then $\Lambda = \ln[(1 - \theta)/\theta]$. In the present work $\theta = 0.05$ (Kim et al., 1998; Ammar et al., 2009a).

The densities f_α and f_β are chosen to be quadratic functions of the concentration only:

$$f_\alpha(c) = \frac{k_\alpha}{2}(c - a_\alpha)^2 \quad \text{and} \quad f_\beta(c) = \frac{k_\beta}{2}(c - a_\beta)^2 \tag{III.28}$$

where a_α and a_β are the unstressed equilibrium concentrations of both phases which correspond respectively to the minima of f_α and f_β in the present model. k_α and k_β are the curvatures of the free energies.

Moreover, the positiveness of the intrinsic dissipation is ensured by the choice of a convex dissipation potential of its arguments. Consequently, the chemical and phase field dissipation potentials can be taken as:

$$\Omega_\phi(\pi_{\rm dis}) = \frac{1}{2}(1/\beta)\pi_{\rm dis}^2 \quad \text{and} \quad \Omega_c(\boldsymbol{\nabla}\mu) = \frac{1}{2}L(\phi)\boldsymbol{\nabla}\mu.\boldsymbol{\nabla}\mu \tag{III.29}$$

where π_{dis} is given by Eq. (III.19), β is inversely proportional to the interface mobility and $L(\phi)$ is the Onsager coefficient, related to the chemical diffusivities D_α and D_β in both phases by means of the interpolation function $h(\phi)$ as:

$$L(\phi) = h(\phi)D_\alpha/k_\alpha + (1-h(\phi))D_\beta/k_\beta \tag{III.30}$$

Once the particular forms of free energy Eq. (III.25) and dissipation potential Eq. (III.29) are known, the state laws Eq. (III.16) and the complementary evolutions Eqs. (III.23–III.24) for the phase field and chemical contributions can be derived as:

$$\underline{\boldsymbol{\xi}} = \alpha \boldsymbol{\nabla}\phi \quad , \quad \mu = \frac{\partial f_{\text{ch}}}{\partial c} + \frac{\partial f_u}{\partial c} \tag{III.31}$$

$$\dot{\phi} = -(1/\beta)\pi_{\text{dis}} = -(1/\beta)\left(\pi + \frac{\partial f_{\text{ch}}}{\partial \phi} + \frac{\partial f_u}{\partial \phi}\right) \quad , \quad \underline{\boldsymbol{J}} = -L(\phi)\boldsymbol{\nabla}\mu \tag{III.32}$$

Substituting the previous equations into the balance equations for generalized stresses and mass concentration, the Ginzburg-Landau and usual diffusion equations are retrieved, which represent respectively the evolution equations for order parameter and concentration:

$$\boldsymbol{\nabla}.\underline{\boldsymbol{\xi}} + \pi = -\beta\dot{\phi} + \boldsymbol{\nabla}.(\alpha\boldsymbol{\nabla}\phi) - \frac{\partial f_{\text{ch}}}{\partial \phi} - \frac{\partial f_u}{\partial \phi} = 0 \tag{III.33}$$

$$\dot{c} = -\boldsymbol{\nabla}.(-L(\phi)\boldsymbol{\nabla}\mu) = -\boldsymbol{\nabla}.\left[-L(\phi)\left(\boldsymbol{\nabla}\frac{\partial f_{\text{ch}}}{\partial c} + \boldsymbol{\nabla}\frac{\partial f_u}{\partial c}\right)\right] \tag{III.34}$$

Note the coupling of mechanics and diffusion and phase field evolution through the partial derivatives $\dfrac{\partial f_u}{\partial c}$ and $\dfrac{\partial f_u}{\partial \phi}$.

III.3.3 Mechanical contribution

The second contribution to the free energy density is due to mechanical effects. Assuming that elastic behaviour and hardening are uncoupled, the mechanical part of the free energy density f_u is decomposed into a coherent elastic energy density f_e and a plastic part f_p as:

$$f_u(\phi, c, \underset{\sim}{\boldsymbol{\varepsilon}}, V_k) = f_e(\phi, c, \underset{\sim}{\boldsymbol{\varepsilon}}) + f_p(\phi, c, V_k) \tag{III.35}$$

Moreover, the irreversible mechanical behaviour, related to the dissipative processes, is obtained by a plastic dissipation potential $\Omega_u(\phi, c, \underset{\sim}{\boldsymbol{\sigma}}, A_k)$. It is assumed to be a function of order parameter, concentration, Cauchy stress tensor as well as the set of thermodynamic force associated variables A_k in order to describe the hardening state in each phase. The specific form of $f_u(\phi, c, \underset{\sim}{\boldsymbol{\varepsilon}}, V_k)$ and $\Omega_u(\phi, c, \underset{\sim}{\boldsymbol{\sigma}}, A_k)$ will be detailed in the next sections.

III.4 Phase field approach and homogenization methods

III.4.1 Multiphase approach

In the region where both phases coexist, we propose to use well-known results of homogenization theory to interpolate the local behaviour. The homogenization procedure in the mechanics of heterogeneous materials consists in replacing an heterogeneous medium by an equivalent homogeneous one, which is defined by an effective constitutive law relating the macroscopic variables, namely macroscopic stress $\underset{\sim}{\boldsymbol{\sigma}}$ and strain $\underset{\sim}{\boldsymbol{\varepsilon}}$ tensors, which are obtained by averaging

the corresponding non-uniform local stress and strain in each phase. In the case of a two-phase materials:

$$\underset{\sim}{\varepsilon} = \frac{1}{\mathcal{V}} \sum_{k=\alpha,\beta} \int_{\mathcal{V}_k} \underset{\sim}{\varepsilon}_k \, dv \quad \text{and} \quad \underset{\sim}{\boldsymbol{\sigma}} = \frac{1}{\mathcal{V}} \sum_{k=\alpha,\beta} \int_{\mathcal{V}_k} \underset{\sim}{\boldsymbol{\sigma}}_k \, dv \tag{III.36}$$

where $\mathcal{V} = \{\mathcal{V}_\alpha \cup \mathcal{V}_\beta,\ \mathcal{V}_\alpha \cap \mathcal{V}_\beta = \emptyset\}$ is the underlying material representative volume element.

Following a naive representation depicted in Fig. III.1, each material point, i.e. $\mathcal{V}$, within a diffuse interface can be seen as a local mixture of the two abutting phases α and β with proportions fixing $\mathcal{V}_\alpha$ and $\mathcal{V}_\beta$ given by complementary functions of ϕ. It must be emphasized that this representation involves the presence of fields Ψ_α and Ψ_β in phases β and α respectively, which has no incidence on the bulk of those phases.

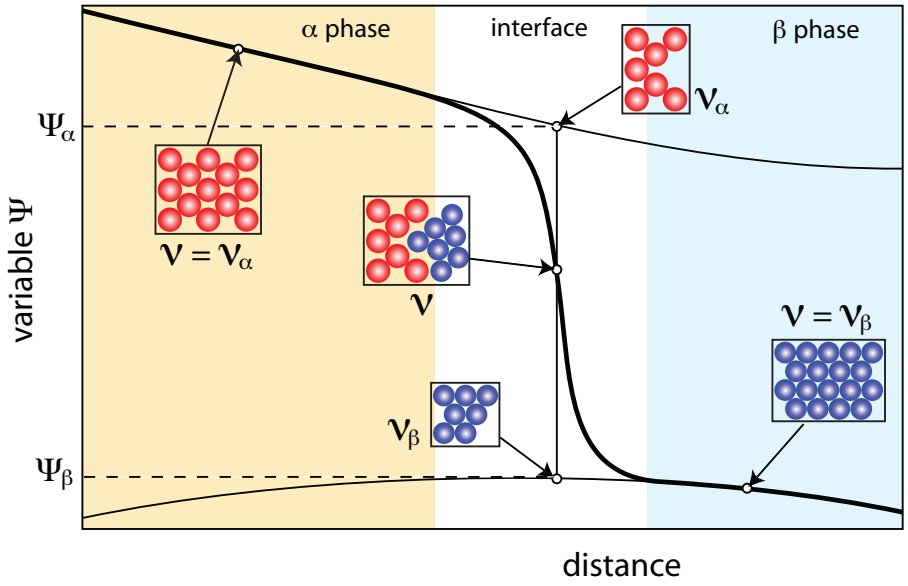

Figure III.1 : Schematic illustration of the underlying material representative volume element $\mathcal{V}$ at each material point of a diffuse interface: the real effective variable Ψ appears with a thick line, whereas the variables attached to each phase Ψ_α and Ψ_β are with thin lines.

For illustrating the way to apply homogenization schemes in a diffuse interface, the case of two elastoplastic materials with hardening can be considered. The strain and stress at each material point are defined by the following mixture laws which would proceed from space averaging in a conventional homogenization problem, but which must be seen as arbitrary interpolations in the present case:

$$\underset{\sim}{\varepsilon} = \chi \, \underset{\sim}{\varepsilon}_\alpha + (1-\chi) \, \underset{\sim}{\varepsilon}_\beta \quad \text{and} \quad \underset{\sim}{\boldsymbol{\sigma}} = \chi \, \underset{\sim}{\boldsymbol{\sigma}}_\alpha + (1-\chi) \, \underset{\sim}{\boldsymbol{\sigma}}_\beta \tag{III.37}$$

where $\underset{\sim}{\varepsilon}_\alpha$, $\underset{\sim}{\varepsilon}_\beta$ are the local strains and $\underset{\sim}{\boldsymbol{\sigma}}_\alpha$, $\underset{\sim}{\boldsymbol{\sigma}}_\beta$ are the local stresses in α and β phases respectively and $\chi(\underline{\boldsymbol{x}}, t)$ is a shape function which must verify:

$$\begin{cases} \chi(\underline{\boldsymbol{x}}, t) = 0 \ \text{ if } \ \underline{\boldsymbol{x}} \in \beta \\ \\ \chi(\underline{\boldsymbol{x}}, t) = 1 \ \text{ if } \ \underline{\boldsymbol{x}} \in \alpha \end{cases} \tag{III.38}$$

In this work, the simplest choice has been done for this shape function:

$$\chi(\underline{\boldsymbol{x}}\,,t) = \phi(\underline{\boldsymbol{x}}\,,t) \tag{III.39}$$

The partition hypothesis, already used for the effective total strain tensor in Eq. (III.11), requires, in a similar way, a decomposition of the total strain in each phase into elastic, eigen and plastic parts:

$$\underset{\sim}{\boldsymbol{\varepsilon}}_\alpha = \underset{\sim}{\boldsymbol{\varepsilon}}^e_\alpha + \underset{\sim}{\boldsymbol{\varepsilon}}^\star_\alpha + \underset{\sim}{\boldsymbol{\varepsilon}}^p_\alpha \quad \text{and} \quad \underset{\sim}{\boldsymbol{\varepsilon}}_\beta = \underset{\sim}{\boldsymbol{\varepsilon}}^e_\beta + \underset{\sim}{\boldsymbol{\varepsilon}}^\star_\beta + \underset{\sim}{\boldsymbol{\varepsilon}}^p_\beta \tag{III.40}$$

where each point may depend on the local concentration c, but not on order parameter ϕ.

In the proposed model, the elastoplastic and phase field behaviours of each phase are treated independently and the effective behaviour is obtained using homogenization relation (III.37). It is assumed that the mechanical state of α and β phases at a given time are completely described by a finite number of local state variables, defined at each point as:

$$(\underset{\sim}{\boldsymbol{\varepsilon}}^e_k, V_k) \quad \text{where} \quad V_k = \left(r_k, \underset{\sim}{\boldsymbol{\alpha}}_k\right) \quad \text{and} \quad k = \{\alpha, \beta\} \tag{III.41}$$

The set of internal variables V_k, of scalar or tensorial nature, represents the state of hardening of phase k: for instance, a scalar isotropic hardening variable r_k, and a tensorial kinematic hardening variable $\underset{\sim}{\boldsymbol{\alpha}}_k$.

The reversible mechanical behaviour of each individual phase is governed by a convex mechanical free energy, which can be decomposed, using Eq. (III.35), into local elastic and plastic energy densities. According to the homogenization theory, the effective elastic and plastic free energy densities are given by the rule of mixtures as follows:

$$f_e(\phi, c, \underset{\sim}{\boldsymbol{\varepsilon}}) = \phi\, f_{e\alpha}(c, \underset{\sim}{\boldsymbol{\varepsilon}}^e_\alpha) + (1-\phi) f_{e\beta}(c, \underset{\sim}{\boldsymbol{\varepsilon}}^e_\beta) \tag{III.42}$$

and

$$f_p(\phi, c, V_k) = \phi\, f_{p\alpha}(c, \underset{\sim}{\boldsymbol{\alpha}}_\alpha) + (1-\phi) f_{p\beta}(c, \underset{\sim}{\boldsymbol{\alpha}}_\beta) \tag{III.43}$$

Similarly, we define a set of thermodynamic forces $A_k = \left(R_k, \underset{\sim}{\boldsymbol{X}}_k\right)$ associated with the internal variables $V_k = \left(r_k, \underset{\sim}{\boldsymbol{\alpha}}_k\right)$ for each phase, represented by the scalar isotropic hardening R_k and the tensor of kinematic hardening $\underset{\sim}{\boldsymbol{X}}_k$.

Consequently, the Cauchy stress tensor and the associated thermodynamic force variables for both phases are deduced from Eqs. (III.16-III.17) as:

$$\underset{\sim}{\boldsymbol{\sigma}}_\alpha = \frac{\partial f_{e\alpha}}{\partial \underset{\sim}{\boldsymbol{\varepsilon}}_\alpha} \quad , \quad \underset{\sim}{\boldsymbol{\sigma}}_\beta = \frac{\partial f_{e\beta}}{\partial \underset{\sim}{\boldsymbol{\varepsilon}}_\beta} \tag{III.44}$$

$$R_\alpha = \frac{\partial f_{p\alpha}}{\partial r_\alpha} \quad , \quad R_\beta = \frac{\partial f_{p\beta}}{\partial r_\beta} \tag{III.45}$$

$$\underset{\sim}{\boldsymbol{X}}_\alpha = \frac{\partial f_{p\alpha}}{\partial \underset{\sim}{\boldsymbol{\alpha}}_\alpha} \quad , \quad \underset{\sim}{\boldsymbol{X}}_\beta = \frac{\partial f_{p\beta}}{\partial \underset{\sim}{\boldsymbol{\alpha}}_\beta} \tag{III.46}$$

In order to describe the irreversible part of the mechanical behaviour in each phase, we define the local mechanical dissipation potentials $\Omega_{u\alpha}(c, \underset{\sim}{\boldsymbol{\sigma}}_\alpha, A_\alpha)$ and $\Omega_{u\beta}(c, \underset{\sim}{\boldsymbol{\sigma}}_\beta, A_\beta)$ for α and β phases respectively, which are convex functions of their arguments. Consequently, the mechanical potential for effective material is defined with respect to the mechanical potentials in both phases by means of the shape function ϕ as:

$$\Omega_u(\phi, c, \underset{\sim}{\boldsymbol{\sigma}}, A_k) = \phi\, \Omega_{u\alpha}(c, \underset{\sim}{\boldsymbol{\sigma}}_\alpha, A_\alpha) + (1-\phi)\, \Omega_{u\beta}(c, \underset{\sim}{\boldsymbol{\sigma}}_\beta, A_\beta) \tag{III.47}$$

Using Eqs. (III.24), the complementary evolution laws of the internal variables in the two phases are derived from the above potential as follows:

$$\dot{\underset{\sim}{\varepsilon}}^p_\alpha = \frac{\partial \Omega_{u\alpha}}{\partial \underset{\sim}{\sigma}_\alpha} \quad , \quad \dot{\underset{\sim}{\varepsilon}}^p_\beta = \frac{\partial \Omega_{u\beta}}{\partial \underset{\sim}{\sigma}_\beta} \tag{III.48}$$

$$\dot{r}_\alpha = -\frac{\partial \Omega_{u\alpha}}{\partial R_\alpha} \quad , \quad \dot{r}_\beta = -\frac{\partial \Omega_{u\beta}}{\partial R_\beta} \tag{III.49}$$

$$\dot{\underset{\sim}{\alpha}}_\alpha = -\frac{\partial \Omega_{u\alpha}}{\partial \underset{\sim}{X}_\alpha} \quad , \quad \dot{\underset{\sim}{\alpha}}_\beta = -\frac{\partial \Omega_{u\beta}}{\partial \underset{\sim}{X}_\beta} \tag{III.50}$$

III.4.2 Voigt/Taylor model

Voigt's model is also referred to as the uniform strain model. Its basic assumptions are that the strain field is uniform among the phases (Nemat-Nasser and Hori, 1999; Qu and Cherkaoui, 2006). Using Voigt's model, we assume a uniform total strain at any point in the diffuse interface between elastoplastically inhomogeneous phases. The effective stress is expressed in terms of the local stress average with respect to both phases weighted by the volume fractions:

$$\underset{\sim}{\sigma} = \phi\, \underset{\sim}{\sigma}_\alpha + (1-\phi)\, \underset{\sim}{\sigma}_\beta \qquad , \qquad \underset{\sim}{\varepsilon} = \underset{\sim}{\varepsilon}_\alpha = \underset{\sim}{\varepsilon}_\beta \tag{III.51}$$

The stresses of both phases $\underset{\sim}{\sigma}_\alpha$ and $\underset{\sim}{\sigma}_\beta$ are given by Hooke's law for each phase:

$$\underset{\sim}{\sigma}_\alpha = \underset{\approx}{C}_\alpha : (\underset{\sim}{\varepsilon}_\alpha - \underset{\sim}{\varepsilon}^\star_\alpha - \underset{\sim}{\varepsilon}^p_\alpha) \quad , \quad \underset{\sim}{\sigma}_\beta = \underset{\approx}{C}_\beta : (\underset{\sim}{\varepsilon}_\beta - \underset{\sim}{\varepsilon}^\star_\beta - \underset{\sim}{\varepsilon}^p_\beta) \tag{III.52}$$

where $\underset{\approx}{C}_\alpha$ and $\underset{\approx}{C}_\beta$ are respectively the tensor of elasticity moduli in α and β phases.

The stress at any point in the interface is computed from the average of the above local stresses as follows:

$$\underset{\sim}{\sigma} = \phi\, \underset{\approx}{C}_\alpha : (\underset{\sim}{\varepsilon}_\alpha - \underset{\sim}{\varepsilon}^\star_\alpha - \underset{\sim}{\varepsilon}^p_\alpha) + (1-\phi) \underset{\approx}{C}_\beta : (\underset{\sim}{\varepsilon}_\beta - \underset{\sim}{\varepsilon}^\star_\beta - \underset{\sim}{\varepsilon}^p_\beta) \tag{III.53}$$

From the above relation, it follows that the strain-stress relationship in the homogeneous effective medium obeys Hooke's law with the following equation:

$$\underset{\sim}{\sigma} = \underset{\approx}{C}_{\text{eff}} : (\underset{\sim}{\varepsilon} - \underset{\sim}{\varepsilon}^p - \underset{\sim}{\varepsilon}^\star)$$

where the effective elasticity tensor $\underset{\approx}{C}_{\text{eff}}$ is obtained from the mixture rule of the elasticity matrix for both phases:

$$\underset{\approx}{C}_{\text{eff}} = \phi\, \underset{\approx}{C}_\alpha + (1-\phi) \underset{\approx}{C}_\beta \tag{III.54}$$

and the effective eigenstrain $\underset{\sim}{\varepsilon}^\star$ and plastic strain $\underset{\sim}{\varepsilon}^p$ vary continuously between their respective values in the bulk phases as follows:

$$\begin{aligned} \underset{\sim}{\varepsilon}^\star &= \underset{\approx}{C}^{-1}_{\text{eff}} : (\phi\, \underset{\approx}{C}_\alpha : \underset{\sim}{\varepsilon}^\star_\alpha + (1-\phi) \underset{\approx}{C}_\beta : \underset{\sim}{\varepsilon}^\star_\beta) \\ \underset{\sim}{\varepsilon}^p &= \underset{\approx}{C}^{-1}_{\text{eff}} : (\phi\, \underset{\approx}{C}_\alpha : \underset{\sim}{\varepsilon}^p_\alpha + (1-\phi) \underset{\approx}{C}_\beta : \underset{\sim}{\varepsilon}^p_\beta) \end{aligned} \tag{III.55}$$

In the case of nonhomogeneous elasticity, it must be noted that $\underset{\sim}{\varepsilon}^\star$ and $\underset{\sim}{\varepsilon}^p$ are not the average of their respective values for each phase.

The local energy stored in the effective homogeneous elastic material is expressed in terms of the average value of the local elastic energy with respect to both phases weighted by their volume fractions:

$$\begin{aligned} f_e &= \frac{1}{2} (\underset{\sim}{\varepsilon} - \underset{\sim}{\varepsilon}^\star - \underset{\sim}{\varepsilon}^p) : \underset{\approx}{C}_{\text{eff}} : (\underset{\sim}{\varepsilon} - \underset{\sim}{\varepsilon}^\star - \underset{\sim}{\varepsilon}^p) \\ &= \phi\, f_{e\alpha} + (1-\phi) f_{e\beta} \end{aligned} \tag{III.56}$$

where the elastic energy densities of α and β phases can be expressed as:

$$\begin{cases} f_{e\alpha} = \dfrac{1}{2}\left(\underset{\sim}{\varepsilon} - \underset{\sim}{\varepsilon}^{\star}_{\alpha} - \underset{\sim}{\varepsilon}^{p}_{\alpha}\right) : \underset{\sim}{\boldsymbol{C}}_{\alpha} : \left(\underset{\sim}{\varepsilon} - \underset{\sim}{\varepsilon}^{\star}_{\alpha} - \underset{\sim}{\varepsilon}^{p}_{\alpha}\right) \\ \\ f_{e\beta} = \dfrac{1}{2}\left(\underset{\sim}{\varepsilon} - \underset{\sim}{\varepsilon}^{\star}_{\beta} - \underset{\sim}{\varepsilon}^{p}_{\beta}\right) : \underset{\sim}{\boldsymbol{C}}_{\beta} : \left(\underset{\sim}{\varepsilon} - \underset{\sim}{\varepsilon}^{\star}_{\beta} - \underset{\sim}{\varepsilon}^{p}_{\beta}\right) \end{cases} \tag{III.57}$$

III.4.3 Reuss/Sachs model

The Reuss/Sachs scheme assumes homogeneity of stress among the phases. The effective strain is obtained by averaging the corresponding strains in each phase:

$$\underset{\sim}{\boldsymbol{\sigma}} = \underset{\sim}{\boldsymbol{\sigma}}_{\alpha} = \underset{\sim}{\boldsymbol{\sigma}}_{\beta} \quad , \quad \underset{\sim}{\varepsilon} = \phi\,\underset{\sim}{\varepsilon}_{\alpha} + (1-\phi)\,\underset{\sim}{\varepsilon}_{\beta} \tag{III.58}$$

Taking Hooke's law into account for each phase, the local total strain in each phase is expressed:

$$\underset{\sim}{\varepsilon}_{\alpha} = \underset{\sim}{\boldsymbol{S}}_{\alpha} : \underset{\sim}{\boldsymbol{\sigma}}_{\alpha} + \underset{\sim}{\varepsilon}^{\star}_{\alpha} + \underset{\sim}{\varepsilon}^{p}_{\alpha} \quad , \quad \underset{\sim}{\varepsilon}_{\beta} = \underset{\sim}{\boldsymbol{S}}_{\beta} : \underset{\sim}{\boldsymbol{\sigma}}_{\beta} + \underset{\sim}{\varepsilon}^{\star}_{\beta} + \underset{\sim}{\varepsilon}^{p}_{\beta} \tag{III.59}$$

where $\underset{\sim}{\boldsymbol{S}}_{\alpha}$ and $\underset{\sim}{\boldsymbol{S}}_{\beta}$ are the tensors of elastic compliance of each phase.

Taking (III.58)$_2$ into account, the effective strain is found as:

$$\underset{\sim}{\varepsilon} = \phi\,\underset{\sim}{\varepsilon}_{\alpha} + (1-\phi)\,\underset{\sim}{\varepsilon}_{\beta} = \underset{\sim}{\boldsymbol{S}}_{\text{eff}} : \underset{\sim}{\boldsymbol{\sigma}} + \underset{\sim}{\varepsilon}^{\star} + \underset{\sim}{\varepsilon}^{p} \tag{III.60}$$

where the expression of the effective eigenstrain $\underset{\sim}{\varepsilon}^{\star}$, the effective plastic strain $\underset{\sim}{\varepsilon}^{p}$ and the effective compliance matrix $\underset{\sim}{\boldsymbol{S}}_{\text{eff}}$ are defined as the average of the local properties of each phase:

$$\begin{aligned} &\underset{\sim}{\varepsilon}^{\star} = \phi\,\underset{\sim}{\varepsilon}^{\star}_{\alpha} + (1-\phi)\underset{\sim}{\varepsilon}^{\star}_{\beta} \quad , \quad \underset{\sim}{\varepsilon}^{p} = \phi\,\underset{\sim}{\varepsilon}^{p}_{\alpha} + (1-\phi)\underset{\sim}{\varepsilon}^{p}_{\beta} \\ &\underset{\sim}{\boldsymbol{S}}_{\text{eff}} = \phi\,\underset{\sim}{\boldsymbol{S}}_{\alpha} + (1-\phi)\underset{\sim}{\boldsymbol{S}}_{\beta} \end{aligned} \tag{III.61}$$

Let us consider a homogeneous material with elastic stiffness $\underset{\sim}{\boldsymbol{S}}^{-1}_{\text{eff}}$. For a given effective elastic strain, the stress is given by Hooke's law as:

$$\underset{\sim}{\boldsymbol{\sigma}} = \underset{\sim}{\boldsymbol{S}}^{-1}_{\text{eff}} : \left(\underset{\sim}{\varepsilon} - \underset{\sim}{\varepsilon}^{\star} - \underset{\sim}{\varepsilon}^{p}\right) \tag{III.62}$$

The elastic energy density of the material is constructed as follows:

$$\begin{aligned} f_e &= \frac{1}{2}\left(\underset{\sim}{\varepsilon} - \underset{\sim}{\varepsilon}^{\star} - \underset{\sim}{\varepsilon}^{p}\right) : \underset{\sim}{\boldsymbol{S}}^{-1}_{\text{eff}} : \left(\underset{\sim}{\varepsilon} - \underset{\sim}{\varepsilon}^{\star} - \underset{\sim}{\varepsilon}^{p}\right) \\ &= \phi\, f_{e\alpha} + (1-\phi) f_{e\beta} \end{aligned} \tag{III.63}$$

where $f_{e\alpha}$ and $f_{e\beta}$ represent elastic energy densities of α and β phases respectively. They are still given by (III.57) with $\underset{\sim}{\boldsymbol{C}}_{\alpha,\beta} = \underset{\sim}{\boldsymbol{S}}^{-1}_{\alpha,\beta}$.

III.4.4 Comparison with existing interpolation schemes

The interface behaviours proposed above can be compared to the most commonly used in phase field models, as popularized by Khachaturyan and co-workers, e.g. (Khachaturyan, 1983). According to these works, mixture rules are adopted respectively for eigenstrain and elasticity moduli tensor:

$$\underset{\sim}{\varepsilon}^{\star} = \phi\,\underset{\sim}{\varepsilon}^{\star}_{\alpha} + (1-\phi)\,\underset{\sim}{\varepsilon}^{\star}_{\beta} \quad , \quad \underset{\sim}{\boldsymbol{C}}_{\text{eff}} = \phi\,\underset{\sim}{\boldsymbol{C}}_{\alpha} + (1-\phi)\,\underset{\sim}{\boldsymbol{C}}_{\beta} \tag{III.64}$$

Hooke's law relates the strain tensor to the stress tensor by the following expression:

$$\begin{aligned} \underset{\sim}{\boldsymbol{\sigma}} &= \underset{\approx}{\boldsymbol{C}}_{\text{eff}} : (\underset{\sim}{\boldsymbol{\varepsilon}} - \underset{\sim}{\boldsymbol{\varepsilon}}^{\star}) \\ &= (\phi\, \underset{\approx}{\boldsymbol{C}}_{\alpha} + (1-\phi)\, \underset{\approx}{\boldsymbol{C}}_{\beta}) : (\underset{\sim}{\boldsymbol{\varepsilon}} - \phi\, \underset{\sim}{\boldsymbol{\varepsilon}}^{\star}_{\alpha} - (1-\phi)\, \underset{\sim}{\boldsymbol{\varepsilon}}^{\star}_{\beta}) \end{aligned} \tag{III.65}$$

Contrary to homogenization schemes, it is clear that the elastic energy of the effective homogeneous material is no longer the average of energy densities of both phases. It is indeed not possible to distinguish an explicit form for the elastic energy densities in each phase. The elastic energy is then postulated as:

$$f_e = (\underset{\sim}{\boldsymbol{\varepsilon}} - \phi\, \underset{\sim}{\boldsymbol{\varepsilon}}^{\star}_{\alpha} - (1-\phi)\, \underset{\sim}{\boldsymbol{\varepsilon}}^{\star}_{\beta}) : \underset{\approx}{\boldsymbol{C}}_{\text{eff}} : (\underset{\sim}{\boldsymbol{\varepsilon}} - \phi\, \underset{\sim}{\boldsymbol{\varepsilon}}^{\star}_{\alpha} - (1-\phi)\, \underset{\sim}{\boldsymbol{\varepsilon}}^{\star}_{\beta}) \tag{III.66}$$

As a result, it appears that Eq. (III.64)$_1$ corresponds to Reuss' approach whereas Eq. (III.64)$_2$ is taken from Voigt's model. The standard phase field microelasticity approach therefore combines two homogenization schemes so that it is not possible to identify consistent definitions for strain/stress components for each phase. Moreover, the study of the plastic accommodation effects in the phase field interface, using this model, requires the definition of additional conditions. They relate the effective plastic activity to the local plastic behaviour of the two phases, such as the linear mixture model of the material parameters (Ubachs et al., 2005). An interpolation scheme of the plastic parameters by means of $\tanh$ function has been proposed in (Gaubert et al., 2008).

III.4.5 Expression of the phase field-elastic coupling terms

In the phase field approach to coherent phase transformations, there are in general three contributions to the interfacial energy: the first one coming from the double well function $g(\phi)$, the second one coming from the variation in concentration within the interface and the last one is due to mechanically stored energy. After substituting the free energy density (III.56) into (III.33), the time evolution of the phase field at thermodynamic equilibrium ($\phi = \phi_{\text{eq}}$) becomes:

$$\begin{aligned} \alpha \frac{d^2\phi}{dx^2} &= \frac{\partial f_{\text{ch}}}{\partial \phi} + \frac{\partial f_e}{\partial \phi} \\ \alpha \frac{d^2\phi}{dx^2} &= \frac{\partial f_{\text{ch}}}{\partial \phi} + \frac{\partial \underset{\sim}{\boldsymbol{\varepsilon}}^{e}}{\partial \phi} : \underset{\approx}{\boldsymbol{C}}_{\text{eff}} : \underset{\sim}{\boldsymbol{\varepsilon}}^{e} + \frac{1}{2}\, \underset{\sim}{\boldsymbol{\varepsilon}}^{e} : \frac{\partial \underset{\approx}{\boldsymbol{C}}_{\text{eff}}}{\partial \phi} : \underset{\sim}{\boldsymbol{\varepsilon}}^{e} \end{aligned} \tag{III.67}$$

The order parameter evolution for coherent transformation is extended to include the variation of the elastic free energy as an elastic driving force for the phase transformation process. It characterizes the effect of mechanically stored energy on the phase field and its evolution. The derivation of the elastic strain and the effective elasticity tensor with respect to the order parameter for the various interpolation schemes are summarised below.

In the case of homogenous elasticity ($\underset{\approx}{\boldsymbol{C}}_{\alpha} = \underset{\approx}{\boldsymbol{C}}_{\beta} = \underset{\approx}{\boldsymbol{C}}_{\text{eff}}$ and $\dfrac{\partial \underset{\approx}{\boldsymbol{C}}_{\text{eff}}}{\partial \phi} = 0$), the evolution equation for order parameter becomes:

$$\alpha \frac{d^2\phi}{dx^2} = \frac{\partial f_0}{\partial \phi} + \frac{\partial \underset{\sim}{\boldsymbol{\varepsilon}}^{e}}{\partial \phi} : \underset{\approx}{\boldsymbol{C}}_{\text{eff}} : \underset{\sim}{\boldsymbol{\varepsilon}}^{e} \tag{III.68}$$

As shown in Table III.1, we have

$$\begin{cases} \dfrac{\partial \underset{\sim}{\boldsymbol{\varepsilon}}^{e}}{\partial \phi} = 0 & \text{for Reuss/Sachs scheme} \\ \dfrac{\partial \underset{\sim}{\boldsymbol{\varepsilon}}^{e}}{\partial \phi} = \underset{\sim}{\boldsymbol{\varepsilon}}^{\star}_{\beta} - \underset{\sim}{\boldsymbol{\varepsilon}}^{\star}_{\alpha} & \text{for Voigt/Taylor and Khachaturyan schemes} \end{cases} \tag{III.69}$$

Khachaturyan	$\begin{cases} \underset{\sim}{\varepsilon}^{\star} = \phi\, \underset{\sim}{\varepsilon}^{\star}_{\alpha} + (1-\phi)\, \underset{\sim}{\varepsilon}^{\star}_{\beta} \\ \underset{\approx}{\boldsymbol{C}}_{\text{eff}}(\phi) = \phi\, \underset{\approx}{\boldsymbol{C}}_{\alpha} + (1-\phi)\, \underset{\approx}{\boldsymbol{C}}_{\beta} \end{cases}$ $\underset{\sim}{\varepsilon}^{e} = \underset{\sim}{\varepsilon} - \underset{\sim}{\varepsilon}^{\star} = \underset{\sim}{\varepsilon} - \phi\, \underset{\sim}{\varepsilon}^{\star}_{\alpha} - (1-\phi)\, \underset{\sim}{\varepsilon}^{\star}_{\beta}$ $\dfrac{\partial \underset{\sim}{\varepsilon}^{e}}{\partial \phi} = \underset{\sim}{\varepsilon}^{\star}_{\beta} - \underset{\sim}{\varepsilon}^{\star}_{\alpha} \quad , \quad \dfrac{\partial \underset{\approx}{\boldsymbol{C}}_{\text{eff}}}{\partial \phi} = \underset{\approx}{\boldsymbol{C}}_{\alpha} - \underset{\approx}{\boldsymbol{C}}_{\beta}$
Voigt/Taylor	$\begin{cases} \underset{\sim}{\varepsilon}_{\alpha} = \underset{\sim}{\varepsilon}_{\beta} = \underset{\sim}{\varepsilon} \\ \underset{\sim}{\boldsymbol{\sigma}} = \phi\, \underset{\sim}{\boldsymbol{\sigma}}_{\alpha} + (1-\phi)\, \underset{\sim}{\boldsymbol{\sigma}}_{\beta} \end{cases}$ $\underset{\sim}{\varepsilon}^{e} = \underset{\approx}{\boldsymbol{C}}^{-1}_{\text{eff}} : (\phi \underset{\approx}{\boldsymbol{C}}_{\alpha} : \underset{\sim}{\varepsilon}^{e}_{\alpha} + (1-\phi) \underset{\approx}{\boldsymbol{C}}_{\beta} : \underset{\sim}{\varepsilon}^{e}_{\beta})$ $\underset{\approx}{\boldsymbol{C}}_{\text{eff}} = (\phi\, \underset{\approx}{\boldsymbol{C}}_{\alpha} + (1-\phi) \underset{\approx}{\boldsymbol{C}}_{\beta})$ $\dfrac{\partial \underset{\sim}{\varepsilon}^{e}}{\partial \phi} = \dfrac{\partial \underset{\approx}{\boldsymbol{C}}^{-1}_{eff}}{\partial \phi} : (\phi \underset{\approx}{\boldsymbol{C}}_{\alpha} : \underset{\sim}{\varepsilon}^{e}_{\alpha} + (1-\phi) \underset{\approx}{\boldsymbol{C}}_{\beta} : \underset{\sim}{\varepsilon}^{e}_{\beta}) + \underset{\approx}{\boldsymbol{C}}^{-1}_{\text{eff}} : (\underset{\approx}{\boldsymbol{C}}_{\alpha} : \underset{\sim}{\varepsilon}^{e}_{\alpha} - \underset{\approx}{\boldsymbol{C}}_{\beta} : \underset{\sim}{\varepsilon}^{e}_{\beta})$ $\dfrac{\partial \underset{\approx}{\boldsymbol{C}}_{\text{eff}}}{\partial \phi} = \underset{\approx}{\boldsymbol{C}}_{\alpha} - \underset{\approx}{\boldsymbol{C}}_{\beta} \quad , \quad \dfrac{\partial \underset{\approx}{\boldsymbol{C}}^{-1}_{\text{eff}}}{\partial \phi} = -\underset{\approx}{\boldsymbol{C}}^{-1}_{\text{eff}} : \dfrac{\partial \underset{\approx}{\boldsymbol{C}}_{\text{eff}}}{\partial \phi} : \underset{\approx}{\boldsymbol{C}}^{-1}_{\text{eff}}$
Reuss/Sachs	$\begin{cases} \underset{\sim}{\varepsilon} = \phi\, \underset{\sim}{\varepsilon}_{\alpha} + (1-\phi)\, \underset{\sim}{\varepsilon}_{\beta} \\ \underset{\sim}{\boldsymbol{\sigma}}_{\alpha} = \underset{\sim}{\boldsymbol{\sigma}}_{\beta} = \underset{\sim}{\boldsymbol{\sigma}} \end{cases}$ $\underset{\sim}{\varepsilon}^{e} = \phi\, \underset{\sim}{\varepsilon}^{e}_{\alpha} + (1-\phi) \underset{\sim}{\varepsilon}^{e}_{\beta}$ $\underset{\approx}{\boldsymbol{C}}_{\text{eff}} = (\phi\, \underset{\approx}{\boldsymbol{S}}_{\alpha} + (1-\phi) \underset{\approx}{\boldsymbol{S}}_{\beta})^{-1}$ $\dfrac{\partial \underset{\sim}{\varepsilon}^{e}}{\partial \phi} = \underset{\sim}{\varepsilon}^{e}_{\alpha} - \underset{\sim}{\varepsilon}^{e}_{\beta} = (\underset{\approx}{\boldsymbol{S}}_{\beta} - \underset{\approx}{\boldsymbol{S}}_{\alpha}) : \underset{\sim}{\boldsymbol{\sigma}} \quad , \quad \dfrac{\partial \underset{\approx}{\boldsymbol{C}}_{\text{eff}}}{\partial \phi} = \underset{\approx}{\boldsymbol{C}}_{\text{eff}} : (\underset{\approx}{\boldsymbol{S}}_{\beta} - \underset{\approx}{\boldsymbol{S}}_{\alpha}) : \underset{\approx}{\boldsymbol{C}}_{\text{eff}}$

Tableau III.1 : Derivations of the elastic strain and the effective elasticity tensor with respect to the order parameter for various interpolation schemes (See Appendix B).

Using Reuss' model, we clearly show that there is no mechanical contribution on the phase field equation in the case of homogenous elasticity. It must be noted that this equation is different from equation (24) presented in (Steinbach and Apel, 2006) for the same scheme. Moreover, the same mechanical contribution ($\frac{\partial \underset{\sim}{\boldsymbol{\varepsilon}}^e}{\partial \phi} = \underset{\sim}{\boldsymbol{\varepsilon}}^{\star}_{\beta} - \underset{\sim}{\boldsymbol{\varepsilon}}^{\star}_{\alpha}$) on the phase field equation is shown for Voigt/Taylor and Khachaturyan schemes.

III.5 Two-phase elastoplastic alloy with hardening

Now, we consider that the system consists of a two-phase elastoplastic binary alloy with one non-linear isotropic hardening and one non-linear kinematic hardening in each phase. The specific free energy taken as the state potential of the material is chosen as a function of all state variables. Assuming again that there is no coupling between elasticity and hardening, the free energy is split into three terms, corresponding to the elastic energy, the kinematic hardening part and the isotropic part. To satisfy the condition of thermodynamic stability, it is sufficient to choose a positive definite quadratic function in the components of elastic strain tensor and all internal state variables as follows:

$$f_k = \frac{1}{2}\left(\underset{\sim}{\boldsymbol{\varepsilon}}_k - \underset{\sim}{\boldsymbol{\varepsilon}}^{\star}_k\right) : \underset{\approx}{\boldsymbol{C}}_k : \left(\underset{\sim}{\boldsymbol{\varepsilon}}_k - \underset{\sim}{\boldsymbol{\varepsilon}}^{\star}_k\right) + \frac{1}{3} c_k \underset{\sim}{\boldsymbol{\alpha}}_k : \underset{\sim}{\boldsymbol{\alpha}}_k + \frac{1}{2} b_k Q_k r_k^2 \tag{III.70}$$

b_k, Q_k and c_k are the material parameters for isotropic and kinematic hardening states and $k = \{\alpha, \beta\}$ corresponding to the two phases (Lemaitre and Chaboche, 1994).

A classical treatment of the Clausius-Duhem inequality provides the state laws (Eqs. (III.44-III.46)), defining the Cauchy stress tensor $\underset{\sim}{\boldsymbol{\sigma}}$ and the hardening variables $\underset{\sim}{\boldsymbol{X}}$ and R in each phase:

$$\underset{\sim}{\boldsymbol{\sigma}}_k = \underset{\approx}{\boldsymbol{C}}_k : \left(\underset{\sim}{\boldsymbol{\varepsilon}}_k - \underset{\sim}{\boldsymbol{\varepsilon}}^{\star}_k - \underset{\sim}{\boldsymbol{\varepsilon}}^{p}_k\right) \quad , \quad R_k = b_k Q_k r_k \quad \text{and} \quad \underset{\sim}{\boldsymbol{X}}_k = \frac{2}{3} C_k \underset{\sim}{\boldsymbol{\alpha}}_k \tag{III.71}$$

Furthermore, the mechanical dissipation is assumed to be due to three mechanisms: the inelastic strain, the kinematic hardening and the isotropic hardening. Thus, the dissipation potential can be split into a plastic contribution, which is called the yield function, a nonlinear kinematic hardening term and a nonlinear isotropic hardening term and can be expressed as a convex scalar valued function as follows (Lemaitre and Chaboche, 1994):

$$\Omega_{uk}(\sigma_k, \underset{\sim}{\boldsymbol{X}}_k, R_k) = g_k(\underset{\sim}{\boldsymbol{\sigma}}_k, \underset{\sim}{\boldsymbol{X}}_k, R_k) + \frac{3\Gamma_k}{4C_k} \underset{\sim}{\boldsymbol{X}}_k : \underset{\sim}{\boldsymbol{X}}_k + \frac{R_k^2}{2Q_k} \tag{III.72}$$

Assuming that the elastoplastic phase field behaviour of each phase is treated independently, we define a yield function for each phase as:

$$g_k(\sigma_k, \underset{\sim}{\boldsymbol{X}}_k, R_k) = \sigma_k^{\text{eq}} - R_k - \sigma_k^0 \tag{III.73}$$

where

$$\sigma_{\text{eq}} = \sqrt{\frac{3}{2}\left(\underset{\sim}{\boldsymbol{s}}_k - \underset{\sim}{\boldsymbol{X}}_k\right) : \left(\underset{\sim}{\boldsymbol{s}}_k - \underset{\sim}{\boldsymbol{X}}_k\right)} \qquad \text{where} \qquad \underset{\sim}{\boldsymbol{s}}_k = \underset{\sim}{\boldsymbol{\sigma}}_k - \frac{1}{3}\text{trace}\,\underset{\sim}{\boldsymbol{\sigma}}_k \underset{\sim}{\boldsymbol{1}} \tag{III.74}$$

with σ_k^0 is the initial yield stress, σ_k^{eq} is the von Mises equivalent stress and $\underset{\sim}{\boldsymbol{s}}_k$ is the deviatoric stress tensor.

According to the normality rule for standard materials Eqs.(III.48-III.49-III.50), the evolution laws of the internal variables are derived from the dissipation potential. For phenomena which do not depend explicitly on time, such as rate independent plasticity, the potential is not differentiable.

Then, the partial derivative of Ω_k with respect to g is simply replaced by a plastic multiplier $\dot{\lambda}$ to write a rate independent plastic model. Consequently, the evolution laws can be expressed as:

$$\dot{\underset{\sim}{\varepsilon}}_k^p = \dot{\lambda}_k \frac{\partial \Omega_{uk}}{\partial \underset{\sim}{\boldsymbol{\sigma}}_k} = \dot{\lambda}_k \underset{\sim}{\boldsymbol{n}}_k \tag{III.75}$$

$$\dot{r}_k = \dot{\lambda}_k \frac{\partial \Omega_{uk}}{\partial R_k} = \dot{\lambda}_k \left(1 - \frac{R_k}{Q_k}\right) \tag{III.76}$$

$$\dot{\underset{\sim}{\boldsymbol{\alpha}}}_k = \dot{\lambda}_k \frac{\partial \Omega_{uk}}{\partial X_k} = \dot{\lambda}_k \left(\underset{\sim}{\boldsymbol{n}}_k - \frac{3\Gamma_k}{2C_k} \underset{\sim}{\boldsymbol{X}}_k\right) \tag{III.77}$$

where $\underset{\sim}{\boldsymbol{n}}_k = \partial g_k / \partial \underset{\sim}{\boldsymbol{\sigma}}_k$ is the normal to the yield surface and defines the flow direction.

The plastic multiplier $\dot{\lambda}$ is determined from the consistency condition $dg_k/dt = 0$ [1]. Then, we obtain the following expression of the plastic multiplier (Benallal et al., 1988):

$$\dot{\lambda}_k = \frac{\dfrac{\partial g_k}{\partial \underset{\sim}{\boldsymbol{\sigma}}_k} : \dfrac{\partial^2 f_k}{\partial \underset{\sim}{\varepsilon}_k^2} : \dot{\underset{\sim}{\varepsilon}}_k}{-\dfrac{\partial g_k}{\partial \underset{\sim}{\boldsymbol{\sigma}}_k} : \dfrac{\partial^2 f_k}{\partial \underset{\sim}{\varepsilon}_k \partial \underset{\sim}{\varepsilon}_k^p} : \dfrac{\partial \Omega_{uk}}{\partial \underset{\sim}{\boldsymbol{\sigma}}_k} + \dfrac{\partial g_k}{\partial \underset{\sim}{\boldsymbol{X}}_k} : \dfrac{\partial^2 f_k}{\partial \underset{\sim}{\boldsymbol{\alpha}}_k^2} : \dfrac{\partial \Omega_{uk}}{\partial \underset{\sim}{\boldsymbol{X}}_k} + \dfrac{\partial g_k}{\partial R_k} \dfrac{\partial^2 f_k}{\partial r_k^2} \dfrac{\partial \Omega_{uk}}{\partial R_k}} \tag{III.78}$$

A generalized expression would be necessary in the case of a possible dependence of elastoplastic properties on concentration.

Taking the time rate of the isotropic hardening variable Eq. (III.71)$_2$ and the kinematic hardening variable Eq. (III.71)$_3$ and substituting respectively into Eqs. (III.76) and (III.77), we obtain the following evolution equations:

$$\dot{R}_k = b(Q_k - R_k)\dot{\lambda}_k \quad \text{equivalent to} \quad R_k = Q_k(1 - \exp(-b_k \lambda_k)) \tag{III.79}$$

$$\dot{\underset{\sim}{\boldsymbol{X}}}_k = \frac{2}{3} C_k \dot{\underset{\sim}{\varepsilon}}_k^p - \Gamma_k \underset{\sim}{\boldsymbol{X}}_k \dot{\lambda}_k \tag{III.80}$$

The stress increment $\dot{\underset{\sim}{\boldsymbol{\sigma}}}_k$ is related to the elastic strain increment $\dot{\underset{\sim}{\varepsilon}}_k^e$ by the linear elasticity law, which is classical in nonlinear mechanics (Lemaitre and Chaboche, 1994):

$$\begin{aligned} \dot{\underset{\sim}{\boldsymbol{\sigma}}}_k &= \underset{\approx}{\boldsymbol{C}}_k : \dot{\underset{\sim}{\varepsilon}}_k^e \\ &= \underset{\approx}{\boldsymbol{C}}_k : (\dot{\underset{\sim}{\varepsilon}}_k - \dot{\underset{\sim}{\varepsilon}}_k^\star - \dot{\underset{\sim}{\varepsilon}}_k^p) \end{aligned} \tag{III.81}$$

For simplicity, $\underset{\approx}{\boldsymbol{C}}_k$ and $\underset{\sim}{\varepsilon}_k^\star$ are taken here independent of concentration. After some treatment of Eq. (III.78) by introducing the free energy density Eq. (III.70) and the dissipation potential Eq. (III.72) and using the strain partition, in terms of rates, $\dot{\underset{\sim}{\varepsilon}}_k = \dot{\underset{\sim}{\varepsilon}}_k^e + \dot{\underset{\sim}{\varepsilon}}_k^p$, the plastic multiplier in each phase can then be written as follows:

$$\begin{aligned} \dot{\lambda}_k &= \frac{\underset{\sim}{\boldsymbol{n}}_k : \underset{\approx}{\boldsymbol{C}}_k : \dot{\underset{\sim}{\varepsilon}}_k}{\underset{\sim}{\boldsymbol{n}}_k : \underset{\approx}{\boldsymbol{C}}_k : \underset{\sim}{\boldsymbol{n}}_k + h_k + \frac{3}{2} C_k \underset{\sim}{\boldsymbol{n}}_k : \underset{\sim}{\boldsymbol{n}}_k - \Gamma_k \underset{\sim}{\boldsymbol{n}}_k : \underset{\sim}{\boldsymbol{X}}_k} \\ &= L_k \, \underset{\sim}{\boldsymbol{n}}_k : \underset{\approx}{\boldsymbol{C}}_k : \dot{\underset{\sim}{\varepsilon}}_k \end{aligned} \tag{III.82}$$

where

$$h_k = \frac{dR_k}{dp_k} = Q_k \, b_k \, \exp(-b_k \, p_k) \tag{III.83}$$

[1] The first consistency condition, $g_k = 0$, means that the state of stress is on the actual yield condition, the second $\dot{g}_k = 0$, means that an increase of the state of stress induces an increase of the yield stress. Elastic unloading occurs when $g_k < 0$ or $\dot{g}_k < 0$, the internal variables then keeping a constant value.

and

$$L_k = \frac{1}{\underset{\sim}{\boldsymbol{n}}_k : \underset{\approx}{\boldsymbol{C}}_k : \underset{\sim}{\boldsymbol{n}}_k + h_k + C_k - \Gamma_k \underset{\sim}{\boldsymbol{n}}_k : \underset{\sim}{\boldsymbol{X}}_k} \tag{III.84}$$

Using Voigt's model, the total strain rate is assumed to be the same for both phases, according to Eq. (III.51)$_2$:

$$\dot{\underset{\approx}{\boldsymbol{\varepsilon}}}_\alpha = \dot{\underset{\approx}{\boldsymbol{\varepsilon}}}_\beta = \dot{\underset{\approx}{\boldsymbol{\varepsilon}}} \tag{III.85}$$

According to Reuss model, the total strain rate in each phase is no longer equal to the local total strain rate. After some manipulations, the total strain rate for the α and β phases can be formulated, on the basis of the properties and variables related to the different phases, as (details are provided in Appendix C)

$$\begin{aligned} \dot{\underset{\approx}{\boldsymbol{\varepsilon}}}_\alpha \;=\; & \{\phi \underset{\approx}{\boldsymbol{I}} + (1-\phi)\left[\underset{\approx}{\boldsymbol{C}}_\beta - L_\beta\,(\underset{\approx}{\boldsymbol{C}}_\beta : \underset{\sim}{\boldsymbol{n}}_\beta) \otimes (\underset{\sim}{\boldsymbol{n}}_\beta : \underset{\approx}{\boldsymbol{C}}_\beta)\right]^{-1} \\ & \left[\underset{\approx}{\boldsymbol{C}}_\alpha - L_\alpha\,(\underset{\approx}{\boldsymbol{C}}_\alpha : \underset{\sim}{\boldsymbol{n}}_\alpha) \otimes (\underset{\sim}{\boldsymbol{n}}_\alpha : \underset{\approx}{\boldsymbol{C}}_\alpha)\right]\}^{-1} : (\dot{\underset{\approx}{\boldsymbol{\varepsilon}}} - \dot{\phi}(\underset{\approx}{\boldsymbol{\varepsilon}}_\alpha - \underset{\approx}{\boldsymbol{\varepsilon}}_\beta)) \end{aligned} \tag{III.86}$$

$$\begin{aligned} \dot{\underset{\approx}{\boldsymbol{\varepsilon}}}_\beta \;=\; & \Big\{(1-\phi)\underset{\approx}{\boldsymbol{I}} + \phi\left[\underset{\approx}{\boldsymbol{C}}_\alpha - L_\alpha\,(\underset{\approx}{\boldsymbol{C}}_\alpha : \underset{\sim}{\boldsymbol{n}}_\alpha) \otimes (\underset{\sim}{\boldsymbol{n}}_\alpha : \underset{\approx}{\boldsymbol{C}}_\alpha)\right]^{-1} \\ & \left[\underset{\approx}{\boldsymbol{C}}_\beta - L_\beta\,(\underset{\approx}{\boldsymbol{C}}_\beta : \underset{\sim}{\boldsymbol{n}}_\beta) \otimes (\underset{\sim}{\boldsymbol{n}}_\beta : \underset{\approx}{\boldsymbol{C}}_\beta)\right]\Big\}^{-1} : (\dot{\underset{\approx}{\boldsymbol{\varepsilon}}} - \dot{\phi}(\underset{\approx}{\boldsymbol{\varepsilon}}_\alpha - \underset{\approx}{\boldsymbol{\varepsilon}}_\beta)) \end{aligned} \tag{III.87}$$

These formula are needed for the implementation of the Reuss/Sachs procedure.

III.6 Implementation in a finite element code

The set of partial differential equations, which are the local static equilibrium, the balance of generalized stresses and the balance of mass, is solved using a finite element method to discretize space and a finite difference method to discretize time. The implementation of the proposed model is made in the finite element code ZeBuLon (Foerch and Besson, 1997; Foerch et al., 1997), where order parameter, concentration and displacement are taken as nodal degrees of freedom (ϕ, c, u_i). The variational formulation of the phase field equation and the local static equilibrium are directly derived from the formulated principle of virtual power Eq. (III.5) (Ammar et al., 2009a; Ammar et al., 2009d):

$$\Im(\phi^\star) = \int_V (\pi\phi^\star - \underline{\boldsymbol{\xi}} . \boldsymbol{\nabla}\phi^\star)\, dv + \int_{\partial V} \zeta\phi^\star\, ds = 0 \tag{III.88}$$

$$\Im(\underline{\boldsymbol{u}}^\star) = \int_V (-\underset{\sim}{\boldsymbol{\sigma}} : \boldsymbol{\nabla}\underline{\boldsymbol{u}}^\star + \underline{\boldsymbol{f}} . \underline{\boldsymbol{u}}^\star)\, dv + \int_{\partial V} \underline{\boldsymbol{t}} . \underline{\boldsymbol{u}}^\star\, ds = 0 \tag{III.89}$$

Moreover, usual weak form of the classical diffusion equation is recalled:

$$\Im(c^\star) = \int_V (\dot{c}c^\star - \underline{\boldsymbol{J}} . \boldsymbol{\nabla}c^\star)\, dv + \int_{\partial V} jc^\star\, ds = 0 \tag{III.90}$$

where $\phi^\star$, $c^\star$ and $\underline{\boldsymbol{u}}^\star$ respectively are an arbitrary field of virtual order parameter, concentration and displacement.
Accordingly, the phase field problem can be formulated as follows:

Find $\{\phi(\underline{\boldsymbol{x}}\,,t), c(\underline{\boldsymbol{x}}\,,t), \underline{\boldsymbol{u}}\,(\underline{\boldsymbol{x}}\,,t)\}$ satisfying

$$\left|\begin{array}{l} \text{at} \quad t=0 \\ \quad \phi(\underline{\boldsymbol{x}}\,,0)=\phi_0(\underline{\boldsymbol{x}}\,) \\ \quad c(\underline{\boldsymbol{x}}\,,0)=c_0(\underline{\boldsymbol{x}}\,) \\ \\ \text{at each instant t} > 0 \\ \quad \Im(\phi^\star)=\int_V(\pi\phi^\star-\underline{\boldsymbol{\xi}}\,.\boldsymbol{\nabla}\phi^\star)\,dv+\int_{\partial V}\zeta\phi^\star\,ds=0 \\ \\ \quad \Im(c^\star)=\int_V(\dot{c}c^\star-\underline{\boldsymbol{J}}\,.\boldsymbol{\nabla}c^\star)\,dv+\int_{\partial V}jc^\star\,ds=0 \\ \\ \quad \Im(\underline{\boldsymbol{u}}^\star)=\int_V(-\underset{\sim}{\boldsymbol{\sigma}}:\boldsymbol{\nabla}\underline{\boldsymbol{u}}^\star+\underline{\boldsymbol{f}}\,.\underline{\boldsymbol{u}}^\star)\,dv+\int_{\partial V}\underline{\boldsymbol{t}}\,.\underline{\boldsymbol{u}}^\star\,ds=0 \end{array}\right. \tag{III.91}$$

III.6.1 Discretization

In order to obtain a finite element solution, the spatial domain is subdivided into N elements. The nodal degrees of freedom are the values at nodes of order parameter, concentration and displacement. The fields ϕ, c and $\underline{\boldsymbol{u}}$ are approximated within each element and at every time t, in terms of nodal values by means of interpolation functions, within each element:

$$c(\underline{\boldsymbol{x}}\,,t)=\textstyle\sum_{i=1}^n N_i^e(\underline{\boldsymbol{x}}\,)c_i(t), \qquad c^\star(\underline{\boldsymbol{x}}\,,t)=\sum_{i=1}^n N_i^e(\underline{\boldsymbol{x}}\,)c_i^\star(t)$$

$$\phi(\underline{\boldsymbol{x}}\,,t)=\textstyle\sum_{i=1}^n N_i^e(\underline{\boldsymbol{x}}\,)\phi_i(t), \qquad \phi^\star(\underline{\boldsymbol{x}}\,,t)=\sum_{i=1}^n N_i^e(\underline{\boldsymbol{x}}\,)\phi_i^\star(t)$$

$$\underline{\boldsymbol{u}}\,(\underline{\boldsymbol{x}}\,,t)=\textstyle\sum_{i=1}^n N_{ij}^e(\underline{\boldsymbol{x}}\,)\underline{\boldsymbol{u}}_{\,j}(t), \qquad \underline{\boldsymbol{u}}^\star(\underline{\boldsymbol{x}}\,,t)=\sum_{i=1}^n N_{ij}^e(\underline{\boldsymbol{x}}\,)\underline{\boldsymbol{u}}_{\,j}^\star(t)$$

A Voigt notation (denoted by the underbar) is used to introduce the discretized equations where n is the number of nodes in the element e containing $\underline{\boldsymbol{x}}\,$. N_i and N_{ij} respectively are the vector and the matrix shape functions, which are expressed as:

$$\{N(\underline{\boldsymbol{x}}\,)\}=\{N_1(\underline{\boldsymbol{x}}\,),N_2(\underline{\boldsymbol{x}}\,),\ldots,N_n(\underline{\boldsymbol{x}}\,)\}$$

and

$$[N(\underline{\boldsymbol{x}}\,)]=\begin{bmatrix} N_1^e & 0 & N_2^e & 0 & \cdots & N_n^e & 0 \\ \\ 0 & N_1^e & 0 & N_2^e & \cdots & 0 & N_n^e \end{bmatrix}$$

$$\boldsymbol{\nabla}c(\underline{\boldsymbol{x}}\,,t)=\textstyle\sum_{i=1}^n B_{ij}^e(\underline{\boldsymbol{x}}\,)c_j(t), \qquad \boldsymbol{\nabla}c^\star(\underline{\boldsymbol{x}}\,,t)=\sum_{i=1}^n B_{ij}^e(\underline{\boldsymbol{x}}\,)c_j^\star(t)$$

$$\boldsymbol{\nabla}\phi(\underline{\boldsymbol{x}}\,,t)=\textstyle\sum_{i=1}^n B_{ij}^e(\underline{\boldsymbol{x}}\,)\phi_j(t), \qquad \boldsymbol{\nabla}\phi^\star(\underline{\boldsymbol{x}}\,,t)=\sum_{i=1}^n B_{ij}^e(\underline{\boldsymbol{x}}\,)\phi_j^\star(t)$$

$$\boldsymbol{\nabla}\underline{\boldsymbol{u}}\,(\underline{\boldsymbol{x}}\,,t)=\textstyle\sum_{i=1}^n \underset{\sim}{\boldsymbol{B}}_{ij}^e(\underline{\boldsymbol{x}}\,)\underline{\boldsymbol{u}}_{\,j}(t), \qquad \boldsymbol{\nabla}\underline{\boldsymbol{u}}^\star(\underline{\boldsymbol{x}}\,,t)=\sum_{i=1}^n \underset{\sim}{\boldsymbol{B}}_{ij}^e(\underline{\boldsymbol{x}}\,)\underline{\boldsymbol{u}}_{\,j}^\star(t)$$

In the 2d case, the matrices $[B^e(\underline{\boldsymbol{x}}\,)]$ and $\left[\underset{\sim}{\boldsymbol{B}}^e(\underline{\boldsymbol{x}}\,)\right]$ are defined by the first derivatives of the shape functions as

$$[B^e(\underline{\boldsymbol{x}}\,)]=\left[\underline{\boldsymbol{grad}}\,(N^e(\underline{\boldsymbol{x}}\,)\right]=\begin{bmatrix} \dfrac{\partial N_1^e}{\partial x} & \dfrac{\partial N_2^e}{\partial x} & \cdots & \dfrac{\partial N_n^e}{\partial x} \\ \\ \dfrac{\partial N_1^e}{\partial y} & \dfrac{\partial N_2^e}{\partial y} & \cdots & \dfrac{\partial N_n^e}{\partial y} \end{bmatrix} \tag{III.92}$$

and

$$\left[\underset{\sim}{\boldsymbol{B}}^{e}(\underline{\boldsymbol{x}})\right] = \begin{bmatrix} \frac{\partial N_1^e}{\partial x} & 0 & \frac{\partial N_2^e}{\partial x} & 0 & \cdots & \frac{\partial N_n^e}{\partial x} & 0 \\ 0 & \frac{\partial N_1^e}{\partial y} & 0 & \frac{\partial N_2^e}{\partial y} & \cdots & 0 & \frac{\partial N_n^e}{\partial y} \\ \frac{\partial N_1^e}{\partial y} & \frac{\partial N_1^e}{\partial x} & \frac{\partial N_2^e}{\partial y} & \frac{\partial N_2^e}{\partial x} & \cdots & \frac{\partial N_n^e}{\partial y} & \frac{\partial N_n^e}{\partial x} \end{bmatrix} \tag{III.93}$$

Regarding time discretization, the differential equations are integrated at each Gauss point in an incremental procedure using a Euler implicit scheme ($\theta-$method). Using the notation $c(t)$ and $\phi(t)$ for the known values of the current time step t, $\phi(t+\Delta t)$ and $c(t+\Delta t)$ at time $t+\Delta t$ are estimated by solving the following equations:

$$\dot{c}(t+\Delta t) = \frac{c(t+\Delta t) - c(t)}{\Delta t} \tag{III.94}$$

$$\dot{\phi}(t+\Delta t) = \frac{\phi(t+\Delta t) - \phi(t)}{\Delta t} \tag{III.95}$$

$$c(0) = c_0, \quad \phi(0) = \phi_0 \tag{III.96}$$

Δt indicates the time increment, and c_0, ϕ_0 are the initial conditions for the concentration and order parameter.

After substituting the nodal approximation and the time discretization into Eq. (III.91), we deduce the element residual, which can be written in the following form:

$$\{\mathcal{R}^e(u,c,\phi)\} \quad = \quad \begin{Bmatrix} \mathcal{R}_u^e \\ \mathcal{R}_c^e \\ \mathcal{R}_\phi^e \end{Bmatrix} \tag{III.97}$$

where $\mathcal{R}_u^e$, $\mathcal{R}_c^e(c,\phi)$ and $\mathcal{R}_\phi^e(\phi)$ are respectively the element residuals for the variational formulation of classical mechanics, diffusion (III.90) and phase field (III.88), defined as follow:

$$(\mathcal{R}_u^e)_i = \int_{V^e} \left(- \left[\underset{\sim}{\boldsymbol{B}}^e\right]_{ij} \sigma_j \; + \; [N^e]_{ij} \, f_j \right) dv + \left[N^e\right]_{ij} t_j ds \tag{III.98}$$

$$(\mathcal{R}_c^e)_i = \int_{V^e} \left(N_i^e N_j^e \, \dot{c}_j^e - [B^e]_{ij} \, J_j \right) dv + \int_{\partial V^e} N_i^e j \, ds \tag{III.99}$$

$$(\mathcal{R}_\phi^e)_i = \int_{V^e} \left(N_i^e \pi(\phi) \; - [B^e]_{ij} \, \xi_j \right) dv + \int_{\partial V^e} N_i^e \zeta \, ds \tag{III.100}$$

The global residual vector can be obtained by assembling the element residuals for all finite elements using the matrix assembly $[A^e]$:

$$\{\mathcal{R}(\phi)\} = \sum_{e=1}^{N} [A^e] \, . \, \{\mathcal{R}^e(\phi)\} = \{0\} \tag{III.101}$$

following the usual definition in computational mechanics (Besson et al., 2001).

A standard Newton-Raphson's method is used to solve the system of non-linear equations in an iterative manner, where three residual vectors for the degrees of freedom (ϕ, c, u_i) and generalized stiffness matrix are calculated (Ammar et al., 2009a), following the usual rules in computational

mechanics (Besson et al., 2001). An implicit Newton algorithm is used for the resolution method for global integration, based on the computation of the local consistent tangent matrix (Simo and Hughes, 1998).

Given a known set of nodal degrees of freedom at time t, and assuming that the residual vanishes at the next time step $t + \Delta t$, a set of non-linear equations results for the nodal degrees of freedom at $t + \Delta t$.

It is solved with the Newton-Raphson method in an iterative manner. This requires the computation of the element generalized stiffness matrix which is obtained by derivation of the residual vector with respect to the degrees of freedom (c, ϕ):

$$[K_t^e] = \left[\frac{\partial \mathcal{R}^e}{\partial \delta^e}\right] = \begin{bmatrix} [K_{uu}^e] & [K_{uc}^e] & \left[K_{u\phi}^e\right] \\ [K_{cu}^e] & [K_{cc}^e] & \left[K_{c\phi}^e\right] \\ \left[K_{\phi u}^e\right] & \left[K_{\phi c}^e\right] & \left[K_{\phi\phi}^e\right] \end{bmatrix} \tag{III.102}$$

$$\text{with} \quad \{\delta^e\} = \begin{Bmatrix} \{\underline{\boldsymbol{u}}^e\} \\ \{c^e\} \\ \{\phi^e\} \end{Bmatrix}$$

The element generalized stiffness matrix is divided into nine submatrices. See Appendix D for the definition of the individual components of the submatrices.

III.6.2 Programming of finite element constitutive equations

This section is specifically devoted to the implementation of the proposed non-linear elastoplastic phase field model with different homogenization schemes in the finite element code Zebulon. Specific classes must be defined following the philosophy of object oriented programming. The eventual programming of material characteristics within a finite element code entails defining the appropriate variables used to characterize a material behaviour, which are grouped into sets according to their functionality in the physics of the material problem as follows

- GRAD/FLUX variables (`primal/dual`): The grad variables are the set of primary imposed problem variable over which the behavior is integrated. These are generally either the unknown variables of the problem. The flux variables are the dual variables to the grad, which represent the response of the behavior to the primal variable (Tab. III.2).
- $\mathcal{V}_{\text{int}}^t$: These are the primary integration variables over a given time increment in order to arrive at the new flux. In general they are the state variables. During a time step, these variables are subject to updates at each time step.
- $\mathcal{V}_{\text{aux}}^t$: These are interesting additional variables (informations) which does not directly define the material state. They are not necessary for the computation, but used in the post-processing.
- `COEFF`: These are the material parameters, which are used to represent a specific material within a general behavior.

The finite element resolution is performed by means of an incremental procedure. The unknown fields are estimated at different steps of the calculation to satisfy the global equilibrium equation. At the beginning of each global time increment, which is indicated by

	primal	dual
mechanical contributions (part, processes)	$\underset{\sim}{\varepsilon}$	$\underset{\sim}{\boldsymbol{\sigma}}$
diffusion contributions	$\boldsymbol{\nabla} c$	$\underline{\boldsymbol{J}}$
phase field contributions	$\boldsymbol{\nabla} \phi$	$\underline{\boldsymbol{\xi}}$

Tableau III.2 : Primal/dual variables

the subscripts t, the appropriate variables $(\mathcal{V}_{\text{int}}^{t}, \mathcal{V}_{\text{aux}}^{t}, \texttt{primal}^{t}, \texttt{dual}^{t})$ are known. Prescribing an increment of the primary variables $\Delta\texttt{primal}$ for an increment of time, the primary numerical task for material simulation code for FEA calculations is to provide the values of $(\mathcal{V}_{\text{int}}^{t+1}, \mathcal{V}_{\text{aux}}^{t+1}, \texttt{dual}^{t+1}, (\partial\Delta\texttt{dual}/\partial\Delta\texttt{primal})^{t+1})$ at the end of each loading increment (Besson et al., 2001; Foerch et al., 1997). Finite element algorithms, providing these necessary variables, are displayed in Fig. III.2 for Voigt/Taylor scheme, in Fig. III.3 for Reuss/Sachs scheme and in Fig. III.4 for Khachaturyan scheme.

The size of the global time increments during simulations is mainly controlled by the convergence of the global resolution of the equilibrium equation. For each time step, some iterations are needed before the global residual $\mathcal{R}$ becomes smaller than a fixed value r. This global residual would vanish if the global equilibrium equations were fully satisfied.

$$\mathcal{R}^{\text{abs}} = |\mathbf{F_{ext}} - \mathbf{F_{int}}| < r \text{ for an absolute ratio} \tag{III.103}$$

$$\mathcal{R}^{\text{rel}} = \frac{|\mathbf{F_{ext}} - \mathbf{F_{int}}|}{|\mathbf{F_{ext}}|} < r \text{ for a relative ratio} \tag{III.104}$$

where $\mathbf{F_{ext}}$ is the "external force" vector, and $\mathbf{F_{int}}$ is the "internal force" vector.

During the local integration procedure, the constitutive equations, expressed as a first order ordinary differential system, are integrated at each Gauss point using one of the two following numerical methods:

- Explicit Runge-Kutta method with automatic time stepping.
- Implicit θ-method solved with a Newton-Raphson method.

III.6.2.1 Runge-Kutta method

The Runge-Kutta method is a numerical technique used to solve an ordinary differential equation of the form:

$$\dot{\mathbf{Z}} = \mathbf{F}(t, \mathbf{Z}) \tag{III.105}$$

$$\mathbf{Z}^{t=0} = \mathbf{Z}^{0} \tag{III.106}$$

We begin by writing the Taylor's series expansion for the solution $\mathbf{Z}$ in the form

$$\mathbf{Z}^{t+\Delta t} = \mathbf{Z}^{t} + \dot{\mathbf{Z}}^{\mathbf{t}} \Delta t + \mathcal{O}(\Delta t^2) \tag{III.107}$$

The differential equation (III.105) is used to evaluate $\dot{\mathbf{Z}}^{\mathbf{t}}$. The Runge-Kutta method is to aim for the desirable features of the Taylor series method, but with the replacement of the requirement for the evaluation of higher order derivatives with the requirement to evaluate the solution within the step t to $t + \Delta t$. This method becomes obviously inaccurate when increasing the global time increment Δt, even if it allows "rapid prototyping" of material models.

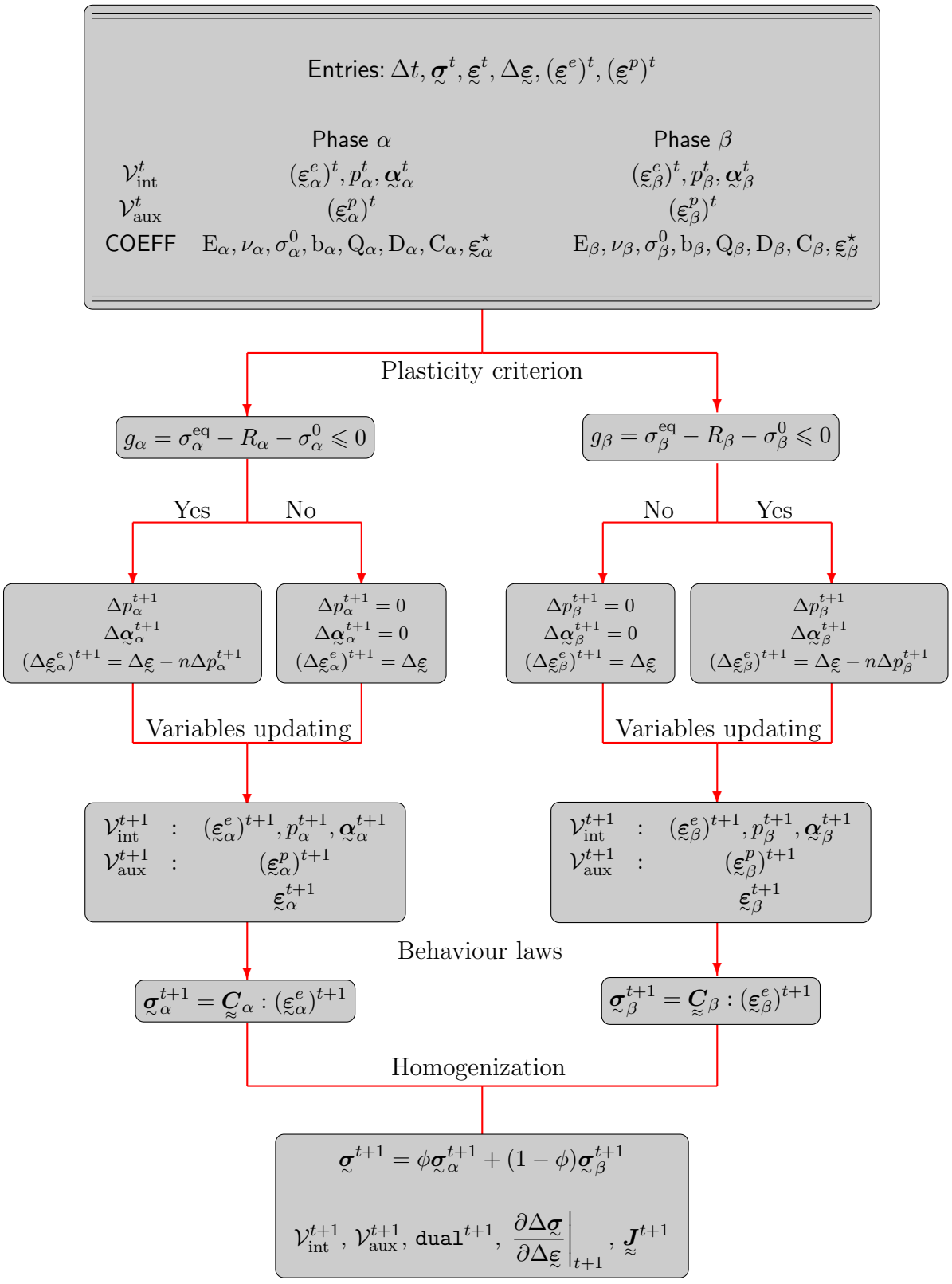

Figure III.2 : Integration of constitutive equations for Voigt/Taylor scheme. p_α and p_β are respectively the accumulated plastic strain in α and β phases

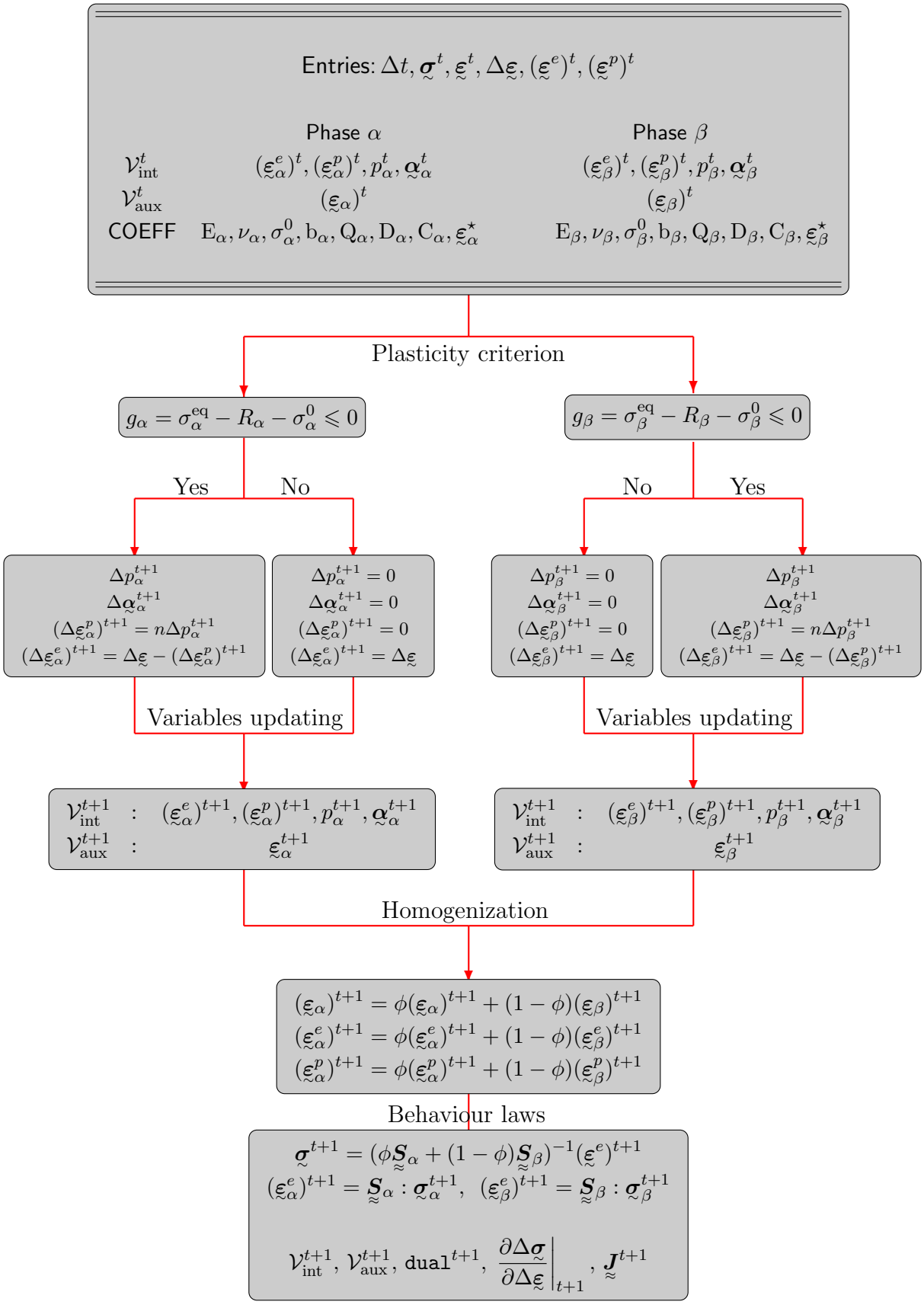

Figure III.3 : Integration of constitutive equations for Reuss/Sachs scheme

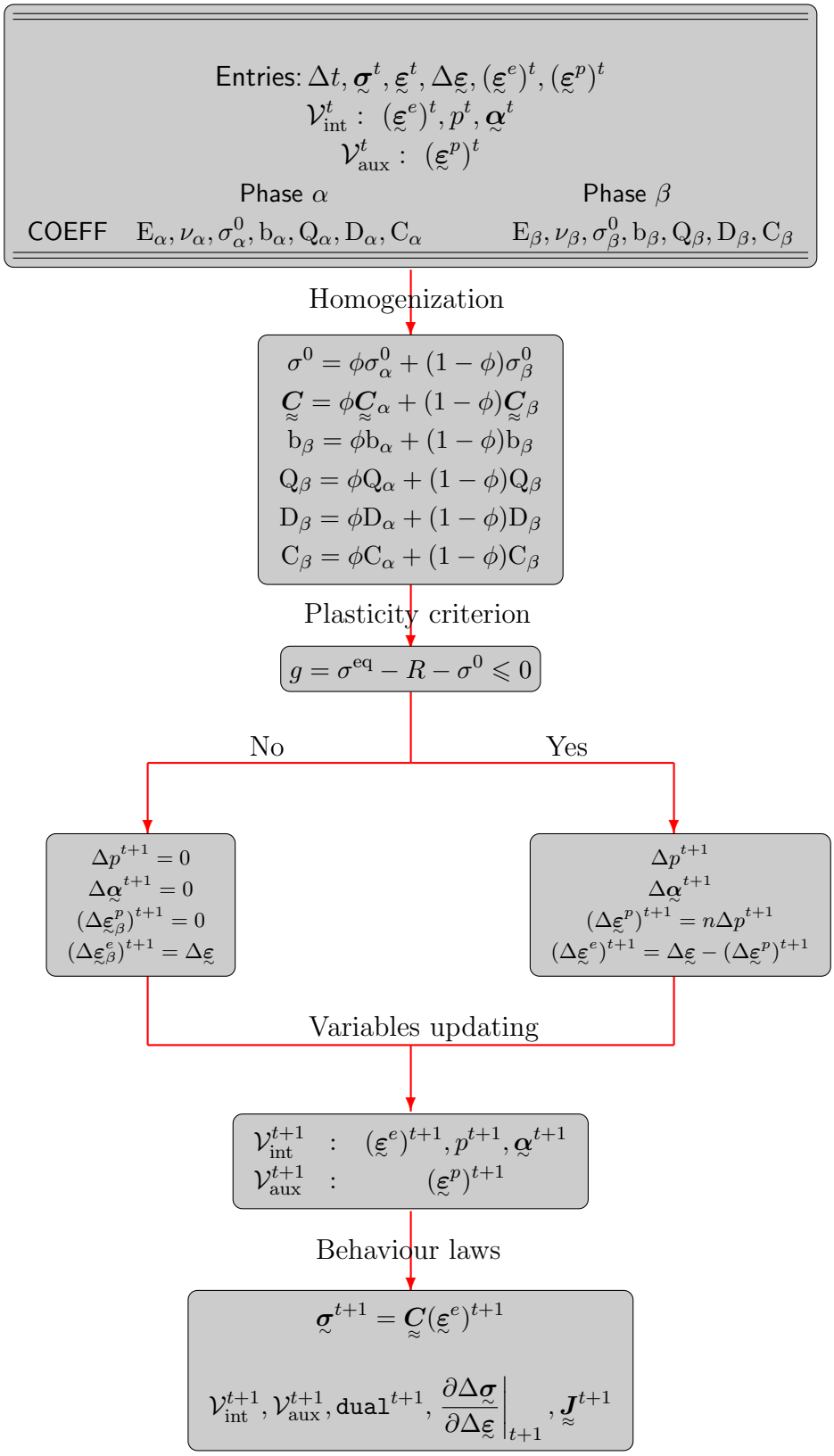

Figure III.4 : Integration of constitutive equations for Khachaturyan scheme

III.6.2.2 Θ-method

We use a generalized mid-point rule, the evaluation of the state variable increment $\Delta\mathbf{Z}$ being performed by using an intermediate point $t + \Theta t$ (III.108). A linearization is applied to compute the value of the state variables at this instant (III.108):

$$\Delta\mathbf{Z} = \Delta t\dot{\mathbf{Z}}^{\mathbf{t+\Theta\Delta t}} = \Delta t\mathbf{F}(\mathbf{Z}^{t+\Theta\Delta t}) \tag{III.108}$$

$$\mathbf{Z}^{\mathbf{t+\Theta\Delta t}} = \mathbf{Z}^{t} + \Theta\Delta\mathbf{Z} \tag{III.109}$$

Θ belongs to the interval $[0:1]$. $\Theta = 0$ corresponds to the forward Euler scheme, and $\Theta = 1$ is a fully implicit integration. This method provides high confidence in the stability of the integration scheme provided $\Theta > 0$, but can become rather expensive during calculation (Besson et al., 2001).

Over each time increment Δt, the constitutive equations are written in terms of assumed increments of the state variables. The variable increment $\Delta\mathbf{Z}$ is then evaluated by solving the following non-linear system with respect to $\Delta\mathbf{Z}$:

$$\mathcal{R} = \Delta\mathbf{Z} - \Delta t\mathbf{F}(\mathbf{Z}^{t} + \Theta\Delta\mathbf{Z}) < \epsilon \tag{III.110}$$

where $\mathcal{R}$ is called the local residual, which will be close (by an adjustable tolerance ϵ) to zero. A Newton-Raphson algorithm is used to solve the non-linear system to find the increment of state dependent variables. It requires the definition of the Jacobian matrix associated to system (III.110), which is computed from the partial derivatives of the residual in terms of the integrated variables increment as follows

$$\mathbf{J} = \frac{\partial\mathcal{R}}{\partial\Delta\mathbf{Z}} = \mathbf{1} - \Delta t\left.\frac{\partial\mathbf{F}}{\partial\Delta\mathbf{Z}}\right|^{t+\Theta\Delta t} \tag{III.111}$$

The Jacobian matrix for the proposed elastoplastic phase field model is given in Appendix E.

III.7 Conclusions

A general constitutive framework has been proposed to incorporate, in a systematic way, linear and nonlinear mechanical behaviour laws into a phase field model. The systematic procedure can be summarized as follows:

1. Select a diffusion/phase field model with its corresponding free energy and dissipation potentials for the chemical processes. In the examples given here, we have retained a variant of the approach proposed by (Kim et al., 1998).

2. Select for each individual phase a set of mechanical constitutive equations. Following the standard generalized framework settled in (Germain et al., 1983; Lemaitre and Chaboche, 1994), the mechanical part of the free energy and dissipation potentials can be chosen. The nonlinear behaviour is accounted for by means of appropriate internal variables. In the present approach, the mechanical properties and parameters associated with each phase may depend on concentrations, exclusively, but not on the order parameter.

3. Attach to each material point stress and strain tensors associated with each considered phase, that are related to the classical stress and strain at that point by the following average formula:

$$\underset{\sim}{\boldsymbol{\varepsilon}} = \chi\underset{\sim}{\boldsymbol{\varepsilon}}_{\alpha} + (1-\chi)\underset{\sim}{\boldsymbol{\varepsilon}}_{\beta} \tag{III.112}$$

$$\underset{\sim}{\boldsymbol{\sigma}} = \chi\underset{\sim}{\boldsymbol{\sigma}}_{\alpha} + (1-\chi)\underset{\sim}{\boldsymbol{\sigma}}_{\beta} \tag{III.113}$$

$$f_u = \chi f_{\alpha u} + (1-\chi)f_{\beta u} \tag{III.114}$$

where the indicator function χ is a function of order parameter. In the examples provided in this work, we take:

$$\chi = \phi \tag{III.115}$$

4. Select a homogenization scheme in order to determine the previous variables $\underset{\sim}{\varepsilon}_{\alpha,\beta}, \underset{\sim}{\sigma}_{\alpha,\beta}$ for given stress and strain values $\underset{\sim}{\varepsilon}, \underset{\sim}{\sigma}$ at each material point. This scheme also implies specific definitions of the effective stiffness, eigenstrain and plastic deformation at each material point, which are especially important in the diffuse interface zone. According to the explored Voigt model, the effective stiffness is the arithmetic mean of the stiffness tensors of the individual phases. The effective eigenstrains, including plastic strain, are not given by such simple means. The correct relations have been provided. According to Reuss' approach, the effective compliance and the effective eigenstrains are arithmetic means of the corresponding values of the phases.

The performed analysis has shown that the usual interpolation rules used in microelastic phase field models combine aspects of both Reuss and Voigt approaches in the sense that they take simultaneously arithmetic mean values for elastic moduli and eigenstrains. Combining different homogenization schemes is acceptable since there is no clear physical motivation for selecting one or another scheme in the present context as long as no specific hypothesis is made on the atomic arrangement inside the representative volume element underlying each material point, and as long as no specific discrete–continuum homogenization scheme is constructed. Other general homogenization schemes could be tested and may be computationally more efficient under circumstances, like the Hashin–Shtrikman procedure or the self–consistent method.

Applications of the proposed theory will deal with the case of equilibrium concentrations in the presence of heterogeneous elastic behaviour and then in the presence of plastic deformation, which are still poorly known fields of phase transformation.

In particular, the question of inheritance of plastic deformation during migration of phase boundaries has not been addressed in this work. It remains to be explored in order to reach realistic comparison with experimental results.

Abstract

A general constitutive framework is proposed to incorporate linear and nonlinear mechanical constitutive equations into a standard phase field model. Using the principles of the thermodynamics of irreversible processes, the balance and boundary conditions of a fully coupled phase field/diffusion/mechanical problem are presented. The constitutive equations for chemical and mechanical processes are formulated, within the framework of generalized standard materials, by means of the expression of the free energy potential and the dissipation potential. In the diffuse interface region where both phases coexist, two mixture rules for strain and stress are introduced, which are based on the Voigt/Taylor and Reuss/Sachs well–known homogenization schemes and compared to the commonly used mixture rules in phase field models. The programming of the proposed non-linear elastoplastic phase field model in the finite element code with different homogenization schemes was presented.

Chapitre -IV-

Some elementary initial boundary values problems in coupled diffusion-elastoplasticity

Contents

IV.1 Introduction . . . 72
IV.2 Two-dimensional problems . . . 72
IV.2.1 Plane strain . . . 72
IV.2.2 Axisymmetric case . . . 73
IV.2.3 Generalized plane strain element (2.5D) . . . 74
IV.3 Coherent phase diagram in microelasticity . . . 74
IV.3.1 Cahn-Larché coherent phase diagram . . . 74
IV.3.1.1 Cahn-Larché analytical solutions . . . 74
IV.3.1.2 Phase field calculations . . . 77
IV.3.2 Effect of composition-dependent elastic strain . . . 81
IV.3.2.1 Analytical solutions . . . 81
IV.3.2.2 Numerical calculations . . . 82
IV.4 Growth kinetics of an oxide layer . . . 84
IV.4.1 Mechanical behavior of the misfitting planar oxide layer problem . . . 84
IV.4.2 Interfacial equilibrium concentration . . . 85
IV.4.3 Growth kinetics . . . 86
IV.4.4 Numerical results . . . 87
IV.5 Growth of an isotropic misfitting cylindrical precipitate . . . 91
IV.5.1 Elastic analysis . . . 91
IV.5.2 Numerical calculations against the analytical solutions . . . 93
IV.6 Growth of an isotropic spherical matrix . . . 97
IV.6.1 Analytical analysis . . . 97
IV.6.2 Equilibrium concentration at the interface . . . 99
IV.6.3 Phase field calculations . . . 99
IV.7 Conclusion . . . 103

IV.1 Introduction

Diffusional phase transitions in solids are often isothermal and accompanied by deformation induced by a difference in a lattice parameters between the two phases. Elastic interactions arising from a difference of the lattice spacing between two coherent phases can have a strong influence on the phase separation of alloys. It may accelerate, slow down or even stop the phase separation process. The introduction of the elastic coherency strains in the phase field models for solid-solid phase transformations, initiated by Khachaturyan (Khachaturyan, 1983), has enabled the understanding of very complex microstructure evolutions driven by the interplay of diffusion and elasticity (Wang and Khachaturyan, 1995a; Wang et al., 1998; Le Bouar et al., 1998; Boussinot et al., 2009). First attempts to couple a diffuse interface model with elasto-plasticity and elasto-viscoplasticity models have been only very recently proposed by (Ubachs et al., 2006; Uehara et al., 2007; Guo et al., 2008; Yamanaka et al., 2008; Zhou et al., 2008; Gaubert et al., 2009), extending the range of applications and materials which can be handled by the phase field approach.

In the present chapter, the proposed non-linear elastoplastic phase field model has been used to illustrate the implication of the choice of specific mixture rules for these behaviour laws in the diffuse interface region on the coherent two-phase equilibria. Some elementary initial boundary value problem in coupled diffusion-elasto-plasticity on finite size specimens has been solved and validated against corresponding sharp interface analytical solutions. In the section IV.3, the model is used to predict coherent phase diagram in microelasticity when internal stresses are generated by transformation eigenstrains (Cahn and Larché, 1984). It demonstrates that the choice of such an interpolation scheme can have serious consequences on the predicted coherent phase diagram. Consequently, calculating this phase diagram is used to rule out some unacceptable mixture rules. In the section IV.4, the attention is focused on the mechanical effect through the phase field on the transformation kinetics of a planar layer growing at the surface of a pure zirconium slab. The study of the oxide layer growth in a purely chemical process, which was presented in the first chapter II.6, is extended here by taking the influence of the misfit generated stress into account. The growth mechanism of the oxide layer has been studied considering the effects of the misfit generated stress, the oxide elasticity moduli and the plastic relaxation of the transformation strain energy. To validate the numerical finite element implementation and to show the ability of the proposed model to handle precipitation together with mechanical contribution effect, the mechanical analysis of the isotropic cylindrical particle growing in a cylindrical matrix is given in section IV.5. In this section IV.6, the growth of a single spherical precipitate in an infinite matrix is investigated. The proposed model has been used to study the stored elastic energy effect on the diffusion-controlled growth of an isolated precipitate in a supersaturated matrix and to investigate the effect of plastic accommodation processes on the transformation kinetics, compared with the corresponding pure elastic state and pure chemical transformation.

IV.2 Two-dimensional problems

Analytical closed-form solution of elasticity problems for the general case of fully three-dimensional bodies involves great mathematical difficulties to accomplish. That is why most solutions are developed for reduced problems, using simplifying assumptions, which can be strictly checked for the studied situation or represent an approximation of the real problem. The nature and accuracy of the approximation depend on the symmetry of the problem and loading geometry.

IV.2.1 Plane strain

The deformation of bodies is described as plane strain if the displacement vector of any point is parallel to a certain plane called the plane of deformation and is independent of the distance from

the point under consideration to this plane. Assuming that a body is subjected to plane strain, perpendicular to z, the displacements are thus

$$u_x = u_x(x,y), \qquad u_y = u_y(x,y), \qquad u_z = 0 \tag{IV.1}$$

The corresponding components of the strain tensor are obtained as

$$\varepsilon_{xx} = \frac{\partial u_x}{\partial x}, \qquad \varepsilon_{yy} = \frac{\partial u_y}{\partial y}, \qquad \varepsilon_{xy} = \frac{1}{2}\left(\frac{\partial u_x}{\partial y} + \frac{\partial u_y}{\partial x}\right) \tag{IV.2}$$

These components are in general different from zero and independent of z. However, the remaining components are null

$$\varepsilon_{xz} = \varepsilon_{yz} = \varepsilon_{zz} = 0 \tag{IV.3}$$

In isotropic elasticity, the stress tensor takes the following form

$$[\underset{\sim}{\boldsymbol{\sigma}}] = \begin{bmatrix} \sigma_{xx}(x,y) & \sigma_{xy}(x,y) & 0 \\ \sigma_{yx}(x,y) & \sigma_{yy}(x,y) & 0 \\ 0 & 0 & \sigma_{zz}(x,y) \end{bmatrix} \tag{IV.4}$$

Using Hooke's law, the component σ_{zz} is expressed in function of the plane stress components as

$$\sigma_{zz} = \nu(\sigma_{xx} + \sigma_{yy}) \tag{IV.5}$$

Thus, a purely two-dimensional form for the elasticity law is given as follows

$$\begin{bmatrix} \varepsilon_{xx} \\ \varepsilon_{yy} \\ 2\varepsilon_{xy} \end{bmatrix} = \frac{1-\nu^2}{E} \begin{bmatrix} 1 & -\dfrac{\nu}{1-\nu} & 0 \\ -\dfrac{\nu}{1-\nu} & 1 & 0 \\ 0 & 0 & \dfrac{2}{1-\nu} \end{bmatrix} \begin{bmatrix} \sigma_{xx} \\ \sigma_{yy} \\ \sigma_{xy} \end{bmatrix} \tag{IV.6}$$

IV.2.2 Axisymmetric case

A problem is axisymmetric when the three-dimensional problem domain is geometrically a solid of revolution and the material properties, the boundary conditions and all loading conditions are symmetric about the axis of revolution. Consequently, the three-dimensional field problem can be solved using a two-dimensional domain, which is most conveniently described in cylindrical (r,θ,z) coordinates. The field variables are independent of the circumferential coordinate θ and are function of the radial and axial (r,z) coordinates only:

$$\underline{\boldsymbol{u}} = u_r(r,z)\underline{\boldsymbol{e}}_r + u_z(r,z)\underline{\boldsymbol{e}}_z \tag{IV.7}$$

and the strain tensor is:

$$[\underset{\sim}{\boldsymbol{\varepsilon}}] = \begin{bmatrix} \dfrac{\partial u_r}{\partial r} & 0 & \dfrac{1}{2}\left(\dfrac{\partial u_r}{\partial z} + \dfrac{\partial u_z}{\partial r}\right) \\ 0 & \dfrac{u_r}{r} & 0 \\ \dfrac{1}{2}\left(\dfrac{\partial u_r}{\partial z} + \dfrac{\partial u_z}{\partial r}\right) & 0 & \dfrac{\partial u_z}{\partial z} \end{bmatrix} \tag{IV.8}$$

In isotropic elasticity, the stress tensor takes the following form:

$$[\underset{\sim}{\boldsymbol{\sigma}}] = \begin{bmatrix} \sigma_{rr} & 0 & \sigma_{rz} \\ 0 & \sigma_{\theta\theta} & 0 \\ \sigma_{rz} & 0 & \sigma_{zz} \end{bmatrix} \tag{IV.9}$$

IV.2.3 Generalized plane strain element (2.5D)

The generalized plane strain theory assumes that the model lies between two parallel bounding planes, the upper one may move with respect to lower one but remains planar during deformation. The displacement field takes the following form:

$$\underline{\boldsymbol{U}}\,(x,y,z) = u_x(x,y)\underline{\boldsymbol{e}}_x + u_y(x,y)\underline{\boldsymbol{e}}_y + \underline{\boldsymbol{u}}_0\,(x,y,z) \tag{IV.10}$$

where

$$\vec{u}_0\,(x,y,z) = z\left(\vec{t} + \vec{w} \wedge \overrightarrow{OM}\right) \tag{IV.11}$$

where z corresponds to the third direction. O is the center of gravity of the 2D structure.

The displacement expression contains the degrees of freedom in the plane u_x, u_y, for each material point, but also the generalized degrees of freedom $\underline{\boldsymbol{t}}$, $\underline{\boldsymbol{w}}$, due to homogeneous deformation and rotation of $xz-$ and $yz-$ sections. Both vectors $\underline{\boldsymbol{t}}$ and $\underline{\boldsymbol{w}}$ are given by

$$\underline{\boldsymbol{t}} = \begin{pmatrix} t_x \\ t_y \\ t_z \end{pmatrix} \qquad \underline{\boldsymbol{w}} = \begin{pmatrix} w_x \\ w_y \\ w_z \end{pmatrix} \tag{IV.12}$$

$t_x \ldots t_z$ and $w_x \ldots w_z$ are the 6 generalized degrees of freedom.

The displacement field is given by

$$\begin{aligned} U_x &= u_x + z t_x - w_z\,(y - Y_0)\,z \\ U_y &= u_y + z t_y + w_z\,(x - X_0)\,z \\ U_z &= u_z + z t_z + w_x\,(y - Y_0)\,z - w_y\,(x - X_0)\,z \end{aligned}$$

IV.3 Coherent phase diagram in microelasticity

IV.3.1 Cahn-Larché coherent phase diagram

This section aims at demonstrating the consequences of the choice of a specific interface behaviour on the predicted phase diagram when internal stresses are generated by transformation eigenstrains independent of concentration, typically due to lattice mismatches. Indeed, phase field models must at least be able to predict the right equilibrium conditions. This is usually not a big issue, and so it is rarely discussed in the literature, even if subtle features can come out when mechanics is involved. For that purpose, we have chosen to test the different homogenization schemes proposed above against the well-known analytical model of (Cahn and Larché, 1984). For the sake of completeness, we will first recall the main features of the Cahn-Larché model; then we will compare the phase field predictions with the analytical solutions.

IV.3.1.1 Cahn-Larché analytical solutions

Cahn and Larché have proposed a very simple model to exhibit some striking features of phase diagrams when elasticity is accounted for, discovered by (Williams, 1984). The simplifications allowing an explicit formulation of the equilibrium conditions are as follows:

1. The chemical free energies f_α and f_β of the two coexisting phases are quadratic functions of the concentration, such as Eq. (III.28). Equal curvatures $k_\alpha = k_\beta = k$ ensure that the free energies intersect only once along the concentration axis. The minima of the

chemical free energies are located at a_α and a_β ($a_\alpha > a_\beta$ by convention), which define the equilibrium concentrations in the absence of stress. Under stress, the corresponding equilibrium concentrations are different, and noted c_α and c_β.

2. The interfaces between α and β are coherent.

3. Homogeneous isotropic linear elasticity is considered.

4. The eigenstrains are spherical tensors independent of concentration. Choosing β as the stress free reference state and $\underset{\sim}{\mathbf{1}}$ the unit second order tensor, we have:

$$\underset{\sim}{\boldsymbol{\varepsilon}}^\star_\beta = \underset{\sim}{\mathbf{0}} \qquad \text{and} \qquad \underset{\sim}{\boldsymbol{\varepsilon}}^\star_\alpha = \varepsilon^\star \underset{\sim}{\mathbf{1}} \tag{IV.13}$$

5. There is no average stress.

With the four last assumptions, the elastic energy f_e due to coherency strain is independent of the sizes, morphologies and distributions of both phases, as stated by the so-called Bitter-Crum theorem, see e.g. (Eshelby, 1957; Eshelby, 1959) or (Khachaturyan, 1983). f_e depends only on the volume fraction z in the following way:

$$f_e = z(1-z)\,\mathcal{B} \tag{IV.14}$$

where $\mathcal{B} = E\,(\varepsilon^\star)^2/(1-\nu)$ with Young's modulus E and Poisson's ratio ν.

The total free energy is obtained by adding this elastic energy f_e to the free energy of the unstressed state:

$$f = z\,f_\alpha + (1-z)\,f_\beta + f_e \tag{IV.15}$$

where z is the volume fraction of α.

$$0 \leqslant z \leqslant 1 \tag{IV.16}$$

This total free energy is supplied by the mass conservation:

$$c_0 = z\,c_\alpha + (1-z)\,c_\beta \tag{IV.17}$$

where c_0 is the nominal composition of the alloy. The equilibrium conditions are then obtained from the minimization of the lagrangian:

$$\mathcal{L} = z\,f_\alpha + (1-z)\,f_\beta + f_e - \lambda\,[z\,c_\alpha + (1-z)\,c_\beta - c_0] \tag{IV.18}$$

where λ is the Lagrange multiplier associated with constraint Eq. (*IV.17*).

Differentiating this lagrangian with respect to c_α, c_β, z and λ gives:

$$\frac{\partial \mathcal{L}}{\partial c_\alpha} = z\,\frac{\partial f_\alpha}{\partial c_\alpha} - \lambda\,z = 0 \tag{IV.19}$$

$$\frac{\partial \mathcal{L}}{\partial c_\beta} = (1-z)\,\frac{\partial f_\beta}{\partial c_\beta} - \lambda\,(1-z) = 0 \tag{IV.20}$$

$$\frac{\partial \mathcal{L}}{\partial z} = f_\alpha - f_\beta + \frac{\partial f_e}{\partial z} - \lambda(c_\alpha - c_\beta) = 0 \tag{IV.21}$$

$$\frac{\partial \mathcal{L}}{\partial \lambda} = z\,c_\alpha + (1-z)\,c_\beta - c_0 = 0 \tag{IV.22}$$

After eliminating the Lagrange multiplier from the above equations, the conditions of coherent equilibrium can be expressed as:

$$\frac{\partial f_\alpha}{\partial c_\alpha} = \frac{\partial f_\beta}{\partial c_\beta} = \mu_{\text{eq}} \tag{IV.23}$$

$$\omega_\beta - \omega_\alpha = \frac{\partial f_e}{\partial z} \tag{IV.24}$$

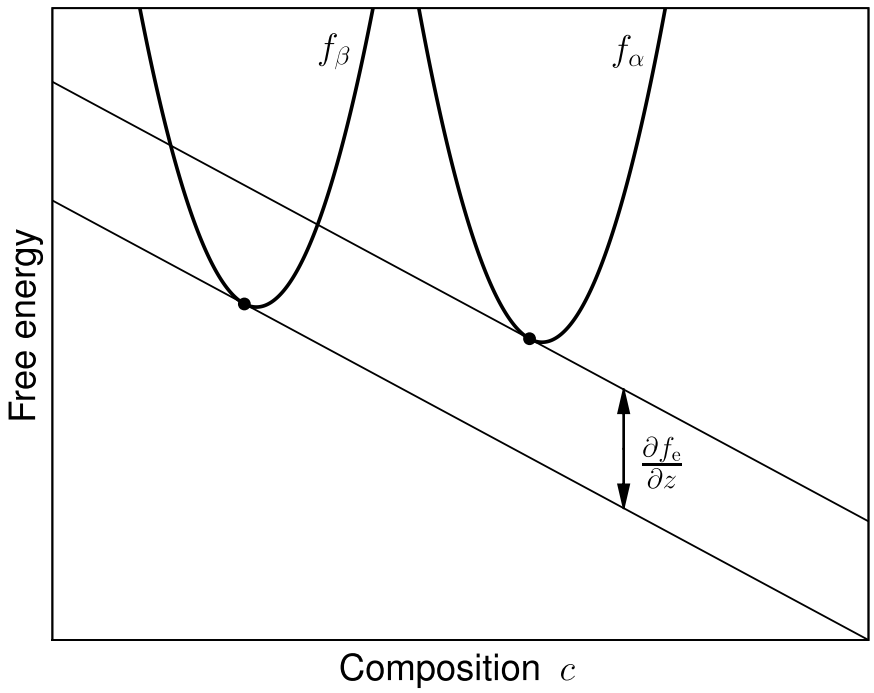

Figure IV.1 : The parallel tangent construction for determining the coexisting phase compositions for a particular value of z, depending on the nominal concentration c_0. The vertical gap between these parallel tangents is equal to $\partial f_e/\partial z$.

where $\mu_{\rm eq}$ is the chemical potential at equilibrium and ω_k the grand potential of phase k defined by $\omega_k = f_k - \mu_{\rm eq}\, c_k$. As shown in Fig. IV.1, Eq. (IV.23) can be interpreted graphically as parallel tangents to the curves f_ϕ vs c, whereas Eq. (IV.24) quantifies the vertical gap between those tangents. When there is no elastic energy, the gap vanishes and the well-known common tangent rule is recovered.

Substituting Eqs. (IV.23–IV.24) into the mass conservation leads to the following expressions for c_α, c_β and z:

$$c_\alpha = a_\alpha + K\,\Lambda \tag{IV.25}$$
$$c_\beta = a_\beta + K\,\Lambda \tag{IV.26}$$
$$z = 1/2 - K/\Delta a \tag{IV.27}$$

where $\Delta a = a_\alpha - a_\beta$, $K = (a_\alpha + a_\beta - 2\,c_0)/[2\,(1-\Lambda)]$ and $\Lambda = 2\,\mathcal{B}/\left(k\,(\Delta a)^2\right)$.

It must be stressed that the equilibrium concentrations and the volume fraction in the phase diagram depend on the elastic energy through Λ and on the average concentration c_0, as explicitly shown by inserting Eq. (IV.27) in the inequality $0 \leq z \leq 1$:

$$a_\beta + \mathcal{B}/\left(k\,\Delta a\right) \leqslant c_0 \leqslant a_\alpha - \mathcal{B}/\left(k\,\Delta a\right) \tag{IV.28}$$

In the particular case where $\varepsilon^\star$ does not follow Vegard's law, the two-phase field can shrink to a single concentration for elastic energies above a threshold called Williams' point (Williams, 1984).

All these features can be summarized on the diagram Λ versus c_0 as shown in Fig. IV.2. In the absence of any elastic effects, the incoherent two-phase equilibrium is obtained and confined to a horizontal segment corresponding to $\Lambda = 0$, and bounded by the equilibrium concentrations

$a_\beta = 0.3$ and $a_\alpha = 0.7$ which are independent of the overall alloy composition c_0.
According to inequality (IV.28), three regions can be plotted in Fig. IV.2. Within the triangle, α and β coexist coherently. The coherent two-phase region spans the ranges $0 < \Lambda < 1$, $a_\beta < c_0 < a_\alpha$ and terminates at Williams' point $(c_0 = 0.5, \Lambda = 1)$. Outside the triangle, the coherent equilibrium between α and β does not occur. Then, beyond Williams' point, i.e. when $\Lambda \geq 1$, only single phase regions are obtained.

IV.3.1.2 Phase field calculations

Phase field calculations using the finite element software ZeBuLon in the generalized plane strain conditions have been performed, with conditions similar to those in Cahn-Larché model. Both phases are purely elastic and possess the same isotropic elastic moduli.
A rectangular region $(0 \leqslant x \leqslant L, 0 \leqslant y \leqslant H)$ has been meshed with linear elements, and the following conditions applied at the boundaries: vanishing order parameter flux, no mass is exchanged with surroundings, and the following boundary conditions were applied to ensure zero average stress

$$\begin{array}{llll} \underline{\boldsymbol{\xi}}.\underline{\boldsymbol{n}} = 0, & \underline{\boldsymbol{J}}.\underline{\boldsymbol{n}} = 0 & & \\ u_x(x=0,y) = 0 & \text{and} \quad u_x(x=L,y) = u_x(L,0) & 0 \leqslant y \leqslant H & \\ u_y(x,y=0) = 0 & \text{and} \quad u_y(x,y=H) = u_y(0,H) & 0 \leqslant x \leqslant L & \end{array} \tag{IV.29}$$

The two boundaries (at $x = L$ and $y = H$) remain straight and a zero resulting force is enforced on the surface. Profiles of ϕ and c as $\tanh$ functions along one direction have been set initially, which correspond to coexisting α and β phases separated by a plane diffuse interface with a thickness roughly equal to δ. This thickness has been chosen to be about one percent of the total size of the system in most of the calculations. The evolution equations are integrated as long as the microstructure evolves with an adaptive time step.
The necessary material data used in the calculations are summarized in Table IV.1. All values are dimensionless and scaled with the chemical free energies curvature k, a mesoscopic length L (typically the system size), and the characteristic time $\tau = \beta/k$ related to the interface motion.

Tableau IV.1 : Data used in the calculations.

E/k	$7 \cdot 10^{10}$	
ν	0.3	
$\gamma/(kL)$	$5 \cdot 10^{-3}$	
δ/L	10^{-2}	
phase	α $(\phi = 1)$	β $(\phi = 0)$
a	0.3	0.7
$D\,\tau/L^2$	0.1	0.1

For each interface behaviour, i.e. Voigt, Reuss and Khachaturyan mixture rules, large series of calculations have been undertaken which span the two-phase field triangle and its boundaries in the diagram Λ versus c_0, by varying the eigenstrain $\varepsilon^\star$ and the average concentration c_0. Each run is represented by one symbol in Fig. IV.2: ▼, • and ○ when phases observed at equilibrium are α, β and $\alpha + \beta$ respectively.
As shown in Fig. IV.2, there is a good agreement between the numerical results using Voigt and Khachaturyan schemes and the theoretical field diagram (Reuss scheme will be discussed below).

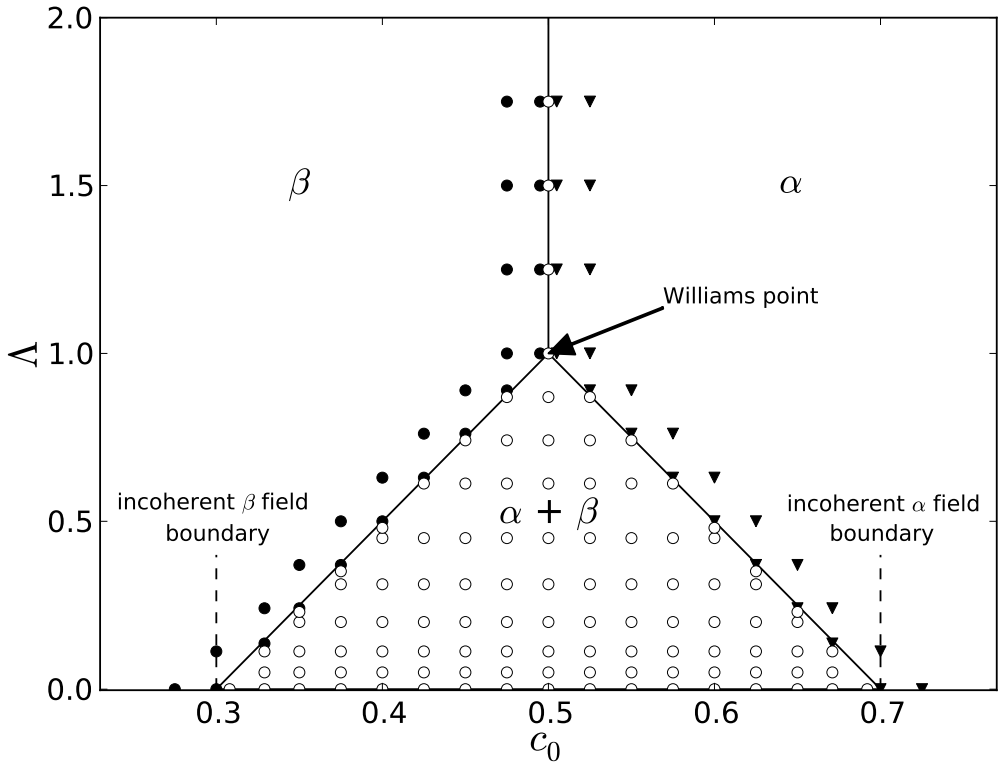

Figure IV.2 : Coherent field diagram showing the two-phase coherent coexistence region in terms of the overall alloy concentration c_0 and the non-dimensional elastic energy Λ. The analytical solution of (Cahn and Larché, 1984) is plotted in continuous lines. The numerical results, using Voigt and Khachaturyan schemes, are plotted with ▼, • and ∘, to locate α, β and $\alpha + \beta$ phase fields respectively.

However, it must be noticed that a slight discrepancy between the numerical and theoretical results appears around Williams point. This can be attributed to the finite thickness of the interface region. Indeed, increasing this thickness changes the scaling factor between f_e and its quadratic dependence $z\,(1-z)$, as shown in Fig. IV.3.

The variation of the equilibrium concentrations c_α and c_β with the average composition c_0 is shown in Fig. IV.4 for different values of Λ. The numerical results obtained with Voigt/Taylor and Khachaturyan schemes are in very good agreement with the analytical solution obtained with Eq. (IV.26). On the contrary, Reuss scheme predicts that the compositions of the two coexisting phases are always equal to their values at incoherent equilibrium ($c_\beta = 0.3$ and $c_\alpha = 0.7$) whatever the value of Λ. Indeed, using Reuss' scheme, there can be no effect of coherency stresses on the two-phase equilibria as shown in section III.4.5. Hence, the numerical results clearly show that this scheme is unsuitable to predict realistic coherent equilibrium conditions.

Figure IV.5 displays variation of the volume fraction with the average composition c_0, for different values of Λ. When $0.3 < c_0 < 0.7$, the mole fraction z changes continuously, showing that the coexisting phase region is reduced when the lattice mismatch between the phases increases. As it can be seen in Fig. IV.5, Voigt and Khachaturyan methods are again in accordance with the analytical solution, given by (IV.27). However, using Reuss scheme, the volume fraction z rises linearly with c_0 in agreement with the lever rule for any value of Λ. This is in accordance with the earlier results (Fig. IV.4), in which the two phases retain constant composition given by the incoherent equilibrium. This again makes Reuss model unacceptable for coupling mechanics and phase transformation.

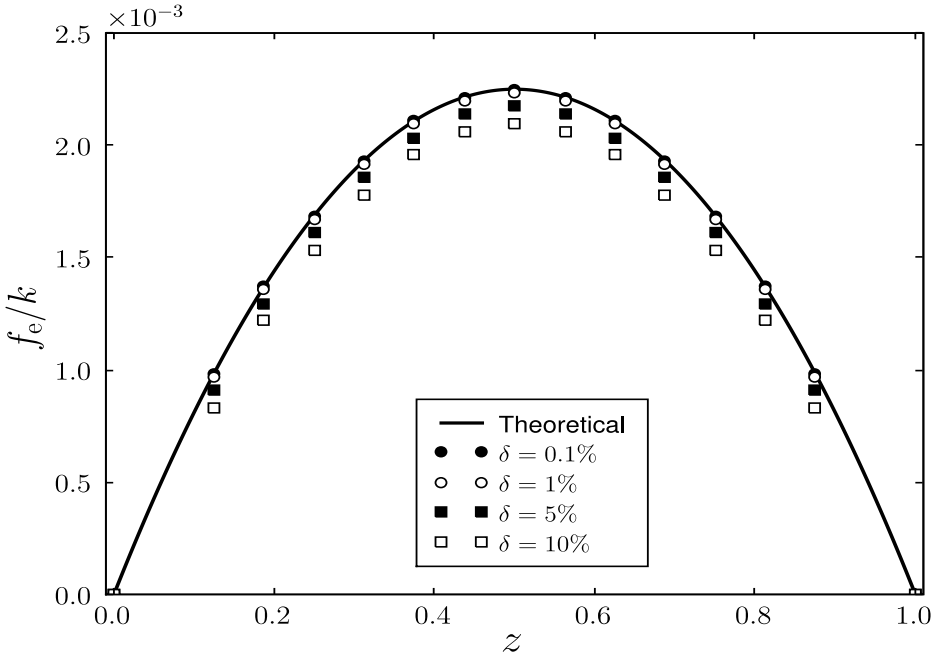

Figure IV.3 : Scaled elastic energy f_e/k versus volume fraction z for different diffuse interface scaled thicknesses $\delta = 10^{-3}$, 10^{-2}, $5 \cdot 10^{-2}$ and 0.1. Equivalent numerical results were obtained using the various homogenization schemes.

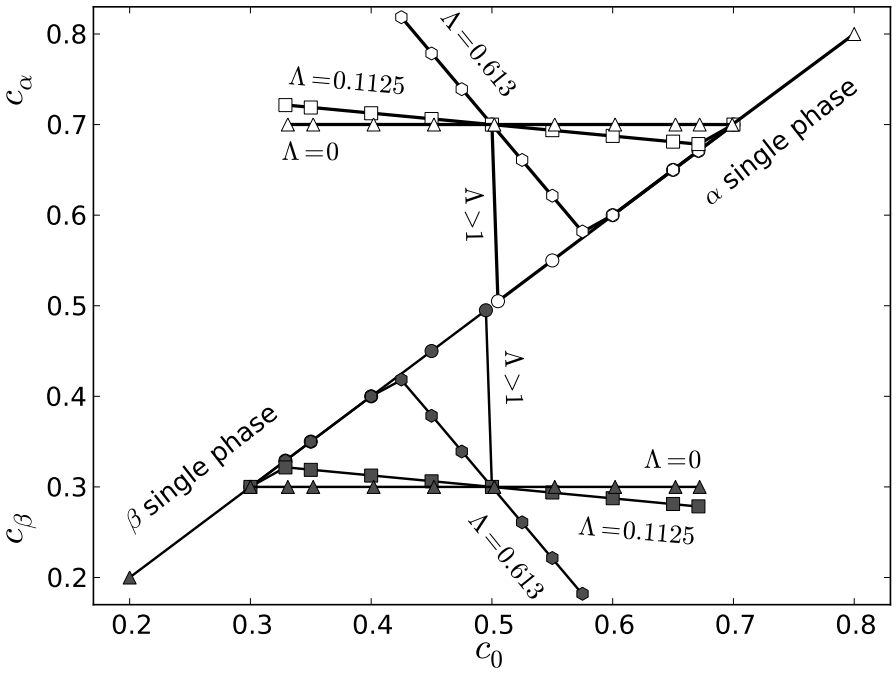

Figure IV.4 : Dependency of the equilibrium phase compositions c_α and c_β on the average alloy concentration c_0 for $\Lambda = 0$ (unstressed case), $\Lambda = 0.1125$ $\Lambda = 0.613$ and $\Lambda = 1$ (Williams point). The continuous lines depicts the analytical solution given by Eq. (IV.26). Symbols are for Voigt and Khachaturyan schemes. Reuss scheme is identical to these schemes with $\Lambda = 0$, whatever the values of Λ.

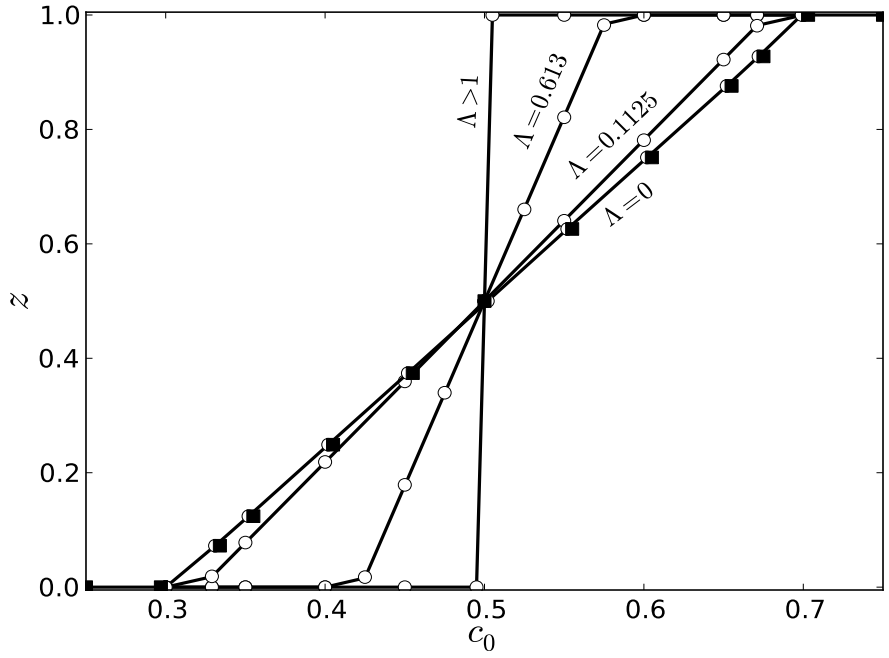

Figure IV.5 : Comparison of analytical/numerical results for the volume fraction evolution z as a function of overall concentration c_0 for $\Lambda = 0,\ 0.1125,\ 0.613$ and 1. The analytical solution, which is given by (IV.27), is represented by the continuous lines. open symbols correspond to numerical results, obtained by Voigt/Taylor and Khachturyan models respectively. The numerical results obtained with these two models are strictly equivalent. Black symbols correspond to Reuss/Sachs results.

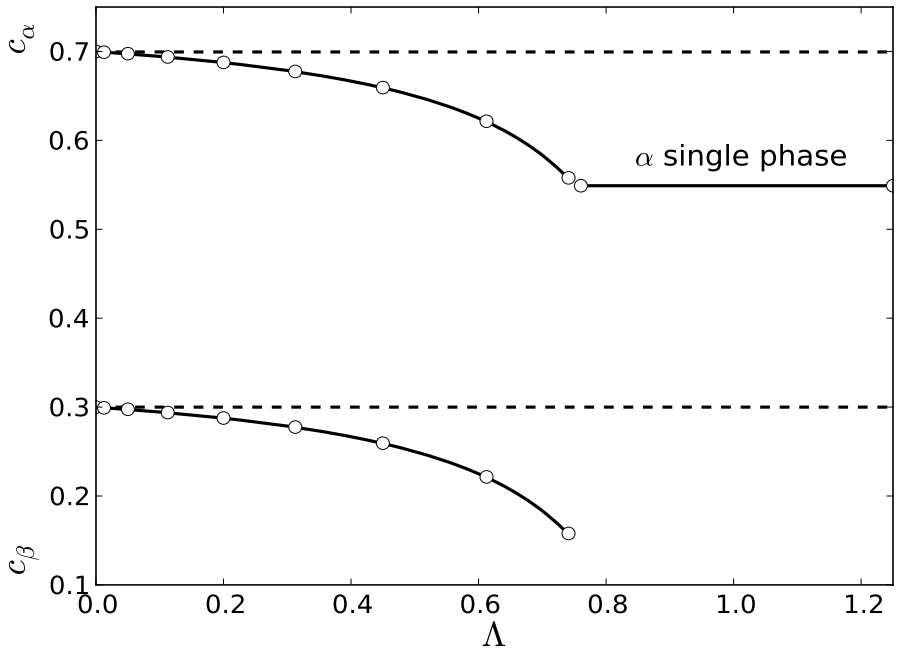

Figure IV.6 : Equilibrium concentrations c_α and c_β versus the scaled elastic energy Λ for $c_0 = 0.55$. The analytical solution Eq. (IV.26) is plotted with continuous lines. Numerical results using Voigt/Taylor and Khachaturyan are with open circles. Reuss/Sachs scheme is plotted with dashed lines.

When $c_0 < 0.3$ or $c_0 > 0.7$, two phases cannot coexist in coherent equilibrium. Thus, the volume fraction is independent of overall alloys composition c_0 and take two values; z=0 and z=1 to indicate the presence either of single phase β or of single phase α respectively.

Coherent equilibria present a singular behaviour in the two-phase domain: equilibrium concentrations defining the tie-lines do not coincide with the boundaries of the two-phase domain. To illustrate this particularity, figure IV.6 depicts how the equilibrium concentrations change with the scaled elastic energy Λ for $c_0 = 0.55$. The numerical results obtained with Voigt and Khachaturyan schemes agree well with the analytical solution. When $\varepsilon^\star > 0.249$, α and β no longer coexist in coherent equilibrium and α only is observed. Moreover, the inability of Reuss scheme to give a consistent description of interface appears clearly in Fig. IV.6. With this scheme, there is indeed no coupling between elastic stress and chemical equilibrium. Whatever the elastic energy, the two-phase field throughout the two-phase region, the two phases retain constant composition; $c_\beta = 0.3$ and $c_\alpha = 0.7$.

IV.3.2 Coherent phase equilibria: Effect of composition-dependent elastic strain

IV.3.2.1 Analytical solutions

In this section, phase equilibrium in a two-phase stressed coherent solid is investigated when lattice parameter, hence coherency strain, is taken to be a function of phase composition. As a rule phase transformation in solids are accompanied by crystal lattice rearrangements. During microstructure evolution, the stress-free strain is related to two principal processes, which can occur in material: the crystal lattice site displacement when the atomic arrangement of the transformed crystal lattice is different from that of the reference phase (IV.13) and the lattice mismatch between both phases, which have different lattice parameters (Khachaturyan, 1983). According to Vegard's law, the lattice parameter variation responsible for the strain is assumed to be a linear function of phase composition with respect to a reference state. Hence, the eigenstrain tensor can be expressed using the concentration field as:

$$\underset{\sim}{\boldsymbol{\varepsilon}}^\star = \varepsilon_0^\star (c_\alpha - c_\beta)\underset{\sim}{\mathbf{1}} \tag{IV.30}$$

where $\varepsilon_0^\star$ represent the linear mismatch between the phases with respect to a reference state, defined by:

$$\varepsilon_0^\star = \frac{2\,(a_\alpha - a_\beta)}{a_\alpha + a_\beta} \tag{IV.31}$$

and a_α and a_β are respectively the equilibrium lattice parameters of the α and β phases.

Assuming that both phases have the same curvatures constant ($k_\alpha = k_\beta = k$) and the same linear isotropic elastic constants, which are independent of the phase composition, the elastic strain energy f_e is given by the Bitter-Crum theorem as shown in the previous section:

$$f_e = z(1-z)\frac{E\,(\varepsilon^\star)^2}{1-\nu} = z(1-z)\Lambda(c_\alpha - c_\beta)^2 \quad \text{with} \quad \Lambda = \frac{E\,(\varepsilon_0^\star)^2}{1-\nu} \tag{IV.32}$$

In order to find the expression of c_α, c_β and z, the minimization of the free energy is conveniently performed by applying the Lagrange method. Introducing a multiplier λ into the equation of local conservation of mass (IV.17), subtracting from the expression of the free energy density (IV.32) and setting the derivatives with respect to c_α, c_β and z to zero, we deduce:

$$\frac{\partial \mathcal{L}}{\partial c_\alpha} = z\,k\,(c_\alpha - a_\alpha) + 2z(1-z)\Lambda(c_\alpha - c_\beta) - \lambda\,z \;=\; 0 \tag{IV.33}$$

$$\frac{\partial \mathcal{L}}{\partial c_\beta} = (1-z)\,k\,(c_\beta - a_\beta) - 2z(1-z)\Lambda(c_\alpha - c_\beta) - \lambda\,(1-z) \;=\; 0 \tag{IV.34}$$

$$\frac{\partial \mathcal{L}}{\partial z} = \frac{1}{2}\,k\,(c_\alpha - a_\alpha)^2 - \frac{1}{2}\,k\,(c_\beta - a_\beta)^2 + (1-2z)\,\Lambda\,(c_\alpha - c_\beta)^2 - \lambda(c_\alpha - c_\beta) \;=\; 0 \tag{IV.35}$$

$$\frac{\partial \mathcal{L}}{\partial \lambda} = z\,c_\alpha + (1-z)\,c_\beta - c_0 \;=\; 0 \tag{IV.36}$$

Equations (IV.33-IV.36) are four algebraic equations in four unknowns (c_α, c_β, z and $\mathcal{L}$). The expressions of the equilibrium compositions c_α, c_β and the volume fraction z can be expressed as follows (details are provided in Appendix F):

$$c_\alpha \;=\; a_\alpha - \Delta a\,[1-K] \tag{IV.37}$$

$$c_\beta \;=\; a_\beta + \Delta a\,[1-K] \tag{IV.38}$$

$$z \;=\; \frac{1}{2} - \frac{\mathcal{B}}{K\Delta a} \tag{IV.39}$$

where $\Delta a = (a_\alpha - a_\beta)/2$, $K = \dfrac{k}{k+2\Lambda}$ and $\mathcal{B} = (a_\alpha + a_\beta - 2\,c_0)/4$

If lattice parameter depends linearly on phase composition following Vegard's law, the equilibrium coherent phase compositions are found to be independent of the bulk alloy composition, where the limit on the range of this latter, by applying the inequality (IV.16) to equation (F.11), is

$$a_\beta + \Delta a\,(1-K) \leqslant c_0 \leqslant a_\alpha + \Delta a\,(K-1) \tag{IV.40}$$

IV.3.2.2 Numerical calculations

In order to investigate the influence of a composition-dependent coherency strain and the alloy composition on coherent phase equilibria and, also on the equilibrium phase compositions, several calculations have been performed, by varying the eigenstrain $\varepsilon^\star$ and the average concentration c_0. The eigenstrain $\varepsilon^\star$ is considered to be a function of the difference in composition between α and β phases, as given by Eq.(IV.31). The initial/boundary conditions and material parameters are the same as in the previous calculation, which is respectively given by (IV.95) and (IV.1).

Figure IV.7 depicts the coherent field-diagram, which indicates the range of conditions over which the same mix of phases coexist in equilibrium, when binary alloy system follows Vegard's law. The axes are the energy ratio Λ and the bulk alloy composition c_0 where the horizontal line, verifying the state without elastic effects ($\Lambda = 0$), corresponds to the incoherent two-phase equilibrium. According to the inequality (IV.40), three domains can exist; α, β and $\alpha+\beta$. Moreover, Williams point, which indicates the termination for the two-phase region, disappears when coherency strain is taken to be a function of phase composition, i.e. the two-phase termination occurs only at an infinite elastic strain. As it can be seen in figure IV.7, there is a good agreement between the numerical coherent phase equilibria using Voigt and Khachaturyan schemes and the theoretical field diagram.

The dependency of the coherent equilibrium phase compositions c_α and c_β on the average alloy concentration c_0 is plotted in Fig. IV.8, for different Λ values, i.e. $\Lambda = 0$, $\Lambda = 0.15$ $\Lambda = 0.525$ and $\Lambda \geq 1$. As it can be seen in this figure, if lattice parameter depends linearly on phase composition following Vegard's law, the equilibrium phase concentrations in a binary alloy

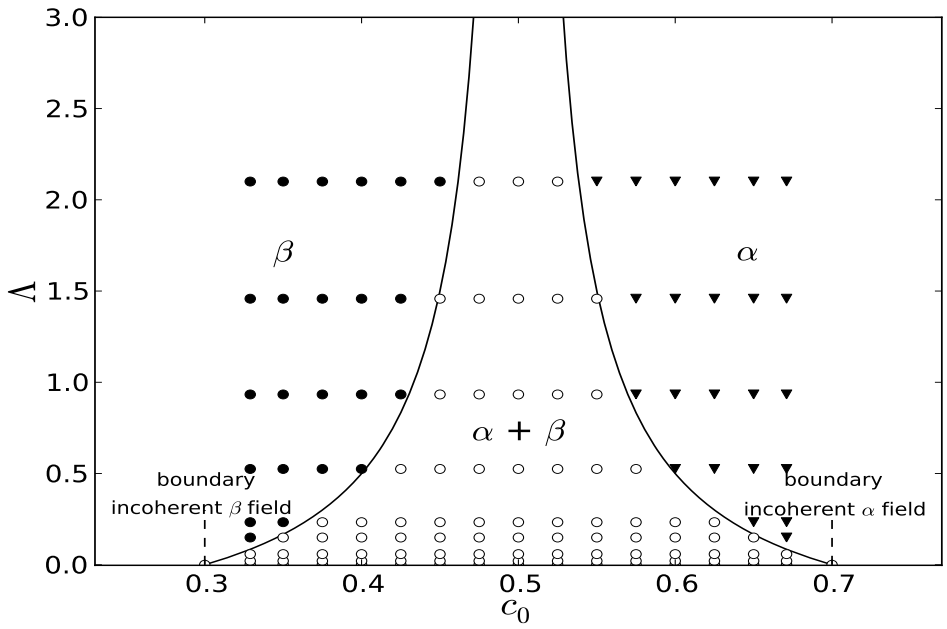

Figure IV.7 : Coherent field diagram in terms of the overall alloy concentration c_0 and the energy radio Λ, for a coherency strain, which taken to be a function of phase composition. The continuous lines correspond to the theoretical field diagram, indicating there is no Williams point for this case. The numerical results are plotted with ▼, • and ○, to represent α, β and $\alpha+\beta$ phase regions respectively.

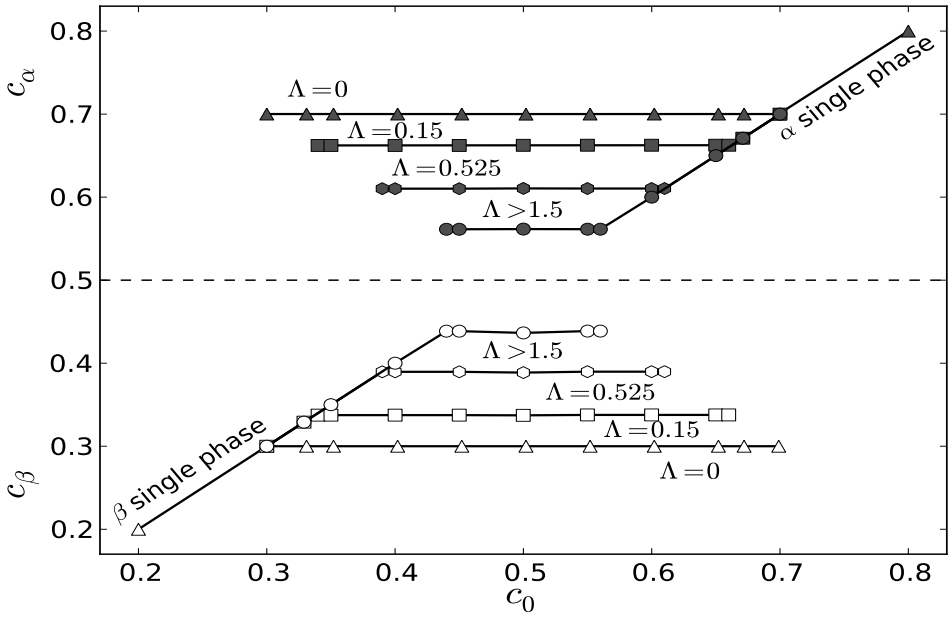

Figure IV.8 : Equilibrium phase compositions c_α and c_β as a function of average alloy concentration c_0 for four different Λ values, i.e, $\Lambda = 0$ (unstressed case), $\Lambda = 0.15$ $\Lambda = 0.525$ and $A \geq 1$. Equilibrium phase concentrations, which are given by Eq.(F.9) and Eq.(F.10) ,are shown to be independent of the alloy composition c_0. The continuous lines depicts the analytical solution and symbols correspond to the obtained with Voigt and Khachaturyan schemes for the different Λ values.

are found to be constant and independent of the alloy composition, for a fixed eigenstrain value. The numerical results, using Voigt and Khachaturyan schemes, are shown to agree quite well with the analytical solutions, which are given by Eq.(F.9) and Eq.(F.10).

IV.4 Modelling of the misfit-generated stress effect on the growth kinetics of an oxide layer

In this section, the attention is focused on the mechanical effect through the phase field on the transformation kinetics of a planar layer growing at the surface of a pure zirconium slab. The study of the oxide layer growth in a purely chemical process, which was presented in the first chapter II.6, is extended here by taking the influence of the misfit generated stress into account.

IV.4.1 Mechanical behavior of the misfitting planar oxide layer problem

First, we shall obtain the mechanical behavior, the interfacial equilibrium conditions and the growth law associated with a misfitting planar oxide layer, considering that both layer and Zr matrix behave in a purely elastic state, i.e. in the absence of plastic relaxation. Choosing the Zr phase as the stress free reference state, the eigenstrain $\varepsilon^{\star}_{\alpha}$, in the phase α, is a spherical tensor independent of concentration:

$$\underset{\sim}{\boldsymbol{\varepsilon}}^{\star}_{\alpha} = \delta_{\mathrm{ZrO_2}}\underset{\sim}{\mathbf{1}} \qquad \text{and} \qquad \underset{\sim}{\boldsymbol{\varepsilon}}^{\star}_{\beta} = \underset{\sim}{\mathbf{0}} \tag{IV.41}$$

where $\underset{\sim}{\mathbf{1}}$ the unit second order tensor.

As shown in Figure IV.9, a parallelepiped slab $(0 \leqslant x \leqslant L, 0 \leqslant y \leqslant H, 0 \leqslant z \leqslant h)$ (of a 1 μm length), has been used, where the mechanical boundary conditions, applied at the boundaries, are the following:

- Free layer surface:

$$\sigma^{\alpha}_{yy}(\forall x, y = 0, \forall z) = 0 \tag{IV.42}$$

- No displacement at the two upper and lower boundaries in the x and z direction.

$$u^{\alpha}_{x}(x = 0, \forall y, \forall z) = u^{\beta}_{x}(x = 0, \forall y, \forall z) = 0 \tag{IV.43}$$
$$u^{\alpha}_{x}(x = L, \forall y, \forall z) = u^{\beta}_{x}(x = L, \forall y, \forall z) = 0 \tag{IV.44}$$
$$u^{\alpha}_{z}(\forall x, \forall y, z = 0) = u^{\beta}_{z}(\forall x, \forall y, z = 0) = 0 \tag{IV.45}$$
$$u^{\alpha}_{z}(\forall x, \forall y, z = h) = u^{\beta}_{z}(\forall x, \forall y, z = h) = 0 \tag{IV.46}$$

- Far away from the interface, no displacement at the external surface of a pure zirconium slab, which is supposed to be semi-infinite

$$u^{\beta}_{y}(\forall x, y = H, \forall z) = 0 \tag{IV.47}$$

Under a purely elastic state, the analytical study on mechanical behaviour of the misfitting planar oxide layer leads to deduce that zero elastic energy stored in the Zr matrix and the stress and strain components in the oxide layer can be expressed as (details are provided in Appendix G):

$$\begin{cases} \sigma^{\alpha}_{xx} = \sigma^{\alpha}_{zz} = -\dfrac{\delta_{\mathrm{ZrO_2}}}{A} \qquad \text{and} \qquad \sigma^{\alpha}_{yy} = 0 \\ \\ \varepsilon^{\alpha}_{xx} = \varepsilon^{\alpha}_{zz} = 0 \qquad \text{and} \qquad \varepsilon^{\alpha}_{yy} = \dfrac{1+\nu_{\alpha}}{E_{\alpha}}\dfrac{\delta_{\mathrm{ZrO_2}}}{A} = \dfrac{1+\nu_{\alpha}}{1-\nu_{\alpha}}\delta_{\mathrm{ZrO_2}} \end{cases} \tag{IV.48}$$

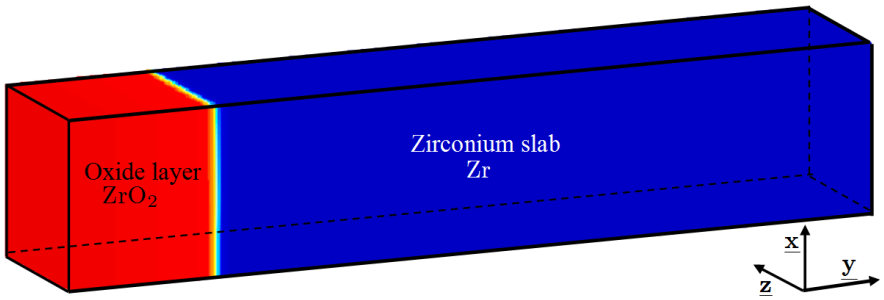

Figure IV.9 : Schematic of the misfitting planar oxide layer (phase α) growing at the surface of a pure zirconium slab (phase β). The unit normal to the interface is in the y direction.

with E_α and ν_α are respectively Young's modulus and Poisson ratio and A is given by

$$A = \frac{\lambda_\alpha + 2\mu_\alpha}{2\mu_\alpha\,(3\lambda_\alpha + 2\mu_\alpha)} = \frac{1-\nu_\alpha}{E_\alpha} \tag{IV.49}$$

where λ_α and μ_α are Lamé's coefficients in α phase.

Based on the previous assumptions, the complete solutions of the same process have been undertaken, assuming ideal plastic behavior for the oxide layer. In absence of a macroscopic applied stress, the Cauchy stress in Zr remains negligible, due to the relative thicknesses of the oxide layer and the bulk material. Hence plastic deformation occurs only in the oxide layer. Using the von Mises yielding criterion, the analytical solution to the problem for the oxide layer is given as:

$$\begin{cases} \sigma^\alpha_{xx} = \sigma^\alpha_{zz} = -\sigma^0_\alpha & \text{and} \quad \sigma^\alpha_{yy} = 0 \\ \varepsilon^\alpha_{xx} = \varepsilon^\alpha_{zz} = 0 & \text{and} \quad \varepsilon^\alpha_{yy} = 3\delta_{ZrO_2} - \dfrac{2(1-2\nu)}{E}\sigma^0_\alpha \\ \varepsilon^{\alpha p}_{xx} = \varepsilon^{\alpha p}_{zz} = -\delta_{ZrO_2} + A\,\sigma^0_\alpha & \text{and} \quad \varepsilon^{\alpha p}_{yy} = 2(\delta_{ZrO_2} - A\,\sigma^0_\alpha) \end{cases} \tag{IV.50}$$

where σ^0_α is the yield stress in the α phase and $\varepsilon^{\alpha p}_{ii}$ is the plastic strain in the i direction.

IV.4.2 Interfacial equilibrium concentration

In order to determine the interfacial equilibrium concentrations of both phases, we recall the two equilibrium conditions at the interface that arise from the assumption of local thermodynamic equilibrium of a stressed solid. The first one requires that the diffusion potentials be uniform everywhere in the system, which is expressed by:

$$\frac{\partial f_\alpha}{\partial c} = \frac{\partial f_\beta}{\partial c} = \mu_{\text{eq}} \tag{IV.51}$$

The second interfacial condition fixes the jump in grand potential ω, across two-phase interface (Johnson and Alexander, 1986):

$$\omega_\beta - \omega_\alpha = \mathcal{E}_{\text{coh}} - \Delta f_e + \kappa\gamma \tag{IV.52}$$

with

$$\mathcal{E}_{\text{coh}} = (\underset{\sim}{\varepsilon}_\beta - \underset{\sim}{\varepsilon}_\alpha) : \underset{\sim}{\boldsymbol{\sigma}}_\beta \qquad \text{and} \qquad \Delta f_e = f_{e\beta} - f_{e\alpha} \tag{IV.53}$$

where κ is the mean curvature of the interface, γ is the interfacial energy and $\mathcal{E}_{\text{coh}}$ represents the elastic energy necessary to keep both lattices coherent across the interface.

It must be noted that in Eq. (IV.24), $\mathcal{E}_{\text{coh}} = 0$. Threfore, equation (IV.24) is a special case of the general equation (IV.52).

Assuming equal free energy curvatures $k_\alpha = k_\beta = k$ and substituting the chemical free energy densities into (IV.51) and (IV.52), the interfacial conditions are then reduced to:

$$c_\alpha - a_\alpha = c_\beta - a_\beta \tag{IV.54}$$

$$k\left(c_\alpha - a_\alpha\right)\left(c_\beta - c_\alpha\right) + f_{e\alpha} - f_{e\beta} = \mathcal{E}_{\text{coh}} \tag{IV.55}$$

From these conditions, the equilibrium concentrations of both phases at the interface are expressed as

$$c_\alpha^{\text{int}} = a_\alpha + \Delta c \qquad \text{and} \qquad c_\beta^{\text{int}} = a_\beta + \Delta c \tag{IV.56}$$

where

$$\Delta c = \frac{\mathcal{E}_{\text{coh}} - \Delta f_{\text{el}} + \kappa\gamma}{k(a_\beta - a_\alpha)} = \frac{\left(\underset{\sim}{\varepsilon}_\alpha^e - \underset{\sim}{\varepsilon}_\beta^e\right) : \underset{\sim}{\boldsymbol{\sigma}}_\beta - \left(f_{e\beta} - f_{e\alpha}\right) + \kappa\gamma}{k(a_\alpha - a_\beta)} \tag{IV.57}$$

Note that due to particular stress-strain field in both phases (IV.48) and (IV.50), zero coherency energy, under purely elastic state and with plastic deformation, is obtained:

$$\mathcal{E}_{\text{coh}} = \left(\underset{\sim}{\varepsilon}_\beta - \underset{\sim}{\varepsilon}_\alpha\right) : \underset{\sim}{\boldsymbol{\sigma}}_\beta = 0 \tag{IV.58}$$

Neglecting the interfacial stress contribution and determining the elastic strain energy inside the oxide layer $f_{e\alpha}$ from Eq. (IV.50), the concentration variation Δc (IV.57), due to the stress effect, is given, under pure elastic behavior and with plastic deformation, by (see Appendix G):

$$\boxed{\begin{array}{ll} \Delta c_{\text{elas}} = c_i^{int} - a_i = \dfrac{\delta_{\text{ZrO}_2}^2}{k\left(a_\alpha - a_\beta\right)A} & \text{Pure elastic behaviour} \\ \\ \Delta c_{\text{plas}} = c_i^{int} - a_i = \dfrac{A(\sigma_\alpha^0)^2}{k\left(a_\alpha - a_\beta\right)} & \text{Elasto} - \text{plastic behaviour} \end{array}} \tag{IV.59}$$

where

$$A = \frac{\lambda_\alpha + 2\mu_\alpha}{2\mu_\alpha\left(3\lambda_\alpha + 2\mu_\alpha\right)} = \frac{1 - \nu_\alpha}{E_\alpha} \tag{IV.60}$$

IV.4.3 Growth kinetics

To express the growth law of oxide layer taking the effect of the misfit generated stress into account, an explicit analytical solution for the profile of the concentration field in both phases is necessary. Indeed, the concentration field in the α phase verifies the Laplace diffusion equation in the oxide layer of thickness e bounded by the surface and the interface. Assuming that the diffusion regime is stationary, the diffusion equation reduces then to:

$$\partial_{yy} c = 0 \tag{IV.61}$$

The interface/boundary conditions for the composition field, which are used for solving the diffusion equation, are:

$$\begin{aligned} &c(\forall x, y = 0, t) = c_\alpha^s = 0.68 \\ &c(\forall x, y = H, t) = c_\infty = 0.22 \\ &c(\forall x, y = r_{int}^-, t) = c_\alpha^{\text{int}} \\ &c(\forall x, y = r_{int}^+, t) = c_\beta^{\text{int}} \end{aligned} \tag{IV.62}$$

where r_{int} denotes the interface position.

The classical linear profile solution of the steady equation (IV.61), for a flat interface is found:

$$c_\alpha = c_\alpha^{\text{int}} + G_\alpha y \tag{IV.63}$$

where $G_\alpha = \dfrac{c_\alpha^s - c_\alpha^{\text{int}}}{e}$ is the concentration gradient in α domain and e the thickness of the oxide layer.

Following the solution of the diffusion problem in a semi-infinite flat domain, the concentration field must verify the second Fick's law. The solution is well-known in a flat semi-infinite medium with Dirichlet boundary conditions:

$$c_\beta = c_\beta^{\text{int}} + (c_\beta^\infty - c_\beta^{\text{int}})\,\text{erfc}(y/(2\sqrt{D_\beta t})) \tag{IV.64}$$

The concentration gradient in β domain at the flat interface is given by

$$G_\beta = (c_\beta^\infty - c_\beta^{\text{int}})/\sqrt{\pi D_\beta t} \tag{IV.65}$$

In order to determine the growth kinetics, we write the solute balance at the plane interface (Appolaire and Aeby-Gautier, 2009):

$$\delta c\,\dot{e} = j_\alpha - j_\beta \tag{IV.66}$$

where $\delta c = c_\alpha^{\text{int}} - c_\beta^{\text{int}}$ and the flux densities $j_\alpha = -D_\alpha G_\alpha$ and $j_\beta = -D_\beta G_\beta$

$$\delta c\,\dot{e} = D_\beta(c_\beta^\infty - c_\beta^{\text{int}})/\sqrt{\pi D_\beta t} + D_\alpha \frac{c_\alpha^{\text{int}} - c_\alpha^s}{e} \tag{IV.67}$$

Making use of the following notations:

$$F_\alpha = D_\alpha \Omega_\alpha/2 > 0 \qquad \text{and} \qquad F_\beta = \sqrt{D_\beta}\Omega_\beta/\sqrt{2\pi} > 0 \tag{IV.68}$$

where the non-dimensional diffusion driving forces are defined as

$$\Omega_\beta = (c_\beta^\infty - c_\beta^{\text{int}})/\delta c \qquad \text{and} \qquad \Omega_\alpha = (c_\alpha^{\text{int}} - c_\alpha^s)/\delta c \tag{IV.69}$$

Thus, the solute balance at the plane interface (IV.66) becomes

$$\frac{1}{2}\delta c\,\dot{e} = -\frac{F_\alpha}{\sqrt{t}} + \frac{F_\beta}{e} \tag{IV.70}$$

When $|D_\alpha G_\alpha| > |D_\beta G_\beta|$, i.e. in the growth case, integration of (IV.70) gives

$$e = K\sqrt{(t)} \tag{IV.71}$$

where

$$K = -F_\beta + \sqrt{F_\beta^2 + 4F_\alpha} \tag{IV.72}$$

IV.4.4 Numerical results

The proposed model has been used to investigate the elastic energy effect on the transformation kinetics of the oxide layer, where the numerical results have been validated against corresponding sharp interface analytical solutions. The finite element mesh, the initial/boundary conditions for the concentration and order parameter and the chemical data are identical to the calculation in the first chapter, section II.6. Moreover, the elastic moduli and Poisson ratio are taken as $\mathsf{E}_{ZrO_2} = 200\text{GPa}$, $\mathsf{E}_{Zr} = 68\text{GPa}$ and $\nu_{ZrO_2} = \nu_{Zr} = 0.3$. The growth mechanism of the oxide

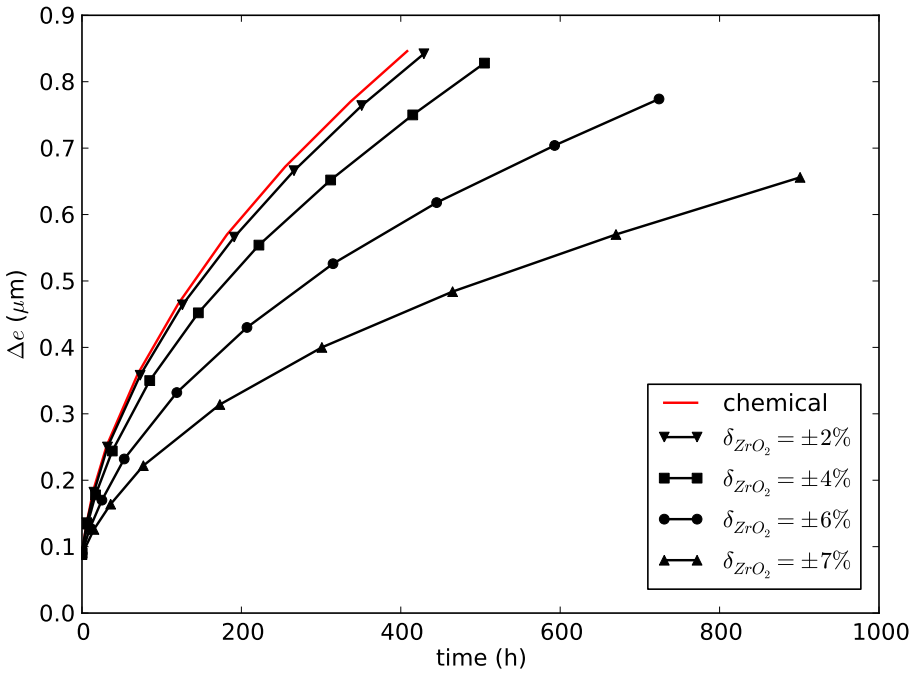

Figure IV.10 : The growth kinetics of the oxide layer for different dilatation misfits in the oxide layer, choosing Zr matrix as the stress free reference state ($\delta_{\mathrm{Zr}} = 0$). Simulations have been performed for four different dilatation misfits $\delta_{ZrO_2} = 2\%, 4\%, 6\%, 7\%$, for the same boundary value problem and material parameters. The pure chemical case is taken as the reference kinetic, which is plotted by a red continuous line.

layer has been studied considering the effects of the misfit generated stress and the oxide elasticity moduli. Finite element calculations have been performed for four different dilatation misfits in the ZrO_2 oxide; $\delta_{ZrO_2} = 2\%, 4\%, 6\%, 7\%$, for the same boundary value problem and material parameters, in order to determine how the magnitude and sign of the misfit strain is crucial on the growth laws of oxide layer. The corresponding time evolutions of the oxide thickness e are plotted in Fig. IV.10. These curves are deduced from the order parameter profiles, at different instants, by tracking the position of $\phi = 0.5$. Taking the pure chemical case as the reference kinetic, which has been presented in section II.6, misfit strain in the oxide leads to slower transformations, as shown in Fig IV.10. Indeed, the oxide growth is decelerated by the increase of the misfit strain.

According to Eq. (IV.56), the effect of dilatational misfit is to raise the equilibrium interfacial concentrations in both phases due to the positive concentration variation Δc_{elas} (IV.59), causing then an increase in the oxide concentration gradient G_α and a decrease in the matrix concentration gradient G_β. Consequently, the profile in the concentration field in the α layer flattens and the flux of oxygen j_α, arriving at the interface from the surface is then decreased. On the contrary, the flux leaving the interface toward the matrix is enhanced and the concentration profile in Zr matrix is steeper. This analysis is coherent with the numerical results. The growth law, for the different misfits, is parabolic, which verifies the solution (IV.71), where decreasing growth constant (IV.72) with increasing of the misfit. For explaining the dependency of the kinetic constants on the misfit, figure IV.11 depicts the corresponding kinetics constants K, for the different growth laws presented in Fig. (IV.10) normalized by the pure chemical case as a function of the dilation misfit. The kinetic growth constant is symmetric with respect to the misfit, seeing that the deviations from the planar equilibrium concentrations depend only on the elastic energies which are proportional to the square of $\delta_{\mathrm{ZrO_2}}$ (IV.59).

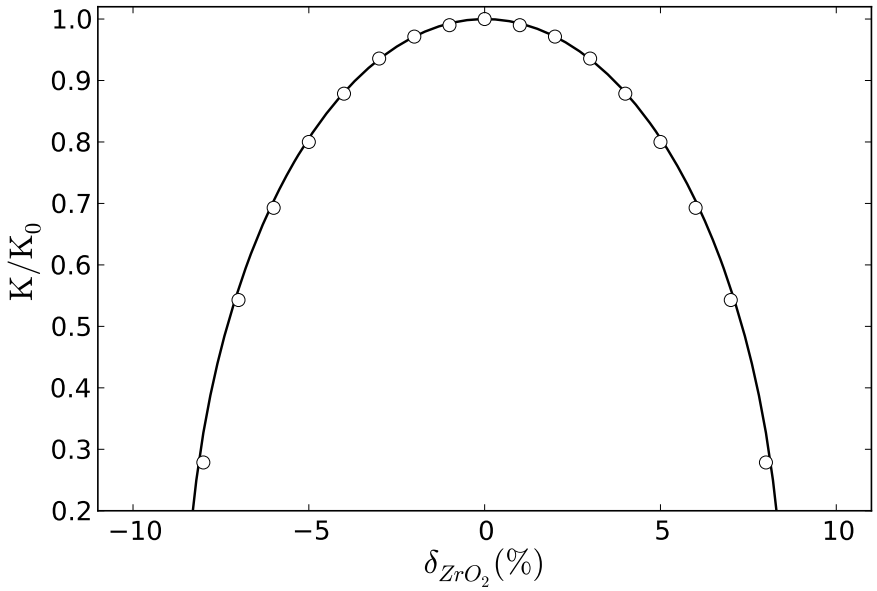

Figure IV.11 : Kinetic constants K normalized by the unstressed (pure chemical) case K_0 versus the dilation misfit. The open symbols correspond to the kinetic constants, related to the oxide layer growth in Fig. IV.10. The continuous black line depicts the analytical solution, given by Eqs. (IV.56) and (IV.72).

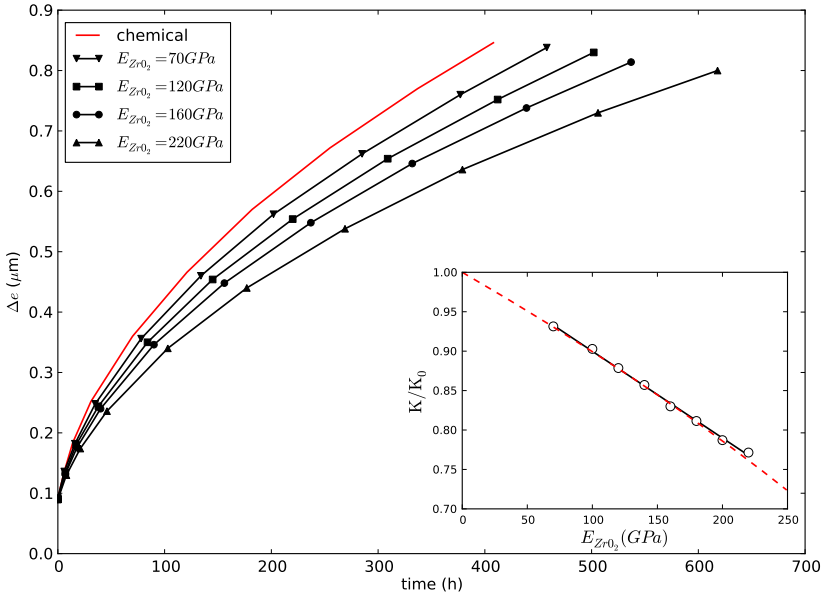

Figure IV.12 : The growth kinetics of the oxide layer for different oxide Young's moduli $E_{\mathrm{ZrO_2}}$; $E = 70, 120, 160, 200$ GPa, taking the Young's modulus of Zr matrix as E_{Zr}=70GPa. The pure chemical case is represented by a red continuous line. Inset shows the dependency of the corresponding kinetic constants K of these different growth laws normalized by the pure chemical case K_0 on $E_{\mathrm{ZrO_2}}$. open symbols corresponds to the numerical results. The analytical solution, which is given by Eqs. (IV.56) and (IV.72), is plotted by the red discontinuous line.

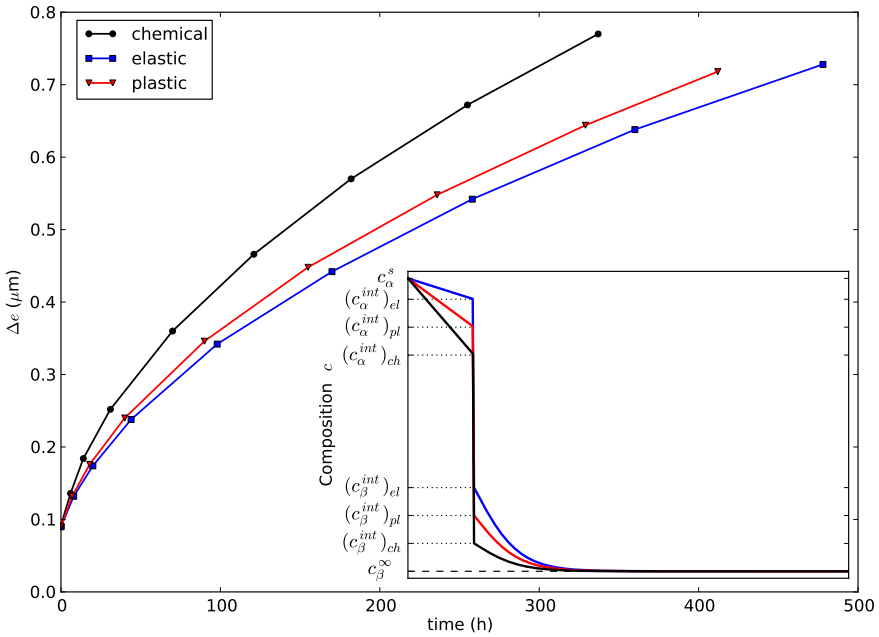

Figure IV.13 : The growth kinetics of ZrO_2 oxide layer in the infinite unstressed Zr matrix. Simulations have been performed for three different cases, assuming a chemical, elastic and ideal plastic behaviour for oxide layer. Inset shown a schematic illustration of the composition profiles in both matrix and oxide layer, for the three different growths, shown in Fig. (IV.13)

The quantitative analysis of the elastic energy effect on the transformation kinetics of the oxide layer growth was carried out here using different oxide Young's moduli E_{ZrO_2}; i.e. $E = 70, 120, 160, 200$ GPa. As shown in Fig. IV.12, the increase in the oxide Young's modulus, i.e. increase in the elastic strain energy, leads to a deceleration of the growth. This is in accordance with the earlier results of Fig. IV.10. A positive concentration variation Δc_{elas} (IV.59), due to the elastic energy effect, is added to the equilibrium concentrations at the interface in both phases, which induces an enhancement in the oxide concentration gradient with a lowering in the matrix supersaturation. A careful examination of the solute balance at the plane interface (IV.66) proves the slowdown of the oxide growth. The inset of Fig. (IV.12) displays the dependency of the corresponding kinetic constant K of these different growth laws normalized by the pure chemical case K_0 on the elasticity modulus E_{ZrO_2}. As it can be seen in this inset, the numerical result proved to agree quite well with the analytical solution, given by Eqs. (IV.56) and (IV.72), where kinetic growth constants decrease linearly with the elasticity modulus, i.e. with the elastic strain energy.

The main result of the oxide growth study, under pure elastic state, is that the parabolic growth law continues to be valid, taking the misfit generated stress into account, but the growth kinetic coefficient depends on (i) dilatation misfit, (ii) the elastic modulus of the oxide layer, which decreases linearly with E_{ZrO_2} and $\delta^2_{ZrO_2}$.

To investigate the effect of plastic accommodation processes on the transformation kinetics, compared with the corresponding pure elastic state and pure chemical transformation, a finite element calculation of the same process has been performed, assuming ideal plastic behaviour for the oxide layer in α phase, growing in the infinite Zr-O binary system. Figure IV.13 shows the time evolution of the oxide thickness e for the three cases, assuming a chemical, elastic and ideal plastic behaviour for α phase. As it can be seen in this figure, parabolic law describes the oxide thickness growth for the three cases with different kinetic constants.

For explaining the different growth rates, shown in Fig. IV.13, we examine the interfacial equilibrium compositions in both phases (IV.56). Adopting the von Mises yield criterion (G.25), which assumes that yielding occurs when the equivalent stress σ_{eq} exceeds the yield stress σ_α^0 and using Eqs. (IV.48,IV.50) , the general form of the plasticity criterion reads:

$$f(\underset{\sim}{\boldsymbol{\sigma}}) = |\sigma_{xx}^\alpha| - \sigma_\alpha^0 = \frac{\delta_{\mathrm{ZrO_2}}}{A} - \sigma_\alpha^0 \leqslant 0 \tag{IV.73}$$

where

$$A = \frac{\lambda_\alpha + 2\mu_\alpha}{2\mu_\alpha\left(3\lambda_\alpha + 2\mu_\alpha\right)} = \frac{1-\nu_\alpha}{E_\alpha} \tag{IV.74}$$

Rearranging Eq.(IV.59) with the above relation, we then deduce:

$$\frac{\Delta c_{\mathrm{elas}}}{\Delta c_{\mathrm{plas}}} \leqslant 1 \tag{IV.75}$$

Consequently, the plastic relaxation of the stresses, due to misfitting oxide layer induces a lowering in the interfacial equilibrium compositions in both phases compared to pure elastic state, causing therefore rise in the supersaturation in the oxide G_α as well as decrease in the matrix concentration gradient G_β. This explanation can be clearly seen in the inset of Fig. IV.13, where the stress effect on the change of the equilibrium interfacial compositions is plotted for the three different cases, i.e. assuming a chemical, elastic and ideal plastic behaviour for oxide layer. This figure illustrates the different growths, plotted in Fig IV.13.

IV.5 Growth of an isotropic misfitting cylindrical precipitate in an isotropic matrix

To validate the numerical finite element implementation and to illustrate the ability of the proposed model to handle precipitation together with mechanical contribution effect, the case of a single misfitting cylindrical precipitate growing in an isotropic matrix is investigated. The misfit is taken as purely dilatational in precipitate, denoted by $\varepsilon^\star$. The discussion here is limited to the pure elastic state for both phases assuming isotropic homogeneous phases

IV.5.1 Elastic analysis

Finite matrix case

The mechanical analysis for this problem is presented in terms of a cylindrical coordinate system, $r\theta z$. The origin of the cylindrical coordinate system coincides with the center of the cylinder, where the $z-$axis runs the length H and the outer radius is R (Figure IV.14).

The equilibrium conditions at a fully coherent interface, obtained from the thermodynamics of stressed solid, imply that there is continuity of both displacement and radial traction σ_{rr} across the α-β interface between both phase, which are:

$$u_r^\alpha(r = r_{int}) = u_r^\beta(r = r_{int}) \tag{IV.76}$$
$$\sigma_{rr}^\alpha(r = r_{int}) = \sigma_{rr}^\beta(r = r_{int}) \tag{IV.77}$$

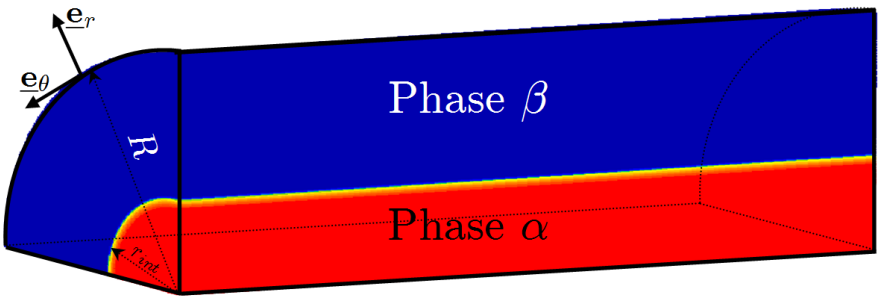

Figure IV.14 : Schematic of the cylindrical α precipitate of radius r_{int}, in the β matrix, with an outer radius R. The matrix-precipitate system is presented in terms of a cylindrical coordinate, $r\theta z$ where the origin of the cylindrical coordinate system coincides with the center of the cylinder and the $z-$axis runs the length H.

Moreover, the following mechanical boundary conditions to the system have been applied:

$$\begin{aligned}
&\sigma^{\beta}_{rr}(r=R)=0 && \text{: Free surface at } r=R\\
&u^{\alpha}_{r}(r=0)=0 && \text{: No displacement at the axis } r=0\\
&u^{\alpha}_{z}(z=0)=u^{\beta}_{z}(z=0)=0 && \text{: No displacement at the axis } z=0\\
&u^{\alpha}_{z}(z=h)=u^{\beta}_{z}(z=h) && \text{: Upper boundary at } z=H \text{ remains plane}
\end{aligned} \tag{IV.78}$$

The analytical expression of the stress fields in both elastic precipitate and matrix are expressed explicitly in the following form (details are provided in Appendix H):

$$\begin{cases}
\sigma_{rr}=\sigma_{\theta\theta}=\left[\left(\dfrac{r_{int}}{R}\right)^2-1\right]p_e & r\leqslant r_{int}\\[2ex]
\sigma_{rr}=\left[\left(\dfrac{r_{int}}{R}\right)^2-\left(\dfrac{r_{int}}{r}\right)^2\right]p_e,\quad \sigma_{\theta\theta}=\left[\left(\dfrac{r_{int}}{R}\right)^2+\left(\dfrac{r_{int}}{r}\right)^2\right]p_e & r\geqslant r_{int}\\[2ex]
\sigma_{zz}=\sigma_{rr}+\sigma_{\theta\theta}
\end{cases} \tag{IV.79}$$

where $p_e=\dfrac{E\varepsilon^\star}{2(1-\nu)}$ and r_{int} is the interface position.

Under the assumption of plane strain, the axial stress σ_{zz} is given by the following relation:

$$\sigma_{zz}=\nu(\sigma_{rr}+\sigma_{\theta\theta}) \tag{IV.80}$$

The complete general solutions to the displacement, stress and strain fields for an isotropic misfitting cylindrical precipitate are provided in Appendix H.

Infinite matrix case

Considering the case of an infinite matrix containing a single cylindrical precipitate, the analytical solution of the stress field in both phases, under pure elastic state, are extended from Eq. (IV.79) assuming an infinite radius

$$\begin{cases}
\sigma_{rr}=\sigma_{\theta\theta}=\dfrac{1}{2}\sigma_{zz}=-p_e \quad \text{inside the particle} & r\leqslant r_{int}\\[2ex]
\sigma_{rr}=-\sigma_{\theta\theta}=-p_e\left(\dfrac{r_{int}}{r}\right)^2 \quad \text{and} \quad \sigma_{zz}=0 & r_{int}\leqslant r
\end{cases} \tag{IV.81}$$

IV.5.2 Numerical calculations against the analytical solutions

The calculation has been performed using the Voigt/Taylor model, since Reuss model has been shown to be inappropriate. The mechanical analysis of the isotropic cylindrical particle growing in a cylindrical matrix β is, firstly, simulated under generalized plane strain conditions. This means that the planes normal to the axis of the cylinder remain planar. Then, another calculation is carried with an assumption of plane strain. The necessary material data used in the calculations are summarized in Table IV.5.2. All parameters are dimensionless and scaled with the chemical free energy curvature k, a mesoscopic length L (typically the system size), and the characteristic time $\tau = \beta/k$ related to the interface motion, where E is the elasticity modulus, ν is Poisson's ratio and D is the chemical diffusivity, that is chosen to be the same in both phases. The interfacial energy and thickness are respectively denoted by γ and δ.

Tableau IV.2 : Data used in the calculations.

E/k	ν	$\gamma/(kL)$	δ/L	$D\tau/L^2$	σ^0_α/k	a_α	a_β
$7 \cdot 10^4$	0.3	$1 \cdot 10^{-4}$	0.1%	$4 \cdot 10^{-9}$	12.5	0.7	0.3

The finite element mesh is composed of quadratic 8-node quadrangular elements, as shown in Fig. IV.15. The following boundary conditions to the system have been applied:

$$\begin{array}{lll} \underline{\boldsymbol{\xi}}.\underline{\boldsymbol{n}} = 0, & \underline{\boldsymbol{J}}.\underline{\boldsymbol{n}} = 0 & \text{on all boundaries} \\ \underset{\sim}{\boldsymbol{\sigma}}(r = R, \theta) = 0 & 0 \leqslant \theta \leqslant \theta_0 & \text{: free surface condition} \\ u_\theta(r, \theta = 0) = 0 & 0 \leqslant r \leqslant R & \\ u_\theta(r, \theta = \theta_0) = 0 & 0 \leqslant r \leqslant R & \text{: symmetric boundary condition} \end{array} \tag{IV.82}$$

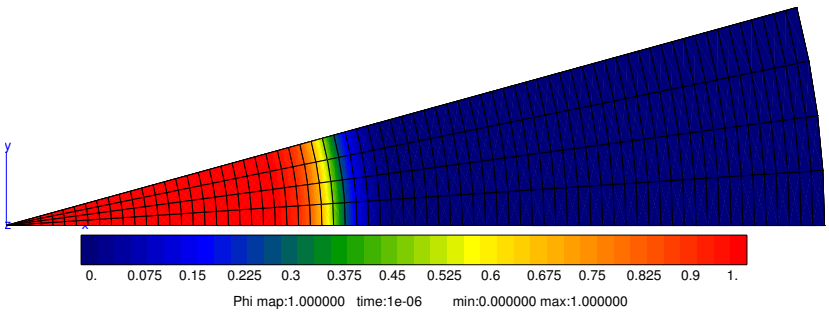

Figure IV.15 : Initial phase field following a variation in $\tanh$ along the cylinder radius in a 2D finite element mesh.

The lower and upper boundaries at $\theta = 0$ and $\theta = \theta_0$ remain straight. Radial profiles as $\tanh$ functions have been imposed initially for ϕ and c, corresponding to the presence of a cylindrical α precipitate in the β matrix with an initial radius $r_0/R = 0.3$, where R is the total radius of the cylindrical system. This initial condition ensures that the precipitate will grow, at least in a pure elastic case, according to Cahn-Larché's coherent diagram.

Figures IV.16 and IV.17 depict the time evolution of the concentration and the stress distributions, σ_{rr}, $\sigma_{\theta\theta}$ and σ_{zz} in a radial direction from the origin of the particle, during the growth of a misfitting cylindrical precipitate in a finite supersaturated matrix, respectively under generalized plane strain and plane strain conditions. The shear components are identical to 0. As shown in these figures with the vertical dotted lines corresponding to the level set $\phi = 0.5$, the interface moves forwards to higher values of r: the precipitate grows at the expense of the β

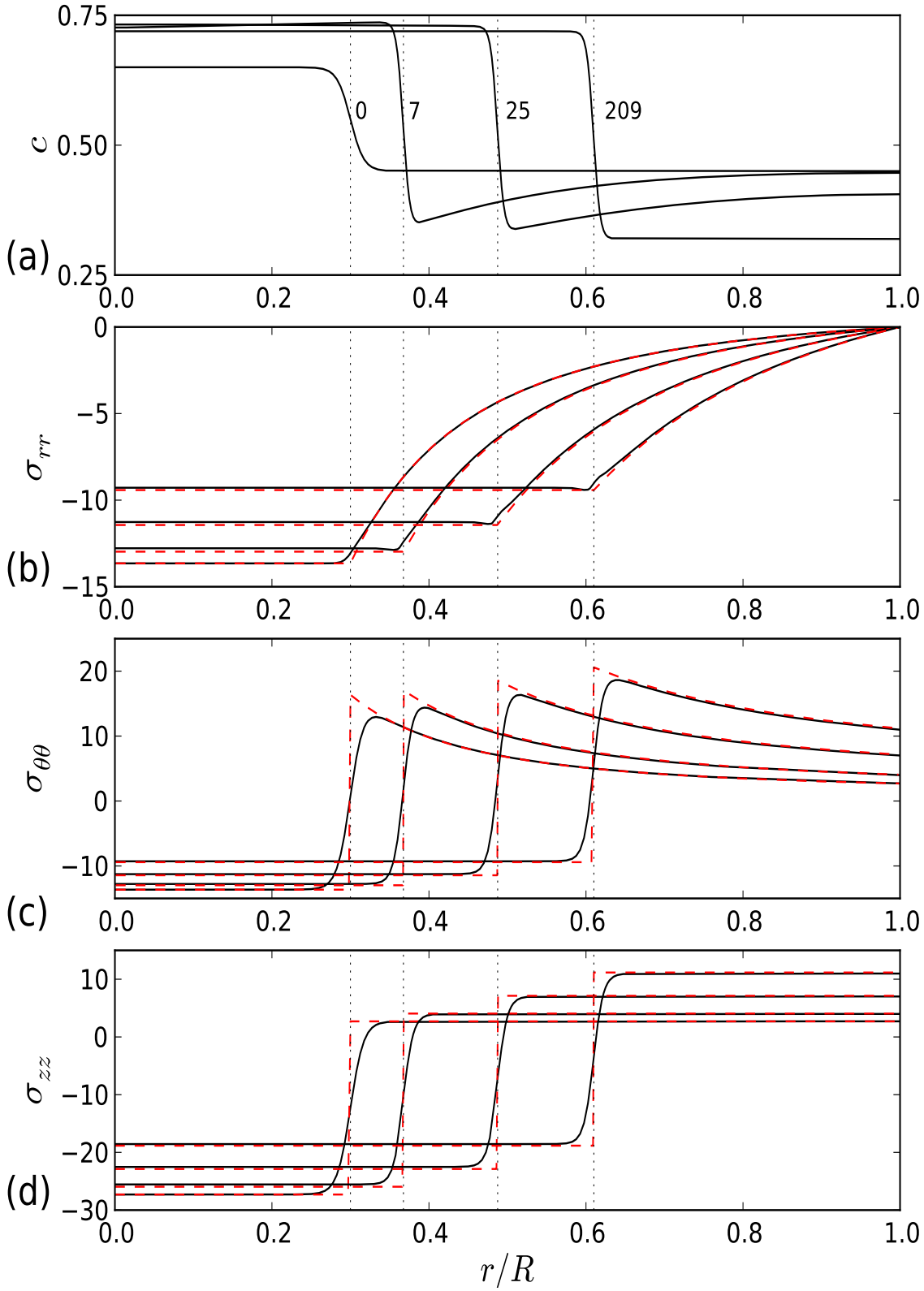

Figure IV.16 : Time evolution of the (a) concentration field, (b) radial stress σ_{rr}, (c) circumferential stress $\sigma_{\theta\theta}$ and (d) axial stress σ_{zz}, during the growth of a misfitting cylindrical precipitate in a finite supersaturated matrix, under generalized plane strain conditions. The radial distance is normalized to the precipitate radius. Dotted lines locate the successive positions of the interface at different time steps indicated in (a). Finite element results are represented by the black curves whereas the red curves correspond to the sharp interface analytical solutions.

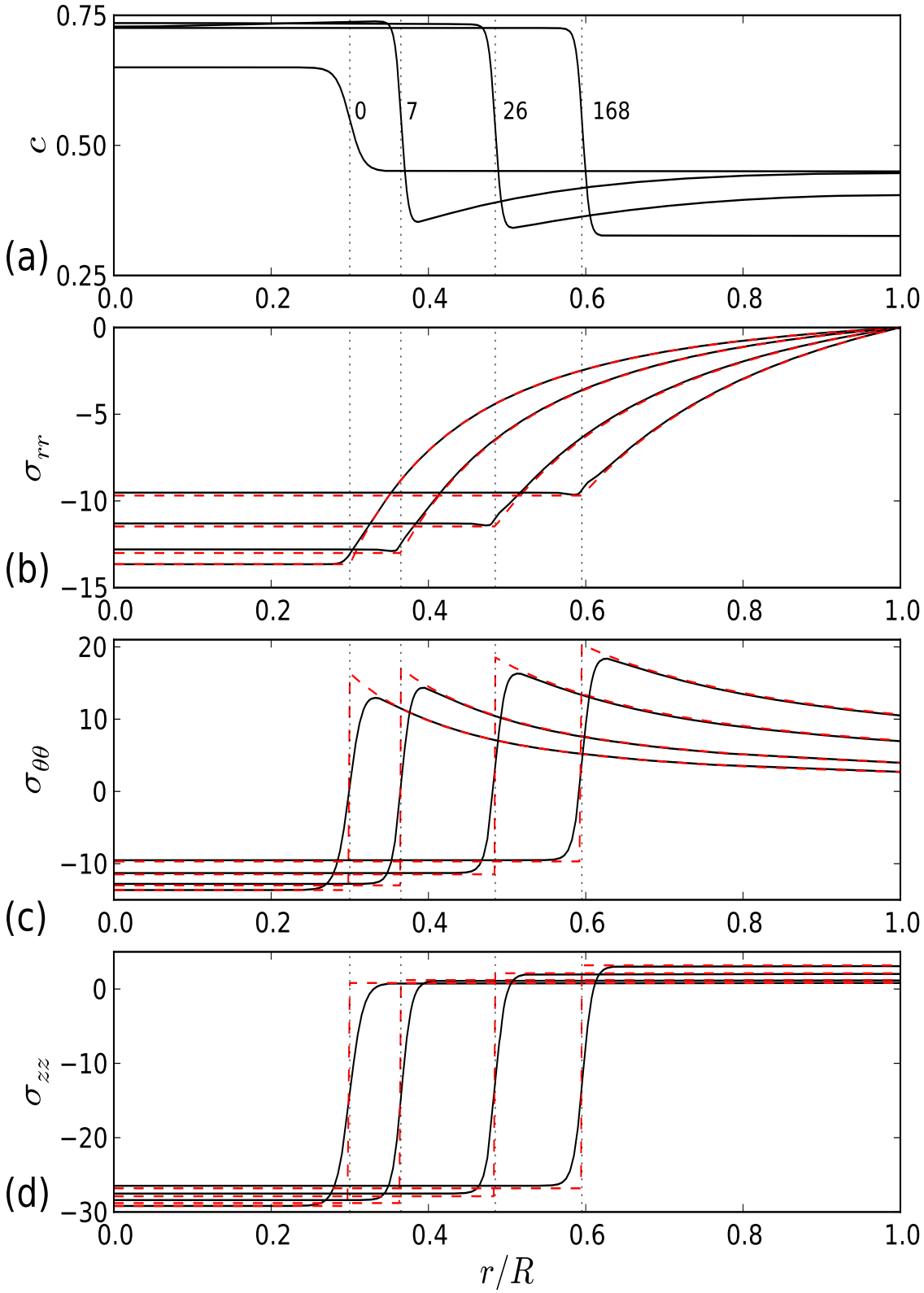

Figure IV.17 : Time evolution of the (a) concentration field, (b) radial stress σ_{rr}, (c) circumferential stress $\sigma_{\theta\theta}$ and (d) axial stress σ_{zz}, during the growth of a misfitting cylindrical precipitate in a finite supersaturated matrix, under plane strain conditions. The radial distance is normalized to the precipitate radius. Dotted lines locate the successive positions of the interface at different time steps indicated in (a). Finite element results are represented by the black curves whereas the red curves correspond to the sharp interface analytical solutions.

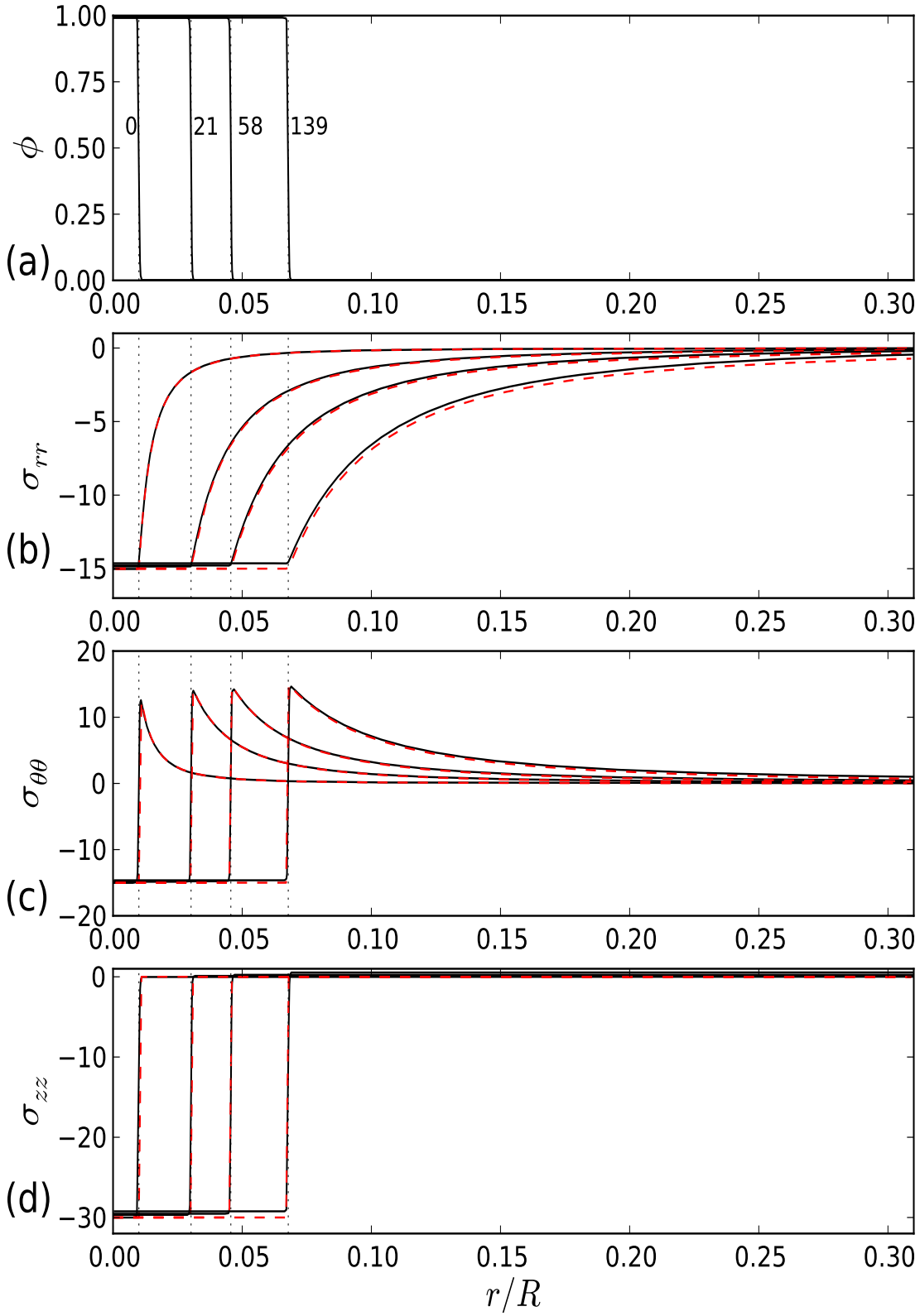

Figure IV.18 : Time evolution of the (a) order parameter field, (b) radial stress σ_{rr}, (c) circumferential stress $\sigma_{\theta\theta}$ and (d) axial stress σ_{zz}, during the growth of a misfitting cylindrical precipitate in an infinite supersaturated matrix, under generalized plane strain conditions. The radial distance is normalized to the precipitate radius. Dotted lines locate the successive positions of the interface at different time steps indicated in (a). Finite element results are represented by the black curves whereas the red curves correspond to the sharp interface analytical solutions.

matrix. The growth is mainly driven by the diffusion of the alloying species from the matrix to the interface as shown in Fig. IV.16a and IV.17a. As the transformation proceeds, the supersaturation in alloying species of the β matrix decreases to zero when the equilibrium concentration c_β is reached.

As it can be seen in Fig. IV.16c and Fig. IV.17, the hoop stress $\sigma_{\theta\theta}$ decreases within the precipitate, but increases at the interface on the side abutting on the β matrix, due to the interaction with the free boundary. The axial stress σ_{zz}, shown in Fig. IV.16d and Fig. IV.17d, remains constant in both precipitate and matrix, with a difference between generalized plane strain condition and plane strain condition, according to the analytical solution (IV.79) and (IV.80) respectively. Thus, these figures show clearly that the numerical results of the presented model follow the analytical stress distribution. However, it must be noticed that the discontinuous hoop $\sigma_{\theta\theta}$ and axial σ_{zz} stresses are smoothed out across the diffuse interface, compared with the theoretical solutions, considering that the interfaces in a phase-field model possess a finite thickness.

The time evolution of the order parameter field and stress distributions, which are the radial stress σ_{rr}, circumferential stress $\sigma_{\theta\theta}$ and axial stress σ_{zz}, are plotted in Fig. IV.18, during the growth of a misfitting cylindrical precipitate in an infinite supersaturated matrix, under generalized plane strain conditions and in a pure elastic state for both phases. The stress distributions at the different time steps are shown to be similar, for each stress component, assuming no interaction with the infinite free boundary. The numerical solution is shown to agree quite well with the analytical results.

IV.6 Growth of an isotropic spherical matrix surrounding a misfitting precipitate

In this section, the growth of a single spherical precipitate in an infinite matrix is investigated. The proposed phase field model has been used to study the stored elastic energy effect on the interfacial compositions and the diffusion-controlled growth of an isolated precipitate in a supersaturated matrix. We consider a misfitting spherical precipitate of radius r_{int}, introduced into an infinite matrix of outer radius R, as shown in Figure IV.19. Using spherical coordinates whose origin is at the precipitate center, the symmetries of geometry, boundary conditions, loading and the isotropic constitutive materials suggest that the variables field are independent of the circumferential coordinates ϕ, θ.

IV.6.1 Analytical analysis

Initially, the β matrix is considered to behave in a purely elastic way where the analytical solution is calculated, for isotropic elasticity (See Appendix I for details):

$$\begin{cases} \sigma_{rr} = \sigma_{\theta\theta} = \sigma_{\phi\phi} = \left[\left(\dfrac{r_{int}}{L}\right)^3 - 1\right] p_e & r \leqslant r_{int} \\ \sigma_{rr} = \left(\left[\dfrac{r_{int}}{L}\right]^3 - \left[\dfrac{r_{int}}{r}\right]^3\right) p_e & r \geqslant r_{int} \\ \sigma_{\theta\theta} = \sigma_{\phi\phi} = \left(\left[\dfrac{r_{int}}{L}\right]^3 + \dfrac{1}{2}\left[\dfrac{r_{int}}{r}\right]^3\right) p_e & r \geqslant r_{int} \end{cases} \tag{IV.83}$$

where

$$p_e = \frac{4\mu(3\lambda+2\mu)\varepsilon^\star_\alpha}{(3\lambda+6\mu)} = \frac{2\varepsilon^\star_\alpha}{3A} \qquad \text{and} \qquad A = \frac{\lambda+2\mu}{2\mu(3\lambda+2\mu)} = \frac{1-\nu}{E} \tag{IV.84}$$

Because of symmetry, the tangential displacements as well as the shear stresses and shear strains are all zero.

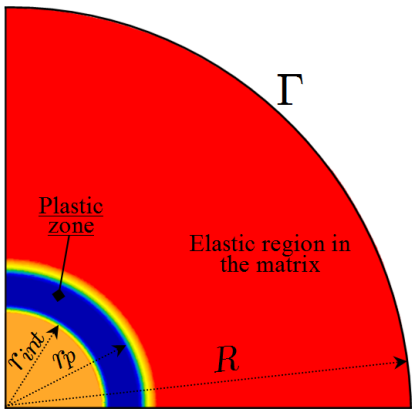

Figure IV.19 : Schematic diagram depicting the assumed two-phase system. The α precipitate of radius r_{int} is embedded in the β matrix with an outer radius R. r_p is the radius of the plastic zone in the matrix, surrounding a misfitting spherical precipitate, which is represented by the blue zone.

For the case of an infinite elastic matrix containing a single spherical precipitate, the above solution is extended assuming an infinite matrix radius:

$$\begin{cases} \sigma_{rr} = \sigma_{\theta\theta} = -p_e \quad \text{inside the particle} & r \leqslant r_{int} \\ \sigma_{rr} = -2\sigma_{\theta\theta} = -p_e \left(\dfrac{r_{int}}{r}\right)^3 & r_{int} \leqslant r \end{cases} \tag{IV.85}$$

Secondly, the misfit energy, stress and strain fields associated with a misfitting spherical precipitate are calculated under the assumption of ideal plastic behaviour in the matrix phase. Taking the symmetry associated with a misfitting sphere in an isotropic matrix into account, the resulting stress field within the precipitate is purely hydrostatic then unable to promote yielding. The plastic relaxation cannot occur in the precipitate and it is confined entirely to the matrix phase.

The analytical solution involves the calculation of the displacement, stress and strain fields and plastic zone size in both the elastic and plastic regions, which are given in (Earmme et al., 1981) for the case of linear and power–law strain hardening and in (Lee et al., 1980; Hill, 1950) for the case of ideal plastic behaviour as follows (See Appendix I):

$$\begin{cases} \sigma_{rr} = \sigma_{\theta\theta} = -p \quad \text{inside the particle} & r \leqslant r_{int} \\ \sigma_{rr} = \sigma_{\theta\theta} - \sigma^0_\beta = -p + 2\sigma^0_\beta \ln(\dfrac{r}{r_{int}}) & r_{int} \leqslant r \leqslant r_p \\ \sigma_{rr} = -2\sigma_{\theta\theta} = -\dfrac{2\sigma^0_\beta}{3}\left(\dfrac{r_p}{r}\right)^3 & r_p \leqslant r \end{cases} \tag{IV.86}$$

where

$$p = 2\sigma^0_\beta \ln(\frac{r_p}{r_{int}}) + \frac{2}{3}\sigma^0_\beta \tag{IV.87}$$

and r_p is the radius of the plastic zone that develops in the matrix. The relationship between the size of the plastic zone and the dimension of the particle

$$r_p = r_{int}\left(\frac{3}{2\sigma^0_\beta} p_e\right)^{1/3} \tag{IV.88}$$

IV.6.2 Equilibrium concentration at the interface

The equilibrium interfacial concentrations are derived from the thermodynamics equilibrium of stressed crystalline solids and thus from the two equilibrium conditions at the interface (IV.51) and (IV.52). These concentrations, which are used as boundary conditions in solving the diffusion equation, are expressed as

$$c_\alpha^{\text{int}} = a_\alpha + \frac{\Delta\mathcal{E} + \kappa\gamma}{k(a_\alpha - a_\beta)} \qquad \text{and} \qquad c_\beta^{\text{int}} = a_\beta + \frac{\Delta\mathcal{E} + \kappa\gamma}{k(a_\alpha - a_\beta)} \tag{IV.89}$$

where

$$\Delta\mathcal{E} = \mathcal{E}_{\text{coh}} - \Delta f_{\text{el}} = \left(\underset{\sim}{\varepsilon}_\beta^e - \underset{\sim}{\varepsilon}_\alpha^e\right) : \underset{\sim}{\boldsymbol{\sigma}}_\beta - (f_{e\beta} - f_{e\alpha}) \tag{IV.90}$$

Once the stress-strain field in both phases is known Eq.(IV.85) and Eq.(IV.86), the elastic energy contribution $\Delta\mathcal{E}$ (IV.57), on the equilibrium concentrations at the interface, under pure elastic behaviour and with plastic deformation, is (see Appendix I):

$$\boxed{\begin{aligned} &\Delta\mathcal{E}_{\text{elas}} = \frac{(\varepsilon^\star)^2}{A} && \text{Pure elastic behaviour} \\ &\Delta\mathcal{E}_{\text{plas}} = 2\sigma_\beta^0\varepsilon^\star\left[\ln\left(\frac{\varepsilon^\star}{A\sigma_\beta^0}\right) + 1\right] - A(\sigma_\beta^0)^2 && \text{Elasto}-\text{plastic behaviour} \end{aligned}} \tag{IV.91}$$

where

$$A = \frac{2\mu + \lambda}{2\mu\,(2\mu + 3\lambda)} = \frac{1-\nu}{E} \tag{IV.92}$$

In order to examine the effect of elastic fields on precipitate growth, we consider the problem of the diffusional growth of a coherent spherical precipitate into a supersaturated matrix. According to (Bourne et al., 1994), the growth law is shown to be parabolic, i.e. the square of the precipitate size (radius) increases linearly with time. When referring to the interfacial concentrations c_α^{int} and c_β^{int} , of both phases, it is assumed that the composition c_α is constant within the particle, i.e. zero concentration gradient in α domain and the precipitate grows only under a matrix supersaturation $(c_\beta^\infty - c_\beta^{\text{int}})$. The concentration field within the matrix is given in (Bourne et al., 1994) as:

$$c_\beta(w) = c_\beta^\infty + (c_\beta^{\text{int}} - c_\beta^\infty)\left[\frac{\sqrt{D_\beta/w}\exp(-w/D_\beta) - \sqrt{\pi}\text{erfc}(w/D_\beta)}{\sqrt{D_\beta/w_0}\exp(-w_0/D_\beta) - \sqrt{\pi}\text{erfc}(w_0/D_\beta)}\right] \tag{IV.93}$$

where erfc(x) is the complementary error function, $c_\beta^\infty$is the far-field matrix concentration, which is assumed to be independent of time and the variable w is introduced as defined implicitly as $x^2 + y^2 + z^2 = 4wt$, with (x, y, z) refers to a Cartesian coordinate system and w_0 defines the interface position of the particle:

$$\begin{aligned} c_\beta &= c_\beta^{\text{int}} \quad \text{when} \quad w = w_0 \\ c_\beta &= c_\infty \quad \text{when} \quad w \to \infty \end{aligned} \tag{IV.94}$$

IV.6.3 Phase field calculations

The calculation here are limited to isotropic homogeneous materials, where the chemical and mechanical parameters are reported in Table IV.5.2. The finite element mesh is composed of quadratic 8-node axisymmetric quadrangular elements, as shown in Fig. IV.15. The following boundary conditions have been applied to the system:

$$\begin{aligned} &\underline{\boldsymbol{\xi}}\,.\underline{\boldsymbol{n}} = 0, \quad \underline{\boldsymbol{J}}\,.\underline{\boldsymbol{n}} && \text{on all boundaries} \quad \Gamma \\ &\sigma_{rr}(r = R, \forall\theta) = 0 && : \text{free surface condition} \\ &u_\theta(\forall r \in \Gamma, \theta) = 0 && : \text{symmetric boundary condition} \end{aligned} \tag{IV.95}$$

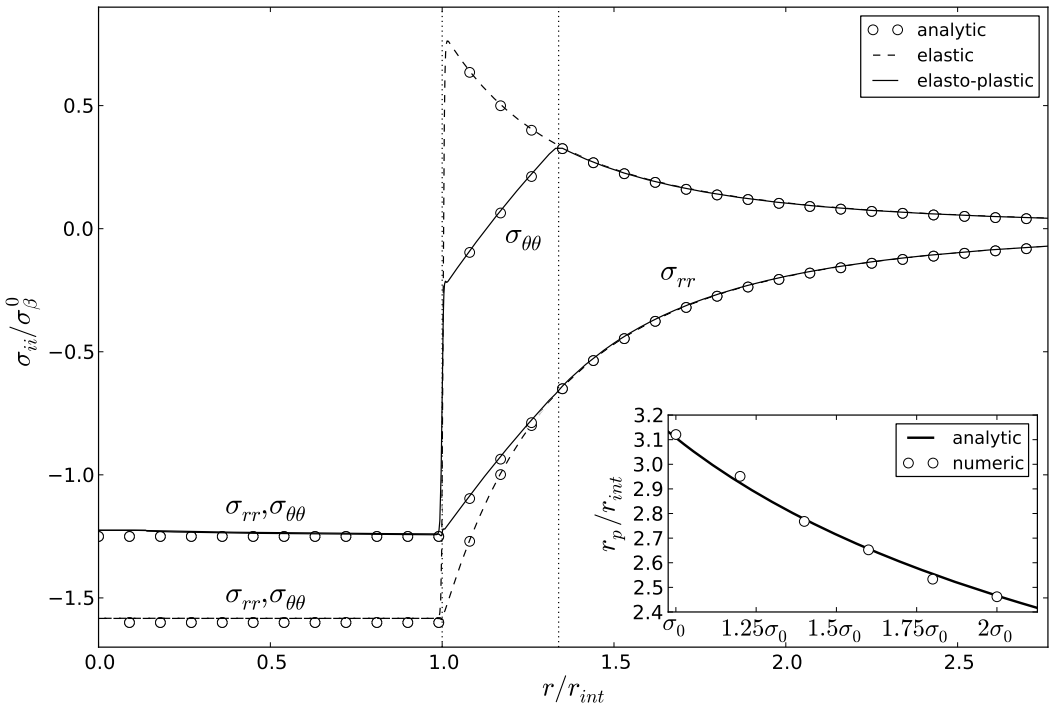

Figure IV.20 : Normal σ_{rr} and tangential $\sigma_{\theta\theta}$ stress distributions in a radial direction from the center of the particle in comparisons with the analytical solutions in a pure elastic state and for the case of ideal plastic behaviour. The stresses are normalized with respect to the yield stress σ^0_β. The matrix precipitate interface lies at $r/r_{int} = 1$. Inset shows the dependency of the plastic zone radius on σ^0_β, which is given by the relation (IV.88)

Radial profiles as $\tanh$ function have been imposed initially for ϕ and c, corresponding to the presence of a spherical α precipitate in the β shell matrix with an initial radius $r_0/R = 1$, where R is the total radius of the spherical assembly.

Figure IV.20 compares the stress distributions of a misfitting spherical precipitate in the purely elastic state to a case of ideal plastic deformation. The radial σ_{rr} and circumferential $\sigma_{\theta\theta}$ are normalized to the yield stress and are plotted as a function of radial distance measured in terms of the precipitate radius. The matrix/precipitate interface is represented by the vertical dotted at $r/r_{int} = 1$ and the plastic zone is bounded by the two vertical dotted lines. The stresses for the elastic case are represented by the dashed lines while those for the ideal plastic solution are depicted by the continuous lines. As shown in this figure, the major differences between the purely elastic and ideal plastic systems are substantial within the precipitate as well as in the plastic zone. Indeed, the tangential stress, σ_θ, inside the plastic zone, differs fundamentally from its counterpart of the pure elastic case in that its sign is reversed. However, the stress fields are practically indistinguishable between both behaviours inside the elastic region of the matrix. Moreover, finite element calculations of the same process have been undertaken with different yield stresses to examine the dependency of the plastic zone radius, normalized to the precipitate radius r_{int}, on the yield stresses. The inset of Fig. IV.20 compares the analytical solution, given by IV.88 to the numerical evolution of the plastic zone as a function σ^0_β.

The time evolution of the circumferential stress $\sigma_{\theta\theta}$, normalized to the yield stress, is plotted in Fig. IV.21 during the growth of a misfitting spherical precipitate, when the infinite supersaturated matrix phase is allowed to deform plastically. As it can be seen in Fig. IV.21, the tangential stress distribution in the precipitate is shown to be constant and identical, for the different time steps, considering no interaction with the infinite free boundary. Inside the matrix, the slope of

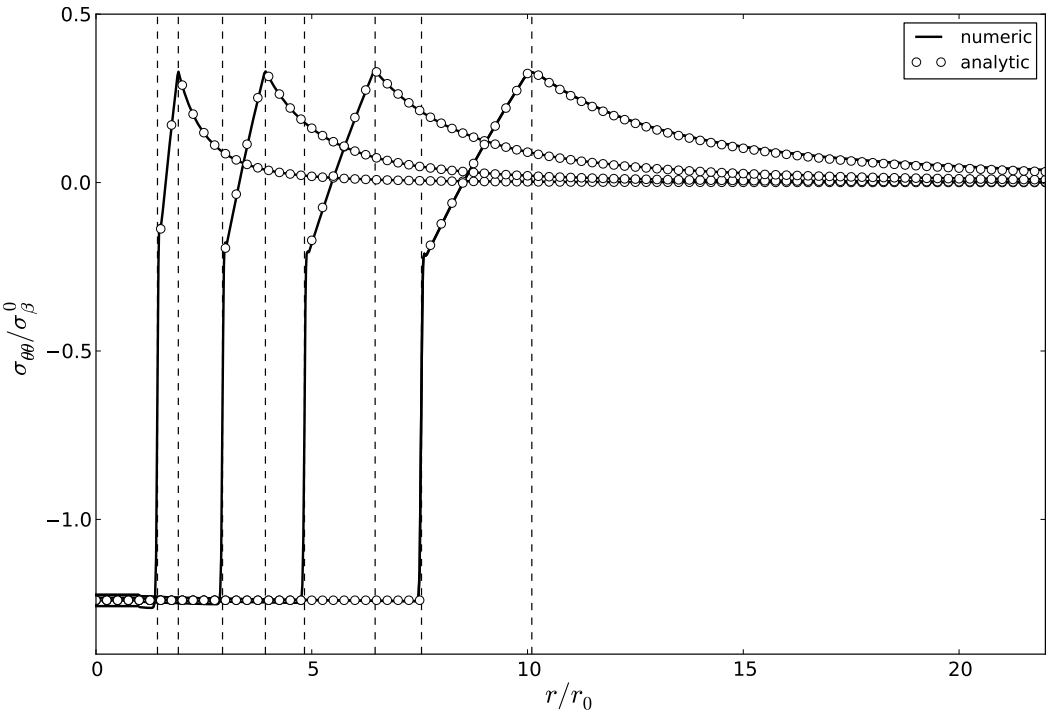

Figure IV.21 : Time evolution of the tangential stress component $\sigma_{\theta\theta}$ for $\varepsilon^\star = 3 \cdot 10^{-4}$ in comparison with the analytical solutions. Black dotted lines locate respectively the successive positions of the interface and the plastic zone at different the time steps where r_0 is the initial precipitate radius

the tangential stress experiences a discontinuity which occurs at the plastic-elastic boundary due to the discontinuity in the slope of the stress-strain curve at the yield point, where the same maximum is reached at this boundary $(r = r_p)$ for the four time steps. However, the plastic zone, which is bounded by the two vertical dotted lines, increases when the interface moves forwards, according Eq. (IV.88). The numerical solution is shown to agree quite well with the analytical results, developed above. However, it must be noticed that a slight discrepancy between the numerical and theoretical results appears at the first step $(t = 0)$, corresponding to the transient period, where the system (initial state) has not yet reached a steady state.

The concentration profiles at three time steps are displayed in Fig. IV.22 for three different cases, assuming a chemical, elastic and ideal plastic behaviour for supersaturated matrix. At the beginning of the process, the concentrations at interface are slightly higher than the equilibrium ones, due to the transient period. The composition in the particle is shown to be constant, assuming zero concentration gradient in α domain $(c^{\mathrm{s}}_\alpha = c^{\mathrm{int}}_\alpha)$, since zero mass exchange through the external surface is imposed. The precipitate grows only under a matrix supersaturation (Bourne et al., 1994). The numerical profiles, for the three cases are shown to be in very good agreement with the analytical solution, given by Eq. (IV.93).

The time evolutions of the precipitate radius, normalized by the initial precipitate radius $\Delta r/r_0$, is shown in Fig. IV.23. The growth kinetics has been deduced from the profiles, plotted in Fig. IV.22, by tracking the position of $\phi = 0.5$, for the three cases, i.e. assuming a chemical, elastic and ideal plastic behaviour for matrix. Apart from the beginning of the process which is strongly influenced by the initial conditions, the growth law is parabolic for the three cases, i.e. $\Delta e = K\sqrt{t}$, which is again in good accordance with the analytical analysis, presented in (Bourne et al., 1994).

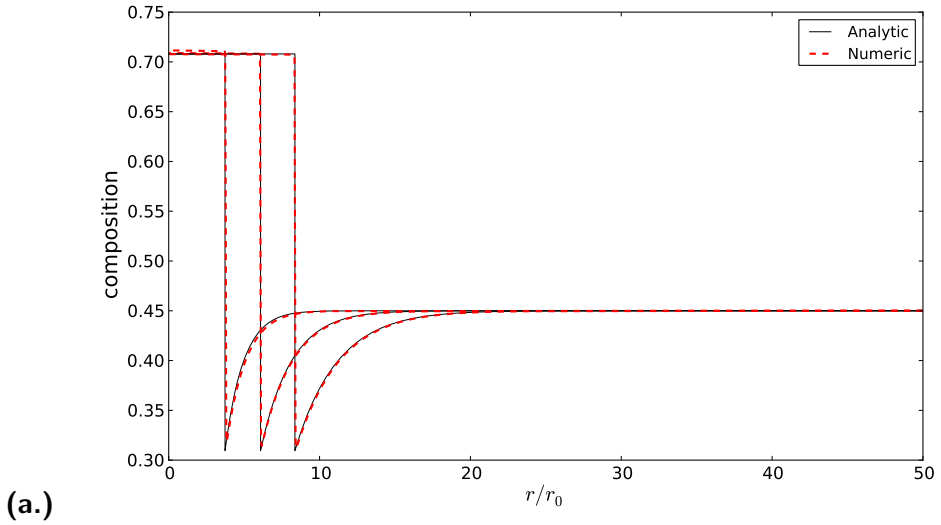

(a.)

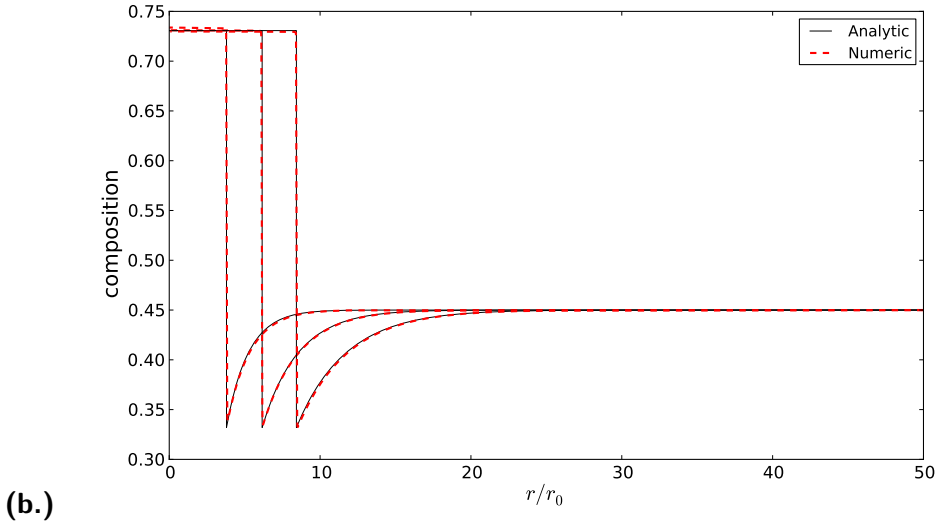

(b.)

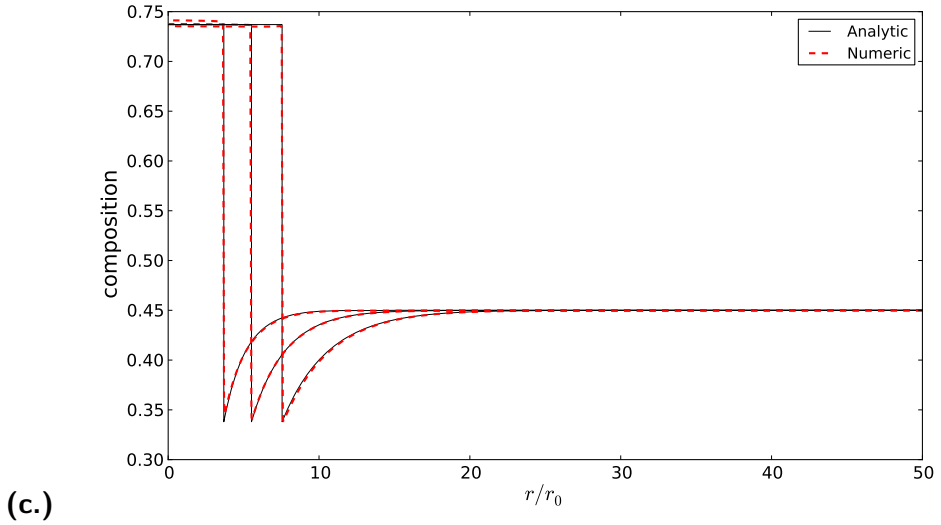

(c.)

Figure IV.22 : Time evolution of the concentration profiles during the growth of a misfitting spherical precipitate for three different cases, assuming a chemical (a.), elastic (b.) and ideal plastic (c.) behaviour for supersaturated matrix. The concentration profiles are plotted at three different time steps. Radial distance is normalized with respect to the initial precipitate radiusr_0. The continuous black lines correspond to the numerical profiles whereas the analytical solution, which is given by (IV.93), is represented by the red discontinuous lines.

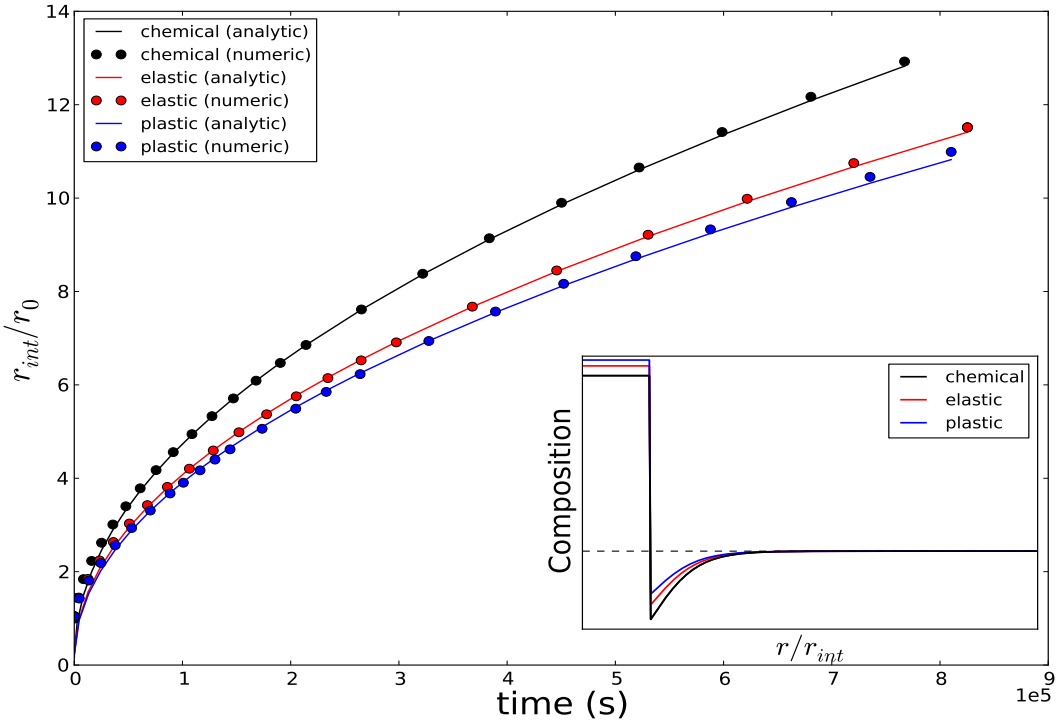

Figure IV.23 : Growth kinetics of a misfitting spherical precipitate in an isotropic infinite matrix. Three finite element calculations have been performed, assuming a chemical (black), elastic (red) and ideal plastic (blue) behaviour for supersaturated matrix, which are plotted with with symbols. The corresponding analytical growths, given in (Bourne et al., 1994), are represented with lines.

IV.7 Conclusion

This chapter is specifically devoted to the application of the proposed non-linear elastoplastic phase field model to solve some elementary initial boundary values problems in coupled diffusion-elastoplasticity where the numerical results have been validated against corresponding sharp interface analytical solutions.

The prediction of coherent phase diagram in microelasticity demonstrates that the choice of such an interpolation scheme can have serious consequences on the predicted coherent phase diagram. Indeed, it is shown that Reuss scheme is unacceptable for coupling mechanics and phase transformation whereas equivalent numerical results were obtained using Voigt/Taylor homogenization method and Khachaturyan mixture rule. Consequently, calculating this phase diagram is used to rule out some unacceptable mixture rules. Moreover, the growth mechanism of the oxide layer at the surface of a pure zirconium slab has been studied considering the effects of the misfit generated stress, the oxide elasticity moduli. The main result of the oxide growth study, under pure elastic state, is that the parabolic growth law continues to be valid, taking the misfit generated stress into account, but the growth kinetic coefficient depends on (i) dilatation misfit, (ii) the elastic modulus of the oxide layer, which decreases linearly with $E_{\mathrm{ZrO_2}}$ and $\delta^2_{\mathrm{ZrO_2}}$. The effect of plastic relaxation of the stresses on the oxide growth kinetic has been studied.

Finally, the growth of an isotropic misfitting precipitate in an isotropic matrix is investigated. Two particle shapes are considered, which cylindrical and spherical particles. The stored elastic energy effect on the diffusion-controlled growth of an isolated precipitate in a supersaturated matrix has been studied to investigate the effect of plastic accommodation processes on the transformation kinetics, compared with the corresponding pure elastic state and pure chemical transformation.

The validation of the numerical finite element implementation is generally based on the ensuring of the steady-state profiles of the composition at equilibrium and the prediction of the diffusion-controlled growth during interface evolution for different shapes as well as the equilibrium concentration at the interface. We can conclude that the numerical results converge to the corresponding sharp interface analytical if the interfacial thickness is sufficiently small. Furthermore, an extension of the present model will be proposed by introducing the continuum crystallographic viscoplastic model as well as the size effects on plasticity in the diffuse interface approach, which are two strong assumptions for the application of the model to a large range of materials.

Conclusions and future work

Main results

The whole work in this thesis has been broadly devised in three main steps: theoretical work, programming step and numerical simulation part. In the first step, a general framework has been proposed to combine standard phase field approaches with a different complex linear or non-linear material behaviour, such as chemical diffusion, mechanics (elasticity, plasticity...) for each phase. Balance equations and boundary conditions of a fully coupled phase field/diffusion/mechanical problem for alloys have been presented within the general framework of continuum thermodynamics in conjunction with the generalized principle of virtual power, which is postulated involving generalized stresses (Gurtin, 1996). The proposed framework offers a number of advantages, which are:

- Balance and constitutive equations are clearly separated in the formulation, which allows the application of any arbitrary form for the free energy functional, such as Khachaturyan model (Wang and Khachaturyan, 1995b), Kim-Kim-Suzuki (KKS) model (Kim et al., 1998; Kim et al., 1999) and Folch-Plapp model (Folch and Plapp, 2005) Indeed, two homogeneous free energy densities are proposed, which are:

  1. Polynomial formulation, which is an extension of KKS energy density, proposed by (Kim et al., 1998). One distinct homogeneous free energy f_k is attributed to each individual phase k. Each phase possesses then its set of chemical parameters, which are the curvature, heights and equilibrium concentrations. The homogeneous free energy of a two-phase material must then be interpolated from the free energies of both phases for intermediate values of ϕ with an interpolating polynomial.

  2. Interpolating free energy densities (extension of Plapp-Folch energy density). This free energy make the concentration contribution across the interface to the interfacial energy, which can be a source of many problems, vanish,. Consequently, it allows an easier calibration of the interfacial energy through the relationship between the parameter α in front of $(\boldsymbol{\nabla}\phi)^2$, and the interfacial thickness δ.

  Equivalent numerical results were obtained using polynomial and interpolating free energy densities for small thickness of the interface region.

- Boundary and initial conditions for the displacement, concentration and order parameter and their dual quantities are clearly stated within the formulation. The formulation is then shown to be well-suited for a finite element formulation of the initial boundary value problems on

finite size specimens with arbitrary geometries and for very general non-periodic or periodic boundary conditions. The clear analogy between the proposed variational formulation and that of conventional computational mechanics leads us to the derivation of an implicit finite element scheme to solve the considered initial boundary value problem, based on time and space discretizations.

- This approach makes possible to mix different types of constitutive equations for each phase, like hyperelastic nonlinear behaviour for one phase and conventional elastic–plastic model with internal variables for the other one. One distinct set of constitutive equations is attributed to each individual phase k at any material point. The local constitutive equation relating the macroscopic variables, at this material point, is obtained by averaging the corresponding non-uniform local stress and strain in each phase using the well–known homogenization schemes inside the smooth interface zone. Each phase at a material point then possesses its own stress/strain tensor $\underset{\sim}{\boldsymbol{\sigma}}_k, \underset{\sim}{\boldsymbol{\varepsilon}}_k$ and each parameter is usually interpolated between the limit values known for each phase. Thus, no correspondence of material parameters is then needed between the phase behaviour laws.

- The formulation allows the use of any arbitrary mixture rules taken from well-known homogenization theory, in the region where both phases coexist, in order to incorporate linear and nonlinear mechanical constitutive equations for each phase into the standard phase field approach. In this work, two mixture rules for strain and stress are introduced, which are based on the Voigt/Taylor and Reuss/Sachs homogenization schemes, inside the smooth interface zone. Moreover, it is also possible to choose the mechanical properties and parameters associated with each phase, i.e. the indicator function χ (III.38), as a function of concentration or order parameter

The second step in this work consists of the programming of finite element constitutive equations in finite element code. Indeed, the proposed non-linear elastoplastic phase field model with different homogenization schemes has been implemented in the finite element code ZeBuLoN:

- Specific classes have been defined following the philosophy of object oriented programming. The eventual programming of material characteristics within a finite element code entails defining the appropriate variables used to characterize a material behaviour, according to their functionality in the physics of the material problem.

- Three different finite element algorithms have been proposed for Voigt/Taylor, Reuss/Sachs scheme and Khachaturyan scheme, as respectively displayed in Figs. III.2, III.3 and III.4

- Two possible numerical techniques have been implemented to integrate the constitutive equations at each Gauss point during the local integration procedure which are the explicit Runge-Kutta method with automatic time stepping and implicit Θ-method solved with a Newton-Raphson method.

The last step is specifically devoted to the modelling and simulation of some elementary initial boundary value problems in both pure diffusion and coupled diffusion-elastoplasticity on finite size specimens. The finite element results have been validated against corresponding sharp interface analytical solutions. The validation of the numerical finite element implementation is generally based on two axes: The ensuring of the steady-state profiles of the composition and order parameter at equilibrium and the prediction of the diffusion-controlled growth kinetics during interface evolution for different shapes as well as the equilibrium concentration at the interface, compared with the analytical solutions. Large series of calculations have been performed with

different interface shapes (plane, cylindrical, spherical), material parameters (elasticity moduli, free energy height and curvature, interface thickness), dilatation misfits, behaviours for both phases (pure chemical , elastic state and perfect plastic behaviour), which are in very good agreement with the analytical solution.

Moreover, in order to illustrate the implication of the choice of specific mixture rules for these behaviour, coherent phase diagram in microelasticity when internal stresses are generated by transformation eigenstrains has been predicted and compared with the theoretical diagram porposed by (Cahn and Larché, 1984). The different results demonstrate that the choice of such an interpolation scheme can have serious consequences on the predicted coherent phase diagram. Indeed, it is shown that Reuss scheme is unacceptable for coupling mechanics and phase transformation whereas equivalent numerical results were obtained using Voigt/Taylor homogenization method and Khachaturyan mixture rule. Consequently, calculating this phase diagram is used to rule out some unacceptable mixture rules.

Future Work

Several questions remain open for future research work:

1. **Inheritance of plastic deformation during migration of phase boundaries:**

   In this work, the question of inheritance of internal variables associated with plastic deformation when an interface sweeps a plastified zone of bulk phase during migration of phase boundaries has not been addressed. As noted in (Petit-Grostabussiat et al., 2004), the inheritance is likely to depend on the nature of the interface, but the question: "Do coherent and incoherent favor recovery of the hardening of the mother phase" has no obvious answer, and will deserve a particular attention in the development of the model in order to reach realistic comparison with experimental results. Indeed, it is very important to know if the new formed phase inherits all, some or no strain hardening of the parent phase, for the prediction of residual stresses by structural calculations for instance. This point is a very delicate issue and it will become a major breakthrough if overcome.

2. **Effect of coherent elastic strain on shape instabilities during growth:**

   Shape change transitions of elastically misfitting inclusions are predicted to occur when the inclusions are softer than the matrix. Softer precipitates induce shape changes with increasing volume as elastic energy contributions become more important. Consequently, elastic inhomogeneity effects become even more important for elastically interacting precipitates or in the presence of an applied stress and the shape transition is then to a lower symmetry shape that is influenced by the elastic contribution (Johnson and Cahn, 1984; Kolling et al., 2003). Finite element calculations will be performed to investigate the influence of various parameters such as particle size, elastic constants and inhomogeneity on the equilibrium morphology and to also explore how the shape of a coherent particle, determined by minimizing the sum fo interfacial and elastic energies, varies with particle size.

3. **Other mixture rules:**

   Combining different homogenization schemes is acceptable since there is no clear physical motivation for selecting one or another scheme in the present context as long as no specific hypothesis is made on the atomic arrangement inside the representative volume element underlying each material point, and as long as no specific discrete–continuum homogenization scheme is constructed. Other general homogenization schemes could be

tested and may be computationally more efficient under circumstances, like the Hashin–Shtrikman procedure or the self–consistent method.

4. **Anisotropic effects:**

   Our proposed model is limited to isotropic homogeneous materials. However, in crystalline solids, interfacial energies are generally anisotropic, attributed to differences in the nature of the interface: coherent, semi-coherent, and incoherent. The interfacial energy anisotropy is usually a function of temperature with the degree or anisotropy larger at low temperatures. The type and degree of interfacial energy anisotropy affect the particle shape instability during precipitate growth in coherent solids (Wang and Khachaturyan, 1995a; Vaithyanathan et al., 2004). Moreover, anisotropy of the eigenstrains and elastic moduli is likely to play a role on the particle shapes or interface orientations during microstructure evolution (Shen et al., 2006).

   An extension of our model will be obtained by accounting for the anisotropic effects, through the interface energies, the elastic coefficients, or the material parameters, such as the chemical diffusivities and the elastic parameters of both phases. Thus, the analyses of precipitate shape stability in the elastically anisotropic coherent system will be investigated. There are essentially a number of approaches, which can be proposed to describe the interfacial energy anisotropy in phase-field models. One straightforward and most often employed approach to introduce interfacial energy anisotropy is to make, the coefficient α of the gradient contribution to the free energy (II.1) have the same directional dependence as the interfacial energy, as proposed in (Eggleston et al., 2001; Eggleston, 2001). Another approach is to add higher order gradient energy terms (Abinandanan and Haider, 2001; Dreyer and Müller, 2003).

5. **Mesh sensitivity and adaptive mesh:**

   Although finite element method is a versatile and robust tool for handling such initial boundary value problems on finite size specimens, numerical calculations, using FE method, are very computationally intensive, particularly for three-dimensional systems and when internal variable are introduced. A mesh sensitivity analysis will be performed considering the effects of finite element type, mesh type and node number in the interface on the numerical results in the presence of elastoplastic deformations. Moreover, the effectiveness of finite element method with respect to the other numerical methods, like the FFT algorithm must be examined. The main questions is: what is the best suited-technique for coupling phase transformation and non-linear mechanics behaviour. Adaptive meshing can be proven as most efficient solution to simulate large-scale two-phase systems of complex microstructure much larger than the width of the interface region. Thus, efficient and accurate numerical algorithms for adaptive mesh refinement should be developed using the phase-field variable as the criterion for dynamic refinement and coarsening of the grid (Provatas et al., 1999; Yue et al., 2006).

6. **Phase field and crystal plasticity:**

   An extension of the present model will be proposed by introducing the continuum crystallographic viscoplastic model in the diffuse interface approach. Continuum crystal plasticity theory has become a well-established framework to account for the anisotropic nonlinear response of single crystals and polycrystal materials, the evolution of lattice orientation during deformation and the strong strain and stress heterogeneities that develop in the grains of a polycrystal during overall homogeneous deformation. Plastic activity is introduced using a continuum crystal plasticity framework, which is mainly due to the movement of one-dimensional crystal defects called dislocations. The description of crystals

plasticity is very difficult in the case of multi-phase metallic alloys, because slip systems of dislocations usually differ from one phase to the other, and because the microstructure evolution and the dislocations dynamics are in principle coupled through the stress fields generated in the material. Continuum crystal plasticity models fit entirely within the more general phenomenological continuum thermo-mechanical framework of modern elasto-viscoplasticity constitutive theory, as settled in (Germain et al., 1983). Using the general framework, proposed in this work, crystal plasticity theory can be rather easily incorporated in the phase field approach (Gaubert et al., 2009). Additional internal hardening variables and scalar dislocation densities are introduced to describe the slips on crystallographic systems. In addition, evolution equations in the form of ordinary differential equations are postulated to describe the plastic flow and the hardening of the material volume element.

7. **Phase field and generalized continuum mechanics (size effects):**

   The coupled phase field/diffusion/mechanical proposed in this work must be enriched by introducing intrinsic length-scale parameters to account for size effects, frequently observed in the mechanical behavior of metals, like grain size and precipitate size effects. In particular, the classical simulations of poly-crystalline behavior are independent of the absolute grain size as shown in (Smyshlyaev and Fleck, 1996; Forest and Barbe, 2000). These size effects are due to the fact that dislocations are moving in a crystal containing obstacles to their motion (e.g. precipitates, grain boundaries ...) and that the crossing of the obstacles is directly related to the distance between obstacles. Therefore, a state-of-the-art continuum plasticity model is needed, where internal lengths associated to dislocations in crystalline materials are incorporated. Size-dependent constitutive models can be obtained by resorting to the mechanics of generalized continua, like second gradient, Cosserat and micromorphic theories.

8. **Asymptotic analysis:**

   Introducing both crystal plasticity and size effects in the phase field approach, asymptotic analysis will be performed to relate the parameters of the diffuse interface model to physical parameters entering sharp interface models.

Bibliography

Abinandanan, T. A. and Haider, F. (2001). An extended Cahn-Hilliard model for interfaces with cubic anisotropy. *Philisophical Magazine A*, 81:2457–2479.

Abrivard, F. (2009). *Coupled Crystal Plasticity-Phase Field Formulation to Describe the Microstructural Evolution in Polycrystalline Aggregates During Thermal Recrystalisation.* Thèse de doctorat, Ecole des Mines de Paris.

Allen, S. and Cahn, J. (1979). A microscopic theory for antiphase boundary motion and its application to antiphase domain coarsening. *Acta Metallurgica*, 27:1085–1095.

Ammar, K., Appolaire, B., Cailletaud, G., Feyel, F., and Forest, S. (2009a). Finite element formulation of a phase field model based on the concept of generalized stresses. *Computational Materials Sciences*, 45:800–805.

Ammar, K., Appolaire, B., Cailletaud, G., Feyel, F., and Forest, S. (2009b). Finite element formulation of an elastoplastic phase–field model for binary alloys based on the concepts of generalized stresses and homogenization methods. In *Plasticity 2009*, pages 3–6.

Ammar, K., Appolaire, B., Cailletaud, G., Feyel, F., and Forest, S. (2009c). Formulation éléments finis des modèles de champ de phases basée sur la théorie de l'équilibre des microforces. In *Plast0x 2007*, pages 117–129. EDP Sciences.

Ammar, K., Appolaire, B., Cailletaud, G., and Forest, S. (2009d). Combining phase field approach and homogenization methods for modelling phase transformation in elastoplastic media. *European Journal of Computational Mechanics.*, 18(5-6):485–523.

Appolaire, B. and Aeby-Gautier, E. (2009). Effect of the misfit-generated stress on the stability of a nitride layer growing in pure iron. *Submitted to Physical Review B*.

Appolaire, B., Aeby-Gautier, E., Da Costa Teixeira, J., Dehmas, M., and Denis, S. (2009). Non coherent interfaces in diffuse interface models. *Philosophical Magazine*. in press.

Appolaire, B. and Gautier, E. (2003). Modelling of phase transformations in titanium alloys with a phase field model. *Lecture Notes in Computational Science & Engineering*, 32:196–201.

Appolaire, B. and Gouné, M. (2006). Linear stability analysis of a γ'-Fe_4N nitride layergrowing in pure iron. *Computational Materials Science*, 38:126–135.

Barbe, F., Quey, R., Taleb, L., and Souza de Cursi, E. (2008). Numerical modelling of the plasticity induced during diffusive transformation. An ensemble averaging approach for the case of random arrays of nuclei. *European Journal of Mechanics A/Solids*, 27:1121–1139.

Benallal, A., Billardon, R., and Doghri, I. (1988). An integration algorithm and the corresponding consistent tangent operator for fully coupled elastoplastic and damage equations. *Comm. Appl. Num. Meth.*, 4:731–740.

Bergheau, J. and Fortunier, R. (2004). *Simulation numérique des transferts thermiques par éléments finis*. Hermès Science Publications.

Besson, J., Cailletaud, G., Chaboche, J.-L., and Forest, S. (2001). *Mécanique non linéaire des matériaux*. Hermès Sciences, France.

Bi, Z. and Sekerka, R. F. (1998). Phase–field model of solidification of a binary alloy. *Physica A*, 261:95–106.

Bourne, J., Atkinson, C., and R.C., R. (1994). Diffusion-controlled growth in ternary systems. *Metallurgical and Materials Transactions A*, 25A:2683–2694.

Boussinot, G., Finel, A., and Le Bouar, Y. (2009). Phase-field modeling of bimodal microstructures in nickel-based superalloys. *Acta Materialia*, 57:921–931.

Bragard, J., Karma, A., Lee, Y. H., and Plapp, M. (2002). Linking phase-field and atomistic simulations to model dendritic solidification in highly undercooled melts. *Interface Science*, 10:121–136.

Cahn, J. and Hilliard, J. (1958). Free energy of a Nonuniform system. I. Interfacial free energy. *The Journal of Chemical Physics*, 28(2):258–267.

Cahn, J. and Hilliard, J. (1959). Free energy of a Nonuniform system. II. Nucleation in a Two–Component incompressible fluid. *The Journal of Chemical Physics*, 31(3):688–699.

Cahn, J. and Larché, F. (1984). A simple model for coherent equilibrium. *Acta Metall.*, 32(11):1915–1923.

Cahn, J. W. (1961). On spinodal decomposition. *Acta Metallurgica*, 9:795–801.

Cha, P.-R., Kim, J., Kim, W.-T., and Kim, S. (2009). Effect of transformation induced stress and plastic deformation on austenite/ferrite transition in low carbon steel. In *Plasticity 2009*, pages 376–378.

Chan, P. and Rey, A. (1995). A numerical method for the nonlinear Cahn–Hilliard equation with nonperiodic boundary conditions. *Computational Materials Sciences*, 3:377–392.

Charach, C. and Fife, P. C. (1999). Phase–field models of solidification in binary alloys: capillarity and solute trapping effects. *Journal of Crystal Growth*, 198/199:1267–1274.

Chen, L. and Hu, S. (2004). Phase–field method applied to strain–dominated microstructure evolution during solid–state phase transformations. In Raabe, D., Roters, F., Barlat, F., and Chen, L., editors, *Continuum Scale Simulation of Engineering Materials*, pages 271–296. Wiley–VCH.

Chen, L.-Q. (2004). Continuum scale simulation of engineering materials: Fundamentals–microstructures–process applications. In Raabe, D., Roters, F., Barlat, F., and Chen, L., editors, *Continuum Scale Simulation of Engineering Materials*, pages 37–56. Wiley–VCH.

Coleman, B. and Gurtin, M. (1967). Thermodynamics with internal variables. *The Journal of Chemical Physics*, 47:597–613.

Coleman, B. and Noll, W. (1963). The thermodynamics of elastic materials with heat conduction and viscosity. *Arch. Rational Mech. and Anal.*, 13:167–178.

Danilov, D. and Nestler, B. (2005). Phase–field simulations of solidification in binary and ternary systems using a finite element method. *Journal of Crystal Growth*, 275:177–182.

Dejmek, M., Folch, R., Parisi, A., and Plapp, M. (2004). Three-dimensional phase-field simulations of directional solidification. *ArXiv Condensed Matter e-prints*.

Dhatt, G., Touzot, G., and Lefrançois, E. (2005). *Méthode des éléments finis*. Hermès Science Publications.

Dreyer, W. and Müller, W. (2000). A study of the coarsening in tin/lead solders. *International Journal of Solids and Structures*, 37:3841–3871.

Dreyer, W. and Müller, W. (2001). Modeling diffusional coarsening in eutectic tin/leadsolders : a quantitative approach. *International Journal of Solids and Structures*, 38:1433–1458.

Dreyer, W. and Müller, W. H. (2003). Toward quantitative modeling of morphology changes in solids withphase field theories: Atomistic arguments for the determinationof higher gradient coefficients. *Engineering Materials*, 240–242:901–914.

Earmme, Y., Johnson, W., and Lee, J. (1981). Plastic relaxation of the transformation strain energy of a misfitting spherical precipitate: Linear and power–law strain hardening. *Metallurgical Transactions A*, 12A:1521–1530.

Echebarria, B., Folch, R., Karma, A., and Plapp, M. (2004). Quantitative phase field model of alloy solidification. *Physical Review E*, 70.

Eggleston, J., McFadden, G., and Voorhees, P. (2001). A phase-field model for highly anisotropic interfacial energy. *Physica D*, 150:91–103.

Eggleston, J. J. (2001). *Phase–Field models for thin film growth and ostwald ripening*. Thèse de doctorat, Northwestern university.

Eiken, J., Böttger, B., and Steinbach, I. (2006). Multiphase–field approach for multicomponent alloys with extrapolation scheme for numerical application. *Physical Review E*, 73.

Emmerich, H. (2003). *The Diffuse Interface Approach in Materials Science: Thermodynamic Concepts & Applications of Phase-field Models*. SPRINGER.

Eshelby, J. (1957). The determination of the elastic field of an ellispoidal inclusion, and related problems. *Proceedings of the Royal Society of London. Series A*, 241:376–396.

Eshelby, J. (1959). The elastic field outside an ellipsoïdal inclusion. *Proceedings of the Royal Society of London. Series A*, 252:561–569.

Fischer, F., Reisner, G., Werner, E., T. K., Cailletaud, G., and Antretter, T. (2000). A new view on transformation induced plasticity (TRIP). *International Journal of Plasticity*, 16:723–748.

Foerch, R. and Besson, J. (1997). Large scale object oriented finite element code design. *Comput. Methods Appl. Mech. Eng.*, 142:165–187.

Foerch, R., Besson, J., Cailletaud, G., and Pilvin, P. (1997). Polymorphic constitutive equations in finite element codes. *Computer Methods in Applied Mechanics and Engineering*, 141(3):355–372.

Folch, R. and Plapp, M. (2005). Quantitative phase–field modeling of two-phase solidification. *Phys. Rev. E*, 72(1):011602.

Forest, S. (2008). The micromorphic approach to plasticity and diffusion. In Jeulin, D. and Forest, S., editors, *Continuum Models and Discrete Systems 11, Proceedings of theinternational conference CMDS11*, pages 105–112, Paris, France. Les Presses de l'Ecole des Mines de Paris.

Forest, S. (2009). The micromorphic approach for gradient elasticity, viscoplasticity and damage. *ASCE Journal of Engineering Mechanics*, 135:117–131.

Forest, S. and Barbe, F.and Cailletaud, G. (2000). Cosserat modelling of size effects in the mechanical behaviour of polycrystals and multiphase materials. *International Journal of Solids and Structures*, 37:7105–7126.

Fratzl, P., Penrose, O., and Lebowitz, J. L. (1999). Modelling of phase separation in alloys with coherent elastic misfit. *Journal of Statistical Physics*, 95:1429–1503.

Fried, E. and Gurtin, M. E. (1993). Continuum theory of thermally induced phase transitions based on an order parameter. *Phys. D*, 68(3-4):326–343.

Fried, E. and Gurtin, M. E. (1994). Dynamic solid-solid transitions with phase characterized by an order parameter. *Phys. D*, 72(4):287–308.

Furtado, A., Castro, J., and Silva, A. (2006). Simulation of the solidification of pure nickel via the phase-field method. *Materials Research*, 9(4):349–356.

Ganghoffer, J., Simonsson, K., Denis, S., Gautier, E., Sjöström, S., and Simon, A. (1994). Martensitic transformation plasticity simulations by finite elements. *Journal de Physique IV (France)*, 4:C3–215–220.

Gaubert, A., Finel, A., Le Bouar, Y., and Boussinot, G. (2008). Viscoplastic phase field modellling of rafting in ni base superalloys. In *Continuum Models and Discrete Systems CMDS11*, pages 161–166. Mines Paris Les Presses.

Gaubert, A., Le Bouar, Y., and Finel, A. (2009). Coupling phase field and visco–plasticity to study rafting in Ni–base superalloys. *Philosophical Magazine*. in press.

George, W. and Warren, J. (2002). A parallel 3D dendritic growth simulator using the Phase–Field method. *Journal of Computational Physics*, 177(2):264–283(20).

Germain, P. (1973a). La méthode des puissances virtuelles en mécanique des milieux continus, première partie : théorie du second gradient. *J. de Mécanique*, 12:235–274.

Germain, P. (1973b). The method of virtual power in continuum mechanics. Part 2: Microstructure. *SIAM J. Appl. Math.*, 25:556–575.

Germain, P., Nguyen, Q.-S., and Suquet, P. (1983). Continuum thermodynamics. *J. Appl. Mech.*, 50:1010–1020.

Grafe, U., Böttger, B., Tiaden, J., and Fries, S. G. (2000a). Coupling of multicomponent thermodynamic databases to a phase field model: Application to solidification and solid state transformations of superalloys. *Scripta Materialia*, 42:1179–1186.

Grafe, U., Böttger, B., Tiaden, J., and Fries, S. G. (2000b). Simulations of the initial transient during directional solidification of multicomponent alloys using the phase field method. *Modelling and Simulation in Materials Science and Engineering*, 8:871–879.

Gránásy, L., Pusztai, T., and Börzsönyi, T. (2006). Phase field theory of nucleation and polycrystalline pattern formation. In Rieth, M. and Schommers, W., editors, *Handbook of Theoretical and Computational Nanotechnology*, volume 9, pages 525–572. North–Holland, Amsterdam.

Guo, X., Shi, S., and Ma, X. (2005). Elastoplastic phase field model for microstructure evolution. *Applied Physics Letters*, 87:221910–1–3.

Guo, X., Shi, S., Zhang, Q., and Ma, X. (2008). An elastoplastic phase-field model for the evolution of hydride precipitation in zirconium, part i: smooth specimens. *Journal of Nuclear Materials*, 378:110–119.

Gurtin, M. (1996). Generalized Ginzburg–Landau and Cahn–Hilliard equations based on a microforce balance. *Physica D*, 92:178–192.

Hill, R. (1950). *The Mathematical Theory of Plasticity*. Oxford University Press.

Hillert, M. (2008). *Phase Equilibria, Phase Diagrams and Phase Transformations: Their Thermodynamic Basis*. University Press, Cambridge.

Jeulin, D. and Ostoja-Starzewski, M. (2001). *Mechanics of Random and Multiscale Microstructures*. CISM Courses and Lectures No. 430, Udine, Springer Verlag.

Johnson, W. and Cahn, J. W. (1984). Elastically induced shape bifurcations of inclusions. *Acta metallurgica*, 32(11):1925–1933.

Johnson, W. C. and Alexander, J. I. D. (1986). Interfacial conditions for thermomechanical equilibrium in two-phase crystals. *Journal of Applied Physics*, 9:2735–2746.

Kaoui, B., Noureddine, M., Nassif, R., and Y., B. (2005). Phase–field modelling of dendritic growth behaviour towards the cooling / heating of pure nickel. *Moroccan Journal of Condensed Matter*, 6(1).

Karma, A., Kessler, D. A., and Levine, H. (2001). Phase–Field model of mode III dynamic fracture. *Phys. Rev. Lett.*, 87(4):045501.

Karma, A. and Lobkovsky, A. E. (2004). Unsteady crack motion and branching in a Phase–Field model of brittle fracture. *Phys. Rev. Lett.*, 92(24):245510.

Khachaturyan, A. (1983). *Theory of Structural Transformations in Solids*. John Wiley & Sons, New York.

Kim, S., Kim, W., and Suzuki, T. (1998). Interfacial compositions of solid and liquid in a phase–field model with finite interface thickness for isothermal solidification in binary alloys. *Physical Review E*, 58(3):3316–3323.

Kim, S., Kim, W., and Suzuki, T. (1999). Phase–field model for binary alloys. *Physical Review E*, 60(6):7186–7197.

Kolling, S., Mueller, R., and Gross, D. (2003). The influence of elastic constants on the shape of an inclusion. *International Journal of Solids and Structures*, 40:4399–4416.

Koslowski, M., Cuitino, A., and Ortiz, M. (2002). A phase–field theory of dislocation dynamics, strain hardening and hysteresis in ductile single crystals. *Journal of the Mechanics and Physics of Solids*, 50:2597–2635.

Koyama, T. (2008). Phase-field modeling of microstructure evolutions in magnetic materials. *Science and Technology of Advanced Materials*, 9.

Krüger, O. (1999). *Modélisation et analyse numérique de problèmes de réaction–diffusion provenant de la solidification d'alliages binaires*. Thèse de doctorat, Ecole Polytechnique Fédérale de Lausanne.

Landheer, H., Offerman, S., Petrov, R., and Kestens, L. (2009). The role of crystal misorientations during solid-state nucleation of ferrite in austenite. *Acta Matarialia*, 57:1486–1496.

Langer, J. and Sekerka, R. (1975). Theory of departure from local equilibrium at the interface of a two-phase diffusion couple. *Acta Metal.*, 23:1225–1237.

Le Bouar, Y., Loiseau, A., and Khachaturyan, A. (1998). Origin of chessboard–like structures in decomposing alloys. Theoretical model and computer simulation. *Acta Metallurgica*, 46(8):2777–2788.

Leblond, J., Mottet, G., and Devaux, J. (1986a). A theoretical and numerical ap proach to the plastic behaviour of steels during phase transformation -I:derivation of general relations. *Journal of the Mechanics and Physics of Solids*, 34:395–409.

Leblond, J., Mottet, G., and Devaux, J. (1986b). A theoretical and numerical approach to the plastic behaviour of steels during phase transformation -II:study of classical plasticity for ideal-plastic phases. *Journal of the Mechanics and Physics of Solids*, 34:411–432.

Lee, J., Earmme, Y., Aaronson, H., and Russell, K. (1980). Plastic relaxation of the transformation strain energy of a misfitting spherical particle: Ideal plastic behavior. *Metallurgical transactions A*, 11A:1837–1847.

Lemaitre, J. and Chaboche, J.-L. (1994). *Mechanics of Solid Materials*. Cambridge University Press.

Liu, Z.-R., Gao, H., Chen, L. Q., and Cho, K. (2003). Patterned nanostructure in AgCo/Pt/MgO(001) thin films. *Phys. Rev. B*, 68(3):035429.

Ma, X., Shi, S., Woo, C., and Chen, L. (2002). Phase–field simulation of hydride precipitation in bi–crystalline zirconium. *Scripta Materialia*, 47:237–241.

Marconi, V. I. and Jagla, E. A. (2005). Diffuse interface approach to brittle fracture. *Physical Review E*, 71(3):036110.

Nakajima, K., Apel, M., and Steinbach, I. (2006). The role of carbon diffusion in ferrite on the kinetics of cooperative growth of pearlite: A multi–phase field study. *Acta Materialia*, 54:3665–3672.

Nemat-Nasser, S. and Hori, M. (1999). *Micromechanics: Overall Properties of heterogeneous Solids*. Elsevier Science Publishers, 2^{nd} edition.

Ode, M., Suzuki, T., Kim, S. G., and Kim, W. T. (2000). Phase–field model for solidification of Fe–C alloys. *Science and Technology of Advanced Materials*, 1:43–49.

Onuki, A. (1989). Ginzburg-landau approach to elastic effects in the phase separation of solids. *Journal of the Physical Society of Japan*, 58:3065–3068.

Parise, M. (1996). *Mécanismes de corrosion des alliages de zirconium : Etude des cinétiques initiales d'oxydation et du comportement mécanique du système métal–oxyde*. Thèse de doctorat, Ecole des Mines de Paris.

Penelle, R., Boisot, P., Béranger, G., and Lacombe, P. (1971). Influence de l'orientation de monocristaux de zirconium sur les textures de croissance de la zircone monoclinique. *Journal of Nuclear Materials*, 30:340–342.

Petit-Grostabussiat, S., Taleb, L., and Jullien, J. (2004). Experimental results on classical plasticity of steels subjected to structural transformations. *International Journal of Plasticity*, 20:1371–1386.

Provatas, N., Goldenfeld, N., and Dantzig, J. (1999). Adaptive mesh refinement computation of solidification microstructures using dynamic data structures. *Journal of Computational Physics*, 148(1):265–290.

Provatas, N., Greenwood, M., Athreya, B., Goldenfeld, N., and Dantzig, J. (2005). Multiscale modeling of solidification: phase-field methods to adaptive mesh refinement. *International Journal of Modern Physics B*, 19:4525–4565.

Qu, J. and Cherkaoui, M. (2006). *Fundamentals of micromechanics of solids*. John Wiley & Sons Inc, Hoboken.

Ratke, L. and Voorhees, P. (2002). *Growth and Coarsening: Ripening in Material Processing*. Springer, Berlin.

Rodney, D., Le Bouar, Y., and Finel, A. (2003). Phase field methods and dislocations. *Acta Materialia*, 51:17–30.

Schrade, D., Mueller, R., Xu, B., and Gross, D. (2007). Domain evolution in ferroelectric materials: A continuum phase field model and finite element implementation. *Computer Methods in Applied Mechanics and Engineering*, 196:4365–4374.

Schrade, D., Müller, R., and Gross, D. (2006). Phase field simulations in ferroelectric materials. *Proc. Appl. Math. Mech.*, 6:455–456.

Seol, D. J., Hu, S. Y., Li, Y. L., Shen, J., Oh, K. H., and Chen, L. Q. (2003). Three-dimensional phase-field modeling of spinodal decomposition in constrained films. *Metals and Materials International*, 9:61–66.

Shen, C., Simmons, J., and Wang, Y. (2006). Effect of elastic interaction on nucleation: I. calculation of the strain energy of nucleus formation in an elastically anisotropic crystal of arbitrary micro structure. *Acta Materialia*, 54:5617–5630.

Simmons, J., Wen, Y., Shen, C., and Wang, Y. (2004). Microstructural development involving nucleation and growth phenomena simulated with the phase field method. *Materials Science and Engineering A*, 365(1):136–143.

Simo, J. and Hughes, T. (1998). *Computational inelasticity*. Springer Verlag, New York.

Smyshlyaev, V. and Fleck, N. (1996). The role of strain gradients in the grain size effect for polycrystals. *Journal of the Mechanics and Physics of Solids*, 44:465–495.

Steinbach, I. and Apel, M. (2006). Multi phase field model for solid state transformation with elastic strain. *Physica D*, 217:153–160.

Steinbach, I. and Apel, M. (2007). The influence of lattice strain on pearlite formation in Fe–C. *Acta Materialia*, 55:4817–4822.

Su, Y. and Landis, C. M. (2007). Continuum thermodynamics of ferroelectric domain evolution: Theory, finite element implementation, and application to domain wall pinning. *Journal of the Mechanics and Physics of Solids*, 55:280–305.

Suquet, P. (1997). *Continuum micromechanics*. CISM Courses and Lectures No. 377, Udine, Springer Verlag, Berlin.

Suzuki, T., Ode, M., Kim, S., and Kim, W. a. (2002). Phase–field model of dendritic growth. *Journal of Crystal Growth*, 237—239:125—131.

Takaki, T., Fukuoka, T., and Y., T. (2005). Phase–field simulation during directional solidification of a binary alloy using adaptive finite element method. *Journal of Crystal Growth*, 283:263–278.

Takaki, T., Yamanaka, A., Higa, Y., and Y., T. (2006). Phase–field simulation during recrystallization process coupled with crystal plasticity theory.

Ubachs, R., Schreurs, P., and Geers, M. (2004). A nonlocal diffuse interface model for microstructure evolution of tin–lead solder. *Journal of the Mechanics and Physics of Solids*, 52:1763–1792.

Ubachs, R., Schreurs, P., and Geers, M. (2005). Phase field dependent viscoplastic behaviour of solder alloys. *International Journal of Solids and Structures*, 42:2533–2558.

Ubachs, R., Schreurs, P., and Geers, M. (2006). Microstructure dependent viscoplastic damage modelling of tin–lead solder. *Journal of the Mechanics and Physics of Solids*, 54:2621–2651.

Uehara, T., Tsujino, T., and Ohno, N. (2007). Elasto-plastic simulation of stress evolution during grain growth using a phase field model. *Journal of Crystal Growth*, 300:530–537.

Vaithyanathan, V., Wolverton, C., and Chen, L. Q. (2004). Multiscale modeling of θ' precipitation in Al-Cu binary alloys. *Acta Materialia*, 52:2973–2987.

Wang, S.-L., Sekerka, R., Wheeler, A., Murray, B., Coriell, S., Braun, R., and McFadden, G. (1993a). Thermodynamically-consistent phase-field models for solidification. *Physica D*, 69:189–200.

Wang, Y., Banerjee, D., Su, C., and Khachaturyan, A. (1998). Field kinetic model and computer simulation of precipitation of Ll_2 ordered intermetallics from F.C.C. solid solution. *Acta Metallurgica*, 46(9):2983–3001.

Wang, Y., Chen, L.-Q., and Khachaturyan, A. (1993b). Kinetics of strain-induced morphological transformation in cubic alloys with a miscibility gap. *Acta Metallurgica et Materialia*, 41:279–296.

Wang, Y., Jin, Y., Cuitinõa, and Khachaturyan, A. (2001). Nano–scale phase field microelasticity theory of dislocations : Model and 3D simulations. *Acta Metallurgica*, 49:1847–1857.

Wang, Y. and Khachaturyan, A. (1995a). Shape instability during precipitate growth in coherent solids. *Acta metall, mater.*, 43(5):1837–1857.

Wang, Y. and Khachaturyan, A. (1995b). Shape instability during precipitate growth in coherent solids. *Acta Metall. mater.*, 43(5):1837–1857.

Warren, J., Kobayashi, R., Lobovsky, A., and W.C., C. (2003). Extending phase field models of solidification to polycrystalline materials. *Acta Metallurgica*, 51:6035–6058.

Williams, R. O. (1984). The calculation of coherent phase equilibria. *Calphad*, 8(1):1–14.

Yamanaka, A., Takaki, T., and Tomita, Y. (2008). Elastoplastic phase-field simulation of self- and plastic accomodations in cubic→tetragonal martensitic transformation. *Materials Science & Engineering A*, 491:378–384.

Yue, P., Zhou, C., Feng, J. J., Ollivier–Gooch, C. F., and Hu, H. H. (2006). Phase–field simulations of interfacial dynamics in viscoelastic fluids using finite elements with adaptive meshing. *Journal of Computational Physics*, pages 47–67.

Zhou, N., Shen, C., Mills, M., and Wang, Y. (2007). Phase field modeling of channel dislocation activity and γ' rafting in single crystal Ni-Al. *Acta Materialia*, 55:5369–5381.

Zhou, N., Shen, C., Mills, M., and Wang, Y. (2008). Contributions from elastic inhomogeneity and from plasticity to γ' rafting in single-crystal ni-al. *Acta Materialia*, 56:6156–6173.

Zhu, J., Liu, Z., Vaithyanathan, V., and Chen, L. (2002). Linking phase–field model to CALPHAD: application to precipitate shape evolution in Ni–base alloys. *Scripta Materialia*, 46:401–406.

Appendices

Annexe -A-

Algorithm to calculate equilibrium concentrations of both phases

Variable : $c_\alpha, c_\beta, b_\alpha, b_\beta, k_\alpha, k_\beta, ENER$

Begin

If $(b_\alpha = b_\beta)$ then

For this case, the tangent line common to f_α and f_β is simply the x axis. Thus, the equilibrium concentrations are expressed as follow

$$\mu_{\text{eq}} = 0 \quad \Longrightarrow \quad \begin{cases} a_\alpha = c_\alpha \\ a_\beta = c_\beta \end{cases}$$

Else

If $(k_\alpha = k_\beta)$ then

Equality of the chemical potentials in both phases in equilibrium :

$$\mu_{\text{eq}} = k_\alpha \left(c_\alpha - a_\alpha\right) = k_\beta \left(c_\beta - a_\beta\right)$$
$$(II.86) : \; -\Delta c\, \mu_{\text{eq}} + \Delta b = 0$$

The equilibrium concentrations are :

$$\mathrm{a}_\alpha = \mathrm{c}_\alpha - \frac{1}{\mathrm{k}_\alpha}\frac{\Delta \mathrm{b}}{\Delta \mathrm{c}} \qquad \text{and} \qquad \mathrm{a}_\beta = \mathrm{c}_\beta - \frac{1}{\mathrm{k}_\beta}\frac{\Delta \mathrm{b}}{\Delta \mathrm{c}}$$

Else

Solve the quadratic equation

$$(II.86) : \Delta\widetilde{\mathrm{k}}\mu_{\text{eq}}^2 - \Delta \mathrm{c}\, \mu_{\text{eq}} + \Delta \mathrm{b} = 0$$
$$\Delta = \Delta \mathrm{c}^2 - 4\Delta\widetilde{\mathrm{k}}\Delta \mathrm{b}$$

If $(\Delta < 0)$ then

There is no solution

Elseif $(\Delta = 0)$ then

One solution : the equilibrium concentrations are expressed as :

$$a_\alpha = c_\alpha - \frac{1}{k_\alpha}\frac{\Delta c}{2\Delta\widetilde{k}} = c_\alpha - \frac{1}{k_\alpha}\frac{2\Delta b}{\Delta c}$$

$$a_\beta = c_\beta - \frac{1}{k_\alpha}\frac{\Delta c}{2\Delta\widetilde{k}} = c_\beta - \frac{1}{k_\alpha}\frac{2\Delta b}{\Delta c}$$

If $((a_\alpha < 0)$ or $(a_\alpha > 1)$ or $(a_\beta < 0)$ or $(a_\beta > 1))$ then

There is no solution

Elseif

One solution (a_α, a_β)

Endif

Else

There are two solutions

$$a'_\alpha = c_\alpha - \frac{1}{k_\alpha}\frac{\Delta c + \sqrt{\Delta}}{2\Delta\widetilde{k}} \quad \text{and} \quad a'_\beta = c_\beta - \frac{1}{k_\beta}\frac{\Delta c + \sqrt{\Delta}}{2\Delta\widetilde{k}}$$

$$a''_\alpha = c_\alpha - \frac{1}{k_\alpha}\frac{\Delta c - \sqrt{\Delta}}{2\Delta\widetilde{k}} \quad \text{and} \quad a''_\beta = c_\beta - \frac{1}{k_\beta}\frac{\Delta c - \sqrt{\Delta}}{2\Delta\widetilde{k}}$$

If $((a'_\alpha < 0)$ or $(a'_\alpha > 1)$ or $(a'_\beta < 0)$ or $(a'_\beta > 1))$ then

If $((a''_\alpha < 0)$ or $(a''_\alpha > 1)$ or $(a''_\beta < 0)$ or $(a''_\beta > 1))$ then

There is no solution

Else

$$a_\alpha = a''_\alpha = c_\alpha - \frac{1}{k_\alpha}\frac{\Delta c - \sqrt{\Delta}}{2\Delta\widetilde{k}}$$

$$a_\beta = a''_\beta = c_\beta - \frac{1}{k_\beta}\frac{\Delta c - \sqrt{\Delta}}{2\Delta\widetilde{k}}$$

Endif

Else

If $((a''_\alpha < 0)$ or $(a''_\alpha > 1)$ or $(a''_\beta < 0)$ or $(a''_\beta > 1))$ then

$$a_\alpha = a'_\alpha = c_\alpha - \frac{1}{k_\alpha}\frac{\Delta c + \sqrt{\Delta}}{2\Delta\widetilde{k}}$$

$$a_\beta = a'_\beta = c_\beta - \frac{1}{k_\beta}\frac{\Delta c + \sqrt{\Delta}}{2\Delta\widetilde{k}}$$

Elseif

There are two possible solutions : (a'_α, a'_β) and (a''_α, a''_β) ($Fig.A.1$)

If $(\mathrm{ENER} = 0)$ then

The equilibrium concentrations are (a'_α, a'_β)

Elseif $(\mathrm{ENER} = 1)$ then

The equilibrium concentrations are (a''_α, a''_β)

Else

ENER must be equal to 0 or 1

Endif

Endif

Endif

Endif

Endif

Endif

Endif

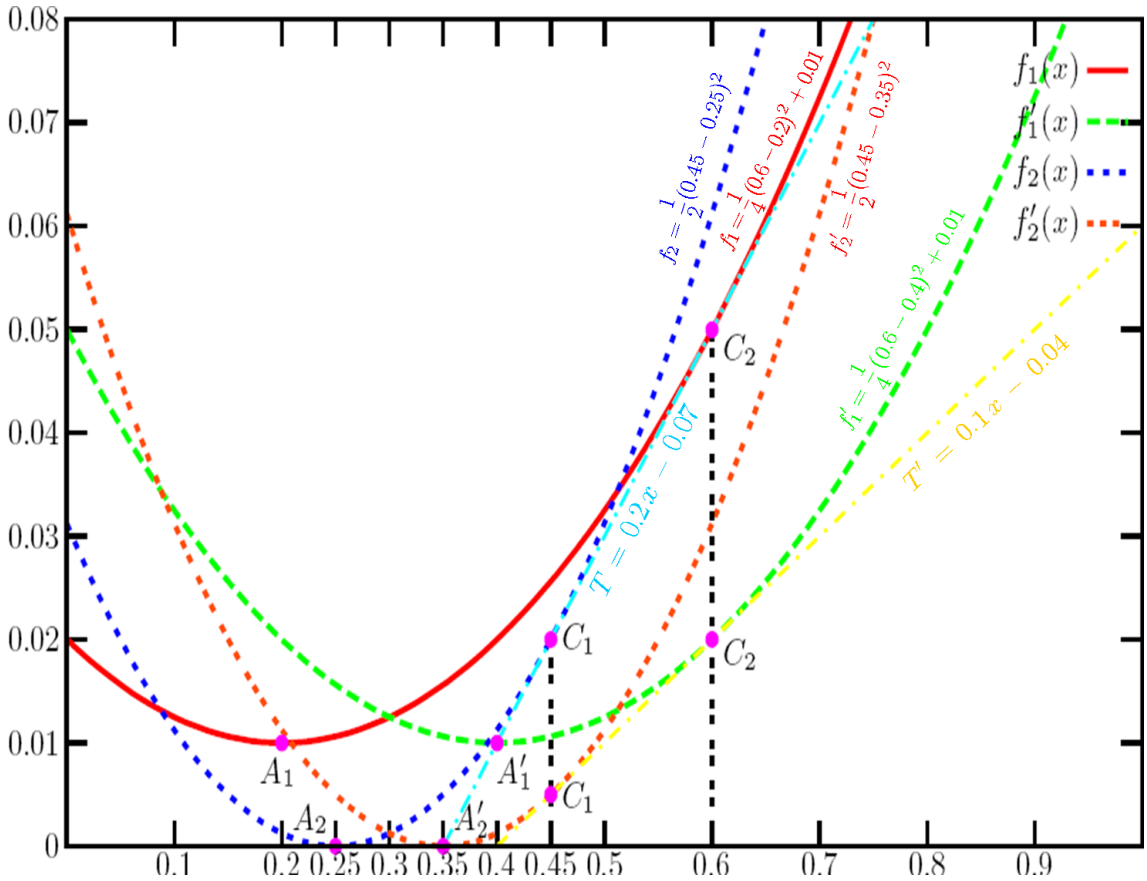

Figure A.1 : Two set of specific free energy densities (f_α, f_β) and (f'_α, f'_β), with two different common tangent lines T and T' respectively, for a fixed equilibrium concentrations (c_α, c_β).

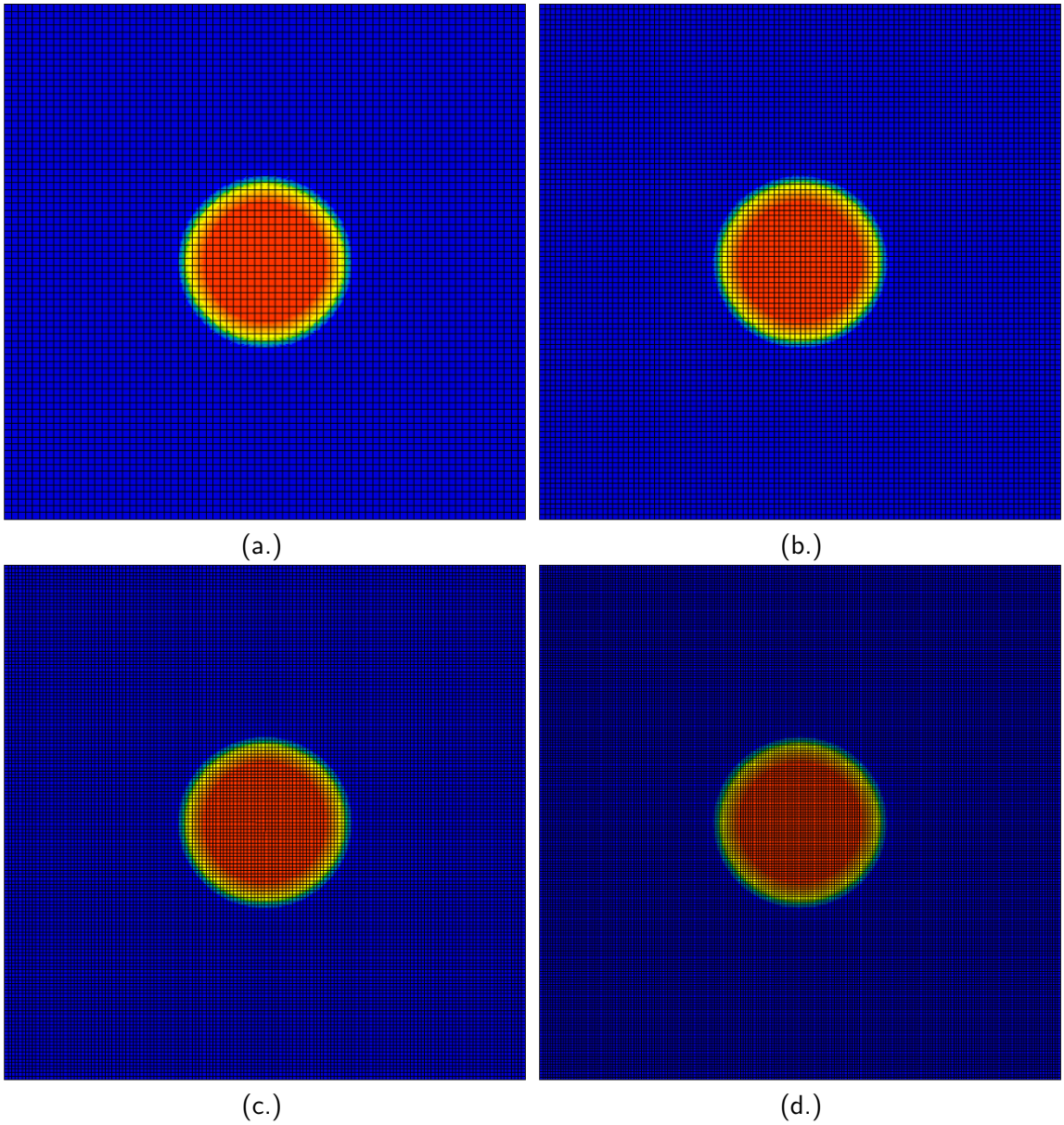

Figure A.2 : Finite element meshes with different mesh densities: 5 (a), 8 (b), 11 (c) and 14(d) nodes in the diffuse interface.

Annexe -B-

Derivation of the elastic strain and the effective elasticity tensor

In order to express the elastic driving force for the phase transformation process, the derivations of the elastic strain and the effective elasticity tensor with respect to the order parameter for various interpolation schemes are summarised below :

Voigt/Taylor $\left\{ \begin{array}{l} \underset{\sim}{\varepsilon}_\alpha = \underset{\sim}{\varepsilon}_\beta = \underset{\sim}{\varepsilon} \\ \underset{\sim}{\boldsymbol{\sigma}} = \phi\, \underset{\sim}{\boldsymbol{\sigma}}_\alpha + (1-\phi)\, \underset{\sim}{\boldsymbol{\sigma}}_\beta \end{array} \right.$

$$\underset{\sim}{\varepsilon}^e = \underset{\approx}{\boldsymbol{C}}_{eff}^{-1} : (\phi \underset{\approx}{\boldsymbol{C}}_\alpha : \underset{\sim}{\varepsilon}_\alpha^e + (1-\phi) \underset{\approx}{\boldsymbol{C}}_\beta : \underset{\sim}{\varepsilon}_\beta^e)$$
$$\underset{\sim}{\varepsilon}^\star = \underset{\approx}{\boldsymbol{C}}_{eff}^{-1} : (\phi \underset{\approx}{\boldsymbol{C}}_\alpha : \underset{\sim}{\varepsilon}_\alpha^\star + (1-\phi) \underset{\approx}{\boldsymbol{C}}_\beta : \underset{\sim}{\varepsilon}_\beta^\star)$$

$$\underset{\approx}{\boldsymbol{C}}_{eff} = (\phi\, \underset{\approx}{\boldsymbol{C}}_\alpha + (1-\phi) \underset{\approx}{\boldsymbol{C}}_\beta)$$

$$\frac{\partial \underset{\approx}{\boldsymbol{C}}_{eff}}{\partial \phi} = \underset{\approx}{\boldsymbol{C}}_\alpha - \underset{\approx}{\boldsymbol{C}}_\beta, \qquad \frac{\partial^2 \underset{\approx}{\boldsymbol{C}}_{eff}}{\partial \phi^2} = 0, \qquad \frac{\partial^3 \underset{\approx}{\boldsymbol{C}}_{eff}}{\partial \phi^3} = 0$$

$$\frac{\partial \underset{\sim}{\varepsilon}^e}{\partial \phi} = \frac{\partial \underset{\approx}{\boldsymbol{C}}_{eff}^{-1}}{\partial \phi} : (\phi \underset{\approx}{\boldsymbol{C}}_\alpha : \underset{\sim}{\varepsilon}_\alpha^e + (1-\phi) \underset{\approx}{\boldsymbol{C}}_\beta : \underset{\sim}{\varepsilon}_\beta^e) + \underset{\approx}{\boldsymbol{C}}_{eff}^{-1} : (\underset{\approx}{\boldsymbol{C}}_\alpha : \underset{\sim}{\varepsilon}_\alpha^e - \underset{\approx}{\boldsymbol{C}}_\beta : \underset{\sim}{\varepsilon}_\beta^e)$$
$$\text{avec } \frac{\partial \underset{\approx}{\boldsymbol{C}}_{eff}^{-1}}{\partial \phi} = \underset{\approx}{\boldsymbol{C}}_{eff}^{-1} : (\underset{\approx}{\boldsymbol{C}}_\beta - \underset{\approx}{\boldsymbol{C}}_\alpha) : \underset{\approx}{\boldsymbol{C}}_{eff}^{-1}$$

$$\frac{\partial^2 \underset{\sim}{\varepsilon}^e}{\partial \phi^2} = \frac{\partial^2 \underset{\approx}{\boldsymbol{C}}_{eff}^{-1}}{\partial \phi^2} : (\phi \underset{\approx}{\boldsymbol{C}}_\alpha : \underset{\sim}{\varepsilon}_\alpha^e + (1-\phi) \underset{\approx}{\boldsymbol{C}}_\beta : \underset{\sim}{\varepsilon}_\beta^e) + \frac{\partial \underset{\approx}{\boldsymbol{C}}_{eff}^{-1}}{\partial \phi} : (\underset{\approx}{\boldsymbol{C}}_\alpha : \underset{\sim}{\varepsilon}_\alpha^e - \underset{\approx}{\boldsymbol{C}}_\beta : \underset{\sim}{\varepsilon}_\beta^e)$$
$$\text{avec } \frac{\partial^2 \underset{\approx}{\boldsymbol{C}}_{eff}^{-1}}{\partial \phi^2} = 2 \underset{\approx}{\boldsymbol{C}}_{eff}^{-1} : (\underset{\approx}{\boldsymbol{C}}_\beta - \underset{\approx}{\boldsymbol{C}}_\alpha) :: \frac{\partial \underset{\approx}{\boldsymbol{C}}_{eff}^{-1}}{\partial \phi}$$

$$\frac{\partial^3 \underset{\sim}{\varepsilon}^e}{\partial \phi^3} = \frac{\partial^3 \underset{\approx}{\boldsymbol{C}}_{eff}^{-1}}{\partial \phi^3} : (\phi \underset{\approx}{\boldsymbol{C}}_\alpha : \underset{\sim}{\varepsilon}_\alpha^e + (1-\phi) \underset{\approx}{\boldsymbol{C}}_\beta : \underset{\sim}{\varepsilon}_\beta^e) + 2\, \frac{\partial^2 \underset{\approx}{\boldsymbol{C}}_{eff}^{-1}}{\partial \phi^2} : (\underset{\approx}{\boldsymbol{C}}_\alpha : \underset{\sim}{\varepsilon}_\alpha^e - \underset{\approx}{\boldsymbol{C}}_\beta : \underset{\sim}{\varepsilon}_\beta^e)$$
$$\text{avec } \frac{\partial^3 \underset{\approx}{\boldsymbol{C}}_{eff}^{-1}}{\partial \phi^3} = 2 \frac{\partial \underset{\approx}{\boldsymbol{C}}_{eff}^{-1}}{\partial \phi} : (\underset{\approx}{\boldsymbol{C}}_\beta - \underset{\approx}{\boldsymbol{C}}_\alpha) : \frac{\partial \underset{\approx}{\boldsymbol{C}}_{eff}^{-1}}{\partial \phi} + 2 \underset{\approx}{\boldsymbol{C}}_{eff}^{-1} : (\underset{\approx}{\boldsymbol{C}}_\beta - \underset{\approx}{\boldsymbol{C}}_\alpha) : \frac{\partial^2 \underset{\approx}{\boldsymbol{C}}_{eff}^{-1}}{\partial \phi^2}$$

Khachaturyan $\left\{ \begin{array}{l} \underset{\sim}{\varepsilon}^{\star} = \phi\, \underset{\sim}{\varepsilon}^{\star}_{\alpha}(c) + (1-\phi)\, \underset{\sim}{\varepsilon}^{\star}_{\beta} \\ \underset{\approx}{\boldsymbol{C}}_{eff} = \phi\, \underset{\approx}{\boldsymbol{C}}_{\alpha} + (1-\phi)\, \underset{\approx}{\boldsymbol{C}}_{\beta} \end{array} \right.$

$$\underset{\sim}{\varepsilon}^{e} = \underset{\sim}{\varepsilon} - \underset{\sim}{\varepsilon}^{\star} = \underset{\sim}{\varepsilon} - \phi\, \underset{\sim}{\varepsilon}^{\star}_{\alpha} + (1-\phi)\, \underset{\sim}{\varepsilon}^{\star}_{\beta}$$

$$\frac{\partial \underset{\sim}{\varepsilon}^{e}}{\partial \phi} = \underset{\sim}{\varepsilon}^{\star}_{\beta} - \underset{\sim}{\varepsilon}^{\star}_{\alpha}, \qquad \frac{\partial^2 \underset{\sim}{\varepsilon}^{e}}{\partial \phi^2} = 0, \qquad \frac{\partial^3 \underset{\sim}{\varepsilon}^{e}}{\partial \phi^3} = 0$$

$$\frac{\partial \underset{\sim}{\varepsilon}^{e}}{\partial c} = \delta_{\beta} - \delta_{\alpha}, \qquad \frac{\partial^2 \underset{\sim}{\varepsilon}^{e}}{\partial c^2} = 0, \qquad \frac{\partial^3 \underset{\sim}{\varepsilon}^{e}}{\partial c^3} = 0$$

$$\frac{\partial \underset{\approx}{\boldsymbol{C}}_{eff}}{\partial \phi} = \underset{\approx}{\boldsymbol{C}}_{\alpha} - \underset{\approx}{\boldsymbol{C}}_{\beta}, \qquad \frac{\partial^2 \underset{\approx}{\boldsymbol{C}}_{eff}}{\partial \phi^2} = 0, \qquad \frac{\partial^3 \underset{\approx}{\boldsymbol{C}}_{eff}}{\partial \phi^3} = 0$$

$$\frac{\partial \underset{\approx}{\boldsymbol{C}}_{eff}}{\partial c} = 0, \qquad \frac{\partial^2 \underset{\approx}{\boldsymbol{C}}_{eff}}{\partial c^2} = 0, \qquad \frac{\partial^3 \underset{\approx}{\boldsymbol{C}}_{eff}}{\partial c^3} = 0$$

Sachs/Reuss $\left\{ \begin{array}{l} \underset{\sim}{\varepsilon} = \phi\, \underset{\sim}{\varepsilon}_{\alpha} + (1-\phi)\, \underset{\sim}{\varepsilon}_{\beta} \\ \underset{\sim}{\sigma}_{\alpha} = \underset{\sim}{\sigma}_{\beta} = \underset{\sim}{\sigma} \end{array} \right.$

$$\underset{\sim}{\varepsilon}^{e} = \phi\, \underset{\sim}{\varepsilon}^{e}_{\alpha} + (1-\phi) \underset{\sim}{\varepsilon}^{e}_{\beta}$$

$$\underset{\sim}{\varepsilon}^{\star}(\phi) = \phi\, \underset{\sim}{\varepsilon}^{\star}_{\alpha} + (1-\phi) \underset{\sim}{\varepsilon}^{\star}_{\beta}$$

$$\underset{\approx}{\boldsymbol{C}}_{eff} = (\phi\, \underset{\approx}{\boldsymbol{S}}_{\alpha} + (1-\phi) \underset{\approx}{\boldsymbol{S}}_{\beta})^{-1}$$

$$\frac{\partial \underset{\approx}{\boldsymbol{C}}_{eff}}{\partial \phi} = \underset{\approx}{\boldsymbol{C}}_{eff} : (\underset{\approx}{\boldsymbol{S}}_{\beta} - \underset{\approx}{\boldsymbol{S}}_{\alpha}) : \underset{\approx}{\boldsymbol{C}}_{eff}$$

$$\frac{\partial^2 \underset{\approx}{\boldsymbol{C}}_{eff}}{\partial \phi^2} = 2\, \underset{\approx}{\boldsymbol{C}}_{eff} : (\underset{\approx}{\boldsymbol{S}}_{\beta} - \underset{\approx}{\boldsymbol{S}}_{\alpha}) : \frac{\partial \underset{\approx}{\boldsymbol{C}}_{eff}}{\partial \phi}$$

$$\frac{\partial^3 \underset{\approx}{\boldsymbol{C}}_{eff}}{\partial \phi^3} = 2\, \frac{\partial \underset{\approx}{\boldsymbol{C}}_{eff}}{\partial \phi} : (\underset{\approx}{\boldsymbol{S}}_{\beta} - \underset{\approx}{\boldsymbol{S}}_{\alpha}) : \frac{\partial \underset{\approx}{\boldsymbol{C}}_{eff}}{\partial \phi} + 2\, \underset{\approx}{\boldsymbol{C}}_{eff} : (\underset{\approx}{\boldsymbol{S}}_{\beta} - \underset{\approx}{\boldsymbol{S}}_{\alpha}) : \frac{\partial^2 \underset{\approx}{\boldsymbol{C}}_{eff}}{\partial \phi^2}$$

$$\frac{\partial \underset{\sim}{\varepsilon}^{e}}{\partial \phi} = \underset{\sim}{\varepsilon}^{e}_{\alpha} - \underset{\sim}{\varepsilon}^{e}_{\beta}$$

$$\frac{\partial^2 \underset{\sim}{\varepsilon}^{e}}{\partial \phi^2} = 0, \qquad \frac{\partial^3 \underset{\sim}{\varepsilon}^{e}}{\partial \phi^3} = 0$$

Annexe -C-

Expression of the total strain rate tensors for both phases

According to Reuss/Sachs' scheme, we have, at each material point:

$$\dot{\underset{\sim}{\sigma}} = \dot{\underset{\sim}{\sigma}}_\alpha = \dot{\underset{\sim}{\sigma}}_\beta \tag{C.1}$$

The linear elastic law is applied for each phase, assuming $\dot{\underset{\approx}{C}}_\alpha = \dot{\underset{\approx}{C}}_\beta = 0$ and taking the partition hypothesis of strain into account:

$$\underset{\approx}{C}_\alpha : (\dot{\underset{\sim}{\varepsilon}}_\alpha - \dot{\underset{\sim}{\varepsilon}}^p_\alpha) = \underset{\approx}{C}_\beta : (\dot{\underset{\sim}{\varepsilon}}_\beta - \dot{\underset{\sim}{\varepsilon}}^p_\beta) \tag{C.2}$$

The substitution of the plastic multiplier (III.82) into (III.75) leads to the evolution equation of the plastic strain:

$$\dot{\underset{\sim}{\varepsilon}}^p_k = (L_k \underset{\sim}{n}_k : \underset{\approx}{C}_k : \dot{\underset{\sim}{\varepsilon}}_k)\underset{\sim}{n}_k \tag{C.3}$$

where L_k is given by (III.84).

After combining Eq.(C.2) and Eq.(C.3), we obtain, therefore:

$$(\underset{\approx}{C}_\alpha - L_\alpha (\underset{\approx}{C}_\alpha : \underset{\sim}{n}_\alpha) \otimes (\underset{\sim}{n}_\alpha : \underset{\approx}{C}_\alpha)) : \dot{\underset{\sim}{\varepsilon}}_\alpha = (\underset{\approx}{C}_\beta - L_\beta (\underset{\approx}{C}_\beta : \underset{\sim}{n}_\beta) \otimes (\underset{\sim}{n}_\beta : \underset{\approx}{C}_\beta)) : \dot{\underset{\sim}{\varepsilon}}_\beta$$

Consequently, we deduce the following relation, which relates the total strain rates of both phases $\dot{\underset{\sim}{\varepsilon}}_\alpha$ and $\dot{\underset{\sim}{\varepsilon}}_\beta$:

$$\dot{\underset{\sim}{\varepsilon}}_\beta = \left[\underset{\approx}{C}_\beta - L_\beta (\underset{\approx}{C}_\beta : \underset{\sim}{n}_\beta) \otimes (\underset{\sim}{n}_\beta : \underset{\approx}{C}_\beta)\right]^{-1} . \left(\underset{\approx}{C}_\alpha - L_\alpha (\underset{\approx}{C}_\alpha : \underset{\sim}{n}_\alpha) \otimes (\underset{\sim}{n}_\alpha : \underset{\approx}{C}_\alpha)\right) : \dot{\underset{\sim}{\varepsilon}}_\alpha \tag{C.4}$$

Moreover, the average strain rate is then written in the following form:

$$\begin{aligned} \dot{\underset{\sim}{\varepsilon}} &= \phi\dot{\underset{\sim}{\varepsilon}}_\alpha + (1-\phi)\dot{\underset{\sim}{\varepsilon}}_\beta + \dot{\phi}(\underset{\sim}{\varepsilon}_\alpha - \underset{\sim}{\varepsilon}_\beta) \\ &= \phi\dot{\underset{\sim}{\varepsilon}}_\alpha + (1-\phi)\left[\underset{\approx}{C}_\beta - L_\beta (\underset{\approx}{C}_\beta : \underset{\sim}{n}_\beta) \otimes (\underset{\sim}{n}_\beta : \underset{\approx}{C}_\beta)\right]^{-1} \\ &\quad . \left(\underset{\approx}{C}_\alpha - L_\alpha (\underset{\approx}{C}_\alpha : \underset{\sim}{n}_\alpha) \otimes (\underset{\sim}{n}_\alpha : \underset{\approx}{C}_\alpha)\right) : \dot{\underset{\sim}{\varepsilon}}_\alpha + \dot{\phi}(\underset{\sim}{\varepsilon}_\alpha - \underset{\sim}{\varepsilon}_\beta) \end{aligned} \tag{C.5}$$

Consequently, the total strain rates in α and β phases are obtained as functions of the total strain rates and the current strain states in each phase:

$$\begin{aligned} \dot{\underset{\sim}{\varepsilon}}_\alpha &= \{\phi\underset{\approx}{I} + (1-\phi)\left[\underset{\approx}{C}_\beta - L_\beta (\underset{\approx}{C}_\beta : \underset{\sim}{n}_\beta) \otimes (\underset{\sim}{n}_\beta : \underset{\approx}{C}_\beta)\right]^{-1} \\ &\quad \left[\underset{\approx}{C}_\alpha - L_\alpha (\underset{\approx}{C}_\alpha : \underset{\sim}{n}_\alpha) \otimes (\underset{\sim}{n}_\alpha : \underset{\approx}{C}_\alpha)\right]\}^{-1} : (\dot{\underset{\sim}{\varepsilon}} - \dot{\phi}(\underset{\sim}{\varepsilon}_\alpha - \underset{\sim}{\varepsilon}_\beta)) \end{aligned} \tag{C.6}$$

$$\begin{aligned}\underset{\approx}{\dot{\boldsymbol{\varepsilon}}}_\beta &= \Big\{(1-\phi)\underset{\approx}{\boldsymbol{I}} + \phi\left[\underset{\approx}{\boldsymbol{C}}_\alpha - L_\alpha\left(\underset{\approx}{\boldsymbol{C}}_\alpha : \underset{\sim}{\boldsymbol{n}}_\alpha\right)\otimes\left(\underset{\sim}{\boldsymbol{n}}_\alpha : \underset{\approx}{\boldsymbol{C}}_\alpha\right)\right]^{-1} \\ &\quad \left[\underset{\approx}{\boldsymbol{C}}_\beta - L_\beta\left(\underset{\approx}{\boldsymbol{C}}_\beta : \underset{\sim}{\boldsymbol{n}}_\beta\right)\otimes\left(\underset{\sim}{\boldsymbol{n}}_\beta : \underset{\approx}{\boldsymbol{C}}_\beta\right)\right]\Big\}^{-1} : \left(\underset{\approx}{\dot{\boldsymbol{\varepsilon}}} - \dot{\phi}(\underset{\approx}{\boldsymbol{\varepsilon}}_\alpha - \underset{\approx}{\boldsymbol{\varepsilon}}_\beta)\right)\end{aligned} \tag{C.7}$$

Annexe -D-

Calculation of the stiffness matrices

The element generalized stiffness matrix (III.102) is divided into the following submatrices:

$$(K^e_{uu})_{ij} = \frac{\partial (\mathcal{R}^e_u)_i}{\partial u^e_j} = -\int_{V^e} \left[\frac{\partial \underset{\sim}{\boldsymbol{\sigma}}}{\partial \underline{\boldsymbol{u}}^e}\right]_{ik} \left[\underset{\sim}{\boldsymbol{B}}^e\right]_{lj} dv = -\int_{V^e} \left[\underset{\sim}{\boldsymbol{B}}^e\right]_{ik} \left[\frac{\partial^2 f_u(c,\phi,\underset{\sim}{\boldsymbol{\varepsilon}})}{\partial \underset{\sim}{\boldsymbol{\varepsilon}}^2}\right]_{kl} \left[\underset{\sim}{\boldsymbol{B}}^e\right]_{lj} dv$$

$$(K^e_{uc})_{ij} = \frac{\partial (\mathcal{R}^e_u)_i}{\partial c^e_j} = -\int_{V^e} \left[\frac{\partial \underset{\sim}{\boldsymbol{\sigma}}}{\partial \underline{\boldsymbol{c}}^e}\right]_{ik} \left[\underset{\sim}{\boldsymbol{B}}^e\right]_{lj} dv = -\int_{V^e} \left[\underset{\sim}{\boldsymbol{B}}^e\right]_{ik} \left(\frac{\partial^2 f_u(c,\phi,\underset{\sim}{\boldsymbol{\varepsilon}})}{\partial c\, \partial \underset{\sim}{\boldsymbol{\varepsilon}}}\right)_k N^e_j \, dv$$

$$(K^e_{u\phi})_{ij} = \frac{\partial (\mathcal{R}^e_u)_i}{\partial \phi^e_j} = -\int_{V^e} \left[\frac{\partial \underset{\sim}{\boldsymbol{\sigma}}}{\partial \underline{\boldsymbol{\phi}}^e}\right]_{ik} \left[\underset{\sim}{\boldsymbol{B}}^e\right]_{lj} dv = -\int_{V^e} \left[\underset{\sim}{\boldsymbol{B}}^e\right]_{ik} \left(\frac{\partial^2 f_u(c,\phi,\underset{\sim}{\boldsymbol{\varepsilon}})}{\partial \phi\, \partial \underset{\sim}{\boldsymbol{\varepsilon}}}\right)_k N^e_j \, dv$$

$$\begin{aligned}
(K^e_{cu})_{ij} &= \frac{\partial (\mathcal{R}^e_c)_i}{\partial u^e_j} = \int_{V^e} -\left[B^e\right]_{ik} \left[\frac{\partial \underline{\boldsymbol{J}}}{\partial \underline{\boldsymbol{u}}^e}\right]_{kj} dv \\
&= \kappa \left[B^e\right]_{ik} \left(\left(\frac{\partial^3 f_u}{\partial \underset{\sim}{\boldsymbol{\varepsilon}}\, \partial c^2}\right)_k (\boldsymbol{\nabla} c)_l + \left(\frac{\partial^3 f_u}{\partial \underset{\sim}{\boldsymbol{\varepsilon}}\, \partial \phi\, \partial c}\right)_k (\boldsymbol{\nabla} \phi)_l\right) \left[B^e\right]_{lj} \\
&+ \kappa \left[\mathcal{R}^e\right]_{ik} \left(\frac{\partial^3 f_u}{\partial \underset{\sim}{\boldsymbol{\varepsilon}}^2\, \partial c}\right)_{kn} \left(\frac{\partial \underset{\sim}{\boldsymbol{\varepsilon}}}{\partial \underline{\boldsymbol{x}}}\right)_{nl} \left[B^e\right]_{lj}
\end{aligned}$$

$$\begin{aligned}
(K^e_{cc})_{ij} &= \frac{\partial (\mathcal{R}^e_c)_i}{\partial c^e_j} = \int_{V^e} \frac{1}{\Delta t} N^e_i N^e_j - \left[B^e\right]_{ik} \left[\frac{\partial \underline{\boldsymbol{J}}}{\partial \underline{\boldsymbol{c}}^e}\right]_{kj} dv \\
&= \int_{V^e} \frac{1}{\Delta t} N^e_i N^e_j + \kappa \left[B^e\right]_{ik} \left(\left(\frac{\partial^3 f_{ch}}{\partial c^3} + \frac{\partial^3 f_u}{\partial c^3}\right) \boldsymbol{\nabla} c + \left(\frac{\partial^3 f_{ch}}{\partial c\, \partial \phi\, \partial c} + \frac{\partial^3 f_u}{\partial c\, \partial \phi\, \partial c}\right) \boldsymbol{\nabla} \phi\right)_k N^e_j \\
&+ \kappa \left[B^e\right]_{ik} \left(\frac{\partial \underset{\sim}{\boldsymbol{\varepsilon}}}{\partial \underline{\boldsymbol{x}}}\right)_{kl} \left(\frac{\partial f_u}{\partial c\, \partial \underset{\sim}{\boldsymbol{\varepsilon}}\, \partial c}\right)_l N^e_j + \kappa \left(\frac{\partial^2 f_{ch}}{\partial c^2} + \frac{\partial^2 f_u}{\partial c^2}\right) \left[B^e\right]_{ik} \left[B^e\right]_{kj} dv
\end{aligned}$$

$$
\begin{aligned}
(K^e_{c\phi})_{ij} &= \frac{\partial(\mathcal{R}^e_c)_i}{\partial \phi^e_j} = \int_{V^e} - [B^e]_{ik} \left[\frac{\partial \underline{\boldsymbol{J}}}{\partial \underline{\boldsymbol{\phi}}^{\,e}} \right]_{kj} dv \\
&= \int_{V^e} \kappa \, [B^e]_{ik} \left(\left(\frac{\partial^3 f_{ch}}{\partial \phi \, \partial c^2} + \frac{\partial^3 f_u}{\partial \phi \, \partial c^2} \right) \boldsymbol{\nabla} c + \left(\frac{\partial^3 f_{ch}}{\partial \phi^2 \partial c} + \frac{\partial^3 f_u}{\partial \phi^2 \, \partial c} \right) \boldsymbol{\nabla} \phi \right)_k N^e_j \\
&+ \kappa \, [B^e]_{ik} \left(\frac{\partial \underset{\sim}{\boldsymbol{\varepsilon}}}{\partial \underline{\boldsymbol{x}}} \right)_{kl} \left(\frac{\partial f_u}{\partial \phi \partial \underset{\sim}{\boldsymbol{\varepsilon}} \partial c} \right)_l N^e_j + \frac{\partial \kappa}{\partial \phi} \left(\boldsymbol{\nabla} \mu \right)_i N^e_j \\
&+ \kappa \left(\frac{\partial^2 f_{ch}}{\partial \phi \, \partial c} + \frac{\partial^2 f_u}{\partial \phi \, \partial c} \right) [B^e]_{ik} \, [B^e]_{kj} \, dv
\end{aligned}
$$

$$
(K^e_{\phi u})_{ij} = \frac{\partial(\mathcal{R}^e_\phi)_i}{\partial u^e_j} = \int_{V^e} [N^e]_{ik} \left[\frac{\partial \pi}{\partial \underline{\boldsymbol{u}}^{\,e}} \right]_{kj} dv = \int_{V^e} - [B^e]_{ik} \left(\frac{\partial^2 f_u}{\partial \underset{\sim}{\boldsymbol{\varepsilon}} \, \partial \phi} \right)_k N^e_j \, dV
$$

$$
(K^e_{\phi c})_{ij} = \frac{\partial(\mathcal{R}^e_\phi)_i}{\partial c^e_j} = \int_{V^e} N^e_i \left(\frac{\partial \pi}{\partial \underline{\boldsymbol{c}}^{\,e}} \right)_j dv = \int_{V^e} (- \frac{\partial^2 f_{ch}(c,\phi)}{\partial c \; \partial \phi} - \frac{\partial^2 f_u(c,\phi,\underset{\sim}{\boldsymbol{\varepsilon}})}{\partial c \, \partial \phi}) N^e_i \, N^e_j dv
$$

$$
\begin{aligned}
(K^e_{\phi\phi})_{ij} &= \frac{\partial(\mathcal{R}^e_\phi)_i}{\partial \phi^e_j} = \int_{V^e} N^e_i \left(\frac{\partial \pi}{\partial \underline{\boldsymbol{\phi}}^{\,e}} \right)_j - [B^e]_{ik} \left[\frac{\partial \underline{\boldsymbol{\xi}}}{\partial \underline{\boldsymbol{\phi}}^{\,e}} \right]_{kj} dv \\
&= \int_{V^e} (- \frac{\beta}{\Delta t} - \frac{\partial^2 f_{ch}(c,\phi)}{\partial \phi^2} - \frac{\partial^2 f_u(c,\phi,\underset{\sim}{\boldsymbol{\varepsilon}})}{\partial \phi^2}) N^e_i \, N^e_j - \alpha \, [B^e]_{ik} \, [B^e]_{kj} \, dv
\end{aligned}
$$

Annexe -E-

Calculation of the residual vector R and jacobian matrix J for the elastoplastic phase field model

- Calculation of the residual of both phases:

$$\mathcal{R} = \Delta\mathbf{Z} - \Delta t\mathbf{F}(\mathbf{Z}^t + \Theta\Delta\mathbf{Z}, \Delta\underset{\sim}{\varepsilon}^{t+\Theta\Delta t}) = \mathbf{0}$$

$$\mathcal{R} = (\underset{\sim}{\boldsymbol{R}}^e_\alpha, R^p_\alpha, \underset{\sim}{\boldsymbol{R}}^\alpha_\alpha, \underset{\sim}{\boldsymbol{R}}^e_\beta, R^p_\beta, \underset{\sim}{\boldsymbol{R}}^\alpha_\beta)$$

$$\underset{\sim}{\boldsymbol{R}}^e_\alpha = \Delta\underset{\sim}{\varepsilon}^e_\alpha + \Delta p_\alpha \underset{\sim}{\boldsymbol{n}}^\theta_\alpha - \Delta\underset{\sim}{\varepsilon}_\alpha \tag{E.1}$$

$$R^p_\alpha = f(\underset{\sim}{\boldsymbol{\sigma}}^{t+\Delta t}_\alpha, \underset{\sim}{\boldsymbol{X}}^{t+\Delta t}_\alpha, R^{t+\Delta t}_\alpha) = (\underset{\sim}{\boldsymbol{\sigma}}^{eq}_\alpha)^\theta - R_\alpha p^\theta_\alpha \tag{E.2}$$

$$\underset{\sim}{\boldsymbol{R}}^\alpha_\alpha = \Delta\underset{\sim}{\boldsymbol{\alpha}}_\alpha - \Delta\underset{\sim}{\varepsilon}^p_\alpha + \Delta p_\alpha \frac{3D_\alpha}{2C_\alpha}\underset{\sim}{\boldsymbol{X}}_\alpha = \Delta\underset{\sim}{\boldsymbol{\alpha}}_\alpha - \Delta p_\alpha \underset{\sim}{\boldsymbol{n}}_\alpha + \Delta p_\alpha D_\alpha \underset{\sim}{\boldsymbol{\alpha}}_\alpha \tag{E.3}$$

$$\underset{\sim}{\boldsymbol{R}}^e_\beta = \Delta\underset{\sim}{\varepsilon}^e_\beta + \Delta p_\beta \underset{\sim}{\boldsymbol{n}}^\theta_\beta - \Delta\underset{\sim}{\varepsilon}_\alpha \tag{E.4}$$

$$R^p_\beta = f(\underset{\sim}{\boldsymbol{\sigma}}^{t+\Delta t}_\beta, \underset{\sim}{\boldsymbol{X}}^{t+\Delta t}_\beta, R^{t+\Delta t}_\beta) = (\underset{\sim}{\boldsymbol{\sigma}}^{eq}_\beta)^\theta - R_\beta p^\theta_\beta \tag{E.5}$$

$$\underset{\sim}{\boldsymbol{R}}^\alpha_\beta = \Delta\underset{\sim}{\boldsymbol{\alpha}}_\beta - \Delta\underset{\sim}{\varepsilon}^p_\beta + \Delta p_\beta \frac{3D_\beta}{2C_\beta}\underset{\sim}{\boldsymbol{X}}_\beta = \Delta\underset{\sim}{\boldsymbol{\alpha}}_\beta - \Delta p_\beta \underset{\sim}{\boldsymbol{n}}_\beta + \Delta p_\beta D_\beta \underset{\sim}{\boldsymbol{\alpha}}_\beta \tag{E.6}$$

- Calculation of the Jacobian matrix :

$$\mathbf{J} = \frac{\partial \mathcal{R}}{\partial \Delta \mathbf{Z}} = \mathbf{1} - \Delta t \left. \frac{\partial \mathbf{F}}{\partial \Delta \mathbf{Z}} \right|^{t+\Theta\Delta t}$$

$$[J] = \begin{bmatrix} \begin{bmatrix} \frac{\partial \underset{\sim}{\boldsymbol{R}}^e_\alpha}{\partial \Delta \underset{\approx}{\boldsymbol{\varepsilon}}^e_\alpha} & \frac{\partial \underset{\sim}{\boldsymbol{R}}^e_\alpha}{\partial \Delta p_\alpha} & \frac{\partial \underset{\sim}{\boldsymbol{R}}^e_\alpha}{\partial \Delta \underset{\sim}{\boldsymbol{\alpha}}_\alpha} \\ \frac{\partial R^p_\alpha}{\partial \Delta \underset{\approx}{\boldsymbol{\varepsilon}}_\alpha} & \frac{\partial R^p_\alpha}{\partial \Delta p_\alpha} & \frac{\partial R^p_\alpha}{\partial \Delta \underset{\sim}{\boldsymbol{\alpha}}_\alpha} \\ \frac{\partial \underset{\sim}{\boldsymbol{R}}^\alpha_\alpha}{\partial \Delta \underset{\approx}{\boldsymbol{\varepsilon}}_\alpha} & \frac{\partial \underset{\sim}{\boldsymbol{R}}^\alpha_\alpha}{\partial \Delta p_\alpha} & \frac{\partial \underset{\sim}{\boldsymbol{R}}^\alpha_\alpha}{\partial \Delta \underset{\sim}{\boldsymbol{\alpha}}_\alpha} \end{bmatrix} & [0] \\ [0] & \begin{bmatrix} \frac{\partial \underset{\sim}{\boldsymbol{R}}^e_\beta}{\partial \Delta \underset{\approx}{\boldsymbol{\varepsilon}}^e_\alpha} & \frac{\partial \underset{\sim}{\boldsymbol{R}}^e_\beta}{\partial \Delta p_\beta} & \frac{\partial \underset{\sim}{\boldsymbol{R}}^e_\beta}{\partial \Delta \underset{\sim}{\boldsymbol{\alpha}}_\beta} \\ \frac{\partial R^p_\beta}{\partial \Delta \underset{\approx}{\boldsymbol{\varepsilon}}_\alpha} & \frac{\partial R^p_\beta}{\partial \Delta p_\beta} & \frac{\partial R^p_\beta}{\partial \Delta \underset{\sim}{\boldsymbol{\alpha}}_\beta} \\ \frac{\partial \underset{\sim}{\boldsymbol{R}}^\alpha_\beta}{\partial \Delta \underset{\approx}{\boldsymbol{\varepsilon}}_\alpha} & \frac{\partial \underset{\sim}{\boldsymbol{R}}^\alpha_\beta}{\partial \Delta p_\beta} & \frac{\partial \underset{\sim}{\boldsymbol{R}}^\alpha_\beta}{\partial \Delta \underset{\sim}{\boldsymbol{\alpha}}_\beta} \end{bmatrix} \end{bmatrix} \tag{E.7}$$

Subscripts X^θ indicates the value of X at $t + \theta\Delta t$, X^t indicates the value at t, and $X^{t+\Delta t}$ at $t + \Delta t$ as:

$$\frac{\partial X^\theta}{\partial \Delta X} = \frac{\partial X^t + \theta \Delta X}{\partial \Delta X} = \theta I$$

$\frac{\partial \underset{\sim}{\boldsymbol{R}}^e_k}{\partial \Delta \mathbf{Z_k}}$:

$$\frac{\partial \underset{\sim}{\boldsymbol{R}}^e_k}{\partial \Delta \underset{\approx}{\boldsymbol{\varepsilon}}^e_k} = \underset{\approx}{\mathbf{1}} + \Delta p_k \frac{\partial \underset{\sim}{\boldsymbol{n}}_k}{\partial \underset{\sim}{\boldsymbol{\sigma}}_k} : \frac{\partial \underset{\sim}{\boldsymbol{\sigma}}_k}{\partial \underset{\approx}{\boldsymbol{\varepsilon}}^e_k} : \frac{\partial \underset{\approx}{\boldsymbol{\varepsilon}}^e_k}{\partial \Delta \underset{\approx}{\boldsymbol{\varepsilon}}^e_k} = \underset{\approx}{\mathbf{1}} + \theta \Delta p_k \underset{\approx}{\boldsymbol{N}}^\theta_k : \underset{\approx}{\boldsymbol{C}}^\theta_k \tag{E.8}$$

$$\frac{\partial \underset{\sim}{\boldsymbol{R}}^e_k}{\partial \Delta p_k} = \underset{\sim}{\boldsymbol{n}}^\theta_k \tag{E.9}$$

$$\frac{\partial \underset{\sim}{\boldsymbol{R}}^e_k}{\partial \Delta \underset{\sim}{\boldsymbol{\alpha}}_k} = \Delta p_k \frac{\partial \underset{\sim}{\boldsymbol{n}}_k}{\partial \underset{\sim}{\boldsymbol{X}}_k} : \frac{\partial \underset{\sim}{\boldsymbol{X}}_k}{\partial \underset{\sim}{\boldsymbol{\alpha}}_k} : \frac{\partial \underset{\sim}{\boldsymbol{\alpha}}_k}{\partial \Delta \underset{\sim}{\boldsymbol{\alpha}}_k} = -\frac{2}{3} \theta \Delta p_k C_k \underset{\approx}{\boldsymbol{N}}^\theta_k \tag{E.10}$$

$\frac{\partial R^p_k}{\partial \Delta \mathbf{Z_k}}$:

$$\frac{\partial R^p_k}{\partial \Delta \underset{\approx}{\boldsymbol{\varepsilon}}^e_k} = \frac{\partial \underset{\sim}{\boldsymbol{\sigma}}^{eq}_k}{\partial \underset{\sim}{\boldsymbol{\sigma}}_k} : \frac{\partial \underset{\sim}{\boldsymbol{\sigma}}_k}{\partial \underset{\approx}{\boldsymbol{\varepsilon}}^e_k} : \frac{\partial \underset{\approx}{\boldsymbol{\varepsilon}}^e_k}{\partial \Delta \underset{\approx}{\boldsymbol{\varepsilon}}^e_k} = \theta \underset{\sim}{\boldsymbol{n}}_k : \underset{\approx}{\boldsymbol{C}}_k = \underset{\sim}{\boldsymbol{n}}^{t+\Delta t}_k : \underset{\approx}{\boldsymbol{C}}^{t+\Delta t}_k \tag{E.11}$$

$$\frac{\partial R^p_k}{\partial \Delta p_k} = -\frac{\partial R_k}{\partial p_k} : \frac{\partial p_k}{\partial \Delta p_k} = -\theta H^\theta_k \tag{E.12}$$

$$\frac{\partial R^p_k}{\partial \Delta \underset{\sim}{\boldsymbol{\alpha}}_k} = \frac{\partial \underset{\sim}{\boldsymbol{\sigma}}^{eq}_k}{\partial \underset{\sim}{\boldsymbol{X}}_k} : \frac{\partial \underset{\sim}{\boldsymbol{X}}_k}{\partial \underset{\sim}{\boldsymbol{\alpha}}_k} : \frac{\partial \underset{\sim}{\boldsymbol{\alpha}}_k}{\partial \Delta \underset{\sim}{\boldsymbol{\alpha}}_k} = -\theta \frac{2}{3} C_k \underset{\sim}{\boldsymbol{n}}^\theta_k \tag{E.13}$$

$\frac{\partial \underset{\sim}{\boldsymbol{R}}_k^{\alpha}}{\partial \Delta \mathbf{Z_k}}$:

$$\frac{\partial \underset{\sim}{\boldsymbol{R}}_k^{\alpha}}{\partial \Delta \underset{\sim}{\boldsymbol{\varepsilon}}_k^e} = -\Delta p_k \frac{\partial \underset{\sim}{\boldsymbol{n}}_k}{\partial \underset{\sim}{\boldsymbol{\sigma}}_k} : \frac{\partial \underset{\sim}{\boldsymbol{\sigma}}_k}{\partial \underset{\sim}{\boldsymbol{\varepsilon}}_k^e} : \frac{\partial \underset{\sim}{\boldsymbol{\varepsilon}}_k^e}{\partial \Delta \underset{\sim}{\boldsymbol{\varepsilon}}_k^e} = -\theta \Delta p_k \underset{\approx}{\boldsymbol{N}}_k^{\theta} : \underset{\approx}{\boldsymbol{C}}_k^{\theta} \tag{E.14}$$

$$\frac{\partial \underset{\sim}{\boldsymbol{R}}_k^{\alpha}}{\partial \Delta p_k} = -\underset{\sim}{\boldsymbol{n}}_k^{\theta} + D_k \underset{\sim}{\boldsymbol{\alpha}}_k^{\theta} \tag{E.15}$$

$$\frac{\partial \underset{\sim}{\boldsymbol{R}}_k^{\alpha}}{\partial \Delta \underset{\sim}{\boldsymbol{\alpha}}_k} = \underset{\approx}{\mathbf{1}} - \Delta p_k \frac{\partial \underset{\sim}{\boldsymbol{n}}_k}{\partial \underset{\sim}{\boldsymbol{X}}_k} : \frac{\partial \underset{\sim}{\boldsymbol{X}}_k}{\partial \underset{\sim}{\boldsymbol{\alpha}}_k} : \frac{\partial \underset{\sim}{\boldsymbol{\alpha}}_k}{\partial \Delta \underset{\sim}{\boldsymbol{\alpha}}_k} + \Delta p_k D_k \frac{\partial \underset{\sim}{\boldsymbol{\alpha}}_k}{\partial \Delta \underset{\sim}{\boldsymbol{\alpha}}_k} \tag{E.16}$$

$$= \underset{\approx}{\mathbf{1}} + \theta \Delta p_k \frac{2}{3} C_k \underset{\approx}{\boldsymbol{N}}_k + \theta \Delta p_k D_k \underset{\approx}{\boldsymbol{I}} \tag{E.17}$$

with:

$$\underset{\sim}{\boldsymbol{n}}_k = \frac{\partial f_k}{\partial \underset{\sim}{\boldsymbol{\sigma}}_k}, \qquad H_k = \frac{\partial R_k}{\partial p_k} \qquad \text{and} \qquad \underset{\approx}{\boldsymbol{N}}_k = \frac{\partial \underset{\sim}{\boldsymbol{n}}_k}{\partial \underset{\sim}{\boldsymbol{\sigma}}_k} = \frac{\partial^2 f_k}{\partial \underset{\sim}{\boldsymbol{\sigma}}_k^2} = \frac{1}{\underset{\sim}{\boldsymbol{\sigma}}_k^{eq}} (\frac{3}{2} \underset{\approx}{\boldsymbol{J}}_k - \underset{\sim}{\boldsymbol{n}}_k \otimes \underset{\sim}{\boldsymbol{n}}_k)$$

where $\underset{\approx}{\boldsymbol{E}}_k$ is the elasticity tensor and $\underset{\approx}{\boldsymbol{J}}_k$ is the fourth-order tensor, which relates the deviatoric stress tensor to the Cauchy-stress tensor by the following expression: $\underset{\sim}{\boldsymbol{s}}_k = \underset{\approx}{\boldsymbol{J}}_k : \underset{\sim}{\boldsymbol{\sigma}}_k$.

- Calculation of the consistent tangent matrix :

The constitutive equation must then supply the consistent tangent matrix $\underset{\approx}{\boldsymbol{L}} = \partial \Delta \texttt{primal} / \partial \Delta \texttt{dual}$ for a given strain increment $\Delta \underset{\sim}{\boldsymbol{\varepsilon}}$, which is expressed in 2D case a:

$$\texttt{primal}: \begin{bmatrix} \boldsymbol{\nabla}.\underline{\boldsymbol{u}} \\ \boldsymbol{\nabla} c \\ \boldsymbol{\nabla} \phi \end{bmatrix} \quad \text{and} \quad \texttt{dual}: \begin{bmatrix} \underset{\sim}{\boldsymbol{\sigma}} \\ \underline{\boldsymbol{J}} \\ \underline{\boldsymbol{\xi}} \end{bmatrix} \tag{E.18}$$

$$\underset{\approx}{\boldsymbol{L}} = \frac{\partial \Delta \texttt{dual}}{\partial \Delta \texttt{primal}} = \begin{bmatrix} \underset{\approx}{\boldsymbol{L}} & \begin{bmatrix} 0 & 0 \\ 0 & 0 \\ 0 & 0 \\ 0 & 0 \end{bmatrix} & \begin{bmatrix} 0 & 0 \\ 0 & 0 \\ 0 & 0 \\ 0 & 0 \end{bmatrix} \\ \underset{\sim}{\boldsymbol{D}} & \begin{bmatrix} A & 0 \\ 0 & A \end{bmatrix} & \begin{bmatrix} B & 0 \\ 0 & B \end{bmatrix} \\ \begin{bmatrix} 0 & 0 & 0 & 0 \\ 0 & 0 & 0 & 0 \end{bmatrix} & \begin{bmatrix} 0 & 0 \\ 0 & 0 \end{bmatrix} & \begin{bmatrix} \alpha & 0 \\ 0 & \alpha \end{bmatrix} \end{bmatrix} \tag{E.19}$$

where

$$\underset{\approx}{\boldsymbol{L}} = \frac{\partial \Delta \underset{\sim}{\boldsymbol{\sigma}}}{\partial \Delta \underset{\sim}{\boldsymbol{\varepsilon}}}, \qquad A = -\kappa \left[\frac{\partial^2 f_0}{\partial c^2} + \frac{\partial^2 \mathcal{W}}{\partial c^2} \right], \qquad B = -\kappa \left[\frac{\partial^2 f_0}{\partial \phi \partial c} + \frac{\partial^2 \mathcal{W}}{\partial \phi \, \partial c} \right]$$

and

$$\underset{\sim}{\boldsymbol{D}} = -\kappa \left(\left[\frac{\partial^3 \mathcal{W}}{\partial \underset{\sim}{\boldsymbol{\varepsilon}} \partial c^2} \right] \boldsymbol{\nabla} c + \left[\frac{\partial^3 \mathcal{W}}{\partial \underset{\sim}{\boldsymbol{\varepsilon}} \partial \phi \partial c} \right] \boldsymbol{\nabla} \phi + \left[\frac{\partial^3 \mathcal{W}}{\partial \underset{\sim}{\boldsymbol{\varepsilon}}^2 \, \partial c} \right] \boldsymbol{\nabla} \underset{\sim}{\boldsymbol{\varepsilon}} \right)$$

The fourth-order operator $\underset{\approx}{\boldsymbol{L}}$ is expressed, for Runge-Kutta method as

$$\underset{\approx}{\boldsymbol{L}} = \frac{\partial \Delta \underset{\sim}{\boldsymbol{\sigma}}}{\partial \Delta \underset{\sim}{\boldsymbol{\varepsilon}}} = \phi \underset{\approx}{\boldsymbol{C}}_{\alpha} + (1-\phi)\underset{\approx}{\boldsymbol{C}}_{\beta} = \underset{\approx}{\boldsymbol{C}}_{\text{eff}} \tag{E.20}$$

and for Θ-method method as

$$\underset{\approx}{\boldsymbol{L}} = \frac{\partial \Delta \underset{\sim}{\boldsymbol{\sigma}}}{\partial \Delta \underset{\sim}{\boldsymbol{\varepsilon}}} = \phi \underset{\approx}{\boldsymbol{C}}_{\alpha} : \underset{\approx}{\boldsymbol{J}}_{ee1} + (1-\phi)\underset{\approx}{\boldsymbol{C}}_{\beta} : \underset{\approx}{\boldsymbol{J}}_{ee2} \tag{E.21}$$

where the tensors $\underset{\approx}{\boldsymbol{J}}_{ee1} = \dfrac{\delta \Delta \underset{\sim}{\boldsymbol{\varepsilon}}^{e}_{\alpha}}{\delta \Delta \underset{\sim}{\boldsymbol{\varepsilon}}_{\alpha}}$ and $\underset{\approx}{\boldsymbol{J}}_{ee2} = \dfrac{\delta \Delta \underset{\sim}{\boldsymbol{\varepsilon}}^{e}_{\beta}}{\delta \Delta \underset{\sim}{\boldsymbol{\varepsilon}}_{\beta}}$ are obtained directly from the jacobian matrix.

Annexe -F-

Expressions of the equilibrium compositions and the molar fraction for the two-phase coherent phase equilibria

The expressions of the equilibrium compositions for both phases c_α and c_β and the molar fraction z are calculated by minimization of the free energy. It is conveniently performed by applying the Lagrange method. Introducing a multiplier λ into the equation of local conservation of mass (IV.17), subtracting from the expression of the free energy density (IV.32) and setting the derivatives with respect to c_α, c_β and z to zero, four algebraic equations (IV.33-IV.36) in four unknowns (c_α, c_β, z and $\mathcal{L}$) are obtained.

Multiplying (Eq.(IV.19) - Eq.(IV.20)) by $(c_\alpha - c_\beta)$, we obtain

$$z\,k\,(c_\alpha - a_\alpha)(c_\alpha - c_\beta) - (1-z)\,k\,(c_\beta - a_\beta)(c_\alpha - c_\beta) + 4z(1-z)\Lambda(c_\alpha - c_\beta)^2 - \lambda\,(2z-1)(c_\alpha - c_\beta) = 0 \tag{F.1}$$

The work of (Eq. (F.1) - $(2z-1)\times$ Eq.(IV.20)) provides

$$\begin{aligned} &\Lambda\,(c_\alpha - c_\beta)^2 - \,k\,(c_\beta - a_\beta)(c_\alpha - c_\beta) + \frac{1}{2}\,k\,(c_\alpha - a_\alpha)^2 - \frac{1}{2}\,k\,(c_\beta - a_\beta)^2 \\ +\;\; &z\left[k\,(c_\alpha - a_\alpha)(c_\alpha - c_\beta) + \,k\,(c_\beta - a_\beta)(c_\alpha - c_\beta) - \,k\,(c_\alpha - a_\alpha)^2 + \,k\,(c_\beta - a_\beta)^2\right] = 0 \end{aligned} \tag{F.2}$$

The operation ($(c_\alpha - c_\beta)\times$(Eq.(IV.19)$/z$ + Eq. (IV.20)$/(1-z)$)) leads to the relations:

$$k\,(c_\alpha - a_\alpha)(c_\alpha - c_\beta) + k\,(c_\beta - a_\beta)(c_\alpha - c_\beta) + 2(1-2z)\Lambda(c_\alpha - c_\beta)^2 - 2\lambda(c_\alpha - c_\beta) = 0 \tag{F.3}$$

By perfonning (Eq.(F.3) - $2\times$ Eq.(IV.21)), we obtain:

$$k\,(c_\alpha - a_\alpha)(c_\alpha - c_\beta) + k\,(c_\beta - a_\beta)(c_\alpha - c_\beta) -, k\,(c_\alpha - a_\alpha)^2 + \,k\,(c_\beta - a_\beta)^2 = 0 \tag{F.4}$$

The substitution of the above equation Eq.(F.4) into Eq.(F.3) leads to

$$\Lambda\,(c_\alpha - c_\beta)^2 - \,k\,(c_\beta - a_\beta)(c_\alpha - c_\beta) + \frac{1}{2}\,k\,(c_\alpha - a_\alpha)^2 - \frac{1}{2}\,k\,(c_\beta - a_\beta)^2 = 0 \tag{F.5}$$

Finally, the operation of ($2\times$ Eq.(F.5) + Eq. (F.4)) yields

$$2\Lambda\,(c_\alpha - c_\beta) + k\,(c_\alpha - a_\alpha) - k\,(c_\beta - a_\beta) = 0 \tag{F.6}$$

Thus, we deduce the following relation, which relate the compositions of both phases:

$$c_\alpha - c_\beta = \frac{k(a_\alpha - a_\beta)}{2\Lambda + k} \tag{F.7}$$

After substituting Eq.(F.7) into Eq.(F.5) and rearranging, we get:

$$\begin{aligned}
\Lambda\,kL^2 - \,k\,(c_\beta - a_\beta)L + \frac{1}{2}\,(c_\beta + kL - a_\alpha)^2 - \frac{1}{2}\,(c_\beta - a_\beta)^2 &= 0 \\
\Lambda\,kL^2 - k\,Lc_\beta + k\,La_\beta + \frac{1}{2}\,(kL - a_\alpha)^2 + (kL - a_\alpha)c_\beta - \frac{1}{2}a_\beta^2 + c_\beta a_\beta &= 0 \\
c_\beta - \frac{1}{2}k\,\frac{(a_\alpha - a_\beta)}{2\Lambda + k} - \frac{1}{2}(a_\alpha + a_\beta) = 0 &= 0
\end{aligned} \tag{F.8}$$

where $L = \dfrac{(a_\alpha - a_\beta)}{2\Lambda + k}$

Consequently, the expressions of the equilibrium compositions c_α, c_β and the volume fraction z can be expressed as follows :

$$c_\alpha = a_\alpha - \Delta a\,[1 - K] \tag{F.9}$$

$$c_\beta = a_\beta + \Delta a\,[1 - K] \tag{F.10}$$

$$z = \frac{1}{2} - \frac{\mathcal{B}}{K\Delta a} \tag{F.11}$$

where $\Delta a = (a_\alpha - a_\beta)/2$, $K = \dfrac{k}{k + 2\Lambda}$ and $\mathcal{B} = (a_\alpha + a_\beta - 2\,c_0)/4$.

Annexe -G-

Mechanical equilibrium of a misfitting planar oxide layer

In this section, the mechanical behavior associated with a misfitting planar oxide layer growing at the surface of a pure zirconium slab is calculated. Firstly, both layer and Zr matrix behave in a purely elastic state, i.e., in the absence of plastic relaxation. Secondly, the solutions to the stress and strain fields are obtained, assuming ideal plastic behavior for the oxide layer.

The conditions necessary for static mechanical equilibrium require that the stress field $\underset{\sim}{\boldsymbol{\sigma}}$ in the two-phase system must satisfy, in the absence of body forces:

$$\boldsymbol{\nabla}.\underset{\sim}{\boldsymbol{\sigma}} = 0 \tag{G.1}$$

Assuming that the coordinate frame is the principal frame for strains and stresses, i.e, $\varepsilon_{ij} = 0$ and $\sigma_{ij} = 0$ for $i \neq j$, the stress and strain tensors at any point are expressed as follows:

$$\underset{\sim}{\boldsymbol{\varepsilon}}_k = \begin{bmatrix} \varepsilon^k_{xx} & 0 & 0 \\ 0 & \varepsilon^k_{yy} & 0 \\ 0 & 0 & \varepsilon^k_{zz} \end{bmatrix} \quad \text{and} \quad \underset{\sim}{\boldsymbol{\sigma}}_k = \begin{bmatrix} \sigma^k_{xx} & 0 & \\ 0 & \sigma^k_{yy} & 0 \\ 0 & 0 & \sigma^k_{zz} \end{bmatrix} \tag{G.2}$$

and $k = \{\alpha, \beta\}$ denotes α and β phases.

After substituting (G.2) into the static mechanical equilibrium (G.1), the stress and the displacement are then found to be of the following form

$$\sigma^k_{ii} = A^k_i \quad \text{and} \quad u_i = \varepsilon^k_{ii}\, i + b^k_i \quad \text{where} \quad i = \{x, y, z\} \tag{G.3}$$

$A^k_i, \varepsilon^k_{ii}$ and b^k_i are constants to be determined from the boundary/interface conditions.

Indeed, the following mechanical boundary conditions to the system have been applied in the parallelepiped region $(0 \leq x \leq L, 0 \leq y \leq H, 0 \leq z \leq h)$

- No displacement at the two upper and lower boundaries in the x direction.

$$u^\alpha_x(x = 0, \forall y, \forall z) = u^\beta_x(x = 0, \forall y, \forall z) = 0 \tag{G.4}$$
$$u^\alpha_x(x = L, \forall y, \forall z) = u^\beta_x(x = L, \forall y, \forall z) = 0 \tag{G.5}$$

From the relation (G.3), we can then deduce

$$u^\alpha_x = u^\beta_x = 0 \quad \text{and} \quad \varepsilon^\alpha_{xx} = \varepsilon^\beta_{xx} = 0 \tag{G.6}$$

- No displacement at the two boundaries in the z direction.

$$u_z^\alpha(\forall x, \forall y, z = 0) = u_z^\beta(\forall x, \forall y, z = 0) = 0 \tag{G.7}$$
$$u_z^\alpha(\forall x, \forall y, z = h) = u_z^\beta(\forall x, \forall y, z = h) = 0 \tag{G.8}$$

  Consequently, we obtain

$$u_z^\alpha = u_z^\beta = 0 \qquad \text{and} \qquad \varepsilon_{zz}^\alpha = \varepsilon_{zz}^\beta = 0 \tag{G.9}$$

- Far away from the interface, into the matrix supposed to be semi-infinite, No displacement at the boundary in the y direction. Using the linear form of the displacement (G.3), we get:

$$u_x^\beta(\forall x, y = H, \forall z) = \varepsilon_{yy}^\beta \; L + b_y^\beta = 0 \tag{G.10}$$

- at the free α surface, there can be no force normal at equilibrium

$$\sigma_{yy}^\alpha(\forall x, y = 0, \forall z) = 0 \tag{G.11}$$

Moreover, the α-β interface is supposed to be coherent. The assumption of a fully coherent interface implies that there be continuity of both displacements and tractions across the α layer-β matrix interface. Assuming that the unit normal $\underline{\boldsymbol{n}}$ to the interface is in the y direction, i.e. $\underline{\boldsymbol{n}} = (0, 1, 0)$, we obtain:

$$u_y^\alpha = u_y^\beta \tag{G.12}$$
$$\sigma_{yy}^\alpha = \sigma_{yy}^\beta \tag{G.13}$$

Pure Elastic State

Firstly, the mechanical behavior associated with a misfitting planar oxide layer growing at the surface of a pure zirconium slab is investigated in a purely elastic state. Choosing the β phase as the stress free reference state, the dilatation misfit in the phase α, is a spherical tensor independent of concentration:

$$\underset{\sim}{\boldsymbol{\varepsilon}}_\alpha^\star = \delta_{\mathrm{ZrO_2}} \underset{\sim}{\mathbf{1}} \qquad \text{and} \qquad \underset{\sim}{\boldsymbol{\varepsilon}}_\beta^\star = 0 \tag{G.14}$$

where $\underset{\sim}{\mathbf{1}}$ the unit second order tensor.

The strain-stress relationship in both phases obeys Hooke's law which can be written, using Eq (G.6) and Eq; (G.9), as follows:

- in oxide layer:

$$\sigma_{xx}^\alpha = \sigma_{zz}^\alpha = \lambda_\alpha \varepsilon_{yy}^\alpha - (3\lambda_\alpha + 2\mu_\alpha)\delta_{\mathrm{ZrO_2}} \tag{G.15}$$

$$\sigma_{yy}^\alpha = (\lambda_\alpha + 2\mu_\alpha)\varepsilon_{yy}^\alpha - (3\lambda_\alpha + 2\mu_\alpha)\delta_{\mathrm{ZrO_2}} = 0 \tag{G.16}$$

- in Zr matrix:

$$\sigma_{xx}^\beta = \sigma_{zz}^\beta = \lambda_\beta \varepsilon_{yy}^\beta \tag{G.17}$$

$$\sigma_{yy}^\beta = (\lambda_\beta + 2\mu_\beta)\varepsilon_{yy}^\beta \tag{G.18}$$

Substituting the free surface condition Eq. (G.11) into Eq.(G.16), we deduce:

$$\sigma_{xx}^{\alpha} = \sigma_{zz}^{\alpha} = -\frac{2\mu_\alpha\,(3\lambda_\alpha + 2\mu_\alpha)}{\lambda_\alpha + 2\mu_\alpha}\delta_{\mathrm{ZrO_2}} = -\frac{E_\alpha}{1-\nu_\alpha}\delta_{\mathrm{ZrO_2}} \tag{G.19}$$

$$\sigma_{yy}^{\alpha} = 0 \tag{G.20}$$

$$\varepsilon_{yy}^{\alpha} = \frac{3\lambda_\alpha + 2\mu_\alpha}{\lambda_\alpha + 2\mu_\alpha}\delta_{\mathrm{ZrO_2}} = \frac{1+\nu_\alpha}{1-\nu_\alpha}\delta_{\mathrm{ZrO_2}} \tag{G.21}$$

The continuity conditions of normal stresses σ_{yy}^{β} (G.18) and σ_{yy}^{α} (G.20), across the interface, leads to deduce that there is no Cauchy stress in the y direction in both phases. Consequently, zero elastic strain energy is found in the Zr matrix, whereas,

$$\underset{\sim}{\boldsymbol{\varepsilon}}_\alpha = \begin{bmatrix} 0 & 0 & 0 \\ 0 & \dfrac{3\lambda_\alpha + 2\mu_\alpha}{\lambda_\alpha + 2\mu_\alpha}\delta_{\mathrm{ZrO_2}} & 0 \\ 0 & 0 & 0 \end{bmatrix}, \qquad \underset{\sim}{\boldsymbol{\varepsilon}}_\alpha^{e} = \begin{bmatrix} -\delta_{\mathrm{ZrO_2}} & 0 & 0 \\ 0 & \dfrac{2\lambda_\alpha}{\lambda_\alpha + 2\mu_\alpha}\delta_{\mathrm{ZrO_2}} & 0 \\ 0 & 0 & -\delta_{\mathrm{ZrO_2}} \end{bmatrix} \tag{G.22}$$

$$\underset{\sim}{\boldsymbol{\sigma}}_\alpha = \begin{bmatrix} -\dfrac{2\mu_\alpha\,(3\lambda_\alpha + 2\mu_\alpha)}{\lambda_\alpha + 2\mu_\alpha}\delta_{\mathrm{ZrO_2}} & 0 & 0 \\ 0 & 0 & 0 \\ 0 & 0 & -\dfrac{2\mu_\alpha\,(3\lambda_\alpha + 2\mu_\alpha)}{\lambda_\alpha + 2\mu_\alpha}\delta_{\mathrm{ZrO_2}} \end{bmatrix} \tag{G.23}$$

Elasto-plastic behavior

Secondly, the solution to the problem of the elasto-plastic deformation is studied. The zirconium slab is considered to remain in a purely elastic state under a zero elastic strain energy in β phase. Hence plastic deformation may be taken to occur only in the oxide layer. Adopting the von Mises yielding criterion, the equivalent stress $\sigma_\alpha^{\mathrm{eq}}$ reads

$$\sigma_\alpha^{\mathrm{eq}} = \frac{1}{\sqrt{2}}\left[\left(\sigma_{xx}^{\alpha} - \sigma_{yy}^{\alpha}\right)^2 + \left(\sigma_{xx}^{\alpha} - \sigma_{zz}^{\alpha}\right)^2 + \left(\sigma_{zz}^{\alpha} - \sigma_{yy}^{\alpha}\right)^2\right]^{1/2} \tag{G.24}$$

$$= -\sigma_{xx}^{\alpha} = -\sigma_{zz}^{\alpha} = \sigma_\alpha^0 \tag{G.25}$$

where σ_α^0 is the yield stress.

Taking Hooke's law into account for oxide layer, the strain-stress relationships are expressed as:

$$2\mu_\alpha\varepsilon_{xx}^{e\alpha} + \lambda_\alpha(\varepsilon_{xx}^{e\alpha} + \varepsilon_{yy}^{e\alpha} + \varepsilon_{zz}^{e\alpha}) = -\sigma_\alpha^0 \tag{G.26}$$

$$2\mu_\alpha\varepsilon_{yy}^{e\alpha} + \lambda_\alpha(\varepsilon_{xx}^{e\alpha} + \varepsilon_{yy}^{e\alpha} + \varepsilon_{zz}^{e\alpha}) = 0 \tag{G.27}$$

$$2\mu_\alpha\varepsilon_{zz}^{e\alpha} + \lambda_\alpha(\varepsilon_{xx}^{e\alpha} + \varepsilon_{yy}^{e\alpha} + \varepsilon_{zz}^{e\alpha}) = -\sigma_\alpha^0 \tag{G.28}$$

Equations ((G.26),(G.27) and G.28) are three algebraic equations in three unknowns ($\varepsilon_{xx}^{e\alpha}, \varepsilon_{yy}^{e\alpha}$ and $\varepsilon_{zz}^{e\alpha}$). Consequently, the solution is given as follows:

$$\varepsilon_{yy}^{e\alpha} = \frac{\lambda_\alpha}{\mu_\alpha\,(3\,\lambda_\alpha + 2\,\mu_\alpha)}\sigma_\alpha^0 \qquad \text{and} \qquad \varepsilon_{xx}^{e\alpha} = \varepsilon_{zz}^{e\alpha} = -\frac{(\lambda_\alpha + 2\,\mu_\alpha)}{2\,\mu_\alpha\,(3\,\lambda_\alpha + 2\,\mu_\alpha)}\sigma_\alpha^0 \tag{G.29}$$

Assuming that no strain in the x and z directions and using the partition hypothesis, which requires a decomposition of the total strain in each phase into elastic, misfit and plastic parts, the plastic strain in the x and z directions can then be written as follows:

$$\begin{aligned} \varepsilon_{xx}^{p\alpha} = \varepsilon_{zz}^{p\alpha} &= -\delta_{\mathrm{ZrO_2}} - \varepsilon_{xx}^{e\alpha} \\ &= -\delta_{\mathrm{ZrO_2}} + \frac{(\lambda_\alpha + 2\,\mu_\alpha)}{2\,\mu_\alpha\,(3\,\lambda_\alpha + 2\,\mu_\alpha)}\sigma_\alpha^0 \end{aligned} \tag{G.30}$$

The compressibility condition for plastic strains leads to the expression of the plastic strain in the y direction:

$$\varepsilon_{yy}^{p\alpha} = -(\varepsilon_{xx}^{p\alpha} + \varepsilon_{zz}^{p\alpha}) = 2\delta_{\mathrm{ZrO_2}} - \frac{(\lambda_\alpha + 2\,\mu_\alpha)}{\mu_\alpha\,(3\,\lambda_\alpha + 2\,\mu_\alpha)}\sigma_\alpha^0 \tag{G.31}$$

Consequently, the total, elastic and plastic strains as well as the stress tensor, in the oxide layer, are found to be:

$$\underset{\sim}{\boldsymbol{\varepsilon}}_\alpha = \begin{bmatrix} 0 & 0 & 0 \\ 0 & 3\delta_{\mathrm{ZrO_2}} - \dfrac{2}{(3\,\lambda + 2\,\mu)}\sigma_\alpha^0 & 0 \\ 0 & 0 & 0 \end{bmatrix}, \qquad \underset{\sim}{\boldsymbol{\sigma}}_\alpha = \begin{bmatrix} -\sigma_\alpha^0 & 0 & 0 \\ 0 & 0 & 0 \\ 0 & 0 & -\sigma_\alpha^0 \end{bmatrix}$$

$$\underset{\sim}{\boldsymbol{\varepsilon}}_\alpha^e = \begin{bmatrix} -\dfrac{(\lambda + 2\,\mu)}{2\,\mu\,(3\,\lambda + 2\,\mu)}\sigma_\alpha^0 & 0 & 0 \\ 0 & \dfrac{\lambda}{\mu\,(3\,\lambda + 2\,\mu)}\sigma_\alpha^0 & 0 \\ 0 & 0 & -\dfrac{(\lambda + 2\,\mu)}{2\,\mu\,(3\,\lambda + 2\,\mu)}\sigma_\alpha^0 \end{bmatrix}$$

$$\underset{\sim}{\boldsymbol{\varepsilon}}_\alpha^p = \begin{bmatrix} -\delta_{\mathrm{ZrO_2}} + \dfrac{(\lambda + 2\,\mu)}{2\,\mu\,(3\,\lambda + 2\,\mu)}\sigma_\alpha^0 & 0 & 0 \\ 0 & 2\delta_{\mathrm{ZrO_2}} - \dfrac{(\lambda + 2\,\mu)}{\mu\,(3\,\lambda + 2\,\mu)}\sigma_\alpha^0 & 0 \\ 0 & 0 & -\delta_{\mathrm{ZrO_2}} + \dfrac{(\lambda + 2\,\mu)}{2\,\mu\,(3\,\lambda + 2\,\mu)}\sigma_\alpha^0 \end{bmatrix}$$

Annexe -H-

Mechanical equilibrium of an isotropic misfitting cylindrical precipitate in an isotropic matrix

The problem of determining analytic expressions for the displacement and stresses for the cylinder in a pure elastic state is discussed. The analytic solution for this problem is presented in terms of a cylindrical coordinate system, $r\theta z$. The cylinder has an outer radius, R. The origin of the cylindrical coordinate system coincides with the centre of the cavity, and the $z-$axis runs the length of the cylinder H. Taking the symmetry about the z-axis into account, the displacement field can be conveniently expressed, from (IV.7), as the form

$$\underline{\boldsymbol{u}}\,(x) = u_r(r)\underline{\boldsymbol{e}}_r + u_z(z)\underline{\boldsymbol{e}}_z \tag{H.1}$$

Consequently, the displacement field results in the following forms for strain and stress fields:

$$\underset{\sim}{\boldsymbol{\varepsilon}} = \mathrm{grad}\underline{\boldsymbol{u}} = \begin{bmatrix} u_{r,r} & 0 & 0 \\ 0 & \dfrac{u_r}{r} & 0 \\ 0 & 0 & u_{z,z} \end{bmatrix} \quad \text{and} \quad \underset{\sim}{\boldsymbol{\sigma}} = \begin{bmatrix} f(r) & 0 & 0 \\ 0 & g(r) & 0 \\ 0 & 0 & l(z) \end{bmatrix} \tag{H.2}$$

According to Hooke's law, the stress components, for an isotropic homogeneous material, are give by

$$\sigma_{rr} = 2\mu u_{r,r} + \lambda(u_{r,r} + \frac{u_r}{r} + u_{z,z}) - (3\lambda + 2\mu)\varepsilon^\star \tag{H.3}$$

$$\sigma_{\theta\theta} = 2\mu\frac{u_r}{r} + \lambda(u_{r,r} + \frac{u_r}{r} + u_{z,z}) - (3\lambda + 2\mu)\varepsilon^\star \tag{H.4}$$

$$\sigma_{zz} = 2\mu u_{z,z} + \lambda(u_{r,r} + \frac{u_r}{r} + u_{z,z}) - (3\lambda + 2\mu)\varepsilon^\star \tag{H.5}$$

where $\lambda = E/2(1+\nu)$ and μ are Lame's two coefficients.

In the absence of body forces, the static equilibrium equation depends only on a radial and axial coordinates r, z, which reduced, in polar (curvilinear) coordinates, to

$$\begin{cases} \sigma_{rr,r} + \dfrac{\sigma_{rr} - \sigma_{\theta\theta}}{r} = 0 \\ \sigma_{zz,z} = 0 \end{cases} \tag{H.6}$$

The substitution of Eqs.((H.3)-(H.4)-(H.5)) into the above equations leads to

$$u_{r,rr} + (\frac{u_r}{r})_{,r} = \left[u_{r,r} + \frac{u_r}{r}\right]_{,r} = 0 \qquad \text{and} \qquad u_{z,zz} = 0 \tag{H.7}$$

which require that the radial and axial displacements are found to be a affine function of coordinates r and z respectively

$$u_r = a\,r + \frac{b}{r} \qquad \text{and} \qquad u_z = c\,z + d \tag{H.8}$$

where a, b, c are constants to be determined from the boundary conditions

For simplicity, homogeneous isotropic elastic properties for both phases are considered. The strain and stress field can then be expressed explicitly in the following form:

$$\begin{cases} \sigma_{rr} &= A - \dfrac{B}{r^2} - D \\ \sigma_{\theta\theta} &= A + \dfrac{B}{r^2} - D \\ \sigma_{zz} &= C - D \\ \sigma_{r\theta} &= \sigma_{rz} = \sigma_{z\theta} = 0 \end{cases} \qquad \begin{cases} \varepsilon_{rr} &= a - \dfrac{b}{r^2} \\ \varepsilon_{\theta\theta} &= a + \dfrac{b}{r^2} \\ \varepsilon_{zz} &= c \\ \varepsilon_{r\theta} &= \varepsilon_{rz} = \varepsilon_{z\theta} = 0 \end{cases} \tag{H.9}$$

where

$$A = (\lambda + \mu)\,2a + \lambda c, \qquad B = 2\mu\,b, \qquad C = (\lambda + 2\mu)\,c + 2\lambda\,a, \qquad D = (3\lambda + 2\mu)\varepsilon^\star \tag{H.10}$$

the solution can be written in cylindrical coordinates, with the same constants A, B and C, determined from the boundary/interface conditions. The equilibrium conditions at a fully coherent interface, obtained from the thermodynamics of stressed solid, imply that there be continuity of both displacement and forces across the α-β interface, which are:

- Continuity of the displacement at the interface between both phase

$$u_r^\alpha(r = r_{int}) = u_r^\beta(r = r_{int}) \quad \Rightarrow \quad a_\alpha\,r_{int} = a_\beta\,r_{int} + \frac{b_\beta}{r_{int}} \qquad \text{when} \qquad r = r_{int} \tag{H.11}$$

  Using Eq.(H.10), we get

$$\frac{1-\nu}{E}(A_\alpha - A_\beta) - \frac{\nu}{E}(C_\alpha - C_\beta) = \frac{B_\beta}{2\mu r_{int}^2} \tag{H.12}$$

- Continuity of the radial component σ_{rr} to preserve balance of the forces normal at the interface

$$\sigma_{rr}^\alpha(r = r_{int}) = \sigma_{rr}^\beta(r = r_{int}) \quad \Rightarrow \quad A_\alpha - D_\alpha = A_\beta - \frac{B_\beta}{r_{int}^2} - D_\beta \qquad \text{when} \qquad r = r_{int} \tag{H.13}$$

Moreover, The following mechanical boundary conditions to the system have been applied:

- No displacement at the axis $r = 0$

$$u_r^\alpha(r = 0) = 0 \quad \Rightarrow \quad b_\alpha = B_\alpha = 0 \qquad \text{when} \qquad r = 0 \tag{H.14}$$

- No displacement at the axis $z = 0$

$$u_z^{\alpha}(z=0) = u_z^{\beta}(z=0) = 0 \quad \Rightarrow \quad d_{\alpha} = d_{\alpha} = 0 \qquad \text{when} \qquad z = 0 \tag{H.15}$$

- Free surface at $r = R$, as there can be no force normal at equilibrium

$$\sigma_{rr}^{\beta}(r=R) = 0 \quad \Rightarrow \quad A_{\beta} - \frac{B_{\beta}}{R^2} - D_{\beta} = 0 \qquad \text{when} \qquad r = R \tag{H.16}$$

- No net force over the ends of the cylinder at $z = H$

$$\int_0^R 2\pi r \sigma_{zz} dr = 0 \qquad \text{when} \qquad z = H \tag{H.17}$$

Using the expression of axial stress, we get

$$\begin{aligned} \sigma_{zz}^{\alpha} r_{int}^2 + \sigma_{zz}^{\beta}(R^2 - r_{int}^2) &= 0 \\ (C_{\alpha} - D_{\alpha}) r_{int}^2 + (C_{\beta} - D_{\beta})(R^2 - r_{int}^2) &= 0 \end{aligned} \tag{H.18}$$

- The boundary (at $z = H$) remains straight

$$u_z^{\alpha}(z=h) = u_z^{\beta}(z=h) \quad \Rightarrow \quad C_{\alpha} - 2\nu A_{\alpha} = C_{\beta} - 2\nu A_{\beta} \qquad \text{when} \qquad z = H \tag{H.19}$$

The mechanical boundary conditions and the continuity conditions across the interface are summarised as

$$b_{\alpha} = B_{\alpha} = 0 \tag{H.20}$$

$$d_{\alpha} = d_{\alpha} = 0 \tag{H.21}$$

$$\frac{1-\nu}{E}(A_{\alpha} - A_{\beta}) - \frac{\nu}{E}(C_{\alpha} - C_{\beta}) - \frac{B_{\beta}}{2\mu r_{int}^2} = 0 \tag{H.22}$$

$$(A_{\alpha} - A_{\beta}) - (D_{\alpha} - D_{\beta}) + \frac{B_{\beta}}{r_{int}^2} = 0 \tag{H.23}$$

$$A_{\beta} - \frac{B_{\beta}}{R^2} - D_{\beta} = 0 \tag{H.24}$$

$$(C_{\alpha} - D_{\alpha}) r_{int}^2 + (C_{\beta} - D_{\beta})(R^2 - r_{int}^2) = 0 \tag{H.25}$$

$$(C_{\alpha} - C_{\beta}) - (2\nu A_{\alpha} - 2\nu A_{\beta}) = 0 \tag{H.26}$$

Equations ((H.22)- (H.23)) are five algebraic equations in five unknowns $(A_{\alpha}, A_{\beta}, B_{\beta}, C_{\alpha} \text{ and } C_{\beta})$.

Choosing β as the stress free reference state ($\underset{\sim}{\varepsilon}^{\star}_{\beta} = 0, D_\beta = 0$), the solution is expressed as follows:

$$
\begin{aligned}
&B_\alpha = 0, \, , D_\beta = 0, \, d_\alpha = d_\beta = 0 \\
&B_\beta = \frac{1-2\nu}{2(1-\nu)} \, D_\alpha \, r_{int}^2, \quad A_\beta = \frac{B_\beta}{R^2} = \frac{(1-2\nu) D_\alpha}{2(1-\nu)} \left(\frac{r_{int}}{R}\right)^2 \\
&A_\alpha = B_\beta \left[\frac{1}{R^2} - \frac{1}{r_{int}^2}\right] + D_\alpha = \frac{D_\alpha}{2(1-\nu)} \left[(1-2\nu)\left(\frac{r_{int}}{R}\right)^2 + 1\right] \\
&C_\alpha = \left(\frac{r_{int}}{R}\right)^2 D_\alpha - \frac{2\nu \, B_\beta}{(1-2\nu)} \left[\frac{1}{R^2} - \frac{1}{r_{int}^2}\right] = \frac{\nu D_\alpha}{(1-\nu)} \left[\frac{1-2\nu}{\nu}\left(\frac{r_{int}}{R}\right)^2 + 1\right] \\
&C_\beta = \left(\frac{r_{int}}{R}\right)^2 D_\alpha - \frac{2\nu \, B_\beta}{(1-2\nu)} \frac{1}{R^2} = \frac{(1-2\nu) D_\alpha}{(1-\nu)} \left(\frac{r_{int}}{R}\right)^2 \\
&a_\alpha = \frac{(1-2\nu)(1+\nu) D_\alpha}{2E(1-\nu)} \left[\frac{(1-3\nu)}{(1+\nu)}\left(\frac{r_{int}}{R}\right)^2 + 1\right], \quad a_\beta = \frac{(1-2\nu)(1-3\nu) D_\alpha}{2E(1-\nu)} \left(\frac{r_{int}}{R}\right)^2 \\
&b_\beta = \frac{(1-2\nu)(1+\nu) D_\alpha}{2E(1-\nu)} \, r_{int}^2, \quad c_\alpha = c_\beta = \frac{(1-2\nu) D_\alpha}{E} \left(\frac{r_{int}}{R}\right)^2
\end{aligned}
\tag{H.27}
$$

Thus, the strain and stress field in the precipitate can then be expressed explicitly, using Eq. H.9, as follows:

$$
\begin{cases}
\sigma_{rr} = \sigma_{\theta\theta} = \left[\left(\frac{r_{int}}{R}\right)^2 - 1\right] p_e & r \leq r_{int} \\
\sigma_{rr} = \left[\left(\frac{r_{int}}{R}\right)^2 - \left(\frac{r_{int}}{r}\right)^2\right] p_e, \quad \sigma_{\theta\theta} = \left[\left(\frac{r_{int}}{R}\right)^2 + \left(\frac{r_{int}}{r}\right)^2\right] p_e & r \geq r_{int} \\
\sigma_{zz} = \sigma_{rr} + \sigma_{\theta\theta} & \forall r
\end{cases}
\tag{H.28}
$$

$$
\begin{cases}
\varepsilon_{rr} = \varepsilon_{\theta\theta} = \frac{(1+\nu)}{E} \left[\frac{(1-3\nu)}{(1+\nu)}\left(\frac{r_{int}}{R}\right)^2 + 1\right] p_e & r \leq r_{int} \\
\varepsilon_{rr} = \varepsilon_{rr}^e = \frac{(1+\nu)}{E} \left[\frac{(1-3\nu)}{(1+\nu)}\left(\frac{r_{int}}{R}\right)^2 - \left(\frac{r_{int}}{r}\right)^2\right] p_e & r \geq r_{int} \\
\varepsilon_{\theta\theta} = \varepsilon_{\theta\theta}^e = \frac{(1+\nu)}{E} \left[\frac{(1-3\nu)}{(1+\nu)}\left(\frac{r_{int}}{R}\right)^2 + \left(\frac{r_{int}}{r}\right)^2\right] p_e & r \geq r_{int} \\
\varepsilon_{zz} = \frac{2(1-\nu)}{E} \left(\frac{r_{int}}{R}\right)^2 p_e & \forall r
\end{cases}
\tag{H.29}
$$

$$\begin{cases} u_r = r\,\varepsilon_{\theta\theta} = \dfrac{(1+\nu)}{E}\ \left[\dfrac{(1-3\nu)}{(1+\nu)}\left(\dfrac{r_{int}}{R}\right)^2 + 1\right]\ p_e\, r & r \le r_{int} \\ u_r = r\,\varepsilon_{\theta\theta} = \dfrac{(1+\nu)}{E}\ \left[\dfrac{(1-3\nu)}{(1+\nu)}\left(\dfrac{r_{int}}{R}\right)^2 + \left(\dfrac{r_{int}}{r}\right)^2\right]\ p_e\, r & r \ge r_{int} \\ u_z = z\,\varepsilon_{zz} = \dfrac{2(1-\nu)}{E}\ \left(\dfrac{r_{int}}{R}\right)^2\ p_e\, z & \forall r \end{cases} \tag{H.30}$$

where $p_e = \dfrac{(1-2\nu)D_\alpha}{2(1-\nu)} = \dfrac{E\varepsilon^\star_\alpha}{2(1-\nu)}$.
It must be noted that we have $c = 0$ and $C = 2\nu A$, under the assumption of plane strain. Thus, the axial stress σ_{zz} is given by:

$$\sigma_{zz} = \nu(\sigma_{rr} + \sigma_{\theta\theta}) \tag{H.31}$$

For the case of infinite matrix, the analytical solution to the stress and strain fields in both phases are deduced from the above solutions for the finite matrix assuming an infinite radius:

$$\begin{cases} \sigma_{rr} = \sigma_{\theta\theta} = \dfrac{1}{2}\sigma_{zz} = -p_e \quad \text{inside the particle} & r \le r_{int} \\ \sigma_{rr} = -\sigma_{\theta\theta} = -p_e\left(\dfrac{r_{int}}{r}\right)^2, \quad \text{and} \quad \sigma_{zz} = 0 & r_{int} \leqslant r \end{cases} \tag{H.32}$$

$$\begin{cases} \varepsilon_{rr} = \varepsilon_{\theta\theta} = \dfrac{1+\nu}{E}p_e \quad \text{inside the particle} & r \le r_{int} \\ \varepsilon_{rr} = -\varepsilon_{\theta\theta} = -\dfrac{(1+\nu)}{E}p_e\ \left(\dfrac{r_{int}}{r}\right)^2 & r_{int} \leqslant r \\ \varepsilon_{zz} = 0 & \forall r \end{cases} \tag{H.33}$$

$$\begin{cases} u_r = \varepsilon_{\theta\theta}\, r = \dfrac{(1+\nu)}{E}pe\ r \quad \text{inside the particle} & r \le r_{int} \\ u_r = \varepsilon_{\theta\theta}\, r = \dfrac{(1+\nu)}{E}p_e\ \dfrac{r_{int}^2}{r} & r_{int} \leqslant r \\ u_z = \varepsilon_{zz}\, z = 0 & \forall r \end{cases} \tag{H.34}$$

Annexe -I-

Mechanical solution for a misfitting spherical precipitate in an isotropic matrix

The complete solutions to the displacement, stress and strain fields for an isotropic misfitting spherical precipitate are obtained, firstly in the absence of plastic relaxation, i.e., under purely elastic conditions. Then, the solutions is extended when plastic deformation takes place in the matrix.

We consider a misfitting precipitate in an isotropic matrix with an outer radius R. The symmetries of geometry, boundary conditions, loading and the isotropic constitutive materials suggest that the variables field are independent of the circumferential coordinates ϕ, θ. The displacement field depends only on a radial coordinate r as

$$\begin{cases} u_r = u_r(r) \\ u_\theta = u_\phi = 0 \end{cases} \tag{I.1}$$

Thus, strain and stress fields have the following forms:

$$\underset{\sim}{\boldsymbol{\varepsilon}} = \mathrm{grad}\underline{\boldsymbol{u}} = \begin{bmatrix} u_{r,r} & 0 & 0 \\ 0 & \dfrac{u_r}{r} & 0 \\ 0 & 0 & \dfrac{u_r}{r} \end{bmatrix} \quad \text{and} \quad \underset{\sim}{\boldsymbol{\sigma}} = \begin{bmatrix} f(r) & 0 & 0 \\ 0 & g(r) & 0 \\ 0 & 0 & g(r) \end{bmatrix} \tag{I.2}$$

Elastic equilibrium

We shall obtain the displacement, stress and strain fields for an isotropic misfitting spherical precipitate, assuming purely elastic behaviour for both phases. The application of Hooke's law provides stress components in both matrix and precipitate as

$$\sigma_{rr} = \frac{\lambda}{\nu}\left[(1-\nu)\frac{\partial u_r}{\partial r} + 2\nu\frac{u_r}{r}\right] - \frac{E}{(1-2\nu)}\varepsilon^\star \tag{I.3}$$

$$\sigma_{\theta\theta} = \sigma_{\phi\phi} = \frac{\lambda}{\nu}\left[\nu\frac{\partial u_r}{\partial r} + \frac{u_r}{r}\right] - \frac{E}{(1-2\nu)}\varepsilon^\star \tag{I.4}$$

where σ_{rr} and $\sigma_{\theta\theta}$ are respectively radial and tangential stress components.

In the absence of body forces, the stresses must satisfy the static equilibrium equation, which is expressed, in spherical coordinate, as

$$\sigma_{rr,r} + \frac{2}{r}(\sigma_{rr} - \sigma_{\theta\theta}) = 0 \tag{I.5}$$

substituting Eqs (I.3) and (I.4) into the static equilibrium equation (I.5), we

$$\frac{\partial^2 u_r}{\partial r^2} + \frac{2}{r}\frac{\partial u_r}{\partial r} - \frac{2}{r^2}u_r = 0 \qquad \text{or} \qquad \left(\frac{1}{r^2}\left(r^2 u_r\right)_{,r}\right)_{,r} = 0 \tag{I.6}$$

the general radial displacement is known to be of the following form

$$u_r = ar + \frac{b}{r^2} \tag{I.7}$$

Once the radial displacement is defined, the strain and stress fields can then be written explicitly in the following form

$$\begin{cases} \varepsilon_{rr} &= a - 2\dfrac{b}{r^3} \\ \varepsilon_{\theta\theta} &= a + \dfrac{b}{r^3} \\ \varepsilon_{r\theta} &= \varepsilon_{r\phi} = \varepsilon_{\phi\theta} = 0 \end{cases} \qquad \begin{cases} \sigma_{rr} &= A - 2\dfrac{B}{r^3} - C \\ \sigma_{\theta\theta} &= \sigma_{\phi\phi} = A + \dfrac{B}{r^3} - C \\ \sigma_{r\theta} &= \sigma_{r\phi} = \sigma_{\phi\theta} = 0 \end{cases} \tag{I.8}$$

where

$$A = (3\lambda + 2\mu)a\,, \qquad B = 2\mu\, b \qquad \text{and} \qquad C = (3\lambda + 2\mu)\varepsilon^\star = \frac{E}{(1-2\nu)}\varepsilon^\star \tag{I.9}$$

A and B are determined, ensuring that the displacement and stress field satisfy the boundary/interface conditions, in terms of the problem specification.

Assuming zero misfit strain in the matrix ($\underset{\sim}{\boldsymbol{\varepsilon}}^\star_\beta = 0$), the eigenstrain in the precipitate is chosen to be a spherical tensor as

$$\underset{\sim}{\boldsymbol{\varepsilon}}^\star_\alpha = \varepsilon^\star \underset{\sim}{\mathbf{1}} \tag{I.10}$$

where $\underset{\sim}{\mathbf{1}}$ the unit second order tensor.

The following mechanical boundary conditions to the system have been applied:

$$\begin{aligned} u^\alpha_r(r=0,\theta) = 0 \quad &\Rightarrow \quad b_\beta = B_\beta = 0 \quad &&: \text{symmetric boundary condition at } r = 0 \\ \sigma^\beta_{rr}(r=R,\theta) = 0 \quad &\Rightarrow \quad A_\beta - 2\frac{B_\beta}{R^3} = 0 \quad &&: \text{free surface condition at } r = R \end{aligned} \tag{I.11}$$

The continuity conditions of both displacement and traction, across the interface between the α and β phases, are given by:

$$u^\alpha_r(r = r_{int}) = u^\beta_r(r = r_{int}) \qquad \Rightarrow \qquad A_\alpha = A_\beta + \frac{(3\lambda + 2\mu)B_\beta}{2\mu_\beta}\frac{1}{r^3_{int}} \tag{I.12}$$

$$\sigma^\alpha_{rr}(r = r_{int}) = \sigma^\beta_{rr}(r = r_{int}) \qquad \Rightarrow \qquad A_\alpha - C_\alpha = A_\beta - 2\frac{B_\beta}{r^3_{int}} \tag{I.13}$$

Equations (I.11), (I.12) and (I.13) are three algebraic equations in three unkowns $(A_\alpha, A_\beta \text{ and } B_\beta)$. the solution is expressed as follows:

$$A_\alpha = \left(\frac{r_{int}^3}{R^3} - 1\right) p_e + C_\alpha \,, \qquad A_\beta = \frac{r_{int}^3}{R^3} p_e \tag{I.14}$$

$$B_\alpha = 0 \,, \qquad B_\beta = \frac{r_{int}^3}{2} p_e \tag{I.15}$$

where

$$p_e = \frac{4\mu(3\lambda + 2\mu)\varepsilon_\alpha^\star}{(3\lambda + 6\mu)} = \frac{2E}{3(1-\nu)}\varepsilon_\alpha^\star \tag{I.16}$$

The substitution of Eq. (I.14) and Eq. (I.15), into Eq. (I.7) and Eq. (I.8), leads to the expression of the stress, strain and displacement in both precipitate and finite matrix, in pure elastic state:

$$\begin{cases} \sigma_{rr} = \sigma_{\theta\theta} = \sigma_{\phi\phi} = \left[\left(\dfrac{r_{int}}{R}\right)^3 - 1\right] p_e & r \leq r_{int} \\ \sigma_{rr} = \left(\left[\dfrac{r_{int}}{R}\right]^3 - \left[\dfrac{r_{int}}{r}\right]^3\right) p_e & r \geqslant r_{int} \\ \sigma_{\theta\theta} = \sigma_{\phi\phi} = \left(\left[\dfrac{r_{int}}{R}\right]^3 + \dfrac{1}{2}\left[\dfrac{r_{int}}{r}\right]^3\right) p_e & r \geqslant r_{int} \end{cases} \tag{I.17}$$

$$\begin{cases} \varepsilon_{rr} = \varepsilon_{\theta\theta} = \varepsilon_{\phi\phi} = \left[\dfrac{1}{3\lambda + 2\mu}\left(\dfrac{r_{int}}{R}\right)^3 + \dfrac{1}{4\mu}\right] p_e & r \leq r_{int} \\ \varepsilon_{rr}^e = \varepsilon_{\theta\theta}^e = \varepsilon_{\phi\phi}^e = \dfrac{1}{3\lambda + 2\mu}\sigma_{rr} = \dfrac{p_e}{3\lambda + 2\mu}\left[\left(\dfrac{r_{int}}{R}\right)^3 - 1\right] & r \leq r_{int} \\ \varepsilon_{rr} = \varepsilon_{rr}^e = \left(\dfrac{1}{3\lambda + 2\mu}\left[\dfrac{r_{int}}{R}\right]^3 - \dfrac{1}{2\mu}\left[\dfrac{r_{int}}{r}\right]^3\right) p_e & r \geqslant r_{int} \\ \varepsilon_{\theta\theta} = \varepsilon_{\theta\theta}^e = \left(\dfrac{1}{3\lambda + 2\mu}\left[\dfrac{r_{int}}{R}\right]^3 + \dfrac{1}{4\mu}\left[\dfrac{r_{int}}{r}\right]^3\right) p_e & r \geqslant r_{int} \end{cases} \tag{I.18}$$

$$\begin{cases} u = (\varepsilon_{rr}^e + \varepsilon^\star)\, r = \dfrac{p_e}{3\lambda + 2\mu}\left[\left(\dfrac{r_{int}}{R}\right)^3 - 1\right] r + \varepsilon^\star r & r \leq r_{int} \\ u = \varepsilon^\star r + \left(\dfrac{r_{int}^3 r}{(3\lambda + 2\mu)R^3} + \dfrac{r_{int}^3}{4\mu r^2}\right) p_e & r \geqslant r_{int} \end{cases} \tag{I.19}$$

For the case of an infinite matrix containing a single spherical precipitate, the above solutions are extended, assuming in infinite radius $(1/R = 0)$, as

$$\begin{cases} \sigma_{rr} = \sigma_{\theta\theta} = \sigma_{\phi\phi} = -\dfrac{2B_2}{r_{int}^3} = -p_e & r \leq r_{int} \\ \sigma_{rr} = -2\sigma_{\theta\theta} = -p_e \left(\dfrac{r_{int}}{r}\right)^3 & r_{int} \leq r \end{cases} \tag{I.20}$$

$$\begin{cases} \varepsilon_{rr} = \varepsilon_{\theta\theta} = \varepsilon_{\phi\phi} = \dfrac{p_e}{4\mu} & r \leq r_{int} \\ \varepsilon^e_{rr} = \varepsilon^e_{\theta\theta} = \varepsilon^e_{\phi\phi} = \dfrac{1}{3\lambda+2\mu}\sigma_{rr} = -\dfrac{p_e}{3\lambda+2\mu} & r \leq r_{int} \\ \varepsilon_{rr} = \varepsilon^e_{rr} = -2\varepsilon_{\phi\phi} = -2\varepsilon^e_{\theta\theta} = -\dfrac{p_e}{2\mu}\left[\dfrac{r_{int}}{r}\right]^3 & r \geqslant r_{int} \end{cases} \tag{I.21}$$

$$\begin{cases} u = (\varepsilon^e_{rr} + \varepsilon^\star)\, r = -\dfrac{p_e}{3\lambda+2\mu} r + \varepsilon^\star r & r \leq r_{int} \\ u = \dfrac{p_e}{4\mu}\dfrac{r^3_{int}}{r^2} & r \geqslant r_{int} \end{cases} \tag{I.22}$$

Elasto-plastic equilibrium

The matrix is now assumed to be an elasto-plastic material. The complete solution of a general problem in plasticity involves a calculation of the stress and the deformation in both elastic and plastic regions. In the former the stress is directly connected with the total strain by means of the elasticity equations. The stress-strain differential relations have to be integrated by following the history of the deformation from the initiation of plasticity at some point of the body. We adopt the von Mises yielding criterion, namely that yielding occurs when an equivalent stress $\sigma_{\rm eq}$ reachs the yield stress σ^0_β, where $\sigma_{\rm eq}$ is given by the following equation:

$$\begin{aligned} \sigma_{\rm eq} &= \frac{1}{\sqrt{2}}\left[(\sigma_{rr}-\sigma_{\theta\theta})^2 + (\sigma_{rr}-\sigma_{\phi\phi})^2 + (\sigma_{\phi\phi}-\sigma_{\theta\theta})^2\right]^{1/2} \\ &= \sigma_{\theta\theta} - \sigma_{rr} \end{aligned} \tag{I.23}$$

Taking the symmetry associated with a misfitting sphere in an isotropic matrix into account, the resulting stress field within the precipitate is purely hydrostatic, then unable to promote yielding. The plastic relaxation cannot occur in the precipitate and it is confined entirely to the matrix phase. Since, by virtue of the symmetry, the state of stress in the matrix is $(\sigma_{rr}, \sigma_{\phi\phi} = \sigma_{\theta\theta})$ whereas in the inclusion is $(\sigma_{rr} = \sigma_{\phi\phi} = \sigma_{\theta\theta})$. Consequently, the yield criterion (I.23) is

$$\sigma^0_\beta = \sigma_{\theta\theta} - \sigma_{rr} = \frac{3}{2} p_e \left(\frac{r_{int}}{r}\right)^3 \tag{I.24}$$

Therefore, according to the above equation, yielding will start at the matrix-precipitate interface when the internal pressure reaches the critical value $2\sigma^0_\beta/3$ at $r = r_p$. As the internal pressure increases beyond the critical value, a plastic zone develops adjacent to the matrix-precipitate interface of radius $r = r_p$:

$$r_p = r_{int}\left(\frac{3}{2\sigma^0_\beta} p_e\right)^{1/3} \tag{I.25}$$

The deformed region of the matrix is subjected to a pressure p at the internal surface of radius r_{int} by the misfitting spherical precipitate. In the elastic region in both precipitate and matrix, the stresses are still of the form

$$\begin{cases} \sigma_{rr} = \sigma_{\theta\theta} = -p & r \leqslant r_{int} \\ \sigma_{rr} = -2\sigma_{\theta\theta} = A\left(\dfrac{r_p}{r}\right)^3 & r_p \leqslant r \end{cases} \tag{I.26}$$

where A parameter to be determined, which corresponds to an internal pressure at the internal surface of radius r_p in the elastic region of the matrix. By substituting the critical value $2\sigma_\beta^0/3$ at $r = r_p$, the stress components in the elastic region of the matrix are obtained as

$$\sigma_{rr} = -2\sigma_{\theta\theta} = -\frac{2\sigma_\beta^0}{3}\left(\frac{r_p}{r}\right)^3 \tag{I.27}$$

Let us study the plastic zone $r_{int} < r < r_p$. We have the equilibrium equation, in conjunction with the plasticity criterion, which must be satisfied in any point:

$$\sigma_{rr,r} + \frac{2}{r}(\sigma_{rr} - \sigma_{\theta\theta}) = 0 \tag{I.28}$$

$$\sigma_{\theta\theta} - \sigma_{rr} = \sigma_\beta^0 \tag{I.29}$$

Combining these two equations, we get:

$$\frac{d\sigma_{rr}}{dr} - \frac{2}{r}\sigma_\beta^0 = 0 \tag{I.30}$$

Integrating the above equation and using the boundary condition $\sigma_{rr} = -p$ at $r = r_{int}$, the radial stress, is known to have the following form in the plastic zone:

$$\sigma_{rr} = 2\sigma_\beta^0 \ln(\frac{r}{r_{int}}) - p \tag{I.31}$$

The solutions in the elastic and plastic regions are interrelated by certain continuity conditions in the stresses and displacement which must be satisfied along the plastic-elastic boundary. Assuming the continuity of the radial stress σ_{rr} at $r = r_p$, we get

$$p = 2\sigma_\beta^0 \ln(\frac{r_p}{r_{int}}) + \frac{2}{3}\sigma_\beta^0 \tag{I.32}$$

Consequently, the analytical expressions of the stress fields, assuming an ideal plastic behaviour for an isotropic matrix are

$$\begin{cases} \sigma_{rr} = \sigma_{\theta\theta} = -p & r \leqslant r_{int} \\ \sigma_{rr} = \sigma_{\theta\theta} - \sigma_\beta^0 = 2\sigma_\beta^0 \ln(\frac{r}{r_{int}}) - p & r_{int} \leqslant r \leqslant r_p \\ \sigma_{rr} = -2\sigma_{\theta\theta} = -\frac{2\sigma_\beta^0}{3}\left(\frac{r_p}{r}\right)^3 & r_p \leqslant r \end{cases} \tag{I.33}$$

According to Hooke's law, the strain components, in the elastic precipitate and the elastic region

of the matrix, are given by:

$$\begin{cases} \varepsilon^e_{rr} = \varepsilon^e_{\theta\theta} = \varepsilon^e_{\phi\phi} = \dfrac{(1-2\nu)}{E}\sigma_{rr} = -\dfrac{(1-2\nu)}{E}p & r \leqslant r_{int} \\ \varepsilon_{rr} = \varepsilon_{\theta\theta} = \varepsilon_{\phi\phi} = \varepsilon^e_{rr} + \varepsilon^\star = \varepsilon^\star - \dfrac{(1-2\nu)}{E}p & r \leqslant r_{int} \\ \varepsilon^e_{rr} = \dfrac{1}{2\mu(1+\nu)}\left[\sigma_{rr} - 2\nu\sigma_{\theta\theta}\right] = \dfrac{2\sigma^0_\beta}{3K}\ln(\dfrac{r}{r_{int}}) - \dfrac{p}{3K} - \dfrac{\nu}{\mu(1+\nu)}\sigma^0_\beta & r_p \leqslant r \\ \varepsilon^e_{\theta\theta} = \dfrac{1}{2\mu(1+\nu)}\left[(1-\nu)\sigma_{\theta\theta} - \nu\sigma_{rr}\right] = \dfrac{2\sigma^0_\beta}{3K}\ln(\dfrac{r}{r_{int}}) - \dfrac{p}{3K} + \dfrac{\sigma^0_\beta}{6\mu\alpha} & r_p \leqslant r \\ \varepsilon^e_{rr} = -2\varepsilon^e_{\theta\theta} = -2\varepsilon^e_{\phi\phi} = \dfrac{\sigma_{rr}}{2\mu} = -\dfrac{\sigma^0_\beta}{3\mu}\left(\dfrac{r_p}{r}\right)^3 & r_p \leqslant r \end{cases} \tag{I.34}$$

knowing that the strains are related to the radial displacement u_r by,

$$\varepsilon_{rr} = \frac{\partial u_r}{\partial r}, \qquad \varepsilon_{\theta\theta} = \frac{u_r}{r} \tag{I.35}$$

the substitution of the strain components (I.34) into the above equation leads to the expression of the displacement:

$$\begin{cases} u = \varepsilon_{\theta\theta} r = \left(\varepsilon^e_{rr} + \varepsilon^\star\right) r = -\dfrac{p}{3\lambda + 2\mu} r + \varepsilon^\star r & r \leqslant r_{int} \\ u = \varepsilon_{\theta\theta} r = \dfrac{\sigma^0_\beta}{6\mu}\dfrac{r^3_p}{r^2} & r_p \leqslant r \end{cases} \tag{I.36}$$

Within the plastic zone, the strain is the sum of the plastic and elastic strains. Since the elastic strain is related to stresses by Hooke's law, we may write:

$$\varepsilon_{rr} = \frac{\partial u_r}{\partial r} = \frac{1}{E}\left[\sigma_{rr} - 2\nu\sigma_{\theta\theta}\right] + \varepsilon^p_r \tag{I.37}$$

$$\varepsilon_{\theta\theta} = \frac{u_r}{r} = \frac{1}{E}\left[(1-\nu)\sigma_{\theta\theta} - \nu\sigma_{rr}\right] + \varepsilon^p_\theta \tag{I.38}$$

where ε^p_r and ε^p_θ denote plastic strain components in the plastic zone. In order to obtain the displacement u in this zone, we use the incompressibility condition for plastic strain, $\varepsilon^p_r + 2\varepsilon^p_\theta = 0$. Multiplying Eq.(I.38) by 2, adding the result to Eq.(I.37) and using the stress components in the plastic region ($\sigma_{rr} = \sigma_{\theta\theta} - \sigma^0_\beta = 2\sigma^0_\beta \ln(\dfrac{r}{r_{int}}) - p$), we obtain:

$$\frac{\partial u_r}{\partial r} + \frac{2u_r}{r} = \frac{1}{3\mathrm{K}}\left[3\sigma_{rr} + 2\sigma^0_\beta\right] = \frac{2\sigma^0_\beta}{K}\ln(\frac{r}{r_{int}}) + \frac{2\sigma^0_\beta - 3p}{3\mathrm{K}} \tag{I.39}$$

where $3\mathrm{K} = \dfrac{E}{(1-2\nu)} = \dfrac{2\mu(1+\nu)}{(1-2\nu)}$

knowing that $\dfrac{\partial u_r}{\partial r} + \dfrac{2u_r}{r} = \dfrac{1}{r^2}\dfrac{\partial r^2 u_r}{\partial r}$, the general solution for the displacement is

$$u_r = \frac{2\sigma^0_\beta}{3K} r \ln(\frac{r}{r_{int}}) - \frac{p}{3\mathrm{K}} r + \frac{C_1}{r^2} \tag{I.40}$$

C_1 is determined, ensuring the continuity of the displacements (I.36) and (I.40) at $r = r_p$ and using the Eq. (I.32)

$$\frac{2\sigma_\beta^0}{3K} r_p \ln(\frac{r_p}{r_{int}}) - \frac{p}{3\mathrm{K}} r_p + \frac{C_1}{r_p^2} = \frac{\sigma_\beta^0}{6\mu} r_p \qquad \Rightarrow \qquad C_1 = \frac{\sigma_\beta^0 (1-\nu)}{2\mu(1+\nu)} r_p^3 \tag{I.41}$$

After substituting the above expression of C_1 in (I.40), the displacement in the plastic zone is found to be:

$$u_r = \frac{2\sigma_\beta^0}{3K} r \ln(\frac{r}{r_{int}}) - \frac{p}{3\mathrm{K}} r + \frac{\sigma_\beta^0}{6\mu\alpha} \frac{r_p^3}{r^2} \quad \text{with} \quad \alpha = \frac{(1+\nu)}{3(1-\nu)} \tag{I.42}$$

Thus, the strain components in the plastic zone are finally given, using Eq. (I.35), as

$$\varepsilon_{rr} = \frac{2\sigma_\beta^0}{3K} \left[\ln(\frac{r}{r_{int}}) + 1 \right] - \frac{p}{3\mathrm{K}} - \frac{\sigma_\beta^0}{3\mu\alpha} \left(\frac{r_p}{r} \right)^3 \tag{I.43}$$

$$\varepsilon_{\theta\theta} = \frac{2\sigma_\beta^0}{3K} \ln(\frac{r}{r_{int}}) - \frac{p}{3\mathrm{K}} + \frac{\sigma_\beta^0}{6\mu\alpha} \left(\frac{r_p}{r} \right)^3 \tag{I.44}$$

Once the elastic and total strains, in the plastic zone, are known; Eqs. (I.44,I.34), the plastic strain is finally given by

$$\varepsilon_{rr}^p = -2\varepsilon_{\theta\theta}^p = \frac{\sigma_\beta^0}{3\mu\alpha} \left\{ 1 - \left(\frac{r_p}{r} \right)^3 \right\} \tag{I.45}$$

Consequently, complete solutions to the stress, displacement, elastic and total strains, for an isotropic misfitting spherical precipitate in an infinite matrix, are summarised as:

$$\begin{cases} \sigma_{rr} = \sigma_{\theta\theta} = -p & r \leqslant r_{int} \\ \sigma_{rr} = \sigma_{\theta\theta} - \sigma_\beta^0 = 2\sigma_\beta^0 \ln(\dfrac{r}{r_{int}}) - p & r_{int} \leqslant r \leqslant r_p \\ \sigma_{rr} = -2\sigma_{\theta\theta} = -\dfrac{2\sigma_\beta^0}{3} \left(\dfrac{r_p}{r} \right)^3 & r_p \leqslant r \end{cases} \tag{I.46}$$

$$\begin{cases} \varepsilon_{rr}^e = \varepsilon_{\theta\theta}^e = \varepsilon_{\phi\phi}^e = \dfrac{(1-2\nu)}{E} \sigma_{rr} = -\dfrac{(1-2\nu)}{E} p & r \leqslant r_{int} \\ \varepsilon_{rr}^e = \dfrac{2\sigma_\beta^0}{3K} \ln(\dfrac{r}{r_{int}}) - \dfrac{p}{3K} - \dfrac{\nu}{\mu(1+\nu)} \sigma_\beta^0 & r_{int} \leqslant r \leqslant r_p \\ \varepsilon_{\theta\theta}^e = \dfrac{2\sigma_\beta^0}{3K} \ln(\dfrac{r}{r_{int}}) - \dfrac{p}{3K} + \dfrac{\sigma_\beta^0}{6\mu\alpha} & r_{int} \leqslant r \leqslant r_p \\ \varepsilon_{rr}^e = -2\varepsilon_{\theta\theta}^e = -2\varepsilon_{\phi\phi}^e = \dfrac{1+\nu}{E} \sigma_{rr} = \dfrac{\sigma_{rr}}{2\mu} = -\dfrac{\sigma_\beta^0}{3\mu} \left(\dfrac{r_p}{r} \right)^3 & r_p \leqslant r \end{cases} \tag{I.47}$$

$$\begin{cases} \varepsilon_{rr} = \varepsilon_{\theta\theta} = \varepsilon_{\phi\phi} = \varepsilon^e_{rr} + \varepsilon^\star = \varepsilon^\star - \dfrac{(1-2\nu)}{E} p & r \leqslant r_{int} \\ \varepsilon_r = \dfrac{2\sigma^0_\beta}{3K}\left[\ln(\dfrac{r}{r_{int}}) + 1\right] - \dfrac{p}{3\mathrm{K}} - \dfrac{\sigma^0_\beta}{3\mu\alpha}\left(\dfrac{r_p}{r}\right)^3 & r_{int} \leqslant r \leqslant r_p \\ \varepsilon_\theta = \dfrac{2\sigma^0_\beta}{3K}\ln(\dfrac{r}{r_{int}}) - \dfrac{p}{3\mathrm{K}} + \dfrac{\sigma^0_\beta}{6\mu\alpha}\left(\dfrac{r_p}{r}\right)^3 & r_{int} \leqslant r \leqslant r_p \\ \varepsilon_{rr} = -2\varepsilon_{\theta\theta} = -2\varepsilon_{\phi\phi} = \dfrac{1+\nu}{E}\sigma_{rr} = \dfrac{\sigma_{rr}}{2\mu} = -\dfrac{\sigma^0_\beta}{3\mu}\left(\dfrac{r_p}{r}\right)^3 & r_p \leqslant r \end{cases} \tag{I.48}$$

$$\begin{cases} u = \varepsilon_{\theta\theta} r = \left(\varepsilon^e_{rr} + \varepsilon^\star\right) r = -\dfrac{p}{3\lambda + 2\mu} r + \varepsilon^\star r & r \leqslant r_{int} \\ u_r = \dfrac{2\sigma^0_\beta}{3K} r \ln(\dfrac{r}{r_{int}}) - \dfrac{p}{3\mathrm{K}} r + \dfrac{\sigma^0_\beta}{6\mu\alpha}\dfrac{r_p^3}{r^2} \quad \text{with} \quad \alpha = \dfrac{(1+\nu)}{3(1-\nu)} & r_{int} \leqslant r \leqslant r_p \\ u = \varepsilon_{\theta\theta} r = \dfrac{\sigma^0_\beta}{6\mu}\dfrac{r_p^3}{r^2} & r_p \leqslant r \end{cases} \tag{I.49}$$

In order to determine the equilibrium concentrations at the interface (IV.89), we must define the energy $\Delta\mathcal{E}$ (IV.90), due to the effect of the dilatation misfit generated stress in both cases, i.e. under purely elastic state and with plastic relaxation in the matrix.

1. **Elastic state**

   Using Eqs. (I.21) and (I.20), the elastic energies in both phases $f_{e\alpha}, f_{e\beta}$ and the coherency energy $\mathcal{E}_{\mathrm{coh}}$ are expressed, at the interface $(r = r_{int})$, as follows:

$$f_{e\alpha} = \frac{1}{2}\underset{\sim}{\boldsymbol{\sigma}}_\alpha : \underset{\sim}{\boldsymbol{\varepsilon}}^e_\alpha = \frac{3}{2}\frac{p_e^2}{3\lambda + 2\mu} \tag{I.50}$$

$$f_{e\beta} = \frac{1}{2}\underset{\sim}{\boldsymbol{\sigma}}_\beta : \underset{\sim}{\boldsymbol{\varepsilon}}_\beta = \frac{3}{8\mu} p_e^2 \tag{I.51}$$

$$\mathcal{E}_{\mathrm{coh}} = \left(\underset{\sim}{\boldsymbol{\varepsilon}}^e_\beta - \underset{\sim}{\boldsymbol{\varepsilon}}^e_\alpha\right) : \underset{\sim}{\boldsymbol{\sigma}}_\beta = \left(\varepsilon^\beta_{rr} - \varepsilon^\alpha_{rr}\right) : \underset{\sim}{\boldsymbol{\sigma}}_\beta = \frac{3}{4\mu} p_e^2 \tag{I.52}$$

$$\Delta\mathcal{E} = \mathcal{E}_{\mathrm{coh}} - \Delta f_{\mathrm{e}} = -\left[\frac{9(\lambda + 2\mu)}{8\mu(3\lambda + 2\mu)}\right] p_e^2 \tag{I.53}$$

   The substitution of Eq (I.16) into (I.53) leads to following relation

$$\boxed{\Delta\mathcal{E} = \frac{(\varepsilon^\star)^2}{A}}$$

   where $A = \dfrac{\lambda + 2\mu}{2\mu(3\lambda + 2\mu)} = \dfrac{1-\nu}{E}$

2. **Plastic deformation**

The elastic energies in the two phases $f_{e\alpha}, f_{e\beta}$ and the coherence energy are given, by the expression of the stress (I.46), elastic strain (I.47) and total strain (I.48), at the interface, as

$$\mathcal{E}_\alpha = \frac{1}{2}\underset{\sim}{\boldsymbol{\sigma}}_\alpha : \underset{\sim}{\boldsymbol{\varepsilon}}^e_\alpha = \frac{3}{2}\frac{(1-2\nu)}{E}p^2 = \frac{3}{2}\frac{1}{3\lambda+2\mu}p^2 = \frac{1}{2K}p^2 \tag{I.54}$$

$$\mathcal{E}_\beta = \frac{1}{2}\underset{\sim}{\boldsymbol{\sigma}}_\beta : \underset{\sim}{\boldsymbol{\varepsilon}}^e_\beta = \frac{1}{2K}p^2 - \frac{2}{3K}\sigma^0_\beta p + \frac{1}{6\mu\alpha}(\sigma^0_\beta)^2 \tag{I.55}$$

$$\mathcal{E}_{\text{coh}} = \left(\varepsilon^\beta_{rr} - \varepsilon^\alpha_{rr}\right) : \underset{\sim}{\boldsymbol{\sigma}}_\beta = p\left(\varepsilon^\star - \frac{(1-2\nu)}{E}p - \frac{2\sigma^0_\beta}{3K} + \frac{p}{3\mathrm{K}} + \frac{\sigma^0_\beta}{3\mu\alpha}\left(\frac{r_p}{r}\right)^3\right) \tag{I.56}$$

where

$$3\alpha = \frac{(1+\nu)}{(1-\nu)} = \frac{3\lambda+2\mu}{\lambda+2\mu}, \qquad 3\mathrm{K} = \frac{E}{(1-2\nu)} \tag{I.57}$$

Substituting Eq. (I.16) into Eq. (I.25),

$$\varepsilon^\star = \frac{3\lambda+6\mu}{4\mu(3\lambda+2\mu)}p_e = A\sigma^0_\beta\left(\frac{r_p}{r_{int}}\right)^3 = \frac{\sigma^0_\beta}{6\mu\alpha}\left(\frac{r_p}{r_{int}}\right)^3 \tag{I.58}$$

and rearranging the result with Eq. (I.56) provides the following expression for the coherency energy at the interface:

$$\mathcal{E}_{\text{coh}} = p\left(3\varepsilon^\star - \frac{2\sigma^0_\beta}{3K}\right) \tag{I.59}$$

where the internal plastic pressure can be expressed, by substituting the expression of the plastic zone radius (I.58) into Eq. (I.32), as

$$p = 2\sigma^0_\beta \ln(\frac{r_p}{r_{int}}) + \frac{2}{3}\sigma^0_\beta = \frac{2}{3}\sigma^0_\beta\left[\ln\left(\frac{\varepsilon^\star}{A\sigma^0_\beta}\right) + 1\right] \tag{I.60}$$

Once the elastic energies and the coherence energy are known in the interface Eqs. (I.54,I.55,I.59) and using the expression of the internal plastic pressure (I.60), the energy $\Delta\mathcal{E}$ is expressed in the interface, when plastic relaxation takes place in the matrix, as :

$$\begin{aligned}
\Delta\mathcal{E} &= \mathcal{E}_{\text{coh}} - \Delta\mathcal{E}_{\text{el}} \\
&= 3\varepsilon^\star p - \frac{1}{6\mu\alpha}(\sigma^0_\beta)^2 \\
&= 3\varepsilon^\star p - \frac{\lambda+2\mu}{2\mu(3\lambda+2\mu)}(\sigma^0_\beta)^2 \\
&= 2\sigma^0_\beta\varepsilon^\star\left[\ln\left(\frac{\varepsilon^\star}{A\sigma^0_\beta}\right) + 1\right] - A(\sigma^0_\beta)^2
\end{aligned} \tag{I.61}$$

$$\boxed{\Delta\mathcal{E} = 2\sigma^0_\beta\varepsilon^\star\left[\ln\left(\frac{\varepsilon^\star}{A\sigma^0_\beta}\right) + 1\right] - A(\sigma^0_\beta)^2}$$